Research Reports from the Communications Research Laboratory
at Ilmenau University of Technology

Nuan Song

Ultra Wideband Communications: from Analog to Digital

TECHNISCHE UNIVERSITÄT
ILMENAU

Fakultät für Elektrotechnik und Informationstechnik
der Technischen Universität Ilmenau

Ultra Wideband Communications: from Analog to Digital

Nuan Song

Dissertation zur Erlangung des
akademischen Grades Doktor-Ingenieur (Dr.-Ing.)

Anfertigung im:	Fachgebiet Nachrichtentechnik Institut für Informationstechnik Fakultät für Elektrotechnik und Informationstechnik
Gutachter:	Univ.-Prof. Dr.-Ing. Martin Haardt Univ.-Prof. Dr.-Ing. Giovanni Del Galdo Dr. Rodrigo C. de Lamare, University of York
Vorgelegt am:	03.07.2012
Verteidigt am:	05.10.2012

urn:nbn:de:gbv:ilm1-2012000336

ACKNOWLEDGMENTS

I owe my gratitude to many people who have made this dissertation possible.

My deepest gratitude goes to my supervisor Prof. Martin Haardt, who provided me such a precious opportunity to work at Communications Research Laboratory. I am greatly thankful to him for his invaluable guidance and immense support, which made my research experience productive and stimulating. His way of expressing ideas, writing technical articles, and making presentations have significantly influenced my professional personality and helped me to become a qualified researcher. I am also very grateful to him for carefully reading and commenting on revisions of this work.

I would like to particularly thank Dr. Mike Wolf for his insightful comments and constructive suggestions during the four-year UKoLoS project, which helped me to form the major contents of this work. He has an in-depth knowledge of the communication areas as well as the issues regarding practical realizations. I appreciate the time spent working with him and many long discussions that improved the technical details of my work.

I am truly thankful to Dr. Rodrigo de Lamare for our fruitful collaboration on widely linear reduced-rank techniques presented in Part II of this dissertation. He has always been there to listen, discuss and give advice. Without his inspiring ideas, perceptive comments, and great patience, our collaboration work would not have been successful. I am also grateful to him for accepting to be a reviewer of this work. Additionally, I would like to thank Dr. Lei Wang, one of the members in his lab, for working together on this topic.

I am grateful to Prof. Giovanni Del Galdo, Marko Milojević, and Prof. Albert Heuberger for the successful cooperation project on satellite to indoor channel modeling, leading to the TU Ilmenau Best Paper Award in the area of “Engineering Sciences”. As one of my former colleagues, Prof. Giovanni Del Galdo supported a lot in this project with crucial suggestions and valuable hints, which helped me to get off to a good start for my PhD pursuit. I also thank to him for being a reviewer of this work.

I am obliged to the past and present group members that have contributed immensely to my personal and professional life at TU Ilmenau. Everything was difficult at the start. However, Ulrike Korger, Marko Hennhöfer, and Martin Fuchs-Lautensack, who helped me a lot with my accommodation, health insurance, banking, and many other bureaucratic issues, made my start much simpler. I am very indebted to them for their generous support. I particularly thank Yao Cheng for helping me to proofread this work and Dominik Schulz for improving the German abstract. I would also like to express my sincere gratitude to the other colleagues, Florain Römer, Veljko Stanković, Bin Song, João Paulo Carvalho Lustosa da Costa, Martin Weis, Jianhui Li, Liane Grobe, Jianshu Zhang, Sheng Li, Bilal Zafar,

and Jens Steinwandt. A special thanks goes to Wolfgang Erdtmann, who has been always available for technical problems. I also thank to our secretary Ms. Christina Patotschka for her organization and help in our group, which make our work more efficient.

An earnest thanks goes to the family Kienast (Prof. Woldemar Kienast, MR Dr. Rosl Kienast, and Sascha Kienast) for their support and encouragement. They do make me feel at home here in Ilmenau. I especially thank my friend Haifeng Xu, whom I also consider as an "elder brother", for sharing both the sadness and the happiness as well as for enriching my life in Ilmenau.

I would like to thank my husband for taking good care of me during my PhD study and helping me overcome the setbacks.

A huge thanks is to my little boy for accompanying me all the time especially "inside my belly", when I strove for writing the dissertation.

Most importantly, none of these would have been possible without the love, the patience, the constant support and encouragement of my parents.

"You raise me up, so I can stand on mountains;
You raise me up, to walk on stormy seas;
I am strong, when I am on your shoulders;
You raise me up, to more than I can be."

Ilmenau, June 2012

Nuan Song

ABSTRACT

The aim of this thesis is to investigate key issues encountered in the design of transmission schemes and receiving techniques for Ultra Wideband (UWB) communication systems. Based on different data rate applications, this work is divided into two parts, where energy efficient and robust physical layer solutions are proposed, respectively.

Due to a huge bandwidth of UWB signals, a considerable amount of multipath arrivals with various path gains is resolvable at the receiver. For low data rate impulse radio UWB systems, suboptimal non-coherent detection is a simple way to effectively capture the multipath energy. Feasible techniques that increase the power efficiency and the interference robustness of non-coherent detection need to be investigated. For high data rate direct sequence UWB systems, a large number of multipath arrivals results in severe inter-/intra-symbol interference. Additionally, the system performance may also be deteriorated by multi-user interference and narrowband interference. It is necessary to develop advanced signal processing techniques at the receiver to suppress these interferences.

Part I of this thesis deals with the co-design of signaling schemes and receiver architectures in low data rate impulse radio UWB systems based on non-coherent detection.

- We analyze the bit error rate performance of non-coherent detection and characterize a non-coherent combining loss, i.e., a performance penalty with respect to coherent detection with maximum ratio multipath combining. The thorough analysis of this loss is very helpful for the design of transmission schemes and receive techniques in non-coherent UWB communication systems.

- We propose to use optical orthogonal codes in a time hopping impulse radio UWB system based on an ***analog*** non-coherent receiver. The "***analog***" means that the major part of the multipath combining is implemented by an integrate and dump filter. The introduced semi-analytical method can help us to easily select the time hopping codes to ensure the robustness against the multi-user interference and meanwhile to alleviate the non-coherent combining loss.

- The main contribution of Part I is the proposal of applying fully ***digital*** solutions in non-coherent detection. The proposed ***digital*** non-coherent receiver is based on a time-domain analog-to-digital converter, which has a high speed but a very low resolution to maintain a reasonable power consumption. Compared to its ***analog*** counterpart, it not only significantly reduces the non-coherent combining loss but also offers a higher

interference robustness. In particular, the one-bit receiver can effectively suppress strong multi-user interference and is thus advantageous in separating simultaneously operating piconets.

The fully ***digital*** solutions overcome the difficulty of implementing long analog delay lines and make differential UWB detection possible. They also facilitate the development of various digital signal processing techniques such as multi-user detection and non-coherent multipath combining methods as well as the use of advanced modulation schemes (e.g., M-ary Walsh modulation).

- Furthermore, we present a novel impulse radio UWB system based on frequency hopping, where both coherent and non-coherent receivers can be adopted. The key advantage is that the baseband bandwidth can be considerably reduced (e.g., $\ll 500$ MHz), which enables low-complexity implementation of the fully ***digital*** solutions. It opens up various research activities in the application field of wireless sensor networks.

Part II of this thesis proposes adaptive widely linear reduced-rank techniques to suppress interferences for high data rate direct sequence UWB systems, where second-order non-circular signals are used. The reduced-rank techniques are designed to improve the convergence performance and the interference robustness especially when the received vector contains a large number of samples (due to a high sampling rate in UWB systems). The widely linear processing takes full advantage of the second-order statistics of the non-circular signals and enhances the estimation performance. The generic widely linear reduced-rank concept also has a great potential in the applications of other systems such as Direct Sequence Code Division Multiple Access (DS-CDMA), Multiple Input Multiple Output (MIMO) system, and Global System for Mobile Communications (GSM), or in other areas such as beamforming.

ZUSAMMENFASSUNG

Ultrabreitband-Signale (Ultra Wideband [UWB]) können einen signifikanten Nutzen im Bereich drahtloser Kommunikationssysteme haben. Es sind jedoch noch einige Probleme offen, die durch Systemdesigner und Wissenschaftler gelöst werden müssen. Ein Funknetzsystem mit einer derart großen Bandbreite ist normalerweise auch durch eine große Anzahl an Mehrwegekomponenten mit jeweils verschiedenen Pfadamplituden gekennzeichnet. Daher ist es schwierig, die zeitlich verteilte Energie effektiv zu erfassen. Außerdem ist in vielen Fällen der naheliegende Ansatz, ein kohärenter Empfänger im Sinne eines signalangepassten Filters oder eines Korrelators, nicht unbedingt die beste Wahl. In der vorliegenden Arbeit wird dabei auf die bestehende Problematik und weitere Lösungsmöglichkeiten eingegangen.

Im ersten Abschnitt geht es um „Impulse Radio UWB"-Systeme mit niedriger Datenrate. Bei diesen Systemen kommt ein inkohärenter Empfänger zum Einsatz. Inkohärente Signaldetektion stellt insofern einen vielversprechenden Ansatz dar, als das damit aufwandsgünstige und robuste Implementierungen möglich sind. Dies trifft vor allem in Anwendungsfällen wie den von drahtlosen Sensornetzen zu, wo preiswerte Geräte mit langer Batterielaufzeit nötig sind. Dies verringert den für die Kanalschätzung und die Synchronisation nötigen Aufwand, was jedoch auf Kosten der Leistungseffizienz geht und eine erhöhte Störempfindlichkeit gegenüber Interferenz (z.B. Interferenz durch mehrere Nutzer oder schmalbandige Interferenz) zur Folge hat.

Um die Bitfehlerrate der oben genannten Verfahren zu bestimmen, wurde zunächst ein inkohärenter Combining-Verlust spezifiziert, welcher auftritt im Gegensatz zu kohärenter Detektion mit Maximum Ratio Multipath Combining. Dieser Verlust hängt von dem Produkt aus der Länge des Integrationsfensters und der Signalbandbreite ab.

Um den Verlust durch inkohärentes Combining zu reduzieren und somit die Leistungseffizienz des Empfängers zu steigern, werden verbesserte Combining-Methoden für Mehrwegeempfang vorgeschlagen.

Ein analoger Empfänger, bei dem der Hauptteil des Mehrwege-Combinings durch einen „Integrate and Dump"-Filter implementiert ist, wird für UWB-Systeme mit Zeit-Hopping gezeigt. Dabei wurde die Einsatzmöglichkeit von dünn besetzten Codes in solchen System diskutiert und bewertet. Des Weiteren wird eine Regel für die Code-Auswahl vorgestellt, welche die Stabilität des Systems gegen Mehrnutzer-Störungen sicherstellt und gleichzeitig den Verlust durch inkohärentes Combining verringert.

Danach liegt der Fokus auf digitalen Lösungen bei inkohärenter Demodulation. Im Vergleich zum Analogempfänger besitzt ein Digitalempfänger einen Analog-Digital-Wandler im Zeitbereich gefolgt von einem digitalen Optimalfilter. Der digitale Optimalfilter dekodiert

den Mehrfachzugriffscode kohärent und beschränkt das inkohärente Combining auf die empfangenen Mehrwegekomponenten im Digitalbereich. Es kommt ein schneller Analog-Digital-Wandler mit geringer Auflösung zum Einsatz, um einen vertretbaren Energieverbrauch zu gewährleisten. Diese Digitaltechnik macht den Einsatz langer Analogverzögerungen bei differentieller Demodulation unnötig und ermöglicht viele Arten der digitalen Signalverarbeitung. Im Vergleich zur Analogtechnik reduziert sie nicht nur den inkohärenten Combining-Verlust, sonder zeigt auch eine stärkere Resistenz gegenüber Störungen. Dabei werden die Auswirkungen der Auflösung und der Abtastrate der Analog-Digital-Umsetzung analysiert. Die Resultate zeigen, dass die verminderte Effizienz solcher Analog-Digital-Wandler gering ausfällt. Weiterhin zeigt sich, dass im Falle starker Mehrnutzerinterferenz sogar eine Verbesserung der Ergebnisse zu beobachten ist. Die vorgeschlagenen Design-Regeln spezifizieren die Anwendung der Analog-Digital-Wandler und die Auswahl der Systemparameter in Abhängigkeit der verwendeten Mehrfachzugriffscodes und der Modulationsart. Wir zeigen, wie unter Anwendung erweiterter Modulationsverfahren die Leistungseffizienz verbessert werden kann und schlagen ein Verfahren zur Unterdrückung schmalbandiger Störer vor, welches auf Soft Limiting aufbaut. Durch die Untersuchungen und Ergebnissen zeigt sich, dass inkohärente Empfänger in UWB-Kommunikationssystemen mit niedriger Datenrate ein großes Potential aufweisen.

Außerdem wird die Auswahl der benutzbaren Bandbreite untersucht, um einen Kompromiss zwischen inkohärentem Combining-Verlust und Stabilität gegenüber langsamen Schwund zu erreichen. Dadurch wurde ein neues Konzept für UWB-Systeme erarbeitet: wahlweise kohärente oder inkohärente Empfänger, welche als UWB-Systeme Frequenz-Hopping nutzen. Der wesentliche Vorteil hiervon liegt darin, dass die Bandbreite im Basisband sich deutlich verringert (z.B. $\ll$ 500 MHz). Mithin ermöglicht dies einfach zu realisierende digitale Signalverarbeitungstechnik mit kostengünstigen Analog-Digital-Wandlern. Dies stellt eine neue Epoche in der Forschung im Bereich drahtloser Sensorfunknetze dar.

Der Schwerpunkt des zweiten Abschnitts stellt adaptiven Signalverarbeitung für hohe Datenraten mit „Direct Sequence"-UWB-Systemen in den Vordergrund. In solchen Systemen entstehen, wegen der großen Anzahl der empfangenen Mehrwegekomponenten, starke Inter- bzw. Intrasymbolinterferenzen. Außerdem kann die Funktionalität des Systems durch Mehrnutzerinterferenz und Schmalbandstörungen deutlich beeinflusst werden. Um sie zu eliminieren, wird die „Widely Linear"-Rangreduzierung benutzt. Dabei verbessert die Rangreduzierungsmethode das Konvergenzverhalten, besonders wenn der gegebene Vektor eine sehr große Anzahl an Abtastwerten beinhaltet (in Folge hoher einer Abtastrate). Zusätzlich kann das System durch die Anwendung der R-linearen Verarbeitung die Statistik zweiter Ordnung des nicht-zirkularen Signals vollständig ausnutzen, was sich in verbesserten Schätzergebnissen widerspiegelt. Allgemeine kann die Methode der „Widely Linear"-Rangreduzierung auch in andern Bereichen angewendet werden, z.B. in „Direct Sequence"-Codemultiplexverfahren (DS-CDMA), im MIMO-Bereich, im Global System for Mobile Communications (GSM) und beim Beamforming.

CONTENTS

LIST OF FIGURES

LIST OF TABLES

1. INTRODUCTION

1.1 Background

Once upon a time, as referred to baseband, carrier-less, impulse, time domain, etc., Ultra Wideband (UWB) was a misnomer until about 1989, when the U.S. Department of Defense (DoD) termed such techniques as UWB [BV01]. The origin of UWB dates back to the spark-gap transmission experiments carried out by Hertz and Marconi in 1890s, where the electromagnetic waves were generated in a form of Impulse Radio (IR). However, during that period, the benefits of a wide bandwidth and the potential of accommodating multiple users by such a radio were never exploited. Only in the 1960s, impulse radar applications facilitated the development of generating baseband sub-nanosecond pulses after their advantages of the fine-time resolution and low-frequency properties to penetrate materials were observed.

The first U.S. patent on the design of a short pulse based communication system by Ross [Ros73] was granted in 1973, which was considered as one of the pioneering contributions to UWB. Later in 1978, Bennet and Ross provided a comprehensive review on the time-domain electromagnetic technology as well as foresaw its applications in the baseband radar and even in communications [BR78]. Following the trend of many other communication technologies, the use of UWB was exclusively restricted in military applications for some decades. After UWB was defined by the DoD in 1989, the research activities on UWB technologies have considerably increased. A milestone contribution to UWB communications was the Time Hopping (TH) IR multiple access technique proposed by Scholtz and Win [Sch93, WS98, WS02]. The concept of the TH spread spectrum IR technique was to employ a sequence of time shifted baseband pulses on the order of sub-nanoseconds in duration. Thus, the bandwidth spanned from near Direct Current (DC) to several GHz with a very low power spectrum density. Due to such a large bandwidth, a significant number of multipath arrivals could be resolved and as a consequence the fading effects would be significantly reduced. The low power spectral density ensured that the IR systems did not interfere with other narrowband radio systems. It was also pointed out that the "baseband" or "carrier-less" feature of IR reduced the complexity of the transceiver design, since no mixers and local oscillators or the carrier recovery were required.

A breakthrough in UWB communications was featured by the release of a First Report and Order by the U.S. Federal Communications Commission (FCC) in February 2002 [Fed02], which allocates an unlicensed bandwidth of several GHz for the commercial use of UWB in both indoor and outdoor applications. It defines the signals that have an absolute bandwidth of at least 500 MHz which needs to be covered within 1 ms or a relative bandwidth of at least

20 % as UWB signals. The operating frequency is limited from 3.1 GHz to 10.3 GHz and the average Effective Isotropic Radiated Power (EIRP) is up to -41.3 dBm/MHz. After this regulation and a subsequent approval for the petition waiver in 2005 by the FCC [FCC05], the unlicensed operation of UWB devices has been widely permitted worldwide in different specified frequency bands. In Europe, the European Communications Commission (ECC) and all national CEPT administrations permit the generic use (unspecified application) of UWB at a power spectral density of -41.3 dBm/MHz ranging from 6.0 to 8.5 GHz without detect and avoid techniques [ECC07, Com08]. By applying detect and avoid, UWB devices are also allowed to operate between 3.1 GHz and 4.8 GHz at -41.3 dBm/MHz. Figure 1.1 illustrates the spectral mask from both the FCC and the ECC. The peak power is also limited, i.e., the maximum peak power is 0 dBm measured in 50 MHz. In contrast to the FCC regulation, the generic UWB reglation in Europe has no resitrictive definition for UWB but specifies that the operation bandwidth shall be greater than 50 MHz. According to the recent regulations and new definitions of UWB, UWB is no longer considered as a technology but a shared spectrum for the unlicensed use. Independent from any modulation and spreading schemes, an UWB emission is spectrum compliant as long as the requirements for the maximum mean/peak power constraints are satisfied. Thereby, UWB signals can be generated by any means, such as TH IR, Direct Sequence (DS), Frequency Hopping (FH), Orthogonal Frequency Division Multiplexing (OFDM), chirps, etc..

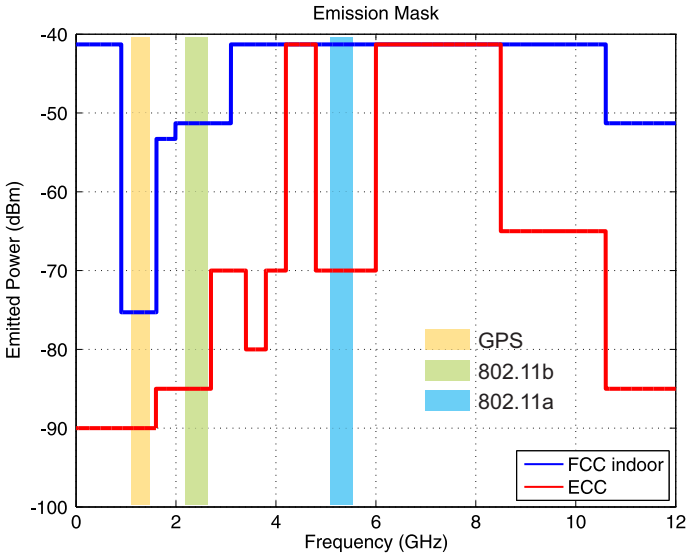

Fig. 1.1: UWB spectral mask from the FCC and the ECC.

The establishment and the evolution of the spectrum regulations have raised a considerable amount of research and development activities in both academia and industry. Several UWB systems were proposed for different data rate applications. Two approaches originally specified in IEEE 802.15.3a proposals, namely DS-UWB [FKLW05] and Multi-Band Orthogonal Frequency Division Multiplexing (MB-OFDM)-UWB [Bat01], are considered for high-speed and short-range Wireless Personal Area Networks (WPANs), where the latter has been stan-

dardized as ECMA-368 by the WiMedia Alliance [Sta08]. The IEEE 802.15.4a specifies an alternative UWB physical layer solution for low-to-medium data rate applications such as WPANs and Wireless Sensor Networks (WSNs) [IEE07]. It is mainly based on TH IR for the purpose of providing both communications as well as high-precision ranging and localization capabilities. It is aimed at low power consumption and low-cost implementations.

1.2 Motivation and Objectives

Regardless of the UWB applications, high data rate or low data rate, commercial, military, or industrial, robust physical layer solutions are of prime importance especially in the scenarios with multipath propagation, Multi-User Interference (MUI), and Narrowband Interference (NBI). Thus, the main purpose of this thesis is to investigate and develop power efficient physical layer solutions for UWB communication systems by considering both the performance and the implementation issues.

The very large bandwidth of UWB signals results in a considerable amount of resolvable multipath components. Fully exploiting such a multipath diversity can significantly reduce the fading margin, providing a high immunity to the small scale fading. The essential issue lies in the effective capture of the energy contained in the multipath arrivals, i.e., the receiver has to combine the multipath energy spread over time. The optimal solution from the point of view of maximizing the signal-to-noise ratio is to apply a coherent receiver, in terms of a channel matched filter or a correlator.

However, as we will discuss in the following, such coherent detection may not be the best choice.

Based on different data rate applications, we divide the overall work into two parts, where the corresponding motivation, the state of the art and research challenges, as well as objectives are presented separately.

Part I: Non-coherent detection for low data rate UWB systems

In low-to-medium data rate (i.e., from several kbps up to tens of Mbps) applications such as Wireless Sensor Networks (WSNs), the critical concern arises from the development of low-complexity and robust techniques that are capable of supporting low-cost devices with a long battery life time.

▽ ***Motivation**: the high complexity of **coherent** detection*

An appropriate coherent RAKE receiver or its matched filter equivalent performs maximum ratio combining and exploits the multipath diversity to a large extent. However, it is only regarded as optimum if all RAKE fingers are realized with the full knowledge of channel amplitudes and phases. Due to the presence of numerous resolvable paths, the coherent RAKE demands a large number of fingers and correlators, which is quite complicated and costly. Channel estimation imposes a higher difficulty on the receiver implementations, since

both the amplitudes and the delays of many channel taps have to be acquired. To solve these problems, simplified coherent receivers have been proposed [CWVM07]. For example, the selective RAKE coherently combines the energy from a small number of strongest paths while the partial RAKE captures the energy from the first group of paths. Although either scheme can reduce the amount of correlators, a sufficient number of combined paths is still indispensable to obtain a satisfying performance. Moreover, the performance of coherent detection is quite sensitive to the clock jitter and thus stringent synchronization on the order of sub-nanosecond is required. The sophisticated signal processing may lead to a prohibitive complexity.

△ ***Solution***:

Non-coherent detection, which can easily collect multipath energy by means of equal gain combining, becomes a promising candidate for low date rate and low-complexity UWB applications [WLJ+09]. A non-coherent receiver can be based on either energy detection or differential detection [Pro01]. The energy detector simply employs a square-law device to remove any phase information and accumulates the multipath energy via an integrator. The differential detection exploits the phase difference or polarity between two subsequent symbols or pulses that are differentially encoded [1], by means of a delay and a mixer.

▽ ***The state of the art and Challenge 1****: poor power efficiency of* ***non-coherent*** *detection*

Compared to the coherent receiver, non-coherent detection is sub-optimal, although it does not require expensive channel estimation and is more immune to synchronization errors. The sub-optimality, or the performance penalty, is caused by the receiver noise that is collected along with the time-spread energy. A lot of work has been carried out to improve the performance [WH04b, TM04, DDdRO05, GQ06, ZOM+07, NS07]. Nevertheless, the penalty of characterizing the behavior of non-coherent detection has not been sufficiently analyzed.

△ ***Objective****:*

On the one hand, we will obtain the origins of such a penalty by analytically evaluating the performance. On the other hand, based on the analysis, simple yet robust transceiver strategies are proposed to increase the power efficiency of non-coherent detection.

▽ ***The state of the art and Challenge 2****: the presence of* ***interferences***

The impact of MUI and NBI should be taken into account.

An appropriate selection of TH codes ensures MUI robustness. This selection is usually achieved by the analytical performance evaluation. In contrast to DS-UWB, the MUI in TH-UWB appears impulsive [DK06]. An exact analysis is challenging, since it should be

[1] Because the channel can be assumed to be constant over two or more symbol periods, its absolute phase is removed.

performed according to the distribution of impulsive interference [DB03, HB04] and non-coherent operation complicates the statistics of the decision variables. A few references have suggested convenient methods to estimate the multiple access performance of non-coherent receivers [SZ08]. There are not yet enough answers concerning how the system design should be tailored to MUI scenarios.

Furthermore, the presence of strong NBI is detrimental to non-coherent UWB systems. Robust receiver designs require the development of simple and efficient NBI suppression techniques. A number of publications have analyzed the performance of non-coherent detection corrupted by NBI [QWD07, SW07] and several mitigation schemes have been proposed accordingly [SW07, DvdV06, AW07]. Most existing schemes are designed for differential receivers and always implemented after non-coherent processing. As a result of such a non-linear operation, the subsequent mitigation algorithm has to handle both the squared NBI term and the cross term between the desired signal and the NBI.

△ ***Objective:***

In this work, we concentrate on these open problems for energy detection, carrying out an appropriate and in-depth analysis of the multiple access performance as well as proposing general system design criteria with simple interference mitigation schemes.

▽ ***The state of the art and Challenge 3:*** *the expensive* ***Analog to Digital Converters***

The Analog-to-Digital Converter (ADC) at the receiver is one of the most important devices that determine the implementation complexity of UWB systems. Due to the huge bandwidth of UWB signals, an ADC has to operate at a sampling rate on the order of GHz, which is power demanding and very expensive. The power consumption of an ADC is determined by the sampling rate and the resolution. Decreasing either/both of them will result in a reduced complexity.

→ ***Alternative solution 1: analog*** *non-coherent combining*

Most existing non-coherent UWB receivers are based on analog devices (e.g., integrate and dump filters), since the sampling rate for the output can be reduced down to symbol rate or frame rate. However, as it has been found out that the performance of these ***analog*** receivers is noticeably degraded due to noise, a lot of transmit and receive techniques have been proposed to enhance the robustness [CS02, TM04, DM05, GQ06]. A major drawback is that these enhanced schemes require long delay lines, which are too difficult to accurately realize in the analog domain. Besides, to deal with interferences, sophisticated signal processing techniques have to be conducted at a high price. Obviously, these problems further restrict the development of the analog non-coherent receivers.

→ ***Alternative solution 2: ADC*** *in the frequency domain*

To reduce the sampling rate, [Nam03] proposes to channelize the spectrum of the signal into several sub-bands using a bank of analog bandpass filters such that the ADCs can operate

at a fraction of the Nyquist rate. Another approach is to apply parallel ADCs after projecting the time-domain signals onto orthogonal basis functions in the frequency domain [HS05]. The resulting sampling rate is thus reduced. However, these methods require several analog filter banks or local basis function generators, mixers, and integrators to integrate multiple signals. Additionally, mismatch among parallel branches may also occur. These problems demand extra efforts due to the increased implementation complexity.

The question that needs to be answered is whether "fully" ***digital*** solutions can overcome the difficulties in Alternative solutions 1 and 2. (*)

→ ***Alternative solution** 3: **ADC** in the time domain*

The resolution of a high-speed ADC can be kept very low for the sake of reducing the power consumption [Wal99, Nam01, VLD06, MN08]. The rapid advances in semiconductor technology have shown the availability and potential of implementing high-rate and low-resolution ADCs [OCWB02, Wah09]. Moreover, fully digital receivers are able to accommodate flexible designs of various digital signal processing algorithms. Whereas plenty of work on digital receivers is often associated with coherent detection [WS02, OCWB02, OK08, MWS03, CM06], the concept of applying fully digital solutions to non-coherent receivers is quite promising [HSA05, TXS07, FM07]. Some interesting conclusions drawn from these publications show that even with a very low ADC resolution the non-coherent UWB system can still maintain its robustness without a significant performance loss. However, what has not been investigated but of great interest is how to characterize the quantization loss due to the sampling rate and the resolution of ADCs as well as the influence of ADCs on the overall system design especially in the presence of interferences.

△ ***Objective**:*

The answer to the previous question (*) is affirmative. We consider the approach using high-speed but very low-resolution ADCs. It will be pointed out why digital non-coherent UWB receivers will become popular. We provide a comprehensive roadmap, portraying the important contributions that indicate how non-coherent detection evolves from ***analog*** to ***digital***. This work deals in detail with the aspects that are missing in the state of the art, with respect to not only the performance analysis, but also modulation/spreading techniques, interference immunity, system design rules and the selection of parameters, the impact of the bandwidth, low-complexity receiver implementations, etc..

Part II: Advanced signal processing for high data rate UWB systems

▽ ***Motivation**:*

In high data rate (i.e., above tens of Mbps) UWB systems, e.g., time-domain based Direct Sequence Ultra Wideband (DS-UWB), severe Inter-/Intra-Symbol Interference (ISI) occurs

as a result of enormous multipath components collected at the receiver. The multiple access system supports multiple users or piconets to operate simultaneously, leading to the presence of MUI. The interference from other non-UWB networks, e.g., OFDM-based IEEE 802.11a wireless local area networks which overlap with the UWB spectrum, also deteriorates the performance of UWB systems. Under such circumstances, a channel matched filter based coherent receiver is no longer optimal. Signal processing techniques such as equalization and interference suppression are thus necessary and required to ensure robust communications.

▽ ***The state of the art and Challenges:***

In this part of the work, advanced signal processing techniques are devised to cope with the interference in a high date rate DS-UWB system. Most interference suppression techniques are based on linear filters [Hay02]. On the one hand, reduced-rank processing is desired [PK01, HG02, dLSN07], since in UWB systems the received signal vector contains a large number of samples due to numerous multipath arrivals. On the other hand, Widely Linear (WL) techniques, which largely exploit the second-order statistics of non-circular signals such as Binary Phase Shift Keying (BPSK) suggested in DS-UWB, can provide a better estimate than the linear schemes [PC95, SS03, SS10]. Therefore, the combination of reduced-rank techniques and WL processing is motivated for interference suppression in DS-UWB systems. Only a few existing WL reduced-rank schemes have been proposed but they rely on the computationally expensive eigen-decomposition [SS03].

△ ***Objective:***

The novelty of our work lies in the utilization of more robust but low-complexity reduced-rank techniques in conjunction with WL processing and the evaluation of their key properties. Our proposed algorithms are not limited to the application of UWB communications, but provide a general concept that can be applied in many other systems or areas such as Direct Sequence Code Division Multiple Access (DS-CDMA) and Global System for Mobile Communications (GSM) systems as well as beamforming applications.

1.3 Overview of the Dissertation

The outline of the work is briefly highlighted in the following.

Chapter 2 present some basics of UWB channels. Understanding UWB channels is essential in designing, evaluating, and comparing various techniques. Several distinguishing features of UWB channels are summarized and we take both the measured channels and the standardized channel models as examples to show how they are modeled and applied in our work.

Part I: Non-coherent detection for low data rate UWB systems

Chapter 3 introduces the fundamentals of non-coherent IR UWB systems. It firstly reviews the early concept of IR UWB and evaluates its spectral properties. The impact of

the FCC regulation on the Power Spectral Density (PSD) of various transmitted signals is then discussed. Finally, this chapter presents several widely applied single-carrier modulation schemes and the corresponding non-coherent receivers based on either energy detection or differential detection.

Chapter 4 deals with the performance evaluation and enhancement of non-coherent multipath combining. It first presents the E_b/N_0 performance [2] analysis and the comparison of different receiver architectures combined with their signaling schemes in multipath and Additive White Gaussian Noise (AWGN) channels. The analysis conveys the key characteristics of non-coherent detection and their impact on the system design. The E_b/N_0 performance loss due to non-coherent combining [3], namely the Non-Coherent Combining Loss (NC-CL), is analytically predicted even without considering concrete channel realizations. The NC-CL is the most important keyword throughout Part I, where the aim is to investigate and develop various transceiver strategies with the purpose of reducing the NC-CL from different perspectives.

The NC-CL can be reduced by effectively capturing the multipath energy. This chapter proposes two non-coherent multipath combining schemes to enhance the receiver performance. It further discusses the performance limit of non-coherent detection in multipath channels.

Chapter 5 investigates and evaluates analog non-coherent receivers in multi-user scenarios. For low-complexity reasons, the major part of most existing non-coherent receivers is implemented in terms of an analog integrator, which we refer to as the analog non-coherent receiver. This chapter describes a unified non-coherent multiple access UWB system and discusses practical issues regarding the implementation and performance. The main focus lies on a Time Hopping combined with Pulse Position Modulation (TH-PPM) UWB system with energy detection. To alleviate the NC-CL induced by multiple access codes, the suitability of applying some sparse TH codes is investigated. This chapter provides a semi-analytical method to evaluate the multiple access performance of the TH-PPM UWB system as well as derives a TH code selection rule to achieve both MUI robustness and NC-CL reduction.

Chapter 6 covers various transmit and receive techniques for low data rate UWB systems applying fully digital non-coherent receivers. It first describes the proposed Digital Code Matched Filter (DCMF)-based non-coherent receiver using a high-speed but very low-resolution ADC.

Compared to the analog counterparts, the main advantage of the digital concept is that the DCMF coherently decodes the multiple access codes and restricts the NC-CL only to the multipath arrivals. Such completely digital solutions can also avoid wideband analog delay lines and facilitate the development of various digital signal processing techniques. Besides the advantages from the NC-CL point of view, Section 6.3 compares analog and digital non-coherent receivers with respect to the interference robustness.

[2] E_b is the energy per bit and N_0 is the noise power spectrum density.
[3] The coherent detection acts as a reference.

To derive a system design rule for TH-PPM using the proposed digital non-coherent receiver, Section 6.4 carries out the performance analysis concerning the quantization and the multiple access behavior. One of the crucial components in the proposed digital receiver is the high-speed but low-resolution ADC. In Section 6.4.1, the quantization loss due to the simplest one-bit ADC is analytically predicted in a single-user multipath scenario. It further analyzes the performance influenced by increasing the resolution of the ADC and addresses the impact of the input signal level on the receiver design. Section 6.4.2 presents how the parameters of the TH codes affect the multiple access performance by analytically deriving the Bit Error Rate (BER) as well as by simulations in different situations.

From the system-level point of view, the proposed physical layer solutions should support their operation in the close proximity of multiple uncoordinated piconets at specific error rates. In Section 6.5, we evaluate the uncoordinated piconet channelization in multipath scenarios employing both analog and digital non-coherent receivers and compare their Simultaneously Operating Piconets (SOP) performances.

The NBI is one of the most severe sources that lead to the performance degradation in the UWB non-coherent receiver. Section 6.6 introduces a novel NBI suppression scheme using a soft limiter for the DCMF-based receiver. The NBI mitigation is implemented before the non-linear part of the non-coherent detection. We investigate the suitability of the proposed method by discussing the effect of the soft limiter threshold, the threshold adaptation, as well as the frequency dependency.

Besides various receiver strategies, better transmission schemes, e.g., M-ary orthogonal modulations, are also promising to improve the power efficiency of non-coherent detection. They are more robust to MUI with increasing M due to their inherent orthogonality. Section 6.7 proposes two TH M-ary Walsh transmission schemes for the digital non-coherent receiver and exploits their potentials to achieve both power and bandwidth efficiencies. It also compares M-Pulse Position Modulation (PPM) and M-Walsh schemes in terms of the quantization impact and the multiple access performance.

From the ADC power consumption point of view, increasing the sampling frequency (oversampling) is better than increasing the ADC resolution, where the latter even requires the adjustment of the input signal level. The Sigma-Delta ($\Sigma\Delta$) ADCs have shown a significant improvement in the signal-to-quantization-noise ratio because of the oversampling and noise shaping characteristics. Section 6.8 proposes a digital non-coherent UWB receiver applying the first-order one-bit $\Sigma\Delta$ADCs. We evaluate the quantization impact of $\Sigma\Delta$ADCs on the UWB system design, taking into account the modulation schemes (M-ary PPM/Walsh), signaling parameters, and receiver requirements on the oversampling rate as well as the complexity.

Chapter 7 proposes a novel UWB system based on the FH technique. Increasing the bandwidth offers a higher robustness to the small scale fading while it may yield a greater performance loss (e.g., NC-CL) since more noise and interferences are incorporated. Section 7.2 discusses the choice of an appropriate bandwidth for non-coherent UWB systems to deal

with such a trade-off. According to the analysis of the impact of the bandwidth on non-coherent receivers, we elaborate the underlying principle of the proposed FH-UWB system and emphasize its advantages compared to most existing UWB systems.

Part II: Advanced signal processing for high data rate UWB systems

Chapter 8 proposes various WL reduced-rank signal processing techniques to suppress interferences in high data rate DS-UWB systems. The WL schemes can largely exploit second-order statistics of non-circular signals, leading to a better performance compared to their linear counterparts. To efficiently process the data which contains a large number of samples, reduced-rank techniques are more promising than the full-rank methods in terms of the convergence performance and robustness against interferences. We combine the reduced-rank schemes with WL processing, taking advantage of both techniques. Section 8.1 reviews some fundamentals of second-order non-circular signals. Sections 8.3 and 8.4 detail the proposed two algorithms, namely the WL-Multistage Wiener Filter (MSWF) and the WL-Auxiliary Vector Filter (AVF). We also evaluate their key properties, complexity, and performances.

The proposed algorithms are not limited to the application of DS-UWB communication systems. The use of the WL-AVF and another WL reduced-rank algorithm named the WL-Joint Iterative Optimization (JIO) to solve adaptive beamforming problems is illustrated in [SSW+11, nso], respectively.

Chapter 9 concludes the work with a summary of the key results and a discussion of potential applications for **Part I** and **Part II**, respectively. It also points out future perspectives in the related research area.

1.4 Summary of Major Contributions

The major contributions are illustrated in Figure 1.2. Our publications and invited talks that are relevant to the dissertation can be found in [SWH07a, SWH09d, SWH09a, WSH09, WS09, SWH09c, WSdLH10, SdLWH10, SWH10b, SWH10a, SWH10d, SdLW+11, SSW+11, SdLHW12, SWH12, SWH07b, SWH08, SWH09b, SWH10c, SWH10e].

Part I: Non-coherent detection for low data rate UWB systems

The partition of different sections is mainly based on two aspects related with the NC-CL, i.e., *the integration interval* T_{i} [4] *and the signal bandwidth* B.

1. Analytical performance evaluation of non-coherent detection for the single-user case in Chapter 4 [SWH08, WSH09, WS09]

   - Comparison of energy detection and differential detection using their corresponding single-carrier modulation schemes in Section 4.1

[4] Here T_{i} is only used as a generalized notation for ease of analysis. It represents the integration interval of the energy that is spread by multipath and/or by the deterministic user-specific code (cf. Section 4.2).

- Prediction of the NC-CL with respect to E_b/N_0, determined by T_i and B in Section 4.2

2. Enhanced non-coherent multipath combining scheme in Section 4.3 of Chapter 4 (*reduction in T_i(multipath)-induced NC-CL*) [SWH07a]

   - Determination of the "best" integration interval by Single Window Combining (SinW-C)
   - Investigation of a simple Weighted Sub-Window Combining (WSubW-C) method
   - Derivation of a performance limit with "quasi" optimal weighting

3. Development and evaluation of analog receivers for TH-PPM in multi-user scenarios in Chapter 5 (*reduction in T_i(code)-induced NC-CL*) [SWH09d]

   - Semi-analytical estimation of the multiple access performance in multipath environments
   - Selection of sparse TH codes for MUI robustness

4. Development and evaluation of fully digital non-coherent receivers in Chapter 6 (*reduction in T_i(code)-induced NC-CL*)

   - Design of DCMF-based non-coherent receivers in Sections 6.3 and 6.4 [SWH09a, SWH10b]
     - Comparison of analog and digital non-coherent receivers in terms of the interference robustness
     - Analysis of the quantization effect due to the resolution of the ADC
     - Evaluation of the multiple access performance in perfect and imperfect power control cases and selection of the TH codes
   - Evaluation of the performance of the Simultaneously Operating Piconets (SOP) considering IEEE 802.15.4a channels in Section 6.5 [SWH12]
   - Development and analysis of NBI mitigation techniques using a soft limiter in Section 6.6 [SWH10a]
     - Analysis of the impact of both the soft limiter threshold and the ADC resolution
     - Investigation of a threshold adaptation scheme for the OFDM-based NBI
     - Discussion of the frequency dependent performance
   - Development and evaluation of advanced modulation schemes for a higher power efficiency in Section 6.7 [SWH10c, SWH10d]
     - Proposal of two TH M-ary Walsh transmission schemes
     - Analysis of the multiple access performance for different combinations of TH code parameters and modulation orders

  - Derivation of a selection criterion with respect to the transmission strategies
  - Comparison of TH M-ary Walsh modulation and TH M-ary PPM in terms of quantization robustness and multiple access performance
- Proposal of digital receivers using oversampling ΣΔADCs in Section 6.8 [SWH12]
  - Analysis of the quantization loss influenced by the oversampling rate, the modulation schemes (M-Walsh/M-PPM), and other transmission parameters.
  - Discussion on the advantages of using ΣΔADCs in the presence of interference

5. Proposal of a low-complexity FH-UWB system concept (*reduction in B-induced NC-CL*) in Chapter 7 [SWH09c, WSH09]
   - Selection of a useful bandwidth for TH-PPM
   - Design of the proposed FH-UWB system
   - Investigation of a non-coherent FH-PPM scheme to determine appropriate baseband bandwidths

Part II: Advanced signal processing for high data rate UWB systems

1. Development of interference suppression techniques for DS-UWB systems in Chapter 8
   - Proposal and analysis of the WL-MSWF algorithm in Section 8.3 [SdLWH10, SdLHW12]
     - Design of the WL-MSWF strategy and discussion of its key properties
     - Analysis of Minimum Mean Square Error (MMSE) of the WL-MSWF
     - Development and convergence analysis of adaptive algorithms for WL-MSWF
     - Analysis of the computational complexity
     - Simulation of the BER convergence performance in the presence of ISI, MUI, and NBI.
     - Evaluation of the rank-dependent performance and proposal of an adaptive rank-selection algorithm
   - Proposal and analysis of the WL-AVF algorithm in Section 8.4 [WSdLH10]
     - Design of the WL-AVF strategy and discussion of its key properties
     - Simulation of the convergence performance and the rank-dependent performance
2. Discussion on the applicability of the proposed WL reduced-rank algorithms in other applications in Section 8.5 (details in [SSW+11, SdLW+11])
   - Investigation of the WL-AVF and the WL-JIO adaptive beamforming algorithms based on the Widely Linear Constrained Minimum Variance (WL-CMV) criterion.
     - Eigenvalue analysis of the WL-AVF beamforming algorithm and characterization of its key properties [SSW+11]

– Development of the augmented and structured Recursive Least Squares (RLS) adaptive algorithms for the WL-JIO beamformer

The authors' publications that are not directly relevant to the dissertation are [SGM+06, MGS+07, MGS+08, MGS+10, CSR+12, TGS+12].

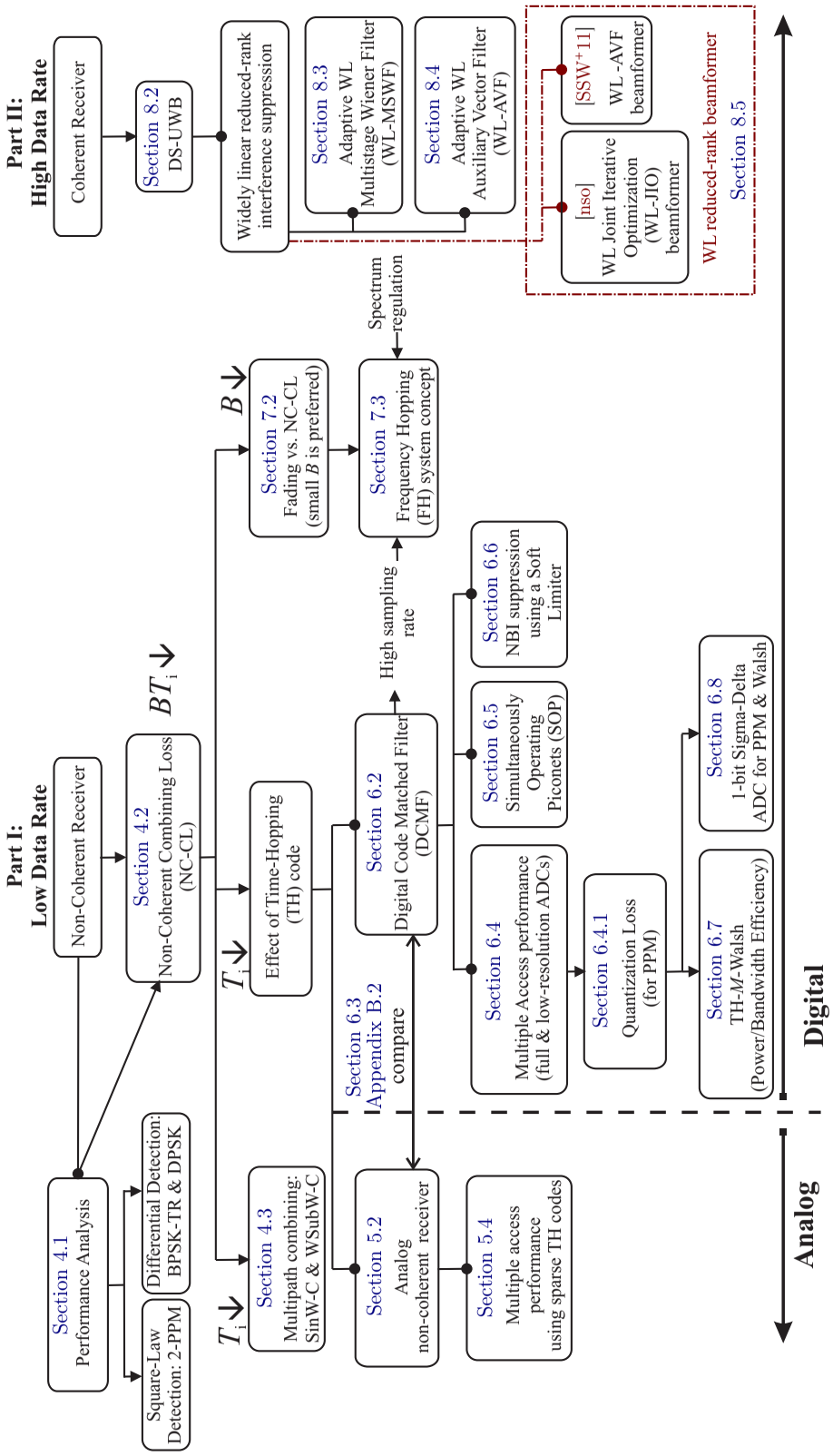

Fig. 1.2: Structure of major contributions. T_i is the size of the integration window and B is the signal bandwidth.

2. ULTRA WIDEBAND CHANNELS

In wireless communications, electromagnetic waves are propagating between the transmitter and the receiver. It is critical to depict such a propagation environment, i.e., a *channel*, since it greatly influences the design and the performance of transceiver strategies. This chapter studies several distinguishing characteristics of UWB channels as well as introduces both the standardized UWB channel models and some realistic measurements. We then describe how the channel impulse responses are modeled and applied throughout our work.

The multipath propagation effect is illustrated in Section 2.1, where a simple tapped-delay-line model is presented. Section 2.2 summarizes several important features of UWB channels. Some examples from measurements as well as standardized channel models are shown in Section 2.3. We also discuss in Section 2.4 their impact on the receiver implementations.

2.1 Multipath Propagation

Due to the existence of many objects in the propagation environment, the transmit signal may undergo reflection, diffraction, or scattering. As a consequence, the signal arrives at the receiver in a superposition fashion, consisting of multiple signal copies each with a distinct delay, attenuation, and direction. These received copies are referred to as multipath components. A widely used model to represent the multipath propagation channel is the tapped-delay-line model given by[1]

$$h(t) = \sum_{l=0}^{L-1} \alpha_l \delta(t - \tau_l), \tag{2.1}$$

where L is the number of resolvable paths, $\delta(t)$ is the Dirac delta function defined by

$$\delta(t) = \begin{cases} +\infty & \text{if } t = 0 \\ 0 & \text{if } t \neq 0 \end{cases}, \tag{2.2}$$

α_l and τ_l are the gain and the delay of the l-th path, respectively. If the receive filter has an infinite bandwidth, all the multipath components are resolvable and the channel model expressed in equation (2.1) is deterministic. In band-limited systems, the multipath components, which cannot be resolved by the receive filter with a bandwidth B, fall into the same delay bin with a resolution $1/B$. The simplified tapped-delay-line model can be then written

[1] Due to the movements of the transmitter, the receiver, and/or the interactive objects, the channel in (2.1) is time (or location) variant. For simplicity, we drop this time (or location) dependence in the equation.

as

$$h(t) = \sum_{l=0}^{L-1} \alpha_l \delta(t - l/B), \tag{2.3}$$

which has equally spaced taps.

The superposition of time-varying (or location-varying) multipath components that constitute one resolvable path or delay bin results in *small scale fading*. Such a fading effect can be either constructive or destructive, depending on the phase information of the superposed multipath components. When the bandwidth B is very small, e.g., in a narrowband system, all the multipath components are added up into a single delay bin with a large duration $1/B$. If the number of these non-resolvable multipath components is significant, according to the central limit theorem it results in Rayleigh fading. In UWB communications, the number of the multipath components that fall into one bin is determined by the environment, the measurement bandwidth, and the delay of the considered bin. Thus, the amplitudes of a given delay bin may not follow a Rayleigh distribution.

2.2 Characteristics of Ultra Wideband Channels

For UWB communications, the channel model in equation (2.1) cannot directly feature the propagation environment because of the distinctive characteristics of UWB channels [Mol09].

- The path gain is both distance- and frequency- dependent. It is obvious that the path gain, which measures the signal attenuation from the transmitter to the receiver, depends on this distance. The UWB signal can be attenuated by different path gains at different frequencies. At higher frequencies, the path gain is smaller and the signal attenuation is more significant compared to the case at lower frequencies.

- As discussed earlier, due to a very large bandwidth of the UWB signal, the small scale fading may not necessarily follow a Rayleigh distribution, since the amount of multipath components in one delay bin may not be large enough. In some cases, it also occurs that no multipath components fall into certain resolvable delay bins. This causes a "sparse" nature of UWB channels in some environments.

- Another key feature is that the multipath components arrive in groups of clusters. For example, such clustering can be well illustrated by the popular Saleh-Valenzuela model [SV87], where the arrival times of the clusters are Poisson distributed and within each cluster the multipath components arrive based on a Poisson process.

- In some environments, the first arriving multipath component is not the strongest one. This so-called "soft onset" provides a special power delay profile of some UWB channels. In ranging, it is required to determine the first arrived signal component. Applying UWB to estimate the time-of-arrival in these scenarios is difficult as the first component is very weak and comparable with the noise level.

- The interaction of the multipath components with objects also depends on the frequency. The coefficients of reflection, diffraction, or scattering suffer from the frequency selective channel and the multipath components are thus distorted.

2.3 The Use of Ultra Wideband Channels

For our work, in order to achieve a sound evaluation of various transceiver techniques and the UWB systems, we employ channel impulse responses obtained from both measurement data [KP02] and the standardized channel models [MBC+05]. The following parts describe the channels and how we use them.

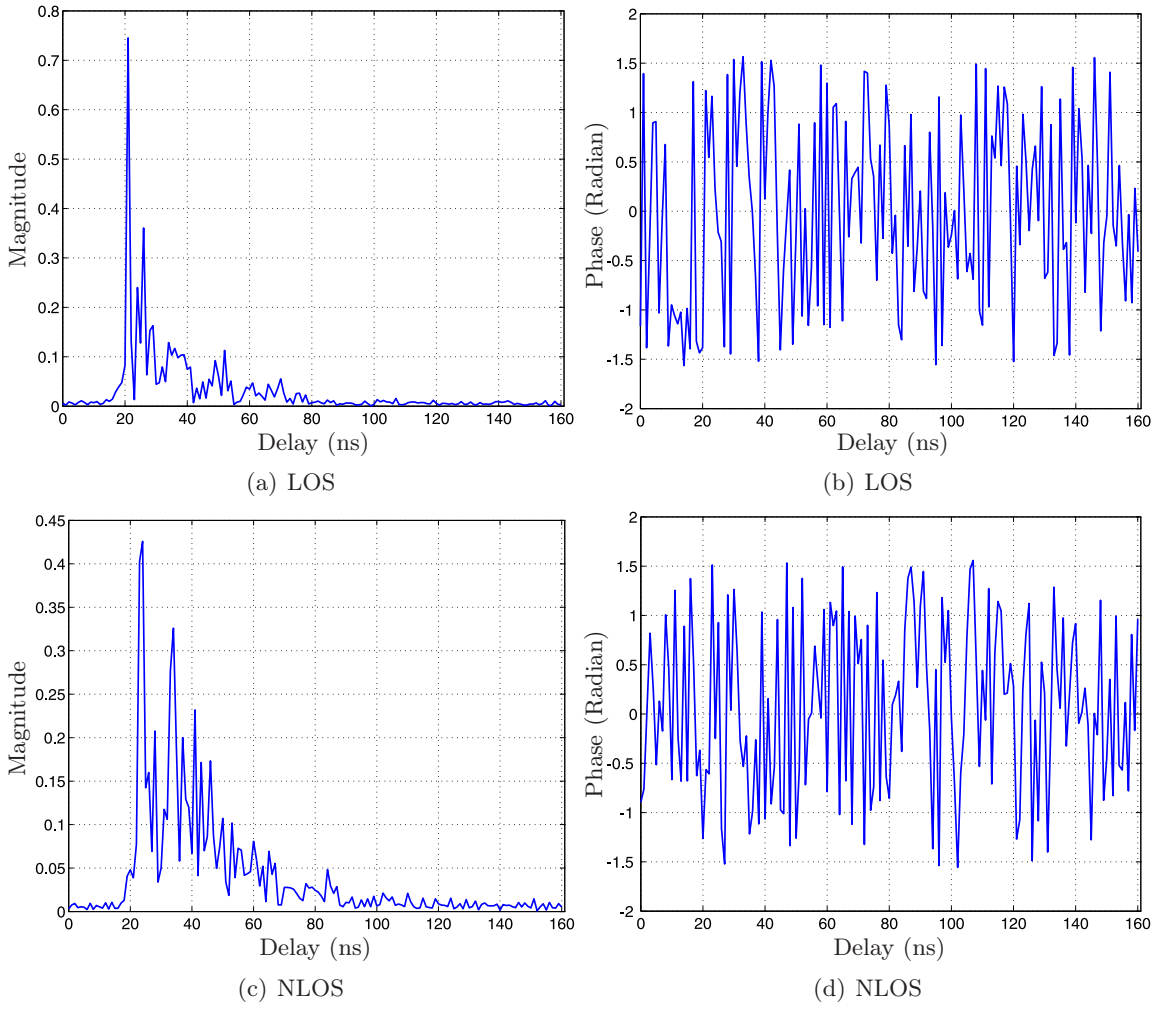

(a) LOS (b) LOS

(c) NLOS (d) NLOS

Fig. 2.1: The complex-valued impulse responses of the measured channels by IMST GmbH.

Measurements: The measurements we consider were carried out by the IMST GmbH [KP02] in an office of size 5 m × 5 m × 2.6 m for both the Line-Of-Sight (LOS) and the Non-Line-Of-Sight (NLOS) scenarios. The antenna effects are also included in the measurement data. At a predefined center frequency ranging from 1 GHz to 11 GHz, the transfer function of

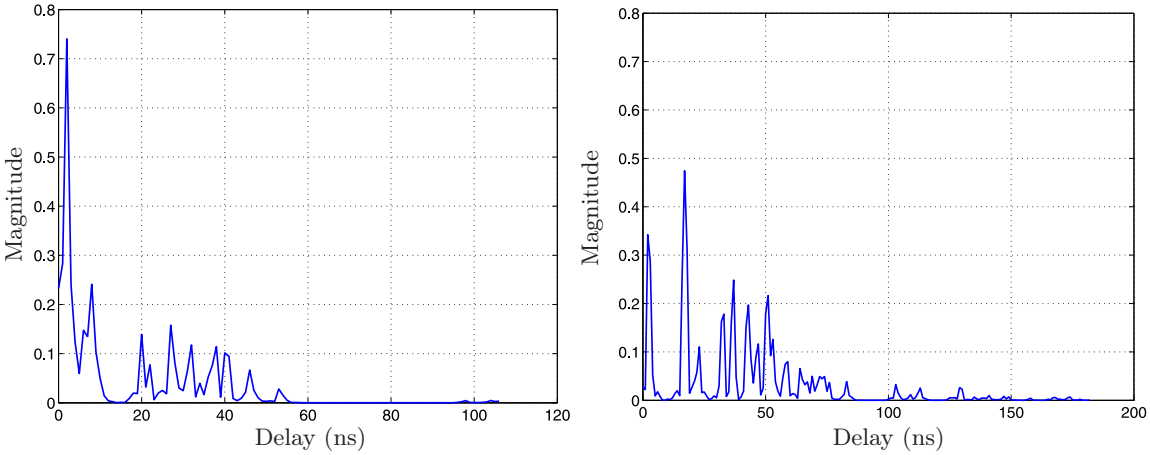

(a) CM1: residential LOS

(b) CM2: residential NLOS

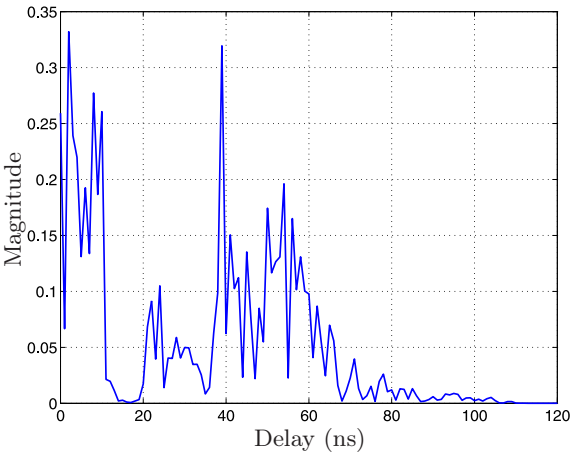

(c) CM3: indoor office LOS

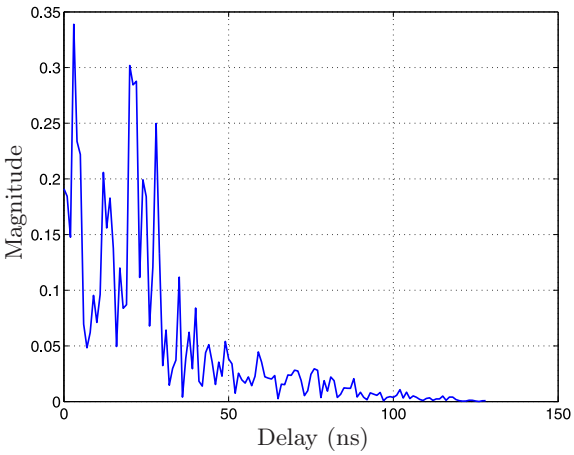

(d) CM4: indoor office NLOS

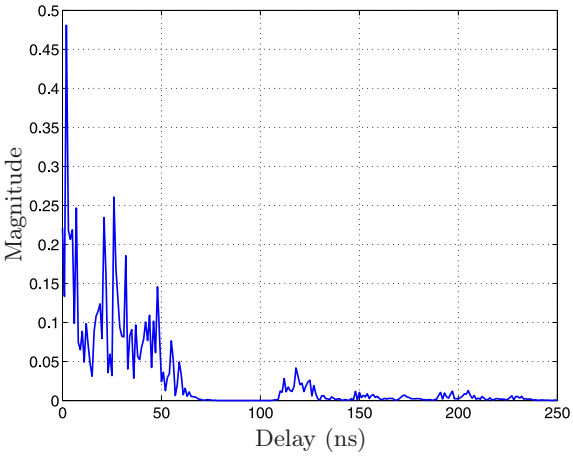

(e) CM5: outdoor LOS

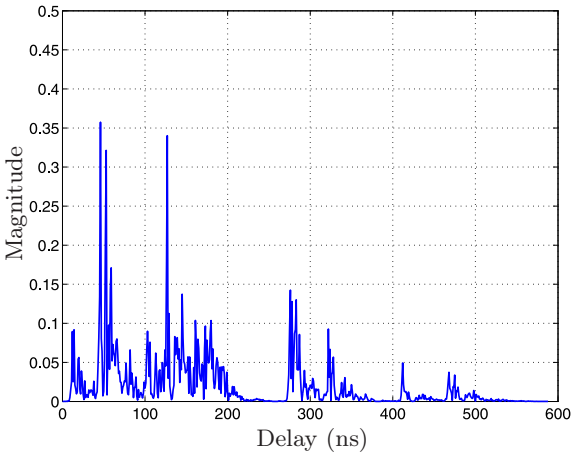

(f) CM6: outdoor NLOS

Fig. 2.2: The channel impulse responses of the IEEE 802.15.4a channels.

a certain channel realization is firstly transferred from the bandpass to the lowpass range and afterwards converted into a tapped-delay-line model as shown in equation (2.3). We choose the Root Raised Cosine (RRC) pulse with a roll-off factor $\beta = 0.3$ and a 3-dB bandwidth $B_3 = 500$ MHz as the pulse waveform. The total bandwidth is $B = (1+\beta)B_3$. If the sampling rate is at least B, the channel can be fully described by its samples using equation (2.3). The tap spacing or the resolution of the delay bin is then equal to $1/B$.

Figure 2.1 shows the complex-valued impulse responses (amplitudes and phases) of the measured channels for LOS and NLOS office scenarios at a center frequency of 4 GHz, where a raised cosine filter with $\beta = 0.3$ and $B = 1$ GHz is used. It has been addressed in [KP02] that the diffused multipath clusters follow an exponential decay rule, the small scale fading approaches Rayleigh distribution, and the phases are uniformly distributed. The channel excess delay within which 99 % of the energy can be captured in the LOS case is around 70 ns and in the NLOS case around 120 ns.

Standardized Channel Models: One general and widely used standardized channel model is the IEEE 802.15.4a model [MBC+05]. It specifies a variety of environments which are important for wireless sensor network applications, such as indoor residential, indoor office, outdoor, industrial environments, body area network, etc., cf. Table 2.1. It is based on the Saleh-Valenzuela model and the parameters are extracted from plenty of measurements. This model comprehensively characterizes the UWB propagation behavior, including the frequency dependent path gain, Nakagami small scale fading, stochastic arrival times of multipath components and clusters, as well as a soft onset power delay profile in certain NLOS cases. Compared to the IEEE 802.15.3a channel model [Foe02], it is more general and the parameterization is derived from more extensive measurements.

Tab. 2.1: Channel models for various environments in IEEE 802.15.4a [MBC+05]

Channel Number	Environments	Propagation
CM1	Indoor residential	LOS
CM2	Indoor residential	NLOS
CM3	Indoor office	LOS
CM4	Indoor office	NLOS
CM5	Outdoor	LOS
CM6	Outdoor	NLOS
CM7	Industrial	LOS
CM8	Industrial	NLOS
CM9	Open outdoor	NLOS
BAN	Body area network	NLOS

In Sections 6.5 and 7.2, we adopt the IEEE 802.15.4a channels to assess the system performance. The time-continuous channels are firstly generated by IEEE 802.15.4a model and then transfered from bandpass to lowpass with respect to a center frequency. Similarly to the way of processing the measured data, the channel impulse responses are obtained in the tapped-delay-line fashion (cf. equation (2.3)). Figure 2.2 plots the impulse responses for

different channel models, e.g., CM1/CM2, CM3/CM4, and CM5/CM6, where a raised cosine filter of $\beta = 0.3, B = 1$ GHz is used.

2.4 Summary and Discussions

The UWB channels and their essential features have been described. We use the measurements from IMST GmbH and the standardized IEEE 802.15.4a channel models to generate channel impulse responses that are expressed in a tapped-delay-line fashion. We can observe from Figures 2.1 and 2.2 that the excess delay of UWB channels ranges from 60 ns to over 500 ns, depending on different scenarios. As a result, the number of resolvable paths may be hundreds or even over a thousand if the signal bandwidth is large. The long delays in conjunction with the sparseness and the "soft onset" of the channel profile impose a high difficulty on acquiring the multipath energy. In such situations, a coherent receiver is too complicated and unaffordable. The energy collection using non-coherent multipath combining is also affected by the channel characteristics, which will be detailed in Chapter 4.

PART I: NON-COHERENT DETECTION FOR LOW DATA RATE ULTRA WIDEBAND SYSTEMS

3. LOW DATA RATE NON-COHERENT ULTRA WIDEBAND SYSTEMS

This chapter covers the basics of Impulse Radio (IR) UWB communication systems as well as non-coherent detection and the corresponding modulation schemes.

Section 3.1 provides fundamentals of IR UWB. It starts with the definition of UWB systems and its generic power constraints in Section 3.1.1. The original concept of pulse shaping is described in Section 3.1.2 by taking the Gaussian pulse and its derivatives as examples, where the properties are discussed in both the time and the frequency domains. Section 3.1.3 further introduces pulse trains and their spectral characteristics, especially with emphasis on the issues of regulation compliance. The influence of the power constraints on the IR UWB signals is discussed in Section 3.1.4. Our considerations for utilizing IR UWB are specified in Section 3.1.5.

In Section 3.2, non-coherent receivers based on energy detection (cf. Section 3.2.1) and differential detection (cf. Section 3.2.2) are presented in conjunction with the corresponding single-carrier modulation schemes.

3.1 Fundamentals of Impulse-Radio Ultra Wideband

This section reviews some fundamentals of IR UWB which are often less emphasized. It includes the original concept of IR UWB, the time- and frequency-domain characteristics of several basic pulses and pulse trains, as well as the impact of the emission rules on the transmit signals. After understanding these fundamentals, Section 3.1.5 points out some recent considerations and our assumptions of using IR UWB.

3.1.1 The FCC Power Constraints

According to the U. S. Federal Communications Commission (FCC), an UWB signal should occupy an absolute bandwidth of at least 500 MHz or a relative bandwidth exceeding 20 %, lying in the frequency band from 3.1 GHz to 10.6 GHz. To protect the users that are operating in the restricted frequency bands from harmful interference, the unlicensed use of UWB should be subject to certain emission limits. Thereby, the FCC issued emission rules with which any UWB devices have to comply [Fed02]. Two constraints for UWB signals are specified.

- *Average power constraint*: The instantaneous Effective Isotropic Radiated Power (EIRP) is measured by a spectrum analyzer with a Resolution Bandwidth (RBW) of 1 MHz and then averaged over 1 ms. The measured Power Spectral Density (PSD) must stay below -41.25 dBm/MHz.

- *Peak power constraint*: The peak of the signal power is measured by a spectrum analyzer with a resolution bandwidth of between 1 MHz and 50 MHz. The maximum peak power must not exceed $(\text{RBW}/50\ \text{MHz})^2$ mW for any frequency between 3.1 GHz and 10.3 GHz. For example, the instantaneous peak power limit is 0 dBm with RBW = 50 MHz.

Note that we only discuss the FCC UWB regulation as a general case. The FCC permits the unlicensed operation of UWB devices in the frequency range from 3.1 GHz to 10.6 GHz on a non-interference and non-protected basis. On the contrary, the European generic UWB regulation permits the operation of UWB devices which meet both the limits of a spectrum mask and other requirements such as the implementation of mitigation techniques [ECC07, Com08]. It ensures the protection of other radio communication systems. The specified frequency range of 6 GHz - 8.5 GHz at -41.3 dBm/MHz is considered as the long-term regulatory solution for UWB in Europe without the requirement for additional mitigation. Within frequency range of 3.1 GHz - 4.8 GHz, the operating devices should apply mitigation techniques, i.e., the detect and avoid as well as the low duty cycle, limited by the maximum mean EIRP spectral density of -41.3 dBm/MHz.

3.1.2 Pulse Shaping

The IR UWB is based on transmitting and receiving very short pulses whose durations are on the order of sub-nanoseconds. Such a short time duration promises a large spectrum in the frequency domain. In this regard, the IR is considered as one spread spectrum technique. In contrast to the conventional communication systems that rely on time-continuous waveforms, e.g., Direct Sequence (DS) or chirp, the IR is obtained by discontinuous emission of impulses.

The widely applied waveforms for IR UWB communications are the Gaussian pulse and its derivatives [WS98, GMK04]. The *Gaussian pulse* is expressed by

$$g(t) = \frac{1}{\sqrt{2\pi\tau_g}} e^{-2\pi\left(\frac{t}{\tau_g}\right)^2}, \tag{3.1}$$

where τ_g is the time-scaling factor that determines the pulse duration. By taking the k-th derivative of a Gaussian pulse, different waveforms denoted by $g_k(t)$ can be generated. For instance, the resulting waveform of the first derivative is called *Gaussian monocycle* and the second derivative is referred to as *Gaussian doublet*.

In contrast to those in the conventional narrowband communication systems, in a traditional IR UWB system the appropriately designed antennas act as the front-end pulse filters and no local oscillators are required [WS98]. In this sense, the IR was exclusively treated as

a baseband or carrier-less technique, implying that the IR UWB transceiver architecture is simpler and cheaper to build.

Let us further discuss the time- and frequency-domain properties of these waveforms. Figure 3.1 shows a Gaussian pulse with $\tau_g = 0.5$ ns and its k-th derivatives ($k = 1, 2, 3, 4, 6, 8$) as well as the corresponding PSD. We can observe that the Gaussian pulse has no zero crossing and only this spectrum contains a Direct Current (DC) component. Taking each derivative leads to an additional zero crossing. For a fixed τ_g, increasing the derivative order, the relative bandwidth of the resulting pulse decreases. Its spectrum also shifts to a higher frequency and there is no DC part any more with $k \geq 1$. It also implies that these baseband pulses are inherently "carrier-modulated". The signal bandwidth, which is related with the pulse duration, is determined by τ_g. In order to satisfy the bandwidth occupation within 3.1 GHz and 10.3 GHz, the derivative order k and the time-scaling factor τ_g need to be adjusted.

3.1.3 IR and Spectral Properties

For communications, a single pulse by itself cannot convey sufficient information. Data or information has to be modulated onto a sequence of pulses named *pulse train*. The basic model of a modulated pulse train $s(t)$ in baseband is given as

$$s(t) = \sqrt{E_g} \sum_{n=-\infty}^{+\infty} a_n g(t - nT_f), \tag{3.2}$$

where $g(t)$ represents the pulse shape with normalized energy and E_g is the energy per pulse, T_f is the interval between pulses or the pulse repetition time, and a_n is the n-th modulated symbol. We define the pulse repetition rate as $R_f = 1/T_f$ and represent the pulse duration as T_g. The signal bandwidth B can be approximately determined by the inverse of T_g but not by modulation schemes or symbol rates. Generally speaking, the key concept of IR UWB is that the signal bandwidth B is much greater than the pulse repetition rate R_f. In other words, the transmit pulses have a very low duty cycle determined by $R_f T_g$ with $R_f T_g < 1$.

The PSD of the signal $s(t)$, $\Phi_{ss}(f)$, is calculated by the Fourier transformation of the signal autocorrelation [Pro01]. It is assumed that the transmit data is random, and the PSD can be obtained as

$$\Phi_{ss}(f) = \underbrace{E_g \sigma_a^2 R_f \left|G(f)\right|^2}_{\text{continuous}} + \underbrace{E_g \mu_a^2 R_f^2 \sum_{n=-\infty}^{+\infty} \left|G(nR_f)\right|^2 \delta\left(f - nR_f\right)}_{\text{discrete}}, \tag{3.3}$$

where σ_a^2 and μ_a are the variance and the mean of the sequence a_n, respectively, $G(f)$ is the Fourier transform of the pulse $g(t)$, and $\delta(t)$ is the Dirac delta function defined in equation (2.2). From equation (3.3), it can be observed that the spectrum consists of both a continuous part and discrete spectral lines.

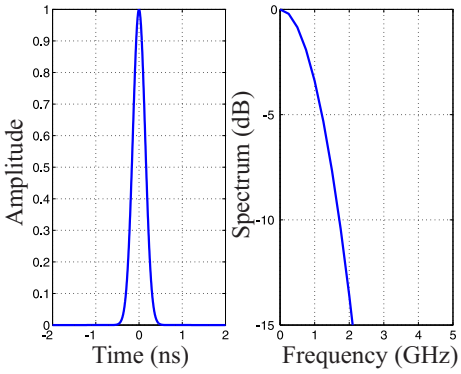

(a) Gaussian pulse

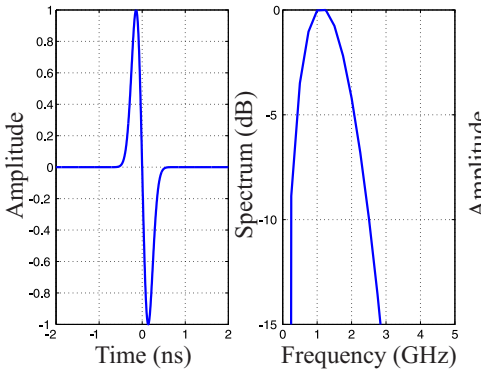

(b) Gaussian monocylce

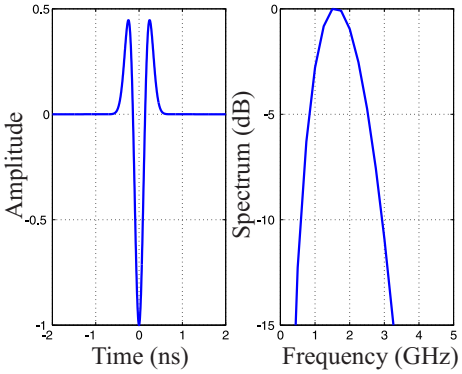

(c) Gaussian doublet

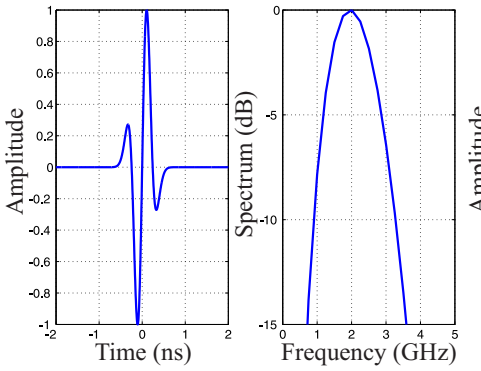

(d) The 3rd derivative of a Gaussian pulse

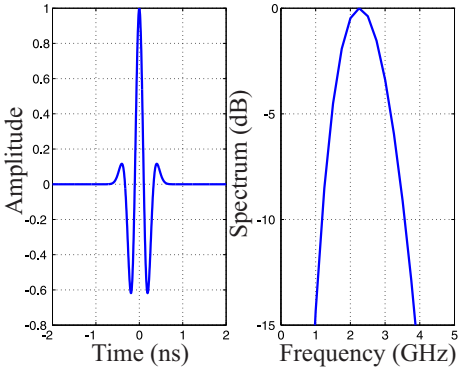

(e) The 4th derivative of a Gaussian pulse

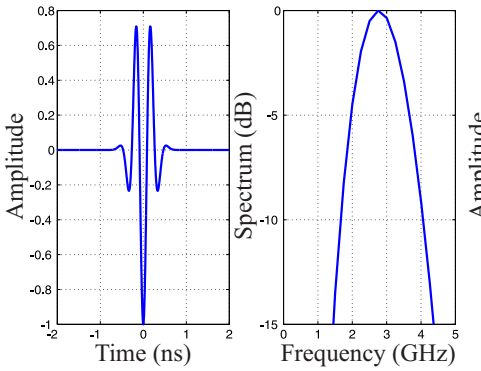

(f) The 6th derivative of a Gaussian pulse

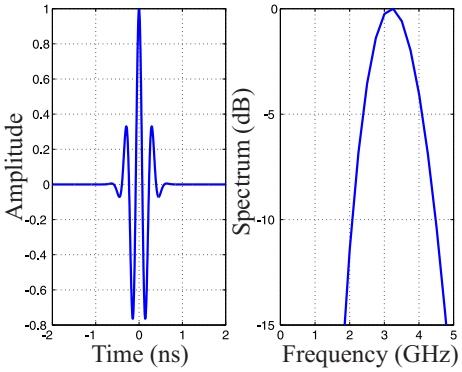

(g) The 8th derivative of a Gaussian pulse

Fig. 3.1: Examples of a Gaussian pulse and its derivatives as well as their spectra. We choose $\tau_g = 0.5$ ns.

In the simplest case for the unmodulated signal or a periodic stream of pulses, i.e.,

$$s(t) = \sqrt{E_g} \sum_{n=-\infty}^{+\infty} g(t - nT_f), \tag{3.4}$$

where $\sigma_a^2 = 0$ and $\mu_a^2 = 1$, the PSD is obtained as

$$\Phi_{ss}(f) = E_g R_f^2 \sum_{n=-\infty}^{+\infty} \left|G(nR_f)\right|^2 \delta\left(f - nR_f\right). \tag{3.5}$$

The resulting spectrum only contains comb lines with power spikes appearing at multiples of the pulse repetition rate R_f. An example of such a PSD is illustrated in Figure 3.2(a), where a Gaussian monocycle with $\tau_g = 0.5$ ns (cf. Section 3.1.2) is adopted.

The existence of such spectral spikes, often higher than the continuous spectral component, is extremely undesired. It may cause the violation of the FCC emission mask, becoming severe interference to other existing systems. Even if the PSD spikes comply with the mask, the average power back-off is significant. Therefore, to reduce the spectral lines, it is required to smooth the signal's PSD. Various methods have been considered [NM03, LH03] and we summarize some in the following as examples.

- **Polarity modulation**: The data symbols a_n in equation (3.2) can be modulated by antipodal modulation schemes such as Binary Phase Shift Keying (BPSK) or Binary Phase Amplitude Modulation (2-PAM), i.e., $a_n \in \{\pm 1\}$. Thus, we will have $\mu_a = 0$, which totally removes the discrete part of the spectrum. Similarly, applying pseudo random codes to modulate pulse trains can also achieve a smooth spectrum.

- **Time/Position modulation**: Pulse Position Modulation (PPM), which will be described in Section 3.2, is one popular modulation scheme in IR UWB communications. Moreover, the Time Hopping (TH) multiple access technique (cf. Section 5) modulates pulses by placing them in different time slots. Both schemes provide pulse shifts in time and such "dithering" gives rise to a reduced amount of spectral lines.

- **Timing jitter**: Besides modulations, a timing jitter is also capable of smoothing the spectrum. In this case, a small time offset is introduced to each pulse so that this pulse is transmitted either earlier or later than the original pulse time. This time offset is often modeled by a uniform distribution over a specified interval and is randomly generated for each pulse.

The resulting PSDs by applying spectrum smoothing schemes are shown in Figure 3.2(b) - 3.2(e) as examples. Compared to Figure 3.2(a) without smoothing the spectrum, 2-PAM and timing jitter are more effective in alleviating the spectral lines than either Binary Pulse Position Modulation (2-PPM) or TH. The combination of the above schemes is also possible and robust.

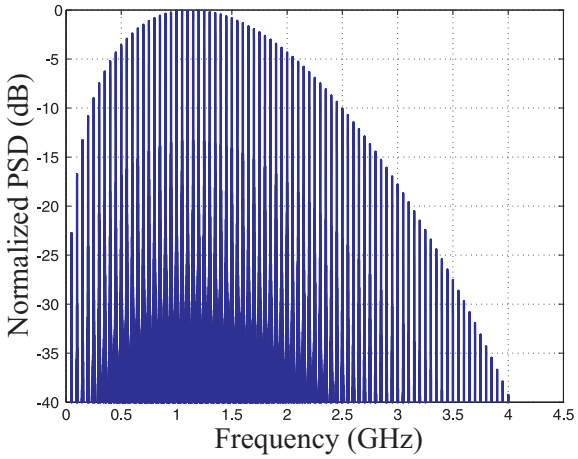

(a) Periodic pulse train

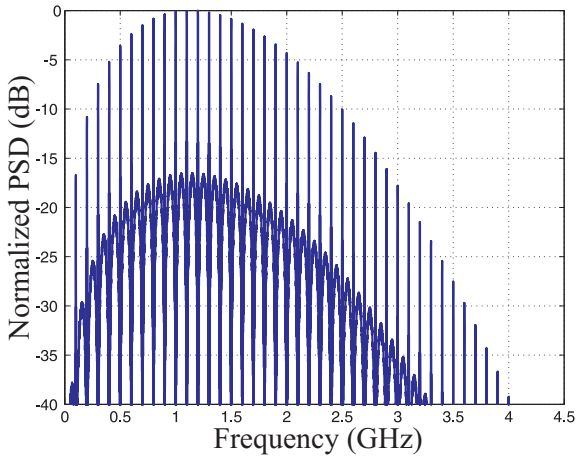

(b) 2-PPM modulated pulse train

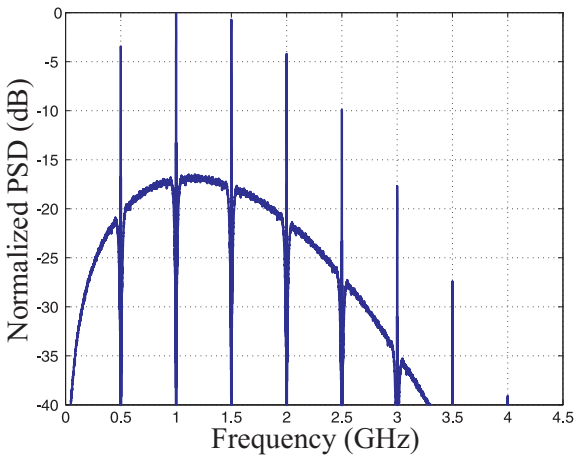

(c) Random TH modulated pulse train

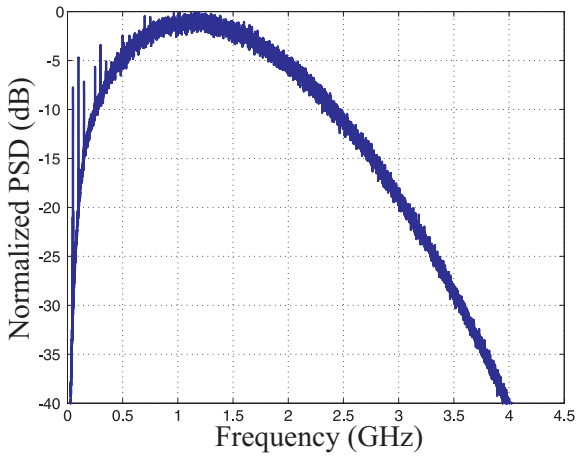

(d) Pulse train with 25 % timing jitter

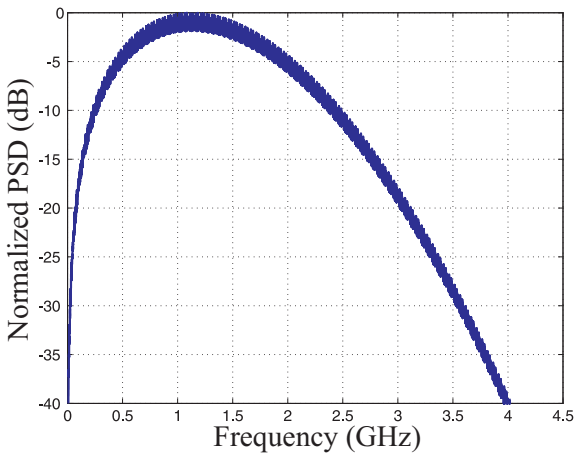

(e) 2-PAM modulated pulse train

Fig. 3.2: Normalized PSDs of different pulse trains.

3.1.4 Maximum Allowed Power Spectral Density

The power constraints have different influences on different IR UWB signals. We then determine the maximum allowed PSD per emitted pulse based on [WH04a] for both a periodic (or non-dithered) pulse train as shown in equation (3.4) and a dithered pulse train represented by

$$s(t) = \sqrt{E_g} \sum_{n=-\infty}^{+\infty} g(t - nT_f - \frac{b_n T_f}{2}), \tag{3.6}$$

where the symbols b_n varies randomly with a uniform distribution over $[0, 1]$. This dithered pulse train is time-jittered with 50 percentage of the pulse repetition interval.

It can be obtained from [WH04a] that under both the average and peak power constraints, the maximum allowed energy per pulse of the periodic pulse train $E^{\max}_{g,\text{unmod}}$ can be obtained as

$$E^{\max}_{g,\text{unmod}} = \begin{cases} \dfrac{P^{\text{FCC}}_{\text{ave}}}{2\ G^2(f_c) B_{\text{ave}} R_f} & 10\text{ kHz} \le R_f < B_{\text{ave}} \\ \dfrac{P^{\text{FCC}}_{\text{ave}}}{2\ G^2(f_c) R_f^2} & R_f \ge B_{\text{ave}} \end{cases} \tag{3.7}$$

and

$$E^{\max}_{g,\text{unmod}} = \begin{cases} \dfrac{0.45^2\ P^{\text{FCC}}_{\text{peak}}}{2\ G^2(f_c) B^2_{\text{peak}}} & 10\text{ kHz} \le R_f < \frac{B_{\text{peak}}}{0.45} \\ \dfrac{P^{\text{FCC}}_{\text{peak}}}{2\ G^2(f_c) R_f^2} & R_f \ge \frac{B_{\text{peak}}}{0.45} \end{cases}, \tag{3.8}$$

where f_c denotes the center frequency. The average and peak power limits specified by the FCC are $P^{\text{FCC}}_{\text{ave}} = -41.25$ dBm $= 75$ nW and $P^{\text{FCC}}_{\text{peak}} = (B_{\text{peak}}/50\text{ MHz})^2$ mW for the RBW $B_{\text{ave}} = 1$ MHz and $1\text{ MHz} \le B_{\text{peak}} \le 50$ MHz, respectively.

Similarly, the maximum allowed energy per pulse of the dithered pulse train $E^{\max}_{g,\text{dither}}$ can be approximated by

$$E^{\max}_{g,\text{dither}} = \frac{P^{\text{FCC}}_{\text{ave}}}{2\ G^2(f_c) B_{\text{ave}} R_f} \quad R_f \ge 10\text{ kHz} \tag{3.9}$$

and

$$E^{\max}_{g,\text{dither}} = \begin{cases} \dfrac{0.45^2\ P^{\text{FCC}}_{\text{peak}}}{2\ G^2(f_c) B^2_{\text{peak}}} & 10\text{ kHz} \le R_f < \frac{B_{\text{peak}}}{2} \\ \dfrac{P^{\text{FCC}}_{\text{peak}}}{20\ G^2(f_c) B_{\text{peak}} R_f} & R_f \ge \frac{B_{\text{peak}}}{2} \end{cases}. \tag{3.10}$$

Figure 3.3 shows the maximum allowed PSD per pulse under the average and peak power limits for the periodic pulse train and the dithered pulse train, where the RBW of the average power measurement is $B_{\text{ave}} = 1$ MHz and for the peak power measurement $B_{\text{peak}} = 1$ MHz, 3 MHz, and 50 MHz. When the pulse repetition rate $R_f < 1$ MHz, the peak power constraint is more restrictive. The maximum allowed PSD per pulse $E^{\max}_g G^2(f_c) R_f$, which is lower than the average power level, is dropping with R_f. When $R_f > 1$ MHz, the average power constraint plays a more important role. An exception is that for the dithered pulse train with

$B_{\text{peak}} = 1$ MHz, the PSD is restrained by the peak power level at any R_f.

In the dithered case with $B_{\text{peak}} \geq 1.875$ MHz and the non-dithered case, only at $R_f = 1$ MHz the maximum PSD can fully exploit both the average and peak power constraints. With $R_f > 1$ MHz, the maximum allowed PSD per pulse of the dithered pulse train stays constant whereas that of the non-dithered one decreases with increased R_f. This implies that at higher data rates the non-dithered pulse train which is FCC compliant is much less efficient than the dithered one with respect to the average power limit.

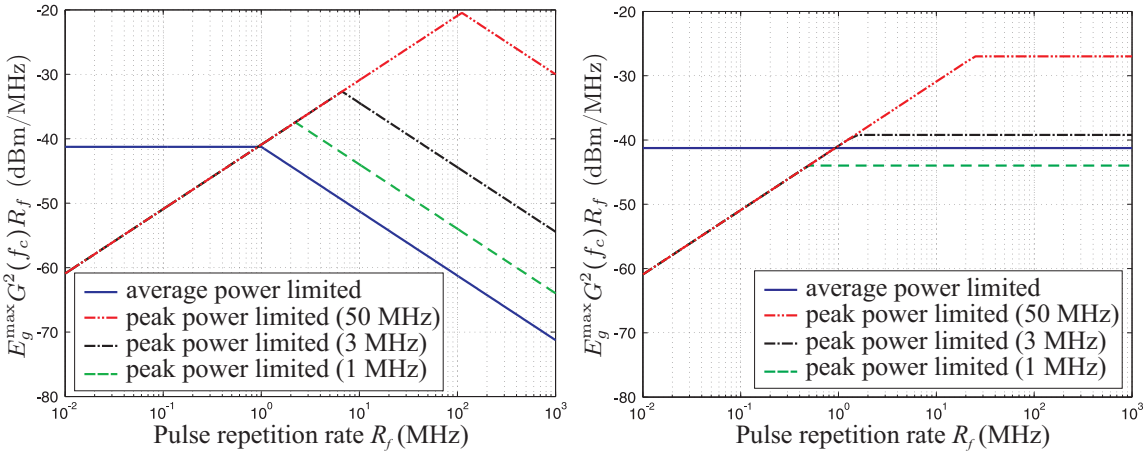

(a) Periodic pulse train (b) Dithered pulse train

Fig. 3.3: Maximum allowed PSD per pulse limited by both the FCC average and peak power constraints.

3.1.5 Considerations

For the baseband pulses as shown in Section 3.1.2, the spectrum can be controlled by the derivative order k and the time-scaling factor τ_g to meet the FCC mask. However, due to the non-flatness of these pulses over the frequency, they cannot utilize the specified spectrum efficiently. This calls for a dedicated design of pulse waveforms [MGK02, PCWD03, WTDG06]. Furthermore, in the "baseband" or "carrier-less" IR UWB systems, there are no front-end filters but the transmit and the receiver antennas perform pulse shaping. As a result, pulse distortion due to the antennas and the propagation environments is a crucial issue, which has to be taken into account in the system modeling and evaluation [CWL+04].

In fact, the FCC defines UWB signals as truly bandpass signals in the range of 3.1 GHz to 10.3 GHz and there are no specifications on how to generate them. Thereby, IR is not necessarily restricted to a "baseband" technique. Accordingly, modern UWB signals are obtained by conventional ways, i.e., modulating a baseband pulse with a sinusoid [IEE07]. Even though it has been argued that the local oscillators may cause an increased transceiver complexity, the required technical efforts for the original "baseband" methods to optimize the pulse shape or to combat the pulse distortion are not trivial.

Therefore, in our work, we simply adopt a carrier modulated Root Raised Cosine (RRC) pulse as the basic IR UWB waveform and assume that it perfectly fits the FCC spectrum mask. Additionally, when the modulated pulse trains are discussed, it is supposed that they are FCC compliant for ease of developing and evaluating various transceiver techniques.

3.2 Modulation and Detection

Without the knowledge of channel state information, non-coherent receivers may easily capture the multipath energy by means of equal gain combining [WLJ+09]. A non-coherent receiver can be based on either energy detection or differential detection. This section describes these two non-coherent detectors and introduces the associated single-carrier modulation schemes.

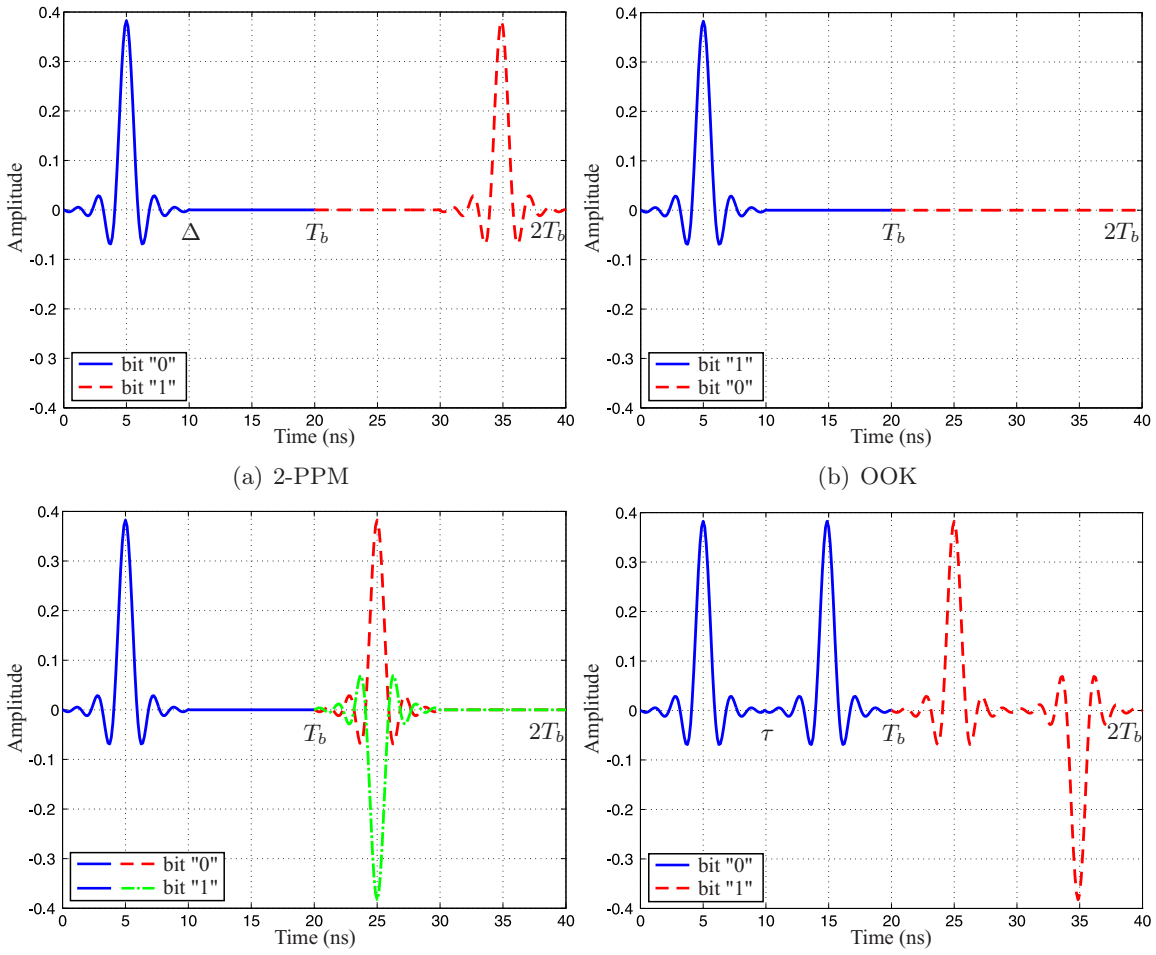

(a) 2-PPM (b) OOK

(c) DPSK (d) TR-BPSK

Fig. 3.4: Representation of different modulated signals using the RRC pulse with $\beta = 0.3$. The bit interval is $T_b = 20$ ns.

3.2.1 Energy Detection

The block diagram of an energy detector using quadrature down conversions is shown in Figure 3.5, where two lowpass filters $g_{\mathrm{R}}(t)$ matched to the pulse shape are utilized. The outputs of two square-law devices are combined and the resulting envelope of the received signal is fed to an integrator. The integrator performs equal gain combining and accumulates the multipath energy within an integration interval T_{i}. The decision is then made after sampling at $t = T_{\mathrm{samp}}$. Compared to coherent detection, the energy receiver removes any phase information simply by adopting square-law devices.

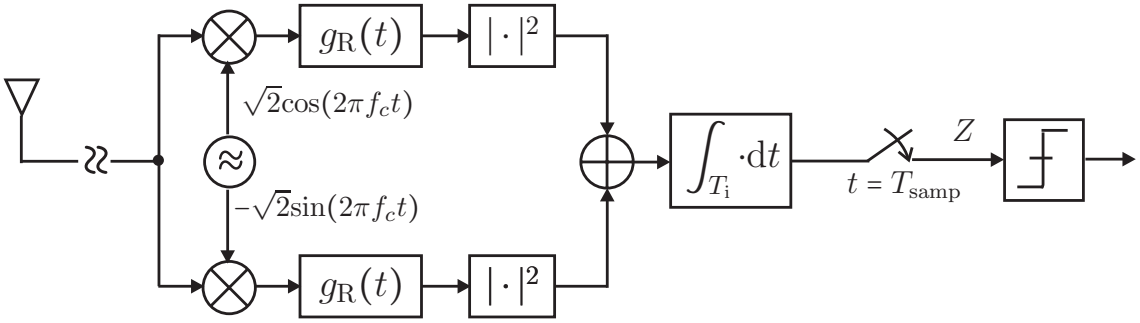

Fig. 3.5: Energy receiver with quadrature down conversions.

There are two popular modulation schemes widely used for energy detection, namely orthogonal PPM and On-Off Keying (OOK).

3.2.1.1 Pulse Position Modulation

An orthogonal 2-PPM modulated signal in the complex baseband can be written as

$$s_{\mathrm{PPM}}(t) = \sqrt{E_b} \sum_{j=-\infty}^{+\infty} g(t - jT_b - a_j\Delta). \tag{3.11}$$

where a_j is the binary information bit, E_b denotes the bit energy, and T_b is the bit duration. As shown in Figure 3.4(a), the bit interval is divided into two time slots spaced by $\Delta = T_b/2$. The information bit $a_j = 0$ or $a_j = 1$ determines whether the pulse $g(t)$ is transmitted at the beginning of the first time slot or Δ seconds later. The pulse shape and its shifted version are orthogonal. Moreover, $g(t)$ has a unit energy, i.e., $\int_{-\infty}^{+\infty} |g(t)|^2 \mathrm{d}t = 1$.

The block diagram of energy detector in the complex baseband is depicted in Figure 3.7(a). The signal received after multipath propagation and the pulse matched filter $g_{\mathrm{R}}(t) = g(T - t)$ can be given by

$$y(t) = s_{\mathrm{PPM}}(t) * h(t) * g(T - t) + \widehat{n}(t) * g(T - t), \tag{3.12}$$

where T represents the delay to ensure that $g_{\mathrm{R}}(t)$ is causal and $*$ denotes convolution. The multipath channel $h(t)$ is expressed by a tapped-delay-line model as shown in equation (2.3) with normalized energy $\sum_{l=0}^{L-1} |\alpha_l|^2 = 1$. We denote the Additive White Gaussian

Noise (AWGN) as $\widehat{n}(t)$, which has zero mean and a PSD N_0.

The energy detector firstly squares the received signal and then collects the multipath energy by an integrator. The resulting decision variables Z_0 and Z_1 as expressed by

$$Z_m = \int_{jT_b+m\Delta}^{jT_b+m\Delta+T_i} |y(t)|^2 \, \mathrm{d}t, \quad m \in \{0,1\} \tag{3.13}$$

are obtained at the sampling time $T_{\text{samp}} = j \cdot T_b$ and $T_{\text{samp}} = j \cdot T_b + \Delta$, respectively. The samples Z_0 and Z_1 are the energy measures in two PPM time slots. The decision is made based on the following rule

$$\widehat{a} = \begin{cases} 1, & \text{if } Z \geq 0 \\ 0, & \text{if } Z < 0 \end{cases} \tag{3.14}$$

with $Z = Z_0 - Z_1$.

3.2.1.2 On-Off Keying

A transmitted signal with OOK modulation (in complex baseband) is given by

$$s_{\text{OOK}}(t) = \sqrt{E_b} \sum_{j=-\infty}^{+\infty} a_j g(t - jT_b), \tag{3.15}$$

where $a_j \in \{0,1\}$ is the information bit. The OOK signaling scheme is illustrated in Figure 3.4(b), where a bit "1" represents the presence of a pulse and a bit "0" means no pulse is transmitted.

In contrast to 2-PPM, after the energy is collected by the integrator, it is sampled at the bit rate $T_{\text{samp}} = j \cdot T_b$. The output decision variable Z is compared with a threshold to determine whether a pulse is present or not. A correct decision requires an appropriate threshold, depending on the transmitted signal, the channel, and the noise level. In this sequel, we consider 2-PPM rather than OOK for energy detection to avoid such threshold problems.

3.2.2 Differential Detection

The block diagram of a differential detector using quadrature down conversions is shown in Figure 3.6, where two pulse matched filters $g_{\text{R}}(t)$ are used. In contrast to energy detection, the differential receiver utilizes delay elements and multipliers to compares the phase or polarity. The down-converted signal is multiplied with its delayed version and thus the phase information is removed. The delay τ corresponds to the duration between two successive symbols or pulses that are differentially encoded. A differential receiver is also referred to as an autocorrelation receiver.

Differential detection is often applied in conjunction with Differential Phase Shift Keying (DPSK) or Transmitted Reference (TR) signaling.

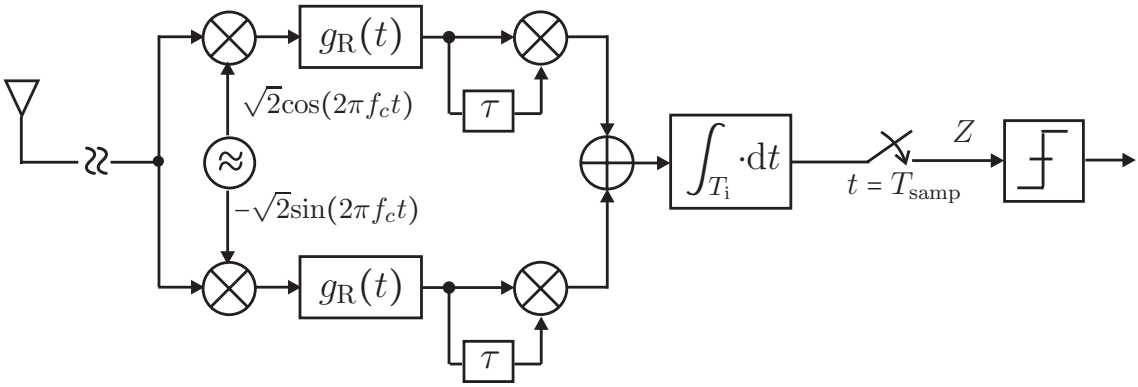

Fig. 3.6: Differential receiver with quadrature down conversions.

3.2.2.1 Differential Phase Shift Keying

Figure 3.4(c) shows a binary DPSK signal, which can be written as

$$s_{\mathrm{DPSK}}(t) = \sqrt{E_b} \sum_{j=-\infty}^{+\infty} (1 - 2\tilde{a}_j)\, g(t - jT_b), \tag{3.16}$$

where the bits $\tilde{a}_j$ are differentially encoded such that $\tilde{a}_j = a_j \oplus \tilde{a}_{j-1}, a_j \in \{0,1\}$. The notation $\oplus$ denotes modulo-2 addition.

At the (complex baseband) receiver shown in Figure 3.7(b), the filtered signal $y(t)$ is multiplied with its complex conjugated and delayed version. The multipath energy is then accumulated by an integrator. The decision variable can be given by

$$Z = \int_{jT_b}^{jT_b+T_i} \Re\{y(t)y^*(t-\tau)\}\, \mathrm{d}t, \tag{3.17}$$

where $\Re\{\cdot\}$ takes the real part of the argument and the delay τ needs to be as large as the symbol interval, i.e., $\tau = T_b$.

3.2.2.2 Transmitted Reference

The TR combined with BPSK signaling scheme, i.e., Transmitted Reference combined with Binary Phase Shift Keying (TR-BPSK), can also be used for differential detection [Sch82]. A TR signal (complex baseband) is expressed as

$$s_{\mathrm{TR}}(t) = \sqrt{E_b/2} \sum_{j=-\infty}^{+\infty} \left[g(t - jT_b) + (1 - 2a_j)\, g(t - jT_b - \tau) \right], \tag{3.18}$$

where the transmitted bits are $a_j \in \{0,1\}$. As illustrated in Figure 3.4(d), each transmitted symbol consists of two pulses, one reference pulse and one modulated pulse which is delayed by an interval τ. In this case, the receiver compares the polarity of the collected energy after multiplying the received reference signal with the modulated one. The decision variables can be calculated similarly as in equation (3.17).

Compared to DPSK, the delay τ of TR-BPSK is not necessarily related with the symbol interval T_b. The disadvantage is that half of the symbol energy is wasted by transmitting the reference pulse.

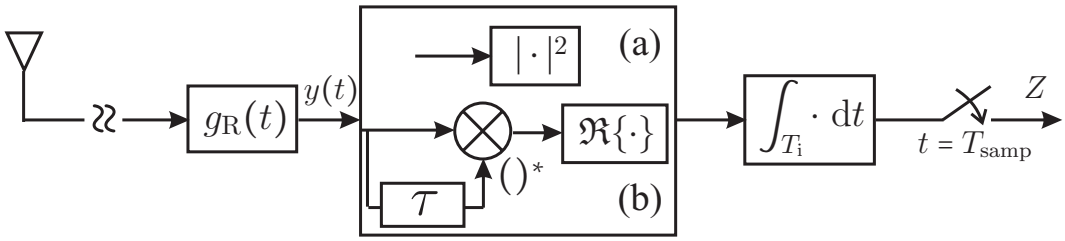

Fig. 3.7: Block diagram of (a) energy detection and (b) differential detection (shown in the complex baseband)

3.3 Summary and Discussions

In this chapter, we have presented the fundamentals of IR UWB systems using non-coherent receivers. IR was originally considered as a "baseband" or "carrier-less" technology, since the pulse shaping came from the transmit and receive antennas and no local oscillators were required. We examine several baseband pulses by taking the Gaussian pulse and its derivatives as an example. The FCC regulation implies that UWB is actually a shared spectrum for unlicensed use in the range of 3.1 GHz to 10.3 GHz, which is truly bandpass. Therefore, in our work, we simply employ a carrier-modulated RRC pulse as the basic IR UWB waveform in the sense that it can easily satisfy the FCC mask.

We also discuss the IR pulse trains and their spectral characteristics. A pulse train should be dithered by timing shifts (TH or timing jitter) and/or scrambled by polarity modulations, so that the spectral peaks can be mitigated to comply with the FCC mask. The influence of the FCC power limits on both non-dithered and dithered pulse trains is investigated, by determining the maximum allowed PSD per emitted pulse as a function of the pulse repetition rate R_f. With R_f = 1 MHz, both the average and peak power constraints can be exploited [1]. Since our focus is on the development of robust and low-complexity physical layer strategies, we assume the utilized pulse trains, e.g., Time Hopping combined with Pulse Position Modulation (TH-PPM), are FCC compliant for simplicity.

Non-coherent detection becomes promising for low-complexity IR UWB systems. We introduce two receiver structures, i.e., energy detection and differential detection, where the energy capture can be carried out by means of an integrator. PPM instead of OOK is considered for the energy detector to avoid the decision threshold problem. Both DPSK and TR-BPSK can be applied for differential detection. TR-BPSK is less efficient than DPSK since half of the symbol energy is wasted on the reference pulse. The delay of the TR-BPSK based differential receiver corresponds to the interval between two pulses, whereas in DPSK

[1] This requires that the RBW of the peak power measurement for the dithered case should be at least 1.875 MHz.

the delay should be as long as the symbol duration. The sampling rate after the integrator for PPM is $2/T_b$, twice that of the DPSK or TR case.

4. NON-COHERENT MULTIPATH COMBINING: PERFORMANCE ANALYSIS AND ENHANCEMENT

To have an insight into the behavior of non-coherent detection, this chapter starts with the performance analysis as well as a comparison of energy detection and differential detection using different modulation schemes in Section 4.1. Section 4.2 evaluates a loss due to non-coherent combining, namely the Non-Coherent Combining Loss (NC-CL), where coherent detection acts as a reference. Several key characteristics with respect to the NC-CL are observed and discussed. This section plays an important role throughout Part I, which is closely relevant to the other chapters. For the sake of reducing the NC-CL, Section 4.3 investigates non-coherent multipath combining schemes to effectively capture the multipath energy.

4.1 Performance Evaluation and Comparison

This section compares the performance of different signaling schemes using the corresponding non-coherent detectors, where low data rate systems are considered. To this end, we assume that there is no interference between pulses or consecutive symbols due to the multipath propagation, i.e., Inter-/Intra-Symbol Interference (ISI).

4.1.1 Performance of Energy Detection

We assume only one symbol a_0 is transmitted. According to Section 3.2.1.1, the received signal after the pulse matched filter $g_{\mathrm{R}}(t)$ is given by

$$y(t) = \sqrt{E_b} \sum_{l=0}^{L-1} \tilde{g}(t - a_0\Delta - \frac{l}{B}) + n(t), \tag{4.1}$$

where B is the total bandwidth of the signal, $\tilde{g}(t) = g(t) * g_{\mathrm{R}}(t)$ and $n(t) = \widehat{n}(t) * g_{\mathrm{R}}(t)$ are filtered (convolved) pulse and noise, respectively. Zero-mean, complex-baseband Additive White Gaussian Noise (AWGN) $\widehat{n}(t)$ has a Power Spectral Density (PSD) N_0. Assuming the

transmitted bit is $a_0 = 0$, the decision variables can be approximated by

$$Z_m \approx \sum_{l=0}^{L_\mathrm{i}-1} r_{m,l}, \quad m \in \{0,1\}, \tag{4.2}$$

where m denotes the index of each Pulse Position Modulation (PPM) time slot within which the decision variable is obtained, the time-bandwidth product $L_\mathrm{i} = T_\mathrm{i} \cdot B$ [1] is the number of taps combined in the integration window, and

$$\begin{cases} r_{0,l} = \left|\sqrt{E_b}\alpha_l + n_{0,l}\right|^2 \\ r_{1,l} = \left|n_{1,l}\right|^2 \end{cases}. \tag{4.3}$$

According to Appendix A.2.3, since $n_{0,l}$ and $n_{1,l}$ are complex Gaussian random variables, $r_{0,1}$ and $r_{1,l}$ exhibit non-central and central χ^2-distributions with 2 degrees of freedom, respectively. The non-centrality parameter for $r_{0,l}$ is $E_b|\alpha_l|^2$. Thus, the sum of $r_{0,l}$ or $r_{1,l}$ with $l = 0, \ldots, L_\mathrm{i}$, i.e., Z_0 or Z_1, still follows non-central or central χ^2-distribution but with $2L_\mathrm{i}$ degrees of freedom. The non-centrality parameter of Z_0 becomes $E = E_b \sum_{l=0}^{L_\mathrm{i}-1} |\alpha_l|^2$. The number of combined paths L_i, which determines the degrees of freedom, can also be interpreted as the dimensionality of independent complex noise variables.

We denote the Probability Density Function (PDF) of χ^2-distribution as a function of x (cf. Appendix A.2.3) by $\chi^2(x, K, \mu^2, \sigma^2)$, where K is the degree(s) of freedom, μ^2 is the non-centrality parameter, σ^2 is the variance of Gaussian random variables that compose x. Thus, Z_0 and Z_1 have distributions represented by

$$\begin{cases} Z_0 \sim \chi^2\left(Z_0, 2L_\mathrm{i}, E, N_0/2\right) \\ Z_1 \sim \chi^2\left(Z_1, 2L_\mathrm{i}, 0, N_0/2\right) \end{cases} \tag{4.4}$$

with $E = E_b \sum_{l=0}^{L_\mathrm{i}-1} |\alpha_l|^2$.

According to the decision rule for energy detection combined with Binary Pulse Position Modulation (2-PPM) as shown in equation (3.14), the probability of error can be calculated by

$$P_b^{\mathrm{NC}} = \frac{1}{2}\Pr\{Z \le 0 | a_0 = 0\} + \frac{1}{2}\Pr\{Z \ge 0 | a_0 = 1\} = \Pr\{Z \le 0 | a_0 = 0\} \tag{4.5}$$

$$= \int_0^\infty f_{Z_0}(Z_0) \int_{Z_0}^\infty f_{Z_1}(Z_1)\,\mathrm{d}Z_1\mathrm{d}Z_0 \tag{4.6}$$

where $Z = Z_0 - Z_1$ and $f_x(x)$ is the PDF of x. Based on the analysis in [HW95], the exact BER can be expressed by

$$P_b^{\mathrm{NC}} = \frac{1}{2^{L_\mathrm{i}}} \exp\left(-\frac{\gamma}{2}\right) \sum_{k=0}^{L_\mathrm{i}-1} \frac{1}{2^k} \mathscr{L}_k^{L_\mathrm{i}-1}\left(-\frac{\gamma}{2}\right), \tag{4.7}$$

where $\gamma = E/N_0$ represents signal to noise ratio for 2-PPM and $\mathscr{L}_k^a(\cdot)$ is a generalized Laguerre

[1] We assume that T_i is chosen such that L_i is an integer.

polynomial of degree k with $a > -1$. In AWGN, i.e., $L_\mathrm{i} = 1, E = E_b$, the corresponding BER can be simplified to $\frac{1}{2}\exp(-E_b/2N_0)$, which is well known in [Pro01].

If the number of combined paths L_i is large (e.g., $L_\mathrm{i} > 15$), we can apply the central limit theorem to the decision variables $Z_m, m \in \{0,1\}$ such that the distribution of Z_m approximates a Gaussian distribution. Thus, the approximated BER can be obtained as

$$P_b^{\mathrm{NC}} \approx \mathrm{Q}\left(\frac{\mathbb{E}\{Z\}}{\sqrt{\mathbb{V}\{Z\}}}\right) = \mathrm{Q}\left(\frac{\gamma}{\sqrt{2\gamma + 2L_\mathrm{i}}}\right), \tag{4.8}$$

where $\mathrm{Q}(\alpha) = \frac{1}{\sqrt{2\pi}}\int_\alpha^\infty e^{-\frac{x^2}{2}}\mathrm{d}x$, $\mathbb{E}\{Z\}$ and $\mathbb{V}\{Z\}$ are the mean and the variance of Z, respectively.

4.1.2 Performance of Differential Detection

Based on Section 3.2.2.1, two consecutive symbols received after the pulse matched filter are represented by

$$\begin{cases} y(t) = \sqrt{E_b}\,(1 - 2\tilde{a}_{-1}) \sum_{l=0}^{L-1} \tilde{g}\left(t - \frac{l}{B}\right) + n(t) \\ y(t-\tau) = \sqrt{E_b}\,(1 - 2\tilde{a}_0) \sum_{l=0}^{L-1} \tilde{g}\left(t - \frac{l}{B} - \tau\right) + n(t-\tau) \end{cases}.$$

The decision variable can thus be written as

$$Z \approx \sum_{l=0}^{L_\mathrm{i}-1} \Re\left\{y_l y_{\mathrm{d},l}^*\right\}, \tag{4.9}$$

where the sampled variables of $y(t)$ and $y(t-\tau)$ are expressed as

$$\begin{cases} y_l = \sqrt{E_b}\alpha_l + n_l \\ y_{\mathrm{d},l} = \sqrt{E_b}\alpha_l + n_{\mathrm{d},l} \end{cases} \tag{4.10}$$

by assuming $\tilde{a}_{-1} = \tilde{a}_0 = 0$, i.e., $a_0 = 0$. To compare the decision variables of energy detection with 2-PPM shown in equation (4.2) to the ones of differential detection with Differential Phase Shift Keying (DPSK) (cf. equation (4.9)), we introduce new noise samples $\tilde{n}_{0,l}$ and $\tilde{n}_{1,l}$ for the latter such that

$$\begin{cases} \tilde{n}_{0,l} = \frac{1}{2}\left(n_{\mathrm{d},l}^* + n_l\right) \\ \tilde{n}_{1,l} = \frac{1}{2}\left(n_{\mathrm{d},l}^* - n_l\right) \end{cases}. \tag{4.11}$$

It can be obtained that the new noise is also Gaussian distributed with zero mean but with variance $N_0/2$. By replacing $n_{\mathrm{d},l}, n_l$ with $\tilde{n}_{0,l}, \tilde{n}_{1,l}$ in equation (4.9), we can have the expression for the decision variable written as

$$Z \approx \sum_{l=0}^{L_\mathrm{i}-1} \left|\sqrt{E_b}\alpha_l + \tilde{n}_{0,l}\right|^2 - \sum_{l=0}^{L_\mathrm{i}-1} \left|\tilde{n}_{1,l}\right|^2 \triangleq \tilde{Z}_0 - \tilde{Z}_1. \tag{4.12}$$

It is obvious that $\tilde{Z}_0$ and $\tilde{Z}_1$ are mathematically equivalent to Z_0 and Z_1 in the 2-PPM case and follow the distribution

$$\begin{cases} \tilde{Z}_0 \sim \chi^2\left(\tilde{Z}_0, 2L_\mathrm{i}, E, N_0/4\right) \\ \tilde{Z}_1 \sim \chi^2\left(\tilde{Z}_1, 2L_\mathrm{i}, 0, N_0/4\right) \end{cases} \tag{4.13}$$

with $E = E_b \sum_{l=0}^{L_\mathrm{i}-1} |\alpha_l|^2$. The only difference compared to Z_0 and Z_1 for the 2-PPM case shown in equation (4.4) is the fact that we have half of the noise variance in the case of DPSK. Therefore, the BER of DPSK with differential detection has the same formulation as shown in equations (4.7) and (4.8) but with $\gamma = 2E/N_0$, which shows exactly a 3 dB advantage over 2-PPM with energy detection. Similarly, in AWGN the BER performance of DPSK becomes $\frac{1}{2}\exp(-E_b/N_0)$.

Due to the fact that Transmitted Reference combined with Binary Phase Shift Keying (TR-BPSK) has half of the energy efficiency compared to DPSK, its decision variables exhibit the following distributions

$$\begin{cases} \tilde{Z}_0 \sim \chi^2\left(\tilde{Z}_0, 2L_\mathrm{i}, E/2, N_0/4\right) \\ \tilde{Z}_1 \sim \chi^2\left(\tilde{Z}_1, 2L_\mathrm{i}, 0, N_0/4\right) \end{cases} . \tag{4.14}$$

Therefore, the BER for TR-BPSK with differential detection can also be represented by equations (4.7) and (4.8) with $\gamma = E/N_0$, which is exactly the same as the BER performance of 2-PPM. We do not take ISI into account and the performance comparison is based on the assumption that the same channel realization as well as the combining method are considered.

4.2 Non-Coherent Combining Loss

If we assume that the whole bit energy is captured within the integration interval T_i, the signal-to-noise ratio becomes $\gamma = E_b/N_0$ for 2-PPM or TR-BPSK and $\gamma = 2E_b/N_0$ for DPSK. The E_b/N_0 performance of non-coherent detection can be predicted analytically even if no concrete channel realizations are considered. We summarize the BER expressions of coherent and non-coherent detection schemes in Table 4.1, where both multipath and AWGN channels are considered.

Tab. 4.1: BER of coherent and non-coherent detection schemes with $\gamma = E_b/N_0$ for 2-PPM and TR-BPSK and $\gamma = 2E_b/N_0$ for DPSK.

	AWGN	Multipath	
Coherent	$\mathrm{Q}\left(\sqrt{\gamma}\right)$ ([Pro01])	$\mathrm{Q}\left(\sqrt{\gamma}\right)$ ([Pro01])	
Non-coherent	$\frac{1}{2}\exp(-\frac{\gamma}{2})$	Exact (4.7): $\frac{1}{2^{L_\mathrm{i}}}\exp\left(-\frac{\gamma}{2}\right)\sum_{k=0}^{L_\mathrm{i}-1}\frac{1}{2^k}\mathscr{L}_k^{L_\mathrm{i}-1}\left(-\frac{\gamma}{2}\right)$	Approximate (4.8): $\mathrm{Q}\left(\frac{\gamma}{\sqrt{2\gamma+2L_\mathrm{i}}}\right)$

Compared to the performance of coherent detection, a performance penalty due to non-

coherent combining with respect to E_b/N_0, i.e., NC-CL, is observed. The NC-CL is mainly determined by the noise dimensionality $L_\mathrm{i} = T_\mathrm{i} \cdot B$ [WSH09, WS09]. Thereby, in Figure 4.1 we plot this NC-CL as a function of L_i at a given BER = 10^{-3} for both energy and differential detectors, where a coherent detection is used as the reference. When $L_\mathrm{i} < 15$, we utilize the exact BER expression as shown in equation (4.7). We can observe that the NC-CL increases with L_i asymptotically by around 1 dB per each doubled L_i. In order to reduce the NC-CL, L_i has to be decreased, i.e., the impacts of either T_i, B, or both on the system performance and design should be taken into account. Several key characteristics and design rules are discussed and summarized in the following.

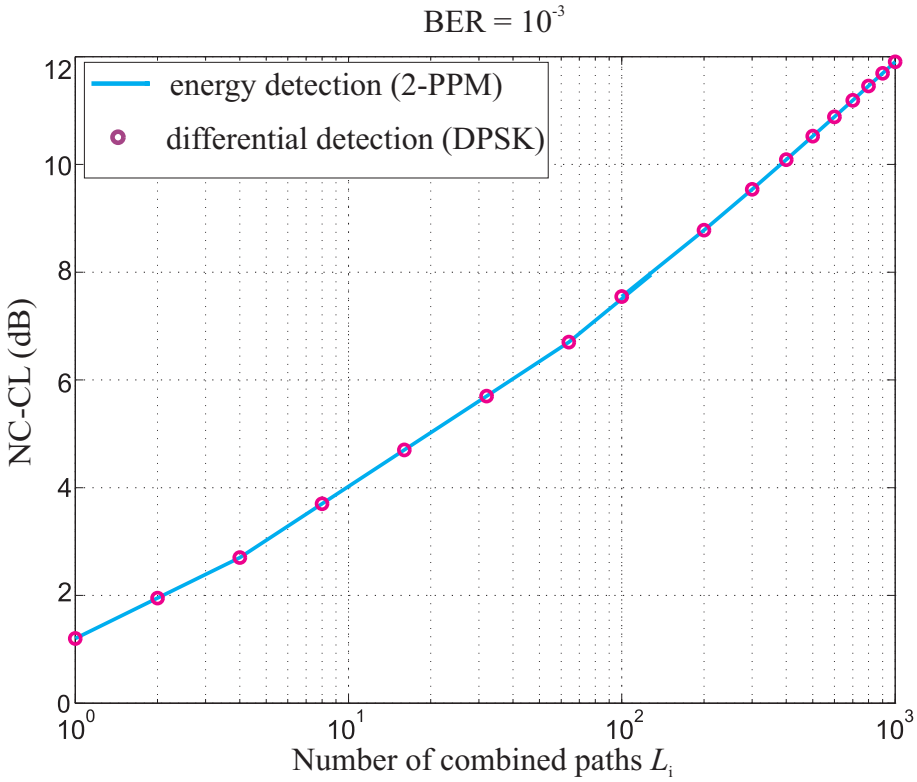

Fig. 4.1: Analytical estimation of the NC-CL at BER = 10^{-3} according to Table 4.1. It is assumed that the whole bit energy is contained in the L_i paths.

- If T_i is chosen as small as $1/B$, i.e., $L_\mathrm{i} = 1$, where the major part of the signal energy is concentrated, the best performance of non-coherent detection can be achieved. In this case, the NC-CL with respect to coherent detection is 1.2 dB. This might be achieved if the received signal contains a very strong Line-Of-Sight (LOS) component or if time-reversal techniques are applied for non-coherent detection [GQS05]. Time reversal is a pre-distortion scheme which can be carried out at a base station transmitter. The corresponding terminal receiver utilizes only a small time interval within which the bit energy is focused. The time-reversal technique is beyond the scope of our work and will not be discussed in detail. In a LOS indoor scenario, if the integration interval is

chosen as around 20 ns to capture sufficient signal energy, with the minimum bandwidth 500 MHz, the resulting number of combined paths is $L_{\mathrm{i}} = 500 \times 10^6 \cdot 20 \times 10^{-9} = 10$. Consequently, in this LOS situation, the NC-CL is 4 dB. The loss is even larger in the case of Non-Line-Of-Sight (NLOS) scenario due to a longer channel excess delay.

- If the interval T_{i} increases, the energy contained within T_{i} is also increased until $E = E_b$. To fully acquire the signal energy contained in the multipath arrivals, $T_{\mathrm{i}} \geq \tau_{\max}$ should be satisfied. However, a longer T_{i} leads to a larger L_{i}, which increases the collected noise power simultaneously. Thus, there exists a trade-off for T_{i} between the captured signal energy E and the accumulated noise power. Section 4.3 will investigate this trade-off and present the corresponding improved non-coherent multipath combining techniques.

- When the IR pulse train with a number of pulse repetitions N_s is adopted, the signal energy is spread over time by both the repetitions and the multipath. On the one hand, a larger N_s is able to provide a higher robustness to Multi-User Interference (MUI) and Narrowband Interference (NBI). On the other hand, if the non-coherent combining is performed with respect to the whole spread energy, the NC-CL will be determined by $T_{\mathrm{i}} = N_s T_{\mathrm{i}}^{\mathrm{mp}}$, where $T_{\mathrm{i}}^{\mathrm{mp}}$ denotes the integration interval of multipath combining [2]. From the energy efficiency point of view, well-designed system parameters are required to reduce the NC-CL (i.e., reduce N_s) and meanwhile to ensure a high MUI rejection capability (cf. Chapter 5). Notwithstanding, if the non-coherent combining is only restricted to multpath, the NC-CL will not depend on N_s anymore, i.e., $T_{\mathrm{i}} = T_{\mathrm{i}}^{\mathrm{mp}}$. This requires that at the receiver a matched filter for the whole spread waveform (e.g., Time Hopping (TH) waveform) should be applied before non-coherent processing. The energy after this matched filter is thus only spread by the multipath components. Chapter 6 will introduce the detailed receiver implementations along with analysis and development of various transmission and reception schemes.

- Besides T_{i}, increasing B also gives rise to a larger L_{i} and consequently a greater NC-CL. However, to determine an appropriate value for B, there is a trade-off between the bandwidth dependent fading rejection and the bandwidth dependent NC-CL. If a narrowband transmission with $B \cdot \tau_{max} \ll 1$ is considered as an extreme case, the NC-CL is only about 1.2 dB. However, in this case the received energy E_b suffers from a strong small scale fading, i.e., to achieve an outage probability of 1%, for Rayleigh fading the fading margin will be 20 dB. In [WGH05] it has been shown (using the measurements data [KP02]) that if the bandwidth is increased to 500 MHz this fading margin can be reduced to about 5 dB for indoor NLOS. The choice of bandwidth B for UWB communications using non-coherent detection will be discussed in Section 7.

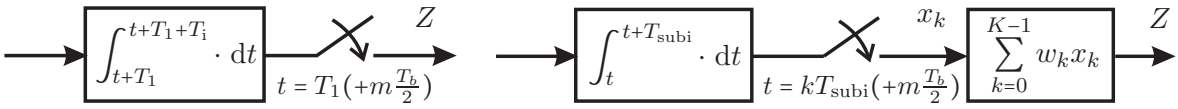

(a) SinW-C (b) WSubW-C

Fig. 4.2: Improved non-coherent multipath combining methods. It is only shown for the detection of the first bit as an example. For 2-PPM, the term $m\frac{T_b}{2}, m \in \{0, 1\}$ is added to the sampling time, representing two samples per each 2-PPM symbol.

4.3 Improved Non-Coherent Multipath Combining Techniques

To effectively capture the multipath energy, two non-coherent multipath combining schemes, namely Single Window Combining (SinW-C) and Weighted Sub-Window Combining (WSubW-C), are proposed in this section. For both schemes, a single integrator is utilized as shown in Figure 3.7. We also obtain the performance limit of non-coherent detection in multipath channels by deriving "quasi" optimal weighting coefficients. The performance is evaluated for both energy detection and differential detection.

4.3.1 Single-Window Combining

Figure 4.2(a) shows the block diagram of the SinW-C method using a single integrator. It is the major part of a non-coherent receiver illustrated in Figure 3.7. The quadrature down-conversion stage required to obtain the complex signal is not shown, and the principle is only shown for the detection of the first bit. There are two parameters affecting the performance (which is measured here as the required E_b/N_0 to achieve a certain BER):

- the integration time T_{i},
- the starting point (synchronization) of the integration window, which is determined by the parameter T_1.

As discussed in Chapter 2, some UWB channels exhibit a "soft onset" power delay profile, indicating that the strong paths often arrive later. It may not be advantageous to start integrating the signal energy at the time of arrival. Moreover, the signal energy is spread over a long excess delay but mostly the energy in the tail is very weak and comparable to the noise level. By increasing T_{i}, more signal energy can be captured but meanwhile the collected noise power becomes more dominant especially in the tail of the excess delay. To solve this trade-off, the SinW-C scheme determines an optimal integration window by adjusting T_{i} and T_1, so that the maximum multipath energy with respect to the noise power can be collected. After the integrator, the sampling rate is $R_b = 1/T_b$ for DPSK as well as TR-BPSK and $2R_b$ for 2-PPM. The main advantage of SinW-C is that the sampling rate is considerably reduced

[2] In this section, T_{i} is only used as a generalized notation for ease of analysis. In the following sections, T_{i} will exclusively represent the integration interval of the energy that is spread by multipath.

to the order of the bit rate. The resulting samples are decision variables and no further digital weighting is used, indicating that only one-bit quantization is required.

4.3.2 Weighted Sub-Window Combining

Due to the sparseness of the UWB channels (cf. Chapter 2), the power delay profile of a certain channel realization contains some regions with more energy and others with less energy. Therefore, the performance can be improved, if the observation window is divided into several weighted sub-windows. Figure 4.2(b) shows the block diagram of the WSubW-C scheme. The integrator (equal gain combining) operates in a smaller window size (sub-window) and the outputs that convey portions of the spread energy $x_k, k = 0, \ldots, K-1$ are combined with different weights after sampling in the digital domain. As a result, the weighting procedure boosts the strong signal components and suppresses the noise components to enhance the performance. To ensure uniform sampling, for DPSK (or TR-BPSK) the whole bit interval T_b is divided into a number of K sub-intervals, corresponding to an integration time $T_{\text{subi}} = T_b/K$. For 2-PPM, the interval of size $T_b/2$ is split into K sub-intervals with $T_{\text{subi}} = T_b/(2K)$. Compared to SinW-C, the sampling rate increases to $K \cdot R_b$ for DPSK or TR-BPSK and $2K \cdot R_b$ for 2-PPM. The weighting coefficients $w_k, k = 0, \ldots, K-1$ are calculated according to the accumulated multipath energy within each sub-window.

4.3.3 Performance Limit of Non-Coherent Detection

Let us take 2-PPM with energy detection as an example to derive the performance limit. We first consider optimal coherent detection. After the lowpass filter with impulse response $g_{\text{R}}(t)$ in Figure 3.7, the output $y(t)$ is sampled with a rate B. The decision variables Z_0 and Z_1 of the optimal coherent 2-PPM detector can be obtained according to

$$Z_0 = \sum_{l=0}^{L-1} \alpha_l^* \cdot y\left(\frac{l}{B}\right), \; Z_1 = \sum_{l=0}^{L-1} \alpha_l^* \cdot y\left(\frac{l}{B} + \frac{T_b}{2}\right), \tag{4.15}$$

where α_l is the complex gain of the l-th channel tap (cf. Chapter 2). In this case, $Z_m, m \in \{0, 1\}$ is equal to the sampled output of a channel matched filter.

If the sampling rate of the WSubW-C is equal to B, i.e., $T_{\text{subi}} = 1/B$, all L multipath arrivals can be resolved and weighted in the non-coherent case. Accordingly, the integrator shown in Figure 3.7 is skipped and the samples $|y(l/B)|^2, |y(l/B + T_b/2)|^2, l = 0, 1, \ldots, L-1$ are used to make the decision. The optimum decision rule can be obtained from the conditional joint PDF of the $2L$ samples.

We assume $a_0 = 0$, which means that the pulse is transmitted at position $t = 0$. In this case, each sample $r_{0,l} = |y(l/B)|^2$, $l = 0, 1, \ldots, L-1$, exhibits a non-central χ^2-distribution with

2 degrees of freedom, i.e.,

$$f_{r_{0,l}}(x|a_0 = 0) = \frac{1}{N_0} \exp\left(-\frac{x + |\alpha_l|^2 E_b}{N_0}\right) \cdot I_0\left(\sqrt{\frac{4|\alpha_l|^2 E_b \cdot x}{N_0^2}}\right), \tag{4.16}$$

where $I_0(\cdot)$ is the 0-th order modified Bessel function of the first kind. The samples $r_{1,l} = |y(l/B + T_b/2)|^2$ exhibit a central χ^2-distribution with 2 degrees of freedom, i.e.,

$$f_{r_{1,l}}(x|a_0 = 0) = \frac{1}{N_0} \exp\left(-\frac{x}{N_0}\right). \tag{4.17}$$

The maximum-likelihood decision rule is based on the conditional joint PDF $f_{\boldsymbol{r}_0,\boldsymbol{r}_1}(\boldsymbol{r}_0, \boldsymbol{r}_1|a_0 = m)$, $m = 0, 1$, where the vectors are given as

$$\boldsymbol{r}_0 = \begin{bmatrix} r_{0,0}, & r_{0,1}, & \ldots, & r_{0,L-1} \end{bmatrix}^T \quad \text{and} \quad \boldsymbol{r}_1 = \begin{bmatrix} r_{1,0}, & r_{1,1}, & \ldots, & r_{1,L-1} \end{bmatrix}^T.$$

If the noise samples are assumed to be uncorrelated, the logarithm of this joint PDF is

$$\log\left(f_{\boldsymbol{r}_0,\boldsymbol{r}_1}(\boldsymbol{r}_0, \boldsymbol{r}_1|a_0 = 0)\right) = C + \sum_{l=0}^{L-1} \log\left[I_0\left(\sqrt{\frac{4|\alpha_l|^2 E_b \cdot r_{n,l}}{N_0^2}}\right)\right], \tag{4.18}$$

where C is a constant irrelevant for the maximization. An optimum non-coherent receiver chooses $\boldsymbol{r}_m, m = 0, 1$ which maximizes equation (4.18). Since $\log[I_0(\cdot)]$ can be well approximated by a linear function [NK96], the maximum likelihood solution is that the weighting coefficients are equal to $|\alpha_l|^2, l = 0, \ldots, L-1$ and accordingly this "quasi" optimum combining rule for non-coherent detection is

$$Z_0 = \sum_{l=0}^{L-1} |\alpha_l|^2 \cdot \left|y\left(\frac{l}{B}\right)\right|^2, \quad Z_1 = \sum_{l=0}^{L-1} |\alpha_l|^2 \cdot \left|y\left(\frac{l}{B} + \frac{T_b}{2}\right)\right|^2. \tag{4.19}$$

We refer this as "quasi" optimal, since some approximations have been made and it is assumed that no correlation between adjacent samples exists. However, a non-coherent receiver will hardly outperform the one that operates according to equation (4.19) and thus this performance can be considered as a practical limit.

4.3.4 Results

In our simulations, the BER performance as a function of E_b/N_0 is determined numerically for 4 different receivers: 1.) a coherent full RAKE receiver (since ISI is not considered, AWGN performance will be obtained), 2.) a non-coherent detector using SinW-C, 3.) a non-coherent detector using WSubW-C, and 4.) a "quasi" optimal non-coherent detector based on fully digital weighted combining. For the performance analyses of different receivers, we use measured NLOS UWB channels [KP02] introduced in Section 2.3. The 3-dB bandwidth of the pulse B_3 is chosen to be 500 MHz.

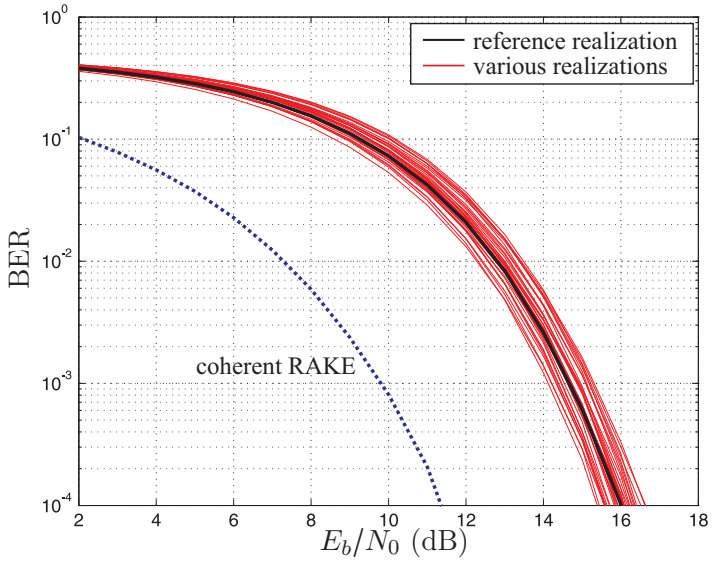

Fig. 4.3: BER for "quasi" optimal non-coherent detection and different channel realizations (thin solid curves in red). The thick solid curve in black corresponds to our reference realization.

In the non-coherent case, the E_b/N_0 performance depends not only on L, but also on the concrete distribution of the multipath energy over time, i.e., on the power delay profile of a given channel realization. For a number of L paths, the worst-case situation is obtained, if all tap weights $\alpha_l, l = 0, \ldots, L-1$ have the same amplitude.

Each thin solid curve in Figure 4.3 corresponds to a different realization of the measured NLOS channels. It can be seen that the E_b/N_0 performance of the "quasi" optimal non-coherent detector exhibits a variation, which is within 1 dB at a BER of 10^{-3}. Compared to a coherent full RAKE, the mean loss is around 4.5 dB. In Figure 4.3, we have additionally introduced a thick solid curve (in black), which also corresponds to a certain realization. This realization is treated as a "reference realization" and is used to compare the BER performance of the other considered receivers.

For SinW-C, at least two parameters need to be adjusted, i.e., the window size T_i and its position T_1. Figure 4.4(a) shows the BER as a function of E_b/N_0 for SinW-C using both energy detection with 2-PPM (lines) and differential detection with TR-BPSK (markers), where different T_is are considered. Along with Figure 4.5, it can be observed that the BER strongly depends on T_i, whereas the position of the integration window is always chosen optimally. For the reference channel realization considered here, T_i between 16 ns and 32 ns provides the best performance, which only loses around 0.5 dB compared to the performance limit.

The BER over T_i performance of the SinW-C may also exhibit several local minima, although this is not the case in Figure 4.5. For this reason, in practice, the determination of T_i and T_1 for SinW-C may require adaptive tracking of the integration window. These problems are avoided by using the WSubW-C. In Figure 4.4(b), the BER performance is shown for the WSubW-C scheme considering different T_{subi}s. In contrast to the SinW-C

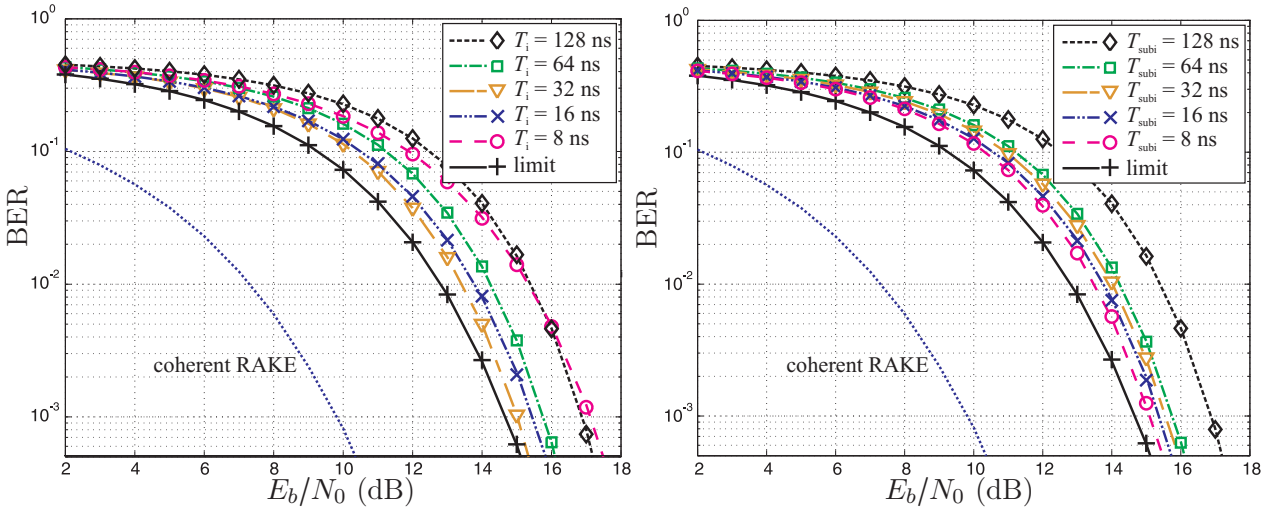

(a) SinW-C for different window sizes T_is

(b) WSubW-C for different sub-window sizes T_{subi}s

Fig. 4.4: BER performance of non-coherent detection using SinW-C and WSubW-C. The lines correspond to envelope detection of 2-PPM. The markers correspond to TR-BPSK signaling.

which requires the synchronization of the integration window, the starting time of the first sub-window is chosen as $T_1 = 0$. We can observe from Figure 4.4(b) that the WSubW-C with $T_{subi} = 8$ ns (which corresponds to a sampling rate of 125 MHz) performs the same as the SinW-C with $T_i = 32$ ns.

For both non-coherent multipath combining schemes, the second-order statistics of the channel profile are required. Taking into account the implementation efforts of both schemes, the WSubW-C not only increases the sampling rate compared to the SinW-C, but also demands a higher resolution of the Analog-to-Digital Converter (ADC), since the digital weighted combining requires soft inputs. The WSubW-C starts integration at $T_1 = 0$ under the assumption of perfect synchronization. Due to the fact that non-coherent combining can significantly alleviate the synchronization impact on the system performance, exact timing for T_1 in both methods is not that critical. All in all, the WSubW-C seems more complicated than the SinW-C.

4.4 Summary and Discussions

Based on the performance analysis, it can be concluded that the 2-PPM and TR-BPSK schemes perform the same but exhibit a 3 dB loss as compared to DPSK [3]. The E_b/N_0 performance can be estimated analytically, even if no concrete channel realizations are considered.

Compared to the coherent detection, there always exists a NC-CL with respect to E_b/N_0 determined by the diversity order or the number of combined paths $L_i = T_i \cdot B$. We can observe

[3] It is assumed that no ISI exists and the same channel realization as well as multipath combining techniques are used.

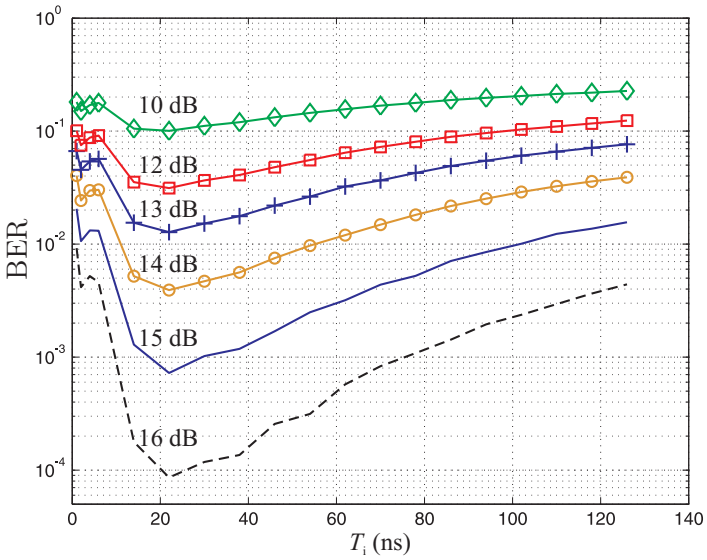

Fig. 4.5: BER of SinW-C as a function of integration interval T_i. 2-PPM is considered as an example.

that the NC-CL increases with L_i asymptotically by around 1 dB per each doubled L_i. In order to enhance the power efficiency for non-coherent detection, such a NC-CL should be alleviated by reducing the integration interval T_i and/or the signal bandwidth B. We have emphasized several key characteristics from the observation of the NC-CL figure and linked these aspects to the following sections.

The SinW-C and the WSubW-C are proposed to effectively collect the multipath energy. In the best case, both multipath combining schemes can reach a similar performance with around 0.5 dB loss away from the performance limit. This limit is achieved by the "quasi" optimal non-coherent detection. From the implementation perspective, SinW-C is preferred to WSubW-C due to a lower complexity of the ADC. The "quasi" optimal receiver is quite complicated, since it requires a Nyquist sampling rate and the norm square of each channel tap should be estimated in order to acquire the weighting coefficients.

5. ANALOG NON-COHERENT RECEIVER IN MULTI-USER SCENARIOS

5.1 Introduction

Motivation:

To support Multiple Access (MA) communications, each transmitted symbol is represented by a stream of pulses which are encoded according to a user-specific code. For example, the MA codes or equivalently Code Division Multiple Access (CDMA) codes can be generated in the form of Time Hopping (TH) for Pulse Position Modulation (PPM) schemes [Sch93, WS98], Delay Hopping (DH) for Transmitted Reference (TR) [HT02], Direct Sequence (DS), or other variants [IEE07, WLJ+09]. In Section 5.2, we will introduce a generic UWB system using an analog non-coherent receiver based on either energy detection or differential detection. We call it "analog" due to the fact that the major part of such a receiver to achieve multipath combining is implemented by means of an analog component, i.e., an integrate and dump filter. The main advantage of such an analog receiver is that after the multipath combining an Analog-to-Digital Converter (ADC) will perform at a low sampling rate on the order of the frame rate and the decoding of the user-specific MA code will be carried out in the digital domain.

The state of the art:

Compared to the DS codes that often contain a high number of non-zero chips, the sparseness of the TH codes facilitates the receiver processing and reduces the complexity. In low-data-rate TH UWB systems, each user is assigned a distinct TH code and the Multi-User Interference (MUI) occurs when impulses are transmitted at the same time. As the TH signaling scheme has been incorporated in the IEEE 802.15.4a standard [IEE07], it is of prime interest to evaluate its MA performance for non-coherent UWB systems in order to obtain suitable system design rules. The performance of the Time Hopping combined with Pulse Position Modulation (TH-PPM) system in the presence of MUI has been analyzed [FNKS02, GA04, SC07], whereas the main focus is on coherent detection. In [SZ08], the MA performance of non-coherent detection is discussed but only random TH codes are considered.

Own Contribution:

In Section 5.4, we consider a TH-PPM UWB system using an analog non-coherent receiver, where "outer" TH codes are used for the MA purpose. In particular, Section 5.4.2 presents a semi-analytical method to evaluate its BER performance in the presence of MUI.

Carefully selecting the codes can reduce the impact from MUI. Non-coherently combining the chips of the user-specific codes may cause an additional loss with respect to the E_b/N_0 performance [1], i.e., Non-Coherent Combining Loss (NC-CL) (cf. Section 4.2). This loss depends on the number of non-zero elements in the TH codes. Therefore, it is preferred to choose "sparse codes" with low code weights, i.e., lots of zeros, to keep the NC-CL as small as possible. In Section 5.4.5.2, the suitability of applying various sparse codes is investigated. According to our analysis, we derive a TH selection rule for the TH-PPM non-coherent systems.

5.2 Multiple Access System

Figure 5.1 shows a generic block diagram of a MA system using an analog non-coherent receiver in the complex baseband. The input bits are firstly encoded by MA codes and then modulated. The transmit pulse shaping filter is denoted as $g_{\mathrm{T}}(t)$. After the transmitted signal goes through the UWB channel and is corrupted by Additive White Gaussian Noise (AWGN) as well as MUI, the received signal is obtained. At the receiver, the analog parts, i.e., the square-law device for energy detection, the analog delay line and the multiplier for differential detection, as well as the integrator, are the same as illustrated in Figure 3.7. The decoding of the MA codes follows after the multipath combining and a low-speed ADC. The decisions are made based on the outputs of the decoding process.

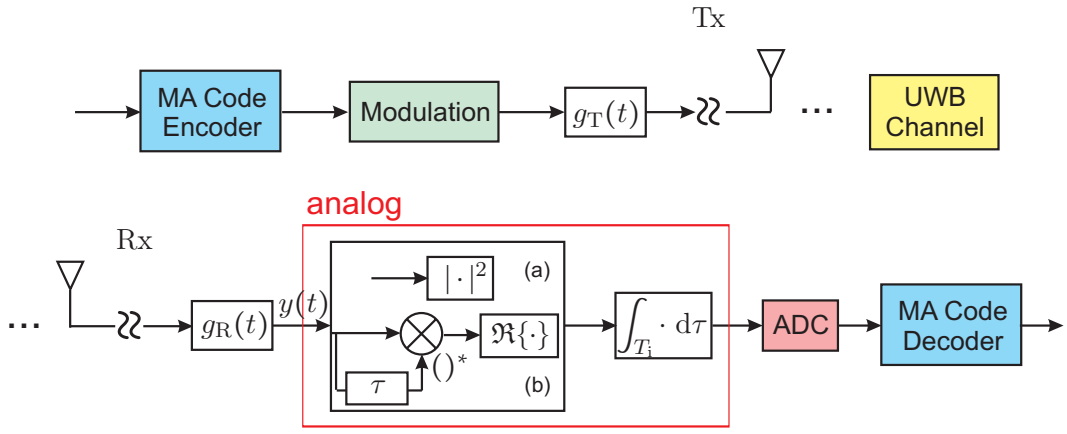

Fig. 5.1: Block diagram of a MA UWB system using an analog non-coherent receiver in complex baseband based on (a) energy detection and (b) differential detection.

[1] where E_b is the energy per bit and N_0 is the noise power density.

5.3 Using Energy Detection

Multiple access systems based on differential detection have been widely investigated in many publications [HT02, WLPK05, CS04, DvdV07]. The major issue lies in the implementation of analog delays (cf. Appendix B.1). The IEEE 802.15.4a standard has incorporated the TH MA technique, while the corresponding performance analysis is rather limited [WLJ+09]. Therefore, we investigate energy detection for the Binary Pulse Position Modulation (2-PPM) signaling scheme combined with the TH.

In the complex baseband, the first transmitted TH-PPM signal for the k-th user in the time interval $0 \le t \le T_b$ is given by

$$s^{(k)}(t) = \sum_{i=0}^{N_s-1} \sqrt{\frac{E_b^{(k)}}{N_s}} g(t - iT_f - C_i^{(k)} T_c - a_0^{(k)} \Delta), \tag{5.1}$$

where $E_b^{(k)}$ is the bit energy for the k-th user and the pulse shape is $g(t)$. Figure 5.2 shows the signal structure. The number of frames per symbol interval T_s is N_s and the number of chips per frame is N_h, where each frame always contains one pulse. The chip interval and the frame duration are represented by T_c and T_f, respectively. The TH code for user k is denoted by $C_i^{(k)}, i = 0, \ldots, N_s - 1$, where $C_i^{(k)}$ takes values in $\{0, 1, \ldots, N_h - 1\}$. For 2-PPM, the information bit of user k satisfies $a_0^{(k)} \in \{0, 1\}$ and $\Delta = T_c/2$ is the modulation delay for 2-PPM.

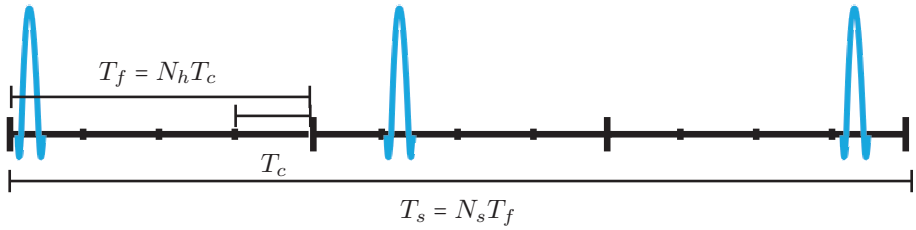

Fig. 5.2: Representation of a TH-PPM signal for the TH code with positions (0,1,3), $N_s = 3, N_h = 4$. The transmitted bit is 0.

As discussed in Chapter 2, the channel impulse response for the k-th user is given by a tapped-delay line model, i.e., $h^{(k)}(t) = \sum_{l=0}^{L-1} \alpha_l^{(k)} \delta(t - l/B)$, where $\alpha_l^{(k)}$ is the l-th complex channel tap for the k-th user with $\sum_{l=0}^{L-1} |\alpha_l^{(k)}|^2 = 1$ and B is the total bandwidth of the signal. Therefore, after pulse matched filtering the signal received from N_u users can be expressed as

$$y^{(1)}(t) = \tilde{s}^{(1)}(t) + v(t) + n(t). \tag{5.2}$$

The delay τ_k for the k-th user is associated with asynchronous transmissions. Assume that τ_1 is known and $\tau_1 = 0$ is chosen without loss of generality. The desired signal component $s^{(1)}(t)$ is given by

$$\tilde{s}^{(1)}(t) = \sum_{i=0}^{N_s-1} \sum_{l=0}^{L-1} \alpha_l^{(1)} \sqrt{\frac{E_b^{(1)}}{N_s}} \tilde{g}(t - \frac{l}{B} - iT_f - C_i^{(1)} T_c - a_0^{(1)} \Delta), \tag{5.3}$$

and the MUI is given by

$$v(t) = \sum_{k=2}^{N_u} \sum_{i=0}^{N_s-1} \sum_{l=0}^{L-1} \alpha_l^{(k)} \sqrt{\frac{E_b^{(k)}}{N_s}} \tilde{g}\left(t - \frac{l}{B} - iT_f - C_i^{(k)} T_c - a^{(k)}_{\lfloor \frac{iN_h + C_i^{(k)} + 1 - q_k}{L_m} \rfloor} \Delta - \tau_k\right), \tag{5.4}$$

where $\tilde{g}(t) = g(t) * g_R(t)$ and $n(t) = \widehat{n}(t) * g_R(t)$ are filtered (convolved) pulse and noise, respectively. Zero-mean, complex-baseband AWGN $\widehat{n}(t)$ has a Power Spectral Density (PSD) N_0. Asynchronous (but chip synchronous) transmission is assumed, meaning that $\tau_1 - \tau_k = q_k T_c$ in equation (5.4) and the random variable q_k takes values in $\{0, \ldots, L_m - 1\}$ with equal probability. The length (or processing factor [2]) of a TH code is denoted by $L_m = N_h N_s$. The floor operator $\lfloor x \rfloor$ rounds the argument x down to the closest integer that is less and equal to x. For simplicity, no Inter-/Intra-Symbol Interference (ISI) is assumed.

With partial knowledge of the channel for the desired user, we use the Single Window Combining (SinW-C) [SWH07a] (cf. Section 4.3.1), which tries to synchronize the integration window of length T_i at time position T_1 so that the maximum signal energy with respect to the noise is received within T_i. The decision variables in two time slots $m \in \{0, 1\}$ are given as

$$Z_m^{(1)} = \sum_{i=0}^{N_s-1} \int_{iT_f + C_i^{(1)} T_c + m\Delta + T_1}^{iT_f + C_i^{(1)} T_c + m\Delta + T_1 + T_i} |\tilde{s}^{(1)}(t) + v(t) + n(t)|^2 \mathrm{d}t. \tag{5.5}$$

The decision is made based on the sign of $Z^{(1)} = Z_0^{(1)} - Z_1^{(1)}$.

5.4 Time Hopping Pulse Position Modulation using Sparse Codes

We consider the following alternatives to construct the sparse codes.

5.4.1 Sparse Code Constructions

Conventional TH Codes

- Random Codes (RCs): each element of the RCs takes value in $\{0, \ldots, N_h - 1\}$, where N_h is the number of chips within one frame. Given the number of frames per symbol interval N_s, RCs can be denoted by (N_h, N_s),
- Maximum Length Sequences (M-Seqs): direct sequence codes such as M-Seqs can be mapped to unipolar sparse sequences [CTBR03]. The M-Seq which contains $\{0, 1\}$ is firstly generated by a maximal linear feedback shift register with the number of stages p, i.e., the length of the code is $N_h = 2^p - 1$. It is then mapped to a sequence of decimal numbers that determine the TH positions using a sliding window. Figure 5.3 illustrates

[2] We use the term "processing factor" instead of the "processing gain" due to the fact that in the multiple access UWB systems based on an analog non-coherent receiver (cf. Section 5.2), although the "gain" comes from the multiple access codes which are used to distinct multiple users, non-coherently combining the code will lead to a NC-CL.

the generation procedure of one TH code based on the M-Seq as an example. There are N_h chips per frame for a unipolar M-Seq and the length is $L_m = N_h N_s$. M-Seqs are represented by the key parameters written in a form of $(2^p - 1, N_s)$, supporting $2^p - 1$ users.

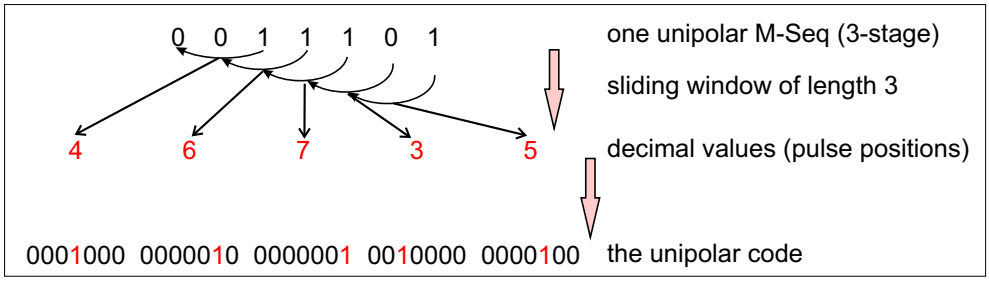

Fig. 5.3: An example of generating TH codes based on M-sequences with $p = 3, N_s = 5$.

Optical Orthogonal Codes

The optical orthogonal codes are characterized by the format $(n, w, \lambda_a, \lambda_c)$, where n denotes the sequence length, w is the number of ones, and λ_a and λ_c represent the maximum value of the off-peak auto-correlation and the maximum value of the cross-correlation, respectively.

- Prime Codes (PCs): PCs are generated in the form of $(p^2, p, p-1, 1 \text{ or } 2)$, where p is a prime [PF86]. There are p different codes in PCs and thus p users can be supported in a system. For PC, there are p frames per symbol duration and p chips per frame, i.e., (p, p).

- Quadratic Congruence Codes (QCCs): QCCs can be constructed in terms of $(p^2, p, 2, 4)$ [MKT93]. Compared to PCs, QCCs have different auto-correlation and cross-correlation properties. There are $p - 1$ different sequences that can be generated. We can also represent the QCCs as (p, p).

- Truncated Costas Codes (TCCs): TCCs are in the form of $(w(2p-3), w, 1, 1)$ [MHT95], where w is an integer, representing the code weight and p is a prime. In the code construction, TCCs satisfy the inequality $1 \leq w \cdot Q \leq p - 1$, where Q is the number of users that can be served. There are $2p - 3$ chips per frame and w frames per symbol interval, i.e., $(2p - 3, w)$.

Table 5.1 shows some examples of the discussed sparse codes, where "1" denotes the position of the transmitted pulse.

Tab. 5.1: Examples of Sparse Codes.

M-Seq	$p = 3, N_s = 5$
Code 1	0001000 0000010 0000001 0010000 0000100
Code 2	0000010 0000001 0010000 0000100 0100000
Code 3	0000001 0010000 0000100 0100000 1000000
Code 4	0010000 0000100 0100000 1000000 0001000
Code 5	0000100 0100000 1000000 0001000 0000010
Code 6	0100000 1000000 0001000 0000010 0000001
Code 7	1000000 0001000 0000010 0000001 0010000
PC	$p = 5$
Code 1	10000 01000 00100 00010 00001
Code 2	10000 00100 00001 01000 00010
Code 3	10000 00010 01000 00001 00100
Code 4	10000 00001 00010 00100 01000
Code 5	10000 10000 10000 10000 10000
QCC	$p = 5$
Code 1	10000 01000 00100 01000 10000
Code 2	10000 00100 01000 00100 10000
Code 3	10000 00010 00001 00010 10000
Code 4	10000 00001 00100 00001 10000
TCC	$p = 7, w = 2$
Code 1	00001000000 00100000000
Code 2	00000100000 00001000000
Code 3	00100000000 00000100000

5.4.2 Multiple Access Performance Analysis

5.4.2.1 Code Correlation Function

In order to avoid MUI, the codes assigned to different users should be orthogonal. In a synchronous transmission (e.g., downlink), the orthogonality can be maintained, i.e., no pulse overlapping takes place among different users. However, in an asynchronous case (e.g., uplink), pulse collisions from the active users cannot be avoided due to the unknown shifts or delays of the signals. The code correlation function of two TH sequences defined in [ZZG03] refers to the number of "hits" (or collisions) between two TH sequences with a certain time delay (i.e., cross-correlation) or between the delayed versions of the same TH code (i.e., auto-correlation).

Although the maximum number of the "hits" in the code correlation function provides information about the code performance, it is more efficient to use the Probability Density Function (PDF) of the "hits" for analyzing the multi-user performance. In [GA04], a mathematical model for the PDF of the MUI is derived based on the histograms of the "hits" obtained by computer simulations. It can be applied to the evaluation of the MA performance for a Binary Phase Shift Keying (BPSK)-based coherent UWB system [DB03].

5.4.2.2 Semi-Analytical Code Performance Evaluation

In the following evaluation, it is assumed that the bit energy $E_b^{(k)} = E_b, k = 1, \ldots, N_u$ is identical for all users, i.e., we consider perfect power control case.

Realistic Measure

The square-law device in the receiver results in the squaring of the MUI. Due to this "non-linearity" of the resulting MUI in the decision variables, the code correlation function cannot totally interpret the TH code performance in a non-coherent system. The statistics of the MUI are required to derive the BER expressions for the non-coherent TH-PPM system. However, it is quite difficult to model the MUI especially when different TH codes are used. Even with a derived MUI model as introduced in [GA04], the non-coherent detection makes the BER calculation more complicated.

Therefore, we propose a realistic method as described in Figure 5.4 to obtain the statistics of the effective "hits". Unlike the Monte Carlo simulations, this method does not take care of the AWGN and the analog implementation of non-coherent detection, but determines the samples of the decision variables conditioned on information bits, user-specific sequences as well as asynchronous transmissions. The 2-PPM bits for the k-th user, $\sum_{m=-\infty}^{\infty}\{a_m^{(k)}\delta[m] + (1-a_m^{(k)})\delta[m-1]\}, a_m^{(k)} \in \{0,1\}$ with m as an integer and $\delta[\cdot]$ as the Kronecker Delta function defined by

$$\delta[m] = \begin{cases} 1 & \text{if } m = 0 \\ 0 & \text{if } m \neq 0 \end{cases}, \tag{5.6}$$

are generated and encoded by TH codes. Asynchronous transmission among different users is modeled by randomly generating a shift for each user $q_k, k = 2, \ldots, N_u$, where q_k is explained below the equation (5.4). These signals from all users are then summed up. The decoder comes after the square operation and the difference calculation of the samples in two PPM slots. The final output gives a series of integer numbers, which are named effective "hits" since they are obtained after the non-coherent demodulation. We denote the total output "hits" as $H = H_0 - H_1$, where H_0 and H_1 are the effective "hits" from two PPM slots, respectively.

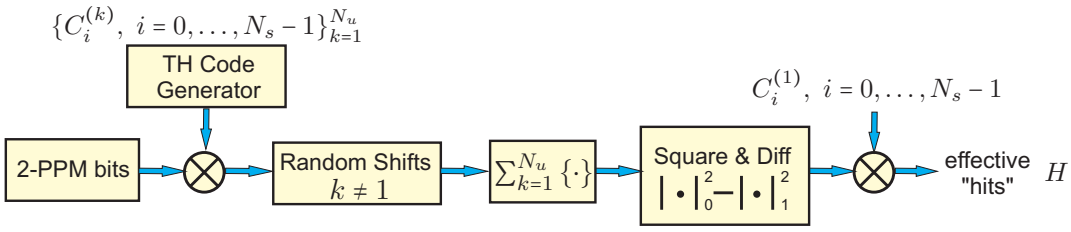

Fig. 5.4: The proposed realistic measure of the code performance.

Performance Analysis

According to the sampling approach [QW05], the decision variables in equation (5.5) can

be expressed by the samples of the received signal as follows

$$\begin{cases} Z_0^{(1)} = \sum\limits_{l\in\mathfrak{L}_\mathrm{i}}\sum\limits_{i=1}^{N_s}\left|\sqrt{\dfrac{E_b}{N_s}}\alpha^{(1)}[l] + \sqrt{\dfrac{E_b}{N_s}}\sum\limits_{k=2}^{N_u} h_{c_0}^{(k)}[i]\alpha^{(k)}[l] + n_0[i,l]\right|^2 \\ Z_1^{(1)} = \sum\limits_{l\in\mathfrak{L}_\mathrm{i}}\sum\limits_{i=1}^{N_s}\left|\sqrt{\dfrac{E_b}{N_s}}\sum\limits_{k=2}^{N_u} h_{c_1}^{(k)}[i]\alpha^{(k)}[l] + n_1[i,l]\right|^2 \end{cases}, \tag{5.7}$$

where $h_{c_0}^{(k)}[i]$ and $h_{c_1}^{(k)}[i]$ take values in $\{0,1\}$ denoting whether there is a collision in the i-th frame for user k and $\mathfrak{L}_\mathrm{i}$ denotes the taps that are included in the single integration window (cf. Section 4.3).

For a moderate number of users we can use a Gaussian approximation to obtain the BER (conditioned on $a_0^{(1)} = 0$) as a function of the decision variable $Z^{(1)}$ by

$$P_{b|a_0^{(1)}=0} \approx \mathrm{Q}\left(\frac{\mathbb{E}\{Z^{(1)}\}}{\sqrt{\mathbb{V}\{Z^{(1)}\}}}\right), \qquad Z^{(1)} = Z_0^{(1)} - Z_1^{(1)}, \tag{5.8}$$

where $\mathrm{Q}(\alpha) = \frac{1}{\sqrt{2\pi}}\int_\alpha^\infty e^{-\frac{x^2}{2}}\mathrm{d}x$ [Pro01]. If the bits "0" and "1" are transmitted with equal probability, the total BER is given by

$$P_b = \frac{P_{b|a_0^{(1)}=0}}{2} + \frac{P_{b|a_0^{(1)}=1}}{2}. \tag{5.9}$$

Using equation (5.7), the expectation $\mathbb{E}\{Z^{(1)}\}$ and the variance $\mathbb{V}\{Z^{(1)}\}$ can be calculated by

$$\begin{cases} \mathbb{E}\left\{Z^{(1)}\right\} = \dfrac{E_b}{N_s}\mathbb{E}\{H\} \\ \mathbb{V}\left\{Z^{(1)}\right\} = 2N_sN_0^2 + 2N_0\dfrac{E_b}{N_s}\left(\mathbb{E}\{H_0\} + \mathbb{E}\{H_1\}\right) + \left(\dfrac{E_b}{N_s}\right)^2\mathbb{V}\{H\} \end{cases} \tag{5.10}$$

in AWGN and

$$\begin{cases} \mathbb{E}\left\{Z^{(1)}\right\} = \dfrac{E_b}{N_s}\mathbb{E}\{H\}\,\mathbb{E}\left\{\sum\limits_{l\in\mathfrak{L}_\mathrm{i}}|\alpha_l|^2\right\} \\ \mathbb{V}\left\{Z^{(1)}\right\} = 2N_sL_\mathrm{i}N_0^2 + 2N_0\dfrac{E_b}{N_s}\left(\mathbb{E}\{H_0\} + \mathbb{E}\{H_1\}\right)\mathbb{E}\left\{\sum\limits_{l\in\mathfrak{L}_\mathrm{i}}|\alpha_l|^2\right\} + \left(\dfrac{E_b}{N_s}\right)^2\mathbb{V}\{H\}\,\mathbb{E}\left\{\left(\sum\limits_{l\in\mathfrak{L}_\mathrm{i}}|\alpha_l|^2\right)^2\right\} \end{cases} \tag{5.11}$$

in multipath channels. It can be observed that the performance depends on the statistics of the effective "hits" H, H_0, and H_1 in the AWGN channel. Additionally, in the case of multipath propagation, the second- and fourth-order moments of the channel impulse response within a time window containing a set of L_i channel taps also influence the performance.

5.4.3 Simulation Results

For the multipath propagation scenario, we use UWB channels measured in the Non-Line-Of-Sight (NLOS) office scenario introduced in Section 2.3. The 3-dB signal bandwidth is $B_3 = 500$ MHz and the channel resolution is chosen to be 1 ns.

In order to obtain the analytical results described in equation (5.11), the knowledge of the channel statistics is required. From the channel model discussed in [KP02], the amplitudes of the channel taps $(\alpha_l, l = 0, 1, \ldots, L-1)$ can be approximated by a Rayleigh distribution, which is given by

$$f_{|\alpha_l|}(x) = \frac{2x}{\Omega}\exp\left(-\frac{x^2}{\Omega}\right), \tag{5.12}$$

where $\Omega = \mathbb{E}\left\{|\alpha_l|^2\right\}$ is the second-order moment of the channel impulse response. From the distribution of the path gains, we can calculate the n-th moment of the path gain $|\alpha_l|$ according to equation (A.30) in Appendix A.2.4 as

$$\mathbb{E}\left\{|\alpha_l|^n\right\} = \begin{cases} \Omega^{\frac{n}{2}}\Gamma\left(1+\frac{n}{2}\right), & n \text{ is even} \\ 0, & n \text{ is odd} \end{cases}, \tag{5.13}$$

where $\Gamma(\cdot)$ is the Gamma function. It is also assumed that channel coefficients for different users are uncorrelated, i.e., $\mathbb{E}\{\alpha_l^{(k_m)}(\alpha_l^{(k_n)})^*\}=0$ for $k_m \neq k_n$.

The power delay profile of the channel follows an exponential decay

$$|\alpha_l|^2 = \kappa^2 \exp\left(-\frac{l}{r}\right), \tag{5.14}$$

where $r = 9.5$ ns for this scenario [KP03]. The channel gain is assumed to satisfy $\sum_{l=0}^{L-1}|\alpha_l|^2 = 1$ so that the total received bit energy equals E_b. Then we can calculate κ^2 via equation (5.14).

In the simulations, we will investigate the following sparse codes: RCs, M-Seqs, PCs, QCCs, and TCCs. For a fair comparison, we choose the lengths of different TH codes as close as possible so as to keep a similar data rate. The parameters of the considered TH sequences are listed in Table 5.2. The BER performance in the multipath scenario is obtained by averaging over various channel realizations.

5.4.4 Code-induced Non-Coherent Combining Loss

In Section 4.2, we have discussed several properties regarding the NC-CL. For a system using multiple access techniques in a multipath channel, if a user-specific code is applied, the signal energy is spread over time by both multipath propagation and coding. From Figure 4.1, it can be concluded that non-coherently combining the deterministic part of the time-domain spreading due to the "outer" code results in an additional loss. Such a NC-CL can be determined by the code weight N_s in the user-specific code.

5.4.5 Evaluation of Multiple Access Performance

5.4.5.1 Using the Code Correlation Function

Based on the code correlation function defined in [ZZG03], we plot the cross-correlation of each considered sparse code in Figure 5.5. The maximum number of "hits" between two sequences of the same kind is summarized in Table 5.2. It can be seen that the M-Seq has the largest maximum number of "hits" in code correlation function, meaning a relatively high probability of collisions and an unsatisfactory performance. RC and QCC produce similar values. PC may have the same maximum number of "hits" (i.e., 1) as TCC, but a larger code weight (i.e., N_s = 23 for PC compared to N_s = 5 for TCC). Since the code-induced NC-CL can be determined by N_s, TCC may lead to a smaller loss than PC.

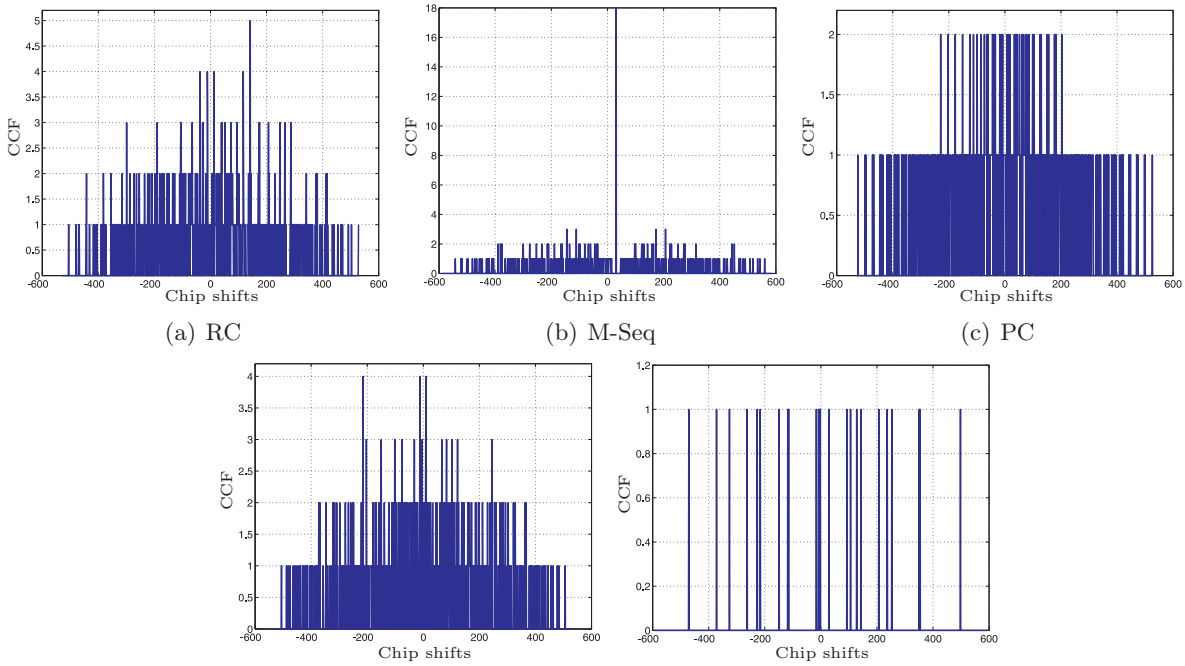

(a) RC (b) M-Seq (c) PC

(d) QCC (e) TCC

Fig. 5.5: Examples of cross-correlation plots for different codes. "CCF" denotes the code correlation function.

Tab. 5.2: Maximum number of "hits" of the code correlation function ("CCF") for any two TH sequences

Codes	RC	M-Seq	PC	QCC	TCC
Parameters	N_h = 23 N_s = 23	p = 5 N_s = 19	p = 23	p = 23	p = 61 w = 5
Code Length	529	589	529	529	595
Max{CCF}	5	18	1 or 2	4	1

5.4.5.2 Semi-Analytical Performance and TH Code Selection

For the considered TH codes with parameters shown in Table 5.2, Table 5.3 lists the corresponding statistics of the "hits" as described in Section 5.4.2.2 which are used to estimate the BER performance. Figure 5.6 and Figure 5.7 show the BER performance of the 2-PPM based non-coherent UWB system employing different sparse TH codes with 11 users in AWGN and multipath channels, respectively. We can conclude that our semi-analytical method (shown by markers) well estimates the BER performance (simulated results are shown by lines). Even though in the AWGN channel, our analytical results cannot completely characterize the error floors in the case of the TCC and the M-Seq, they are sufficient to distinguish and approximate the overall performance when applying different codes. In the multipath channel, the proposed semi-analytical method using the Gaussian approximation is more accurate since a lot of multipath arrivals are collected at the receiver.

In Figure 5.7, we include the single-user performance for TCC (N_s = 5), RC (N_s = 23), and M-Seq (N_s = 19). Comparing these three curves in Figure 5.7, the performance difference only depends on the number of pulses per symbol or the code weight N_s that are non-coherently combined, i.e., code-induced NC-CL. In the presence of MUI, the performance varies with respect to different TH codes. TCC that has the lowest "hits" values provides the best MA performance. Although M-Seq has a smaller weight than RC, QCC, or PC, it performs the worst due to a higher value of "hits". The RC performs the same as QCC. The performance of PC is also satisfactory, but as compared to TCC a higher NC-CL is observed due to a larger N_s. The code-induced NC-CL cannot be distinguished in the presence of MUI when the codes have a similar code weights (19 versus 23). An error rate floor can be observed in the higher Signal to Noise Ratio (SNR) region, especially for M-Seq and TCC. This error floor is caused by the MUI with a relatively high power.

Tab. 5.3: The statistics of the effective "hits" (H, H_0, and H_1) for 11 active users

	$\mathbb{E}\{H_0\}$	$\mathbb{E}\{H_1\}$	$\mathbb{E}\{H\}$	$\mathbb{V}\{H\}$
RC	39	6	33	110
M-Seq	29	4	25	83
PC	39	6	33	87
QCC	39	6	33	107
TCC	5.6	0.2	5.4	2.3

Figure 5.8 shows BER versus the number of active users in AWGN. It can be seen in Figure 5.8(a) that TCC is more advantageous than other TH codes but a smaller number of users can be served. For the codes with N_s = 23 (or 19), PC performs the best. RC and M-Seq can accommodate more users. When E_b/N_0 = 18 dB as illustrated in Figure 5.8(b), PC still has a good performance but TCC loses its advantage due to the error floor.

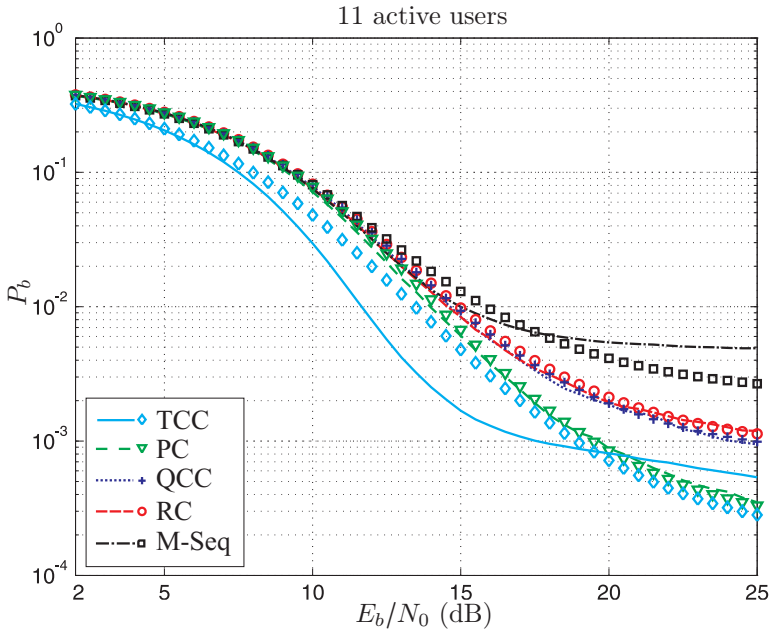

Fig. 5.6: BER performance of the 2-PPM based non-coherent UWB system using different TH codes in AWGN. Lines represent simulated results and markers are analytical results.

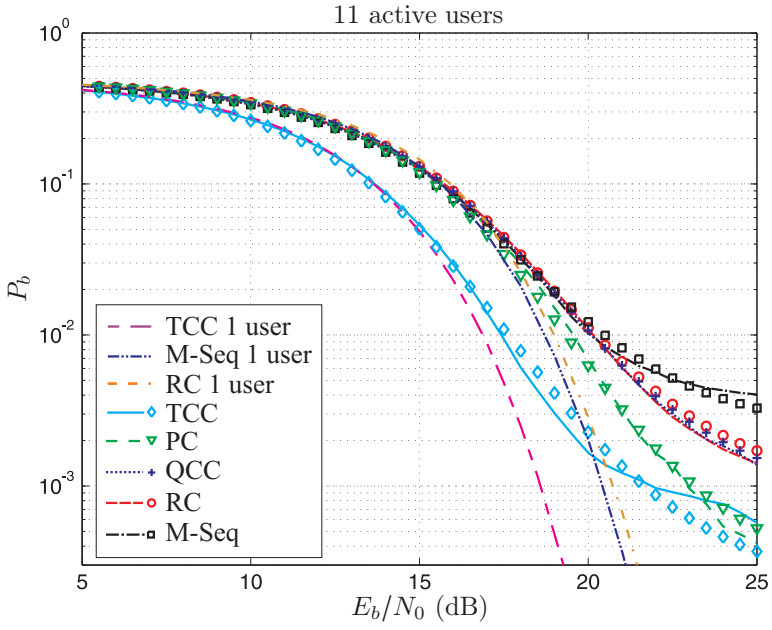

Fig. 5.7: BER performance of the 2-PPM based non-coherent UWB system using different TH codes in the measured multipath channel. SinW-C is used with optimum integration interval T_{i} = 16 ns. Lines represent simulated results and markers are analytical results.

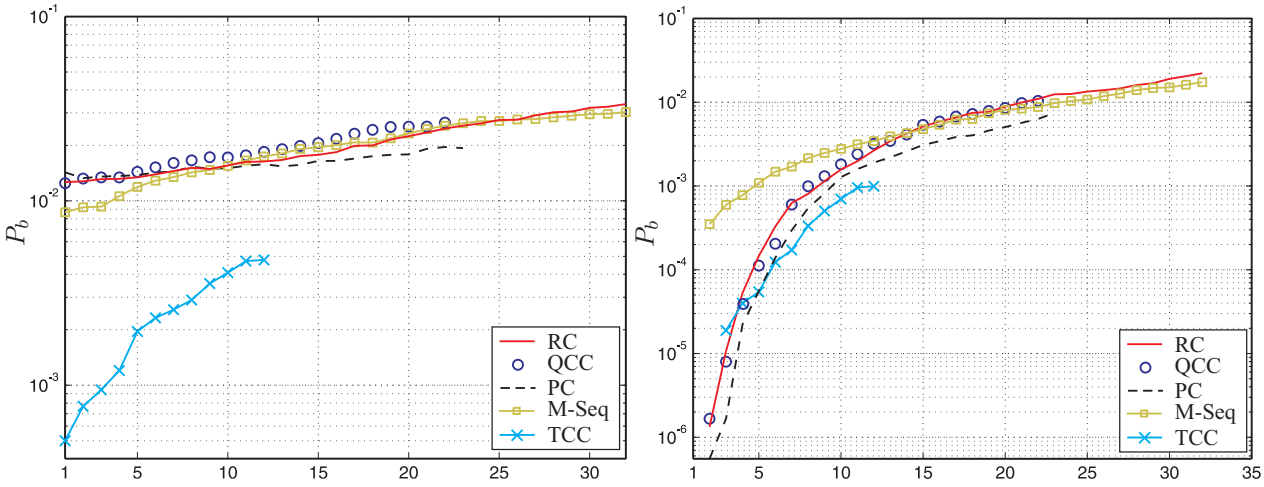

(a) E_b/N_0 = 13 dB (b) E_b/N_0 = 18 dB

Fig. 5.8: BER versus the number of users in AWGN for different SNRs.

5.5 Summary and Discussions

Analog non-coherent receivers, whose major part is carried out in terms of an integrate and dump filter, can significantly reduce the sampling rate of the ADC down to the symbol rate or frame rate. We have introduced a unified MA UWB system using analog non-coherent receivers, where the decoding of the CDMA codes is carried out *after* the non-coherent multipath combining.

The major problem of the system based on differential detection is the implementation of analog delay lines. Furthermore, the MA behavior of the TH technique which is applied for energy detection has not been sufficiently analyzed. Here, we consider a TH-PPM non-coherent UWB system using sparse codes in the MUI scenario. Different sparse codes are constructed and considered as TH codes, for example, RCs, M-Seqs, PCs, QCCs, and TCCs. In order to study the behavior of the MUI in non-coherent systems, we propose a realistic and efficient measure for analyzing the MA performance based on the statistics of the effective number of "hits". Compared to the code correlation function method, our proposed method provides an accurate and complete performance evaluation.

We analyze the BER performance when various sparse codes are employed. Independently of the MUI, there is always an additional NC-CL due to non-coherently combining the chips that are spread by the TH codes. This code-induced NC-CL can be estimated analytically. The sparse codes with a smaller number of pulses per symbol duration N_s are preferred (such as TCC). Meanwhile, the codes with better correlation properties (mainly cross-correlation) are more robust to MUI. From our MA performance analysis, a TH code selection criterion can be obtained. It shows that

- particularly in the lower SNR region, TCC exhibits its advantage due to its very low code weight N_s and a small range of "hits", and

- PC also provides a good performance in the light of a smaller number of "hits" and a lower error rate floor.

Therefore, in the presence of MUI, the sparse optical orthogonal codes with low code weights and a smaller number of cross-correlation "hits" are suitable for non-coherent UWB systems.

6. DIGITAL NON-COHERENT RECEIVER FOR IMPULSE RADIO ULTRA WIDEBAND COMMUNICATIONS

6.1 Introduction

Motivation and The state of the art:

In Chapter 5, we have analyzed the multiple access performance of a Time Hopping combined with Pulse Position Modulation (TH-PPM) system based on non-coherent detection, where the major part of the receiver is carried out in terms of analog devices before the decoding of the Multiple Access (MA) codes. It has been shown that an additional Non-Coherent Combining Loss (NC-CL) with respect to E_b/N_0 arises due to non-coherently combining the chips that are spread by the user-specific Time Hopping (TH) codes. This loss increases with the number of non-zero elements in the TH code.

To eliminate this code-induced NC-CL, an alternative is to apply a matched filter which can coherently combine the MA codes before non-coherent processing (cf. Section 4.2). In [TGM06], a hybrid matched filter correlation receiver is proposed for a Transmitted Reference (TR) system. However, such a receiver relies on the analog filter to resolve the spreading waveform, which is practically impossible since long analog delay lines with a high accuracy are required. In the multi-user scenario, multiple analog receivers should be designed for different users, imposing an even higher complexity on the receiver implementation.

Why not resort to completely ***digital*** solutions? Unlike the concept proposed in [TGM06], our idea here is to apply a Digital Code Matched Filter (DCMF), which is matched to the user-specific TH code, *before* non-coherent processing. The potential of implementing high-speed but very low-resolution Analog-to-Digital Converters (ADCs) has been emphasized in recent advances of semiconductor technology [OCWB02, Wah09]. Their availability for UWB communications has also been studied in [HSA05, TXS07]. In our proposed DCMF-based non-coherent receiver, the DCMF follows after such a time-domain ADC, restricting the NC-CL only to the multipath arrivals. One big advantage is that by applying completely digital solutions to non-coherent detection, the broadband analog delays can be avoided. Furthermore, it also facilitates the development of various techniques, such as non-coherent multipath combining schemes, multi-user detection, differential receivers, etc..

Own Contribution:

We start with Section 6.2, which describes a unified MA system employing the proposed DCMF for energy detection as well as differential detection. Besides the NC-CL, in Section 6.3 we analyze and compare analog as well as digital receivers with respect to their interference rejection capability.

One of the key contributions is that we are able to quantify the quantization induced performance penalty for the single-user case and associate it with the system design parameters. Section 6.4.1 analytically evaluates the one-bit quantization loss and also numerically analyzes the impact of the ADC resolution as well as the input signal level on the system performance. For the multi-user case, the MA performance analysis is carried out in Section 6.4.2. Taking into account the quantization effect, we propose a system design rule for TH-PPM using digital non-coherent receivers.

From the system level point of view, Section 6.5 deals with the uncoordinated piconet channelization in different multipath scenarios (specified in IEEE 802.15.4a channel models [MBC+05]) for both analog and digital non-coherent receivers.

The Narrowband Interference (NBI) is one of the most severe sources that lead to the performance degradation of non-coherent UWB receivers. A novel NBI suppression scheme using a soft limiter is proposed in Section 6.6. We investigate the impact of the soft limiter threshold and discuss an adaptation technique. Both single-tone interference and the interference caused by the Orthogonal Frequency Division Multiplexing (OFDM)-based IEEE 802.11a wireless local area network are considered.

To further improve the power efficiency, Section 6.7 proposes two TH transmission schemes based on Walsh modulation and evaluates the corresponding MA performance. For a given data rate, we derive a selection criterion with respect to the transmission scheme and the modulation order in order to achieve both power efficiency and bandwidth efficiency. This section also compares the proposed M-ary Walsh schemes to M-ary Pulse Position Modulation (PPM) in terms of the MA performance and the robustness against quantization loss.

From the ADC power consumption perspective, oversampling is more favorable than increasing its resolution. Section 6.8 proposes a digital receiver based on one-bit oversampling Sigma-Delta ($\Sigma\Delta$) ADCs. For different modulation schemes such as M-PPM/Walsh and different system parameters, we evaluate how the oversampling rate influences the quantization loss.

As presented in this chapter, the ***digital*** non-coherent receiver is the major achievement of our work. We will summarize the significance and potential of applying fully digital solutions to low-complexity UWB communications in the Section 6.9.

6.2 Digital Code Matched Filter-based Non-Coherent Receiver using Low-Resolution Analog-to-Digital Converters

The proposed DCMF-based non-coherent receiver is shown in Figure 6.1 for both energy detection and differential detection. Unlike the processing for the analog receiver in Figure 5.1, the received signal after filtered by the pulse matched filter $g_{\mathrm{R}}(t)$ is fed directly to a high-speed ADC of a resolution b ($1 \leq b \leq 4$). The output digital signal $y[i]$ will be decoded by a DCMF which is matched to the MA code. Then the square-law device or the delay line as well as the multipath combiner will operate digitally. In comparison with the "analog" receiver, the DCMF restricts the NC-CL only to the multipath arrivals. Figure 6.2(a) depicts the structure of a DCMF, where the delay elements $D_1, \ldots, D_{N_s}$ are the intervals between consecutive pulses and the coefficients $c_1, \ldots, c_{N_s}$ correspond to the weights of MA code. Equivalently, a correlator can also be implemented (cf. Figure 6.2(b)), consisting of an analog MA waveform multiplier, a b-bit ADC, and a digital accumulator with a delay $D_i, i = 1, \ldots, N_s$ controlled by the MA code. The accumulator is a digital feedback loop which is reset every symbol duration in order to combine the energy of the time-spread pulses.

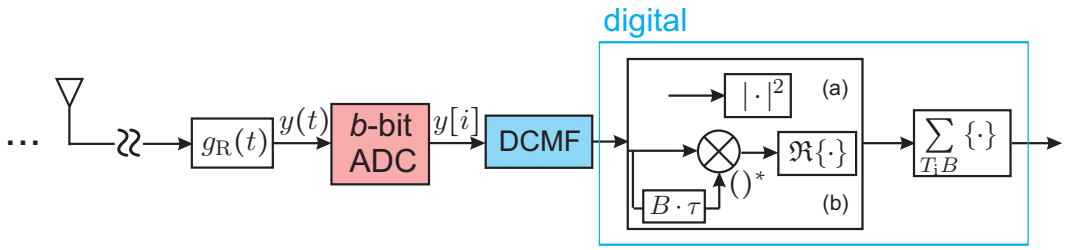

Fig. 6.1: Block diagram of a DCMF-based non-coherent receiver in complex baseband for (a) energy detection and (b) differential detection.

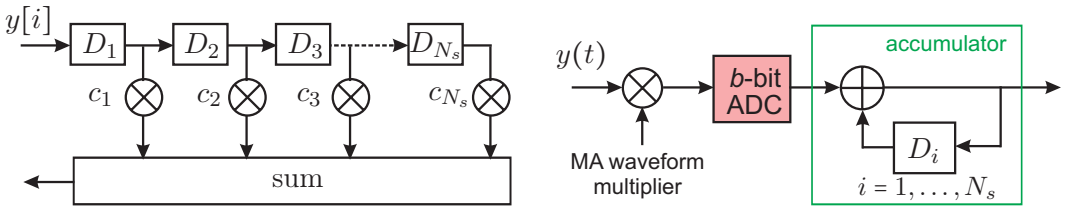

(a) DCMF

(b) An alternative: correlator

Fig. 6.2: The implementation of a DCMF and its variant.

6.3 Comparison: analog versus digital

The DCMF coherently combines the MA code before non-coherent processing and thus avoids the code-induced NC-CL which exists in the "analog" receiver. Apart from this point of view, this section compares the proposed digital receiver with its analog counterpart only in the presence of Multi-User Interference (MUI). The superior performance of the digital receiver

on the Inter-/Intra-Symbol Interference (ISI) resistance capability is discussed in Appendix B.2.

6.3.1 TH-PPM with Energy Detection

The signal model of the TH-PPM has been introduced in Section 5.3. Without considering Additive White Gaussian Noise (AWGN) and any multipath channels, we only evaluate the MUI effect on the performance of the DCMF-based receiver (cf. Figure 6.1(a)) with a full-resolution ADC and the analog one shown in Figure 5.1(a). Figure 6.3 illustrates the corresponding BER as a function of the number of asynchronous users N_u. We consider the perfect power control and the chosen random TH codes have the parameters $N_h = 23, N_s = 23$. The number of users is chosen to be sufficiently large so that the performance can be properly shown. Except for the NC-CL, the DCMF-based receiver also provides a higher robustness to MUI than the analog one.

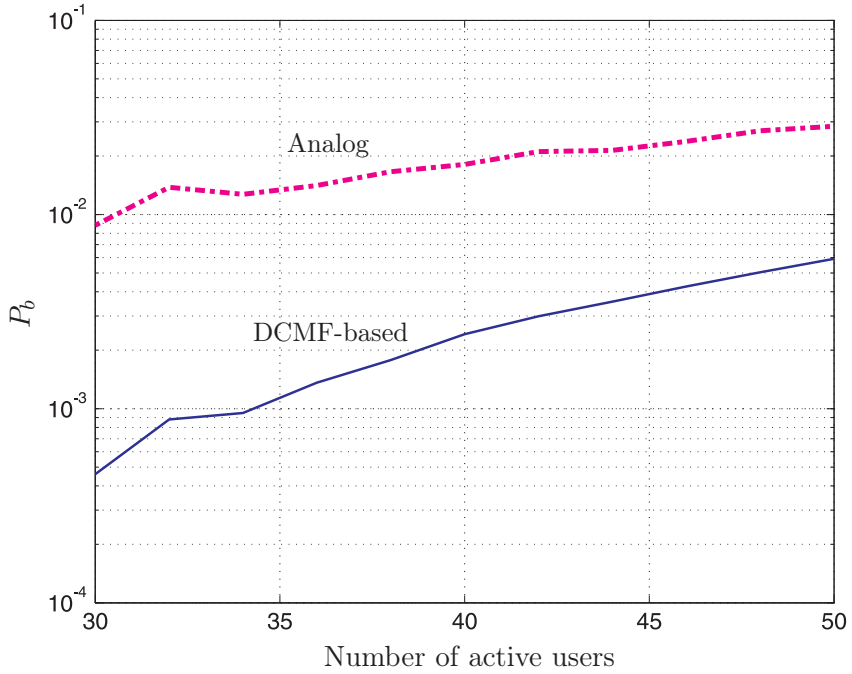

Fig. 6.3: BER versus the number of active users without AWGN for TH-PPM in the case of perfect power control. The chosen random TH codes have the parameters $N_h = 23, N_s = 23$.

6.4 Performance Analysis and System Design Rule

In order to derive a system design rule for TH-PPM, this section analyzes the performance of the proposed DCMF-based receiver influenced by the resolution of the Nyquist rate ADC as well as by the MUI.

6.4.1 Quantization Effect

6.4.1.1 Quantization Model

Our digital solutions greatly rely on an ADC, which operates at a Nyquist sampling rate but has a very low resolution. We denote the ADC resolution as b and assume that this b-bit ADC has a range of ± 1. The sampled received signal $\widehat{y}[i]$ is typically normalized such that $\max_i\{|\widehat{y}[i]|\} = 1$ and scaled by the the input signal level for proper quantization. We consider the b-bit uniform scalar midrise quantizer with step size $1/2^{b-1}$ and the quantization levels $x_l = \pm(l - 1/2)/2^{b-1},\ l = 1, 2, \ldots, 2^{b-1}$. The threshold values $T_{\pm l},\ l = 0, 1, 2, \ldots, 2^{b-1}$ are given by

$$T_l = \begin{cases} 0, & l = 0 \\ (x_l + x_{l+1})/2, & l = 1, 2, \ldots, 2^{b-1} - 1 \end{cases}. \tag{6.1}$$

In our system, the real part and the imaginary part of each received signal sample are quantized respectively by a separate quantizer [MN08]. The quantized received signal can be denoted by $y_p[i] = \mathrm{Q_n}\{G \cdot \widehat{y}_p[i]\}, p \in \{R, I\}$, where $\mathrm{Q_n}\{\cdot\}$ represents "Quantization", the real part is denoted by "R", the imaginary part by "I", and G is the input signal level or gain.

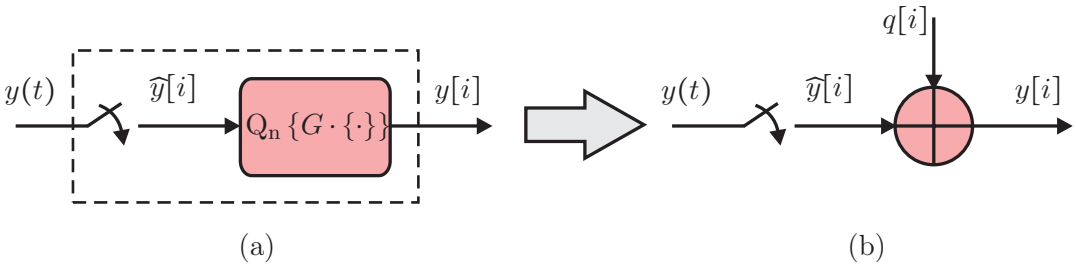

Fig. 6.4: The simplified block diagram of an ADC (a) and its additive noise model (b).

We can use an additive quantization noise model as shown in Figure 6.4 for the b-bit ADC. The quantization noise is written as

$$q_p[i] = \mathrm{Q_n}\{G \cdot \widehat{y}_p[i]\} - \widehat{y}_p[i],\ p \in \{R, I\}. \tag{6.2}$$

There are two kinds of quantization noise. The error induced by the clipping is referred to as the overload noise. The distortion caused by the step size of the quantization is called the granular noise. Figure 6.5 depicts the Probability Density Function (PDF) of a variable x as well as the behavior of a uniform quantizer. The input signal gain G should be properly adjusted so that a balance between the granular noise and the overload noise can be reached. If G is too small, the signal will be concentrated in the bounded region so that the granular noise becomes significant. If G is too large, most of the signal is clipped in the unbounded region and as a result, the overload noise is dominant. The input gain scales $\widehat{y}[i]$ to fit the thresholds so that the influence of the quantization noise on the system performance is minimized. Therefore, an optimal performance using a b-bit ADC can be obtained if G is

properly chosen.

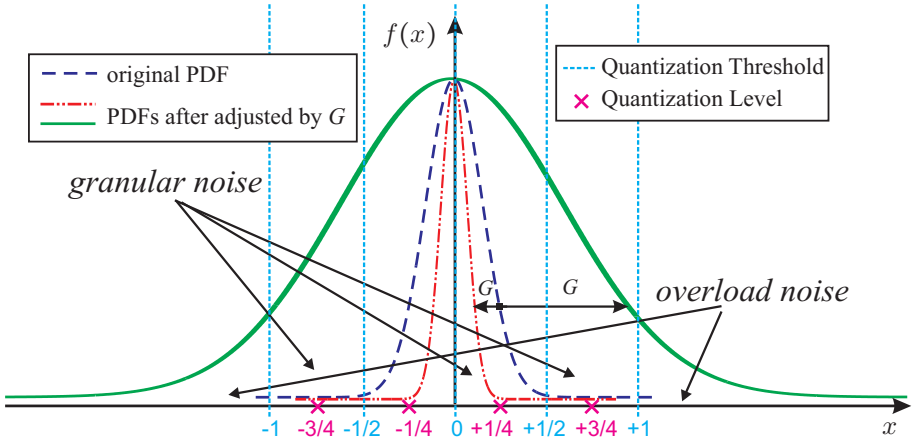

Fig. 6.5: A representation of quantizing the signal x with PDF $f(x)$, where $b = 2$ is chosen.

6.4.1.2 BER Derivation without MUI

For the TH codes discussed in Section 5.3, the impulse response of the DCMF that is matched to the TH sequence of the desired user is given by

$$f^{(1)}_{\mathrm{DCMF}}(n) = \frac{1}{\sqrt{N_s}} \sum_{i=0}^{N_s-1} \delta(n - iN_h - C^{(1)}_i). \tag{6.3}$$

Assuming "0" is transmitted, the decision variables can be expressed as in equation (6.4), where $h^{(k)}_{c_0}[i]$ and $h^{(k)}_{c_1}[i]$ take values in $\{0,1\}$ denoting whether there is a collision in the i-th frame for user k and $\mathfrak{L}_{\mathrm{i}}$ denotes the set of L_{i} taps that are included in the integration window (cf. Section 4.3.1). Moreover, $n_m[i,l], m \in \{0,1\}$ are complex AWGN samples with zero mean and Power Spectral Density (PSD) N_0 and $q_m[i,l]$ are complex quantization noise samples.

$$\begin{cases} Z^{(1)}_0 = \sum\limits_{l\in\mathfrak{L}_{\mathrm{i}}} \left| \sqrt{E^{(1)}_b}\alpha^{(1)}[l] + \sum\limits_{i=1}^{N_s}\sum\limits_{k=2}^{N_u} \dfrac{\sqrt{E^{(k)}_b}}{N_s} h^{(k)}_{c_0}[i]\alpha^{(k)}[l] + \sum\limits_{i=1}^{N_s} \dfrac{n_0[i,l]}{\sqrt{N_s}} + \sum\limits_{i=1}^{N_s} \dfrac{q_0[i,l]}{\sqrt{N_s}} \right|^2 \\ Z^{(1)}_1 = \sum\limits_{l\in\mathfrak{L}_{\mathrm{i}}} \left| \sum\limits_{i=1}^{N_s}\sum\limits_{k=2}^{N_u} \dfrac{\sqrt{E^{(k)}_b}}{N_s} h^{(k)}_{c_1}[i]\alpha^{(k)}[l] + \sum\limits_{i=1}^{N_s} \dfrac{n_1[i,l]}{\sqrt{N_s}} + \sum\limits_{i=1}^{N_s} \dfrac{q_1[i,l]}{\sqrt{N_s}} \right|^2 \end{cases}. \tag{6.4}$$

By comparing the decision variables of both receivers as shown in equations (5.7) and (6.4), it can be observed that the NC-CL discussed in Section 4.2 arises due to non-linearly combining the noise samples (with respect to index i in equation (5.7)). However, these noise samples are linearly combined in the DCMF-based receiver as shown in equation (6.4), which, as a result, reduces the NC-CL significantly. For the MUI terms, the same observation can be made that our proposed receiver may also alleviate the performance degradation caused by MUI compared to the analog receiver.

Similarly in Section 5.4.2, using the central limit theorem and the Gaussian approximation for the decision variables $Z^{(1)} = Z_0^{(1)} - Z_1^{(1)}$, we can calculate the BER by equation (5.8).

Full-Resolution ADC

The ADC with a full resolution provides the benchmark performance of our proposed DCMF-based non-coherent receiver. According to the above discussions, we can calculate the BER performance in multipath channels with

$$\begin{aligned} \mathbb{E}\{Z^{(1)}\} &= E_b \sum_{l\in\mathfrak{L}_\mathrm{i}} \Omega_l \\ \mathbb{V}\{Z^{(1)}\} &= 2E_bN_0 \sum_{l\in\mathfrak{L}_\mathrm{i}} \Omega_l + 2L_\mathrm{i}N_0^2, \end{aligned} \tag{6.5}$$

where $\Omega_l = \mathbb{E}\left\{|\alpha_l|^2\right\},\ l \in \mathfrak{L}_\mathrm{i}$ is the second-order moment of the channel taps.

One-bit ADC

A high-speed ADC with a full resolution performs the best in our case, but it consumes too much power from the low-cost and energy-efficient points of view. Therefore, low-resolution ADCs are preferred in the proposed receiver. We take the simplest one-bit ADC into account, which is rather easy to realize and does not need the automatic gain control. The one-bit DCMF-based receiver with the lowest resolution provides us with the worst performance. The signal $y(t)$ in Figure 6.1 or 6.4 can be represented by a real part $y_R(t)$ and an imaginary part $y_I(t)$. Then the quantized signal $y[i]$ after the one-bit ADC is given by

$$y[i] = \mathrm{sign}\{y_R[i]\} + j\cdot\mathrm{sign}\{y_I[i]\},\ i = 1, 2, \ldots, N_s, \tag{6.6}$$

where $j = \sqrt{-1}$. As a result, the decision variables for the one-bit DCMF-based non-coherent receiver are

$$\begin{cases} Z_0^{(1)} = \sum\limits_{l\in\mathfrak{L}_\mathrm{i}} \left| \sum\limits_{i=1}^{N_s} r_{0,R}[i,l] + j\cdot \sum\limits_{i=1}^{N_s} r_{0,I}[i,l] \right|^2 / N_s \\ Z_1^{(1)} = \sum\limits_{l\in\mathfrak{L}_\mathrm{i}} \left| \sum\limits_{i=1}^{N_s} r_{1,R}[i,l] + j\cdot \sum\limits_{i=1}^{N_s} r_{1,I}[i,l] \right|^2 / N_s \end{cases}, \tag{6.7}$$

where

$$\begin{cases} r_{0,p}[i,l] = \mathrm{sign}\left\{ \sqrt{\dfrac{E_b}{N_s}}\alpha_p^{(1)}[l] + \sqrt{\dfrac{E_b}{N_s}} \sum\limits_{k=2}^{N_u} h_{c_0}^{(k)}[i]\alpha_p^{(k)}[l] + n_{0,p}[i,l] \right\} \\ r_{1,p}[i,l] = \mathrm{sign}\left\{ \sqrt{\dfrac{E_b}{N_s}} \sum\limits_{k=2}^{N_u} h_{c_1}^{(k)}[i]\alpha_p^{(k)}[l] + n_{1,p}[i,l] \right\} \end{cases} \tag{6.8}$$

with p representing real R or imaginary I.

We define the quantization loss as the difference of the required E_b/N_0 (in dB) between the full-resolution receiver and the b-bit one at the same BER. Generally speaking, the largest quantization loss is obtained when $b = 1$.

The BER performance for the one-bit receiver in multipath channels without MUI is discussed as follows. The decision variables can be simplified as $Z_m^{(1)} = \sum_{p\in\{R,I\}} \sum_{l\in\mathfrak{L}_\mathrm{i}} \left| \sum_{i=1}^{N_s} r_{m,p}[i,l] \right|^2 / N_s$, $m \in \{0,1\}$, where $r_{m,p}$ are the quantized samples. For the one-bit case, $r_{0,p}[i,l]$ takes values in $\{-1,\ +1\}$ with the corresponding probability $p_l = \mathrm{Q}\left(\sqrt{E_b \Omega_l / N_0 N_s}\right)$ and $1-p_l$, while for $r_{1,p}[i,l]$ with the probability 0.5. If N_s is large, according to the central limit theorem, the sum of N_s discrete variables $r_{0,p}[i,l]$ (and $r_{1,p}[i,l]$) are approximated by a Gaussian distribution with mean $N_s(1-2p_l)$ (and 0) and variance $4N_s p_l(1-p_l)$ (and 1). Therefore, $Z_{0_\mathrm{1b}}^{(1)}$ ($Z_{1_\mathrm{1b}}^{(1)}$) are the sum of L_i non-central (central) χ^2-distributed random variables each with 2 degrees of freedom. By a Gaussian approximation, the BER performance can thus be analyzed according to

$$\begin{aligned} \mathbb{E}\{Z^{(1)}\} &= (N_s-1)\sum_{l\in\mathfrak{L}_\mathrm{i}} (1-2p_l)^2 \\ \mathbb{V}\{Z^{(1)}\} &= (1-2N_s)\sum_{l\in\mathfrak{L}_\mathrm{i}} (1-2p_l)^4 + 2(N_s-1)\sum_{l\in\mathfrak{L}_\mathrm{i}} (1-2p_l)^2 + 2L_\mathrm{i}. \end{aligned} \tag{6.9}$$

Compared to the full-resolution performance as shown in equation (6.5), at a target BER the quantization loss due to the one-bit ADC can be determined, which mainly varies with the pulse repetition rate N_s. When $b>1$, the loss decreases but also greatly depends on N_s as well as the input gain G. In the presence of MUI, the performance analysis of the b-bit receiver is more complicated and we will only show the simulation results in the next section.

6.4.2 Multiple Access Performance

6.4.2.1 Analysis in AWGN

Full-Resolution ADC

Similar to [QWD07], the analytical BER expressions are obtained using the combination of the characteristic function and the inversion theorem (cf. Appendix A.1.2). Based on the characteristic function of the decision variable $\Phi_{Z^{(1)}}(\omega) = \Phi_{Z_0^{(1)}}(\omega)\Phi_{Z_1^{(1)}}(-\omega)$, the BER expression can be written as

$$P_b = \Pr\{Z^{(1)} < 0\} = \frac{1}{2} + \frac{1}{\pi}\int_0^\infty \Re\left\{\frac{\Phi_{Z^{(1)}}(-\omega)}{j\omega}\right\} \mathrm{d}\omega. \tag{6.10}$$

Without considering the multipath propagation, equation (6.4) can be simplified to

$$\begin{cases} Z_0^{(1)} = \left| \sqrt{E_b} + \dfrac{\sqrt{E_b}}{N_s} \sum\limits_{k=2}^{N_u}\sum\limits_{i=1}^{N_s} h_{c_0}^{(k)}[i] + \sum\limits_{i=1}^{N_s} \dfrac{n_0[i]}{\sqrt{N_s}} \right|^2 \\ Z_1^{(1)} = \left| \dfrac{\sqrt{E_b}}{N_s} \sum\limits_{k=2}^{N_u}\sum\limits_{i=1}^{N_s} h_{c_1}^{(k)}[i] + \sum\limits_{i=1}^{N_s} \dfrac{n_1[i]}{\sqrt{N_s}} \right|^2 \end{cases}, \tag{6.11}$$

Therefore, given the MUI, $Z_0^{(1)}$ and $Z_1^{(1)}$ are the sum of squares of Gaussian random variables

with variance $2\sigma^2$, exhibiting a non-central χ^2 distribution with 2 degrees of freedom and with non-centrality parameters μ_0^2 and μ_1^2, respectively. The exact BER should be obtained by averaging over the distribution of the MUI. However, it is rather difficult to model the MUI precisely and the analysis will become extremely complicated. Hence, we simply estimate the mean and the variance of the MUI to compute the parameters μ_0^2, μ_1^2 and $2\sigma^2$. The calculation can be performed as follows

$$\begin{cases} \mu_0^2 = \left(\mathbb{E}\left\{\sqrt{E_b} + \dfrac{\sqrt{E_b}}{N_s}\displaystyle\sum_{k=2}^{N_u}\sum_{i=1}^{N_s} h_{c_0}^{(k)}[i]\right\}\right)^2 = E_b\left(1+(N_u-1)\mu_h\right)^2 \\ \mu_1^2 = \left(\mathbb{E}\left\{\dfrac{\sqrt{E_b}}{N_s}\displaystyle\sum_{k=2}^{N_u}\sum_{i=1}^{N_s} h_{c_1}^{(k)}[i]\right\}\right)^2 = E_b\left((N_u-1)\mu_h\right)^2 \\ 2\sigma^2 = 2\mathbb{V}\left\{\dfrac{\sqrt{E_b}}{N_s}\displaystyle\sum_{k=2}^{N_u}\sum_{i=1}^{N_s} h_{c_0}^{(k)}[i] + \sum_{i=1}^{N_s}\frac{n_0[i]}{\sqrt{N_s}}\right\} = 2\frac{E_b}{N_s}(N_u-1)\sigma_h^2 + N_0 \end{cases}, \tag{6.12}$$

where μ_h and σ_h^2 are the mean and the variance of the number of collisions $\sum_{i=1}^{N_s} h_{c_m}^{(k)}[i]/\sqrt{N_s}, m \in \{0,1\}$ occurring within one TH code duration from one interfering user k and the 2 in $2\sigma^2$ is due to the complex variables.

If x follows the χ^2 distribution with a PDF shown in equation (A.21), the characteristic function of $Z^{(1)}$ is given by (cf. equation A.22)

$$\Phi_{Z^{(1)}}(\omega) = \frac{1}{1+\omega^2 4\sigma^4}\exp\left(\frac{j\omega\mu_0^2}{1-j\omega 2\sigma^2} + \frac{-j\omega\mu_1^2}{1+j\omega 2\sigma^2}\right). \tag{6.13}$$

Using equation (6.10) we can obtain the analytical multiple access performance for the DCMF-based non-coherent receiver in the presence of AWGN. It can be concluded that the performance for the proposed receiver depends on the code properties, i.e., the mean μ_h and the variance σ_h^2 of the total number of collisions between two TH codes. The performance degrades as σ_h^2 increases and as μ_h decreases.

If the random codes are applied, the statistics of the collisions μ_h and σ_h^2 can be easily calculated. The PDF of $h_{c_0}[i]$ conditioned on transmitting "0" is $f_{h_{c_0}|0}(x) = \frac{1}{N_h}\delta\left(x - \frac{1}{\sqrt{N_s}}\right) + \left(1 - \frac{1}{N_h}\right)\delta(x)$ and on "1" is $f_{h_{c_0}|1}(x) = \delta(x)$. The distribution of one interferer is given by $f_{\mathrm{MUI}|m}(x) = \underbrace{f_{h_{c_0}|m}(x) * \cdots * f_{h_{c_0}|m}(x)}_{N_s-\text{convolution}}$. Thus, it can be computed that $\mu_h = \frac{\sqrt{N_s}}{2N_h}$ and $\sigma_h^2 = \frac{N_s + 2N_h - 1}{4N_h^2}$. If other kinds of TH codes are considered, we can obtain μ_h and σ_h^2 by using the realistic measure as discussed in Section 5.4.2.

One-bit ADC

If only AWGN is taken into account, the decision variables of the one-bit DCMF-based

non-coherent receiver in equation (6.7) can be simplified to

$$\begin{cases} Z_0^{(1)} = \dfrac{1}{N_s}\left(\left|\sum\limits_{i=1}^{N_s} r_{0,R}[i]\right|^2 + \left|\sum\limits_{i=1}^{N_s} r_{0,I}[i]\right|^2\right) \triangleq z_{0,R} + z_{0,I} \\ Z_1^{(1)} = \dfrac{1}{N_s}\left(\left|\sum\limits_{i=1}^{N_s} r_{1,R}[i]\right|^2 + \left|\sum\limits_{i=1}^{N_s} r_{1,I}[i]\right|^2\right) \triangleq z_{1,R} + z_{1,I} \end{cases}, \tag{6.14}$$

where

$$\begin{cases} r_{0,p}[i] = \text{sign}\left\{\sqrt{\dfrac{E_b}{N_s}} + \sqrt{\dfrac{E_b}{N_s}}\sum\limits_{k=2}^{N_u} h_0^{(k)}[i] + n_{0,p}[i]\right\} \\ r_{1,p}[i] = \text{sign}\left\{\sqrt{\dfrac{E_b}{N_s}}\sum\limits_{k=2}^{N_u} h_1^{(k)}[i] + n_{1,p}[i]\right\} \end{cases}. \tag{6.15}$$

The sign operation indicates that $r_{m,p}[i] \in \{\pm 1\}, i = 1, \ldots, N_s, p \in \{R, I\}, m \in \{0, 1\}$, exhibiting Bernoulli distributions. The $r_{m,I}[i]$ only contains noise, taking values in $\{\pm 1\}$ with probability 0.5. If we denote $\Pr\{r_{m,R}[i] = -1\} = p_m$, then p_m is exactly the BER for coherent detection, i.e.,

$$\begin{cases} p_0 = \Pr\left\{x_0 = \sqrt{\dfrac{E_b}{N_s}} + \sqrt{\dfrac{E_b}{N_s}}\sum\limits_{k=2}^{N_u} h_{c_0}^{(k)}[i] + n_{0,p}[i] < 0\right\} \\ p_1 = \Pr\left\{x_1 = \sqrt{\dfrac{E_b}{N_s}}\sum\limits_{k=2}^{N_u} h_{c_1}^{(k)}[i] + n_{1,p}[i] < 0\right\} \end{cases}. \tag{6.16}$$

We apply the characteristic function and inversion theorem method again to calculate the BER p_m. The crucial part is to find the characteristic function of $x_m, m \in \{0, 1\}$ in equation (6.16), which is given by

$$\begin{cases} \Phi_{X_0}(\omega) = \exp\left(j\omega\sqrt{\dfrac{E_b}{N_s}}\right)\Phi_n(\omega)\Phi_{I_0}(\omega) \\ \Phi_{X_1}(\omega) = \Phi_n(\omega)\Phi_{I_1}(\omega) \end{cases}, \tag{6.17}$$

where $\Phi_n(\omega) = \exp(-\omega^2 N_0/4)$ and $\Phi_{I_m}(\omega) = \left(\frac{1}{2N_h}\exp\left(j\omega\sqrt{\frac{E_b}{N_s}}\right) + 1 - \frac{1}{2N_h}\right)^{(N_u-1)}, m \in \{0, 1\}$ are the characteristic functions of the AWGN and the MUI, respectively.

Since the sum of random variables with Bernoulli distributions will result in a binomial distribution (cf. Appendix A.2.1), the PDF of $z_{m,p}, p \in \{R, I\}, m \in \{0, 1\}$ defined in equation (6.14) are obtained as

$$\begin{cases} f_{z_{m,R}}(x) = \sum\limits_{k=0}^{N_s}\binom{N_s}{k} p_m^k (1-p_m)^{(N_s-k)}\delta\left(x - \dfrac{(2k-N_s)^2}{N_s}\right) \\ f_{z_{m,I}}(x) = \dfrac{1}{2^{N_s}}\sum\limits_{k=0}^{N_s}\binom{N_s}{k}\delta\left(x - \dfrac{(2k-N_s)^2}{N_s}\right) \end{cases}, \tag{6.18}$$

where $\binom{N_s}{k}$ is the binomial coefficient and $\delta(x)$ represents the Dirac delta function defined in equation (2.2). Assuming that the discrete random variables $z_{m,p}$ are independent, the total PDF of $Z^{(1)} = z_{0,R} + z_{0,I} - z_{1,R} - z_{1,I}$ is the convolution of each PDF obtained in equation

(6.18), defined by

$$f_{Z^{(1)}}(x) = \sum_{k=0}^{N_s} \Pr\left\{Z^{(1)} = z_k\right\} \delta\left(x - z_k\right). \tag{6.19}$$

Hence, the analytical BER of the DCMF-based receiver using a one-bit ADC is expressed as

$$P_b = \Pr\left\{Z^{(1)} \le 0\right\} = \sum_{k=0}^{N_s} \Pr\left\{Z^{(1)} = z_k | z_k < 0\right\} + \frac{1}{2} \sum_{k=0}^{N_s} \Pr\left\{Z^{(1)} = z_k | z_k = 0\right\}, \tag{6.20}$$

where 1/2 accounts for the uncertainty of the decisions when $Z_{1\mathrm{b}}^{(1)}[k] = 0$. It shows that the BER is also determined by the properties of the TH codes (cf. equation (6.16)).

6.4.2.2 Analysis in Mulitpath

In the case of full-resolution, the quantization noise term can be removed from equation (6.4). The decision variables are denoted by $Z_m^{(1)} = \sum_{l \in \mathfrak{L}_\mathrm{i}} \left|z_{m,l}\right|^2$, $m \in \{0, 1\}$. Given the MUI and the channels, $z_{m,l}$ are Gaussian distributed random variables. Therefore, $Z_m^{(1)}$ is the sum of L_i non-central χ^2-distributed variables each with 2 degrees of freedom. When L_i is large, in the case of perfect power control the multiple access performance of the full-resolution receiver in multipath channels can be obtained via equation (5.8) by a Gaussian approximation, where

$$\begin{aligned}
\mathbb{E}\{Z^{(1)}\} &= E_b \sum_{l \in \mathfrak{L}_\mathrm{i}} \Omega_l \\
\mathbb{V}\{Z^{(1)}\} &= 2E_b^2 \frac{2\sigma_h^2}{N_s}\left(\frac{2\sigma_h^2}{N_s} + 2\mu_h^2\right)(N_u - 1) \sum_{l \in \mathfrak{L}_\mathrm{i}} \left(\Upsilon_l + (N_u - 2)\Omega_l\right) + 2E_b^2 \frac{2\sigma_h^2}{N_s}(N_u - 1) \sum_{l \in \mathfrak{L}_\mathrm{i}} \Omega_l^2 \\
&\quad + 4E_b N_0 (N_u - 1)\left(\frac{2\sigma_h^2}{N_s} + \mu_h^2\right) \sum_{l \in \mathfrak{L}_\mathrm{i}} \Omega_l + 2E_b N_0 \sum_{l \in \mathfrak{L}_\mathrm{i}} \Omega_l + 2L_\mathrm{i} N_0^2,
\end{aligned} \tag{6.21}$$

μ_h and σ_h^2 can be calculated according to the discussions in Section 6.4.2.1 and $\Upsilon_l = \mathbb{E}\left\{|\alpha_l|^4\right\}$ is the fourth-order moment of the channel taps. From equation (6.21), the multiple access performance of the proposed receiver mainly depends on the statistics of the collisions $\frac{2\sigma_h^2}{N_s}$ and μ_h^2. With increasing N_h and N_s, a better performance is obtained. The integration interval L_i, the number of users N_u, and the second- and fourth-order moments Ω_l, Υ_l of the channel taps also influence the BER performance.

6.4.3 Results and Discussions

6.4.3.1 One-bit DCMF-based Receiver

AWGN, No Multipath Channels

First, we compare the simulation results with the analytical performance obtained in Section 6.4.2.1. In this case, the parameters for the random TH codes are $N_s = 23$, $N_h = 23$ and single user as well as multiple asynchronous users (11 active users) are taken into account.

From Figure 6.6(a) we can see that the analytical curves match well with the simulated ones, illustrating the accuracy of the derived BER expressions for the proposed receiver. Second, if we only consider the single-user situation, there is obviously a NC-CL for the analog receiver, arising from the non-coherent combining of the chips spread by the TH codes. With multiple active users, the loss of the DCMF-based receiver due to the MUI is much smaller than that of its analog counterpart, indicating a higher robustness against the MUI which is similarly shown in Section 6.3. Finally, the one-bit ADC results in a certain performance loss (around 2 dB at $P_b = 10^{-3}$) compared to the full-resolution ADC, but even under this worst condition, the proposed receiver still outperforms the analog one.

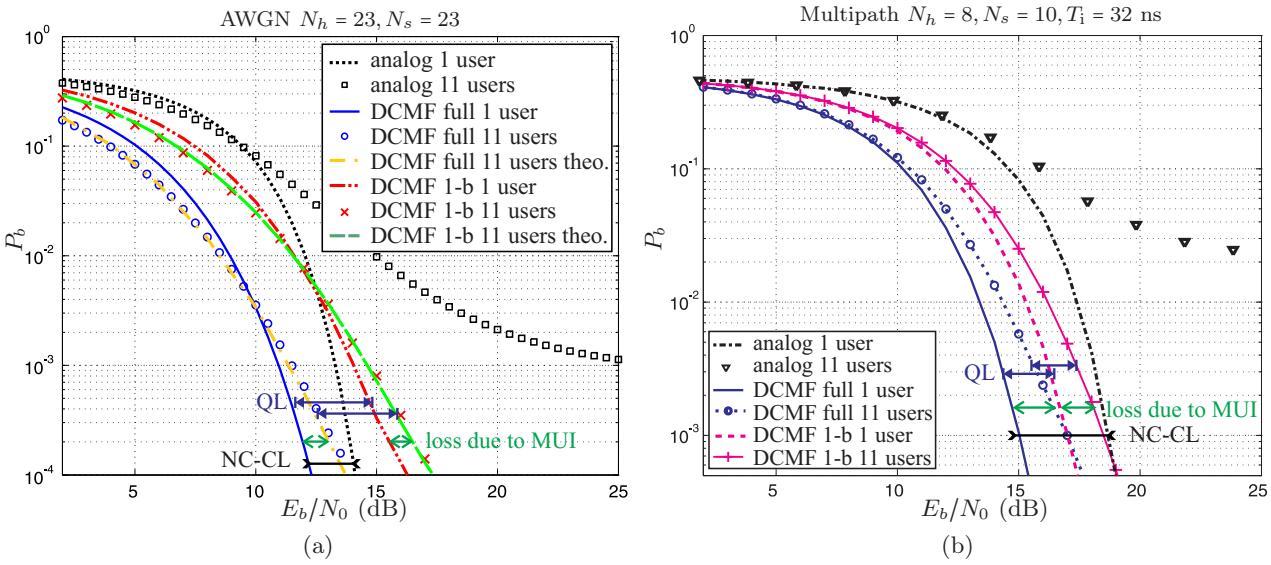

Fig. 6.6: BER performance of the proposed DCMF-based non-coherent receiver and its analog counterpart in the cases of a) AWGN without multipath channel ($N_s = 23, N_h = 23$). b) AWGN and multipath channels ($N_s = 10, N_h = 8$). "QL" represents the loss due to one-bit quantizer. 11 users are considered in the presence of MUI. We denote "full" as full-resolution ADC and "1-b" as one-bit ADC, respectively. Random TH codes are chosen.

Both AWGN and Multipath Channels

For the multipath propagation channel, we use UWB channels obtained from measurements in a Non-Line-Of-Sight (NLOS) office scenario introduced in Section 2.3. The BER performance in the multipath scenario is obtained by averaging over various channel realizations. Figure 6.6(b) shows the corresponding results and similar observations to the case in AWGN can be made.

Influence from System Parameters

Figure 6.7(a) shows the performance of the proposed DCMF-based receiver as a function of the number of pulses per symbol N_s. In the presence of MUI, the performance of using both full-resolution and one-bit ADCs improves with increasing N_s. In contrast to the full-resolution one, the BER of using a one-bit ADC depends on N_s even in the single-user case. It

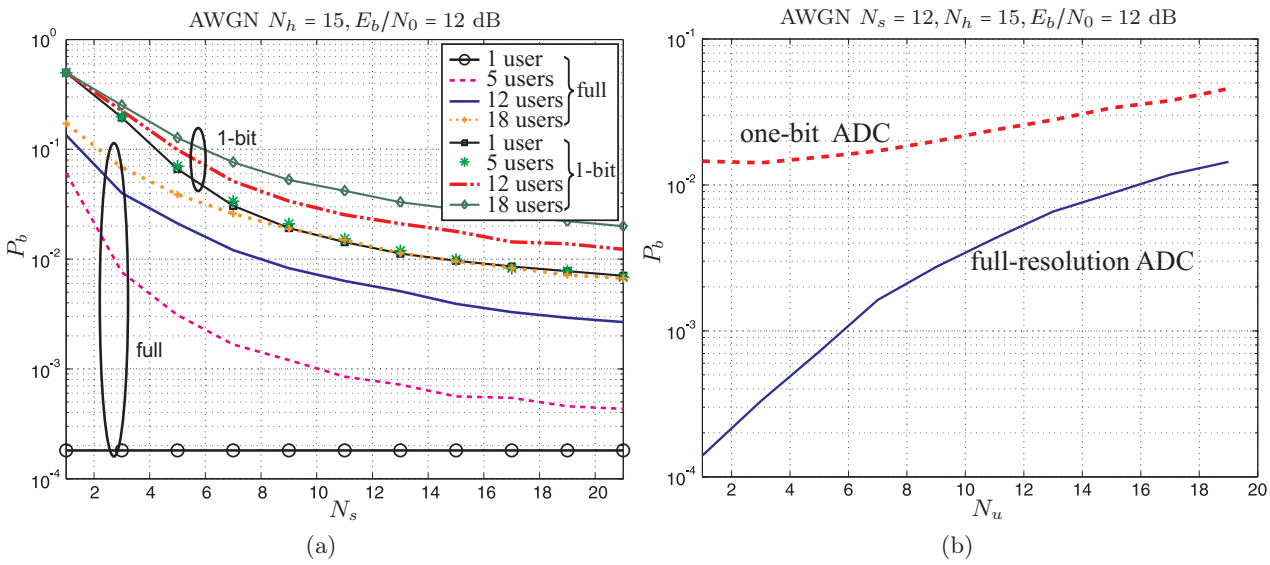

Fig. 6.7: The BER performance of the DCMF-based receiver as a function of a) the number of pulses per symbol N_s in AWGN for $N_h = 15$, SNR = 15 dB and b) the number of users N_u for $N_s = 12, N_h = 15$, SNR = 15 dB. Random TH codes are chosen.

is obvious that the BER increases with the number of users, while for the full-resolution ADC this increase is more significant than the one-bit ADC. Furthermore, Figure 6.7(b) depicts the BER as a function of the number of users N_u, where the system parameters $N_s = 12, N_h = 15$ and SNR = 15 dB are chosen. It can be observed that in both sub-figures of Figure 6.7, the BER of using a one-bit ADC is NOT sensitive to the number of users N_u if N_u is less than 6.

6.4.3.2 Loss due to MUI & One-bit Quantization

According to equation (6.21), the MA performance depends on both N_h and N_s. If the processing factor $L_m = N_h N_s$ is fixed for random codes, the performance of the full-resolution receiver is shown as a function of N_s in Figure 6.8(a), where the loss due to MUI is the additional required E_b/N_0 (dB) with $N_u = 11$ users compared to the 1-user case at BER $= 10^{-3}$. When N_s is very small, the approximated BER in equation (6.21) overestimates the multiple access performance. With a larger N_s, the performance analysis becomes more exact. At a fixed L_m, decreasing N_h (or increasing N_s) gets close to the case of repetition coding, meaning that there are less probabilities to hop and more collisions may occur, which causes a considerable performance degradation. The bigger the L_m is, the better would be the performance but at the cost of the data rate.

By using the analytical BER for the one-user case in equations (6.5) and (6.9), Figure 6.8(b) shows the quantization loss due to the one-bit ADC as a function of the pulse repetition rate N_s. The sum of a large number N_s of quantized samples $r_{m,p}$ that are expressed in equation (6.7) will approximate a Gaussian distribution, which gives a better performance compared to the case of the sparsely distributed samples (e.g., $N_s = 2$). Therefore, the

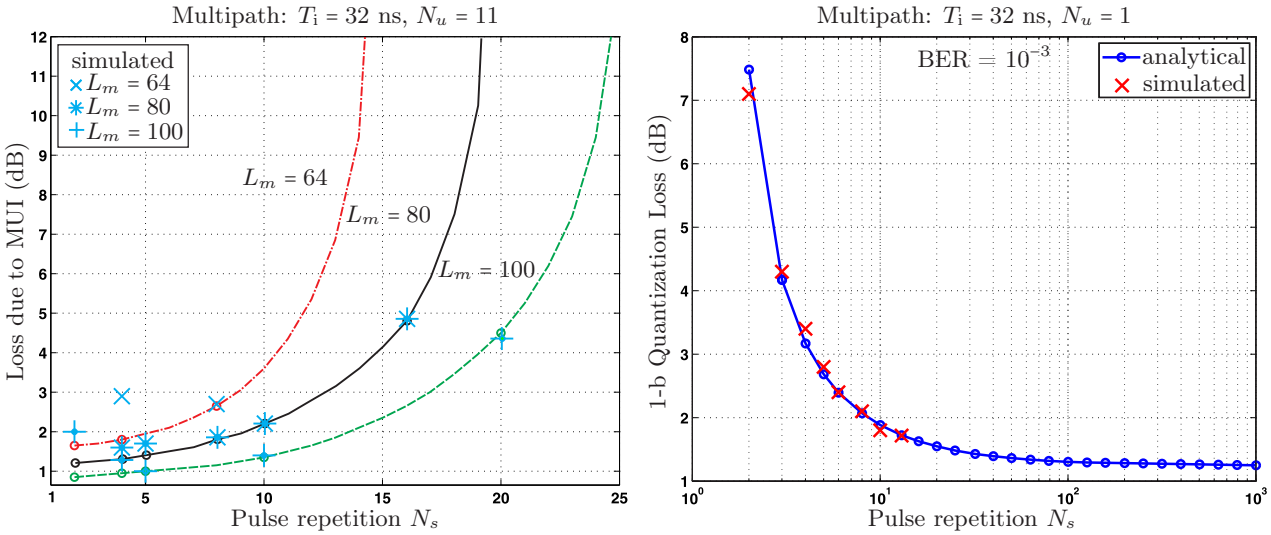

(a) Loss due to MUI (random codes)

(b) Quantization loss due to one-bit ADC

Fig. 6.8: (a) Loss due to MUI (random codes) and (b) quantization loss due to one-bit ADC as a function of the number of pulse repetitions N_s. Reference: E_b/N_0 = 15.1 dB for one-user full-resolution case at BER = 10^{-3}.

strategy to choose a good code for the proposed b-bit non-coherent receiver is that for a fixed processing factor L_m, both N_h and N_s should not be small, $N_s \approx N_h$, and N_h should be slightly larger than N_s. For example, the code with $N_h = 10, N_s = 8$ (for $L_m = 80$) is preferred, since it causes a small loss arising from MUI and quantization.

6.4.3.3 b-bit DCMF-based Receiver

Perfect Power Control (Equal Power)

Figure 6.9 shows the influence of the input gain G of an ADC on the BER performance of the b-bit DCMF-based non-coherent receiver in multipath. Both single-user and multiple-user cases are considered. When G is very small, a higher granular noise results in a performance that is equivalent to the case using a 1-bit ADC. When a large G is applied, most of the signal is clipped, leading to a greater overload noise and accordingly a performance degradation. It can be observed that for the case of 11 users, the optimal G is 3 for both 2-bit and 4-bit ADCs. For the single-user case, the optimal G is 2.5. The input gain G depends on the number of users, since a larger number of users imposes a higher interfering power on the received signal and thus a larger G is required. Furthermore, G will also increase as the Signal to Noise Ratio (SNR) increases and as the Signal to Interference Ratio (SIR) decreases, where we consider MUI and SIR = $10 \log_{10}(E_b^{(1)}/E_b^{(k)})$.

The BER performance of the proposed receiver is shown in Figure 6.10(a). It can be observed that the theoretical estimates in equations (6.5), (6.9), and (6.21) show a good agreement with the simulation results. The 2-bit ADC with optimal G gives rise to a considerable performance improvement compared to the 1-bit case and the performance of the 4-bit

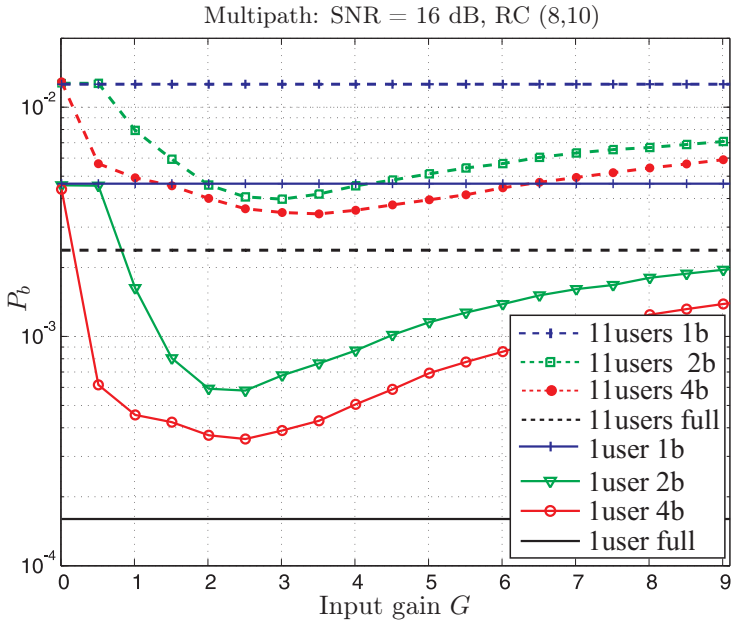

Fig. 6.9: BER versus the input gain G for $N_u = 1$, $N_u = 11$ and various b ($b = 1, 2, 4$) in multipath. "RC" denotes the random code.

DCMF-based receiver with the optimal G can almost achieve the performance of using the full-resolution ADC.

In Chapter 5, different sparse codes are investigated in the non-coherent TH UWB system, where the prime codes and truncated costas codes are good candidates, yielding a better multiple access performance than the random codes. The random code with parameters ($N_h = 11$,$N_s = 11$), prime code (11,11), and truncated costas codes (59,2) are chosen with the closest length for a fair comparison. Figure 6.10(b) illustrates the BER performance of the proposed receiver using different sparse codes in multipath, where $G = 3$ is chosen. When low-resolution ADCs are employed, the prime code is still more favorable than the random code but the truncated costas codes with a small N_s totally loses its advantages due to a large quantization loss. It needs to be mentioned that for truncated costas codes the 2-bit performance is better than the full-resolution case when E_b/N_0 is large, which can be interpreted by the clipping operation of the quantizer as discussed later.

Imperfect Power Control (Near-Far Effect)

In the presence of the near-far problem, the received signal with a low SIR will result in a large dynamic range. Even though the input gain G is used to adjust this range, G cannot be infinitely high in order to minimize the quantization noise and to achieve a minimum BER. Figure 6.11 shows the BER versus SIR using a b-bit non-coherent receiver ($b = 1, 2$, and 4). The AWGN channel is considered with 2 users. For the full-resolution receiver, the BER increases with decreasing SIR. But the performance of the one-bit receiver does not depend on the SIR [1] and it is even better than the full-resolution one when SIR < -14 dB.

[1] When SIR increases further and the MUI can be neglected, the BER will achieve the single-user performance.

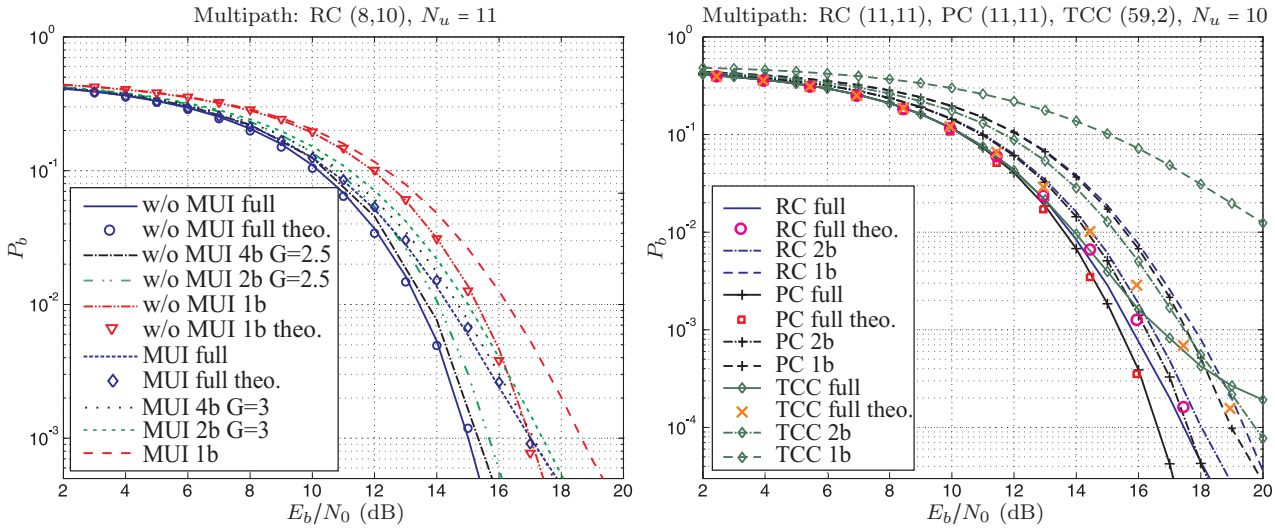

(a) Perfect power control (b) Perfect power control

Fig. 6.10: (a) BER versus SNR for b-bit non-coherent receiver (with optimal G) using random codes in multipath. (b) BER performance using different sparse codes. "RC", "PC", and "TCC" denote the random code, the prime code, and the truncated costas code, respectively.

This superior performance can be ascribed to the hard-decision property of the 1-bit ADC, which clips the high-power MUI and as a result alleviates the effect of the MUI. Compared to the full-resolution case, if the b-bit receiver ($b \neq 1$) with the corresponding optimal and unlimited G is applied, we can achieve a high performance in the region where the SIR is below a certain threshold. However, it is impractical to adjust the gain G without limit for the signal with a very large dynamic range. In this example, a constraint on G is imposed that $G < 3.5$, which corresponds to SIR $\geq$ -8 dB in Figure 6.11 for the 2-bit and 4-bit cases. With a fix and reasonable gain $G = 3$, the solid lines with " $\triangledown$ " for 2-bit and " $\diamond$ " for 4-bit show the inferior performance compared to the full-resolution one.

Therefore, in the presence of the near-far problem, the proposed b-bit non-coherent receiver can be designed to adapt the ADC resolution according to the following rule based on the received SIR:

$$b = \begin{cases} 1, & \text{SIR} < \nu \\ 2 \text{ or } 4 \text{ with } G, & \text{SIR} \geq \nu \end{cases}, \tag{6.22}$$

where ν is a SIR threshold. In the case of Figure 6.11, $\nu = -14$ dB and $G = 3$ for the 2- or 4-bit ADC. The corresponding SIR estimation methods proposed in [CB07] can be applied. Since the SIR estimation is beyond the scope of our work, it will not be specified here.

6.4.4 Summary on System Design Rule

According to the above analysis and simulations, the following conclusions are drawn.

- The TH code selection strategy for the proposed digital receiver follows that, with an appropriate processing factor L_m, both N_s and N_h should not be small, $N_s \approx N_h$,

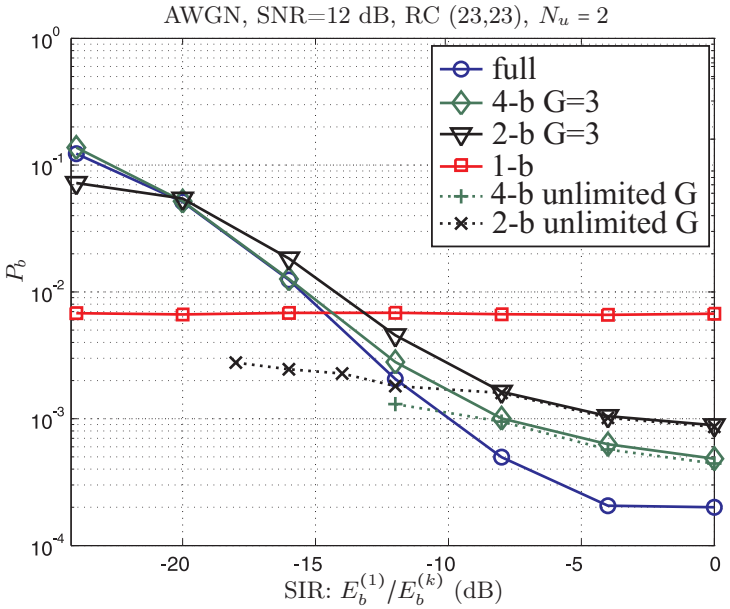

Fig. 6.11: BER versus SIR using b-bit non-coherent receiver in AWGN under the near-far effect. Random codes $(23, 23)$ are chosen.

and N_h should be slightly larger than N_s to trade off the loss from both MUI and quantization. This rule does not only apply to random codes but also to other optical orthogonal codes as discussed in Chapter 5. It can be observed that in compliance with the criteria, prime codes are desired because of their appropriate parameters (i.e., $N_s = N_h$) and good correlation properties.

- It turns out that the number of repetitions should be sufficient to combat the performance degradation due to quantization, e.g., the quantization loss evaluated at a BER $= 10^{-3}$ is below 2 dB if $N_s \geq 8$ and then stays around 1.5 dB (cf. Figure 6.8(b)). The quantized samples of a low-resolution quantizer take values in a subset containing only a few quantization levels. As a result, the sum of a limited number of samples (when N_s is small) is sparsely distributed, yielding a larger quantization loss than in the case with a large N_s [2].

- A larger b $(b > 1)$ provides a better performance but requires a gain G to adjust the input signal before the ADC. An appropriate input gain is determined to minimize the quantization loss as well as to reach a minimal BER. By applying a feasible and fixed input gain, a great performance improvement is obtained with $b = 2$ and it is able to approach the full-resolution performance when $b = 4$. Such performance enhancements are acquired at the expense of the receiver complexity. However, the ADC resolution is kept very low $(1 \leq b \leq 4)$. Additionally, since the performance is not sensitive to the input gain, it can be roughly determined. Under near-far conditions, the one-bit receiver can effectively suppress the strong MUI due to its hard-clipping operation, showing its advantage over the b-bit receivers $(b > 1)$ in severe interference scenarios.

[2] The sum of a large number of quantized samples can be approximated as a Gaussian distribution.

6.5 Performance of Simultaneously Operating Piconets

From the system-level point of view, the proposed physical layer solutions should support their operation in the close proximity of multiple uncoordinated piconets at specific error rates. On the one hand, Simultaneously Operating Piconets (SOP) require the design of modulation, spreading, and coding strategies so that nearly orthogonal channels can be supported among uncoordinated piconets. On the other hand, given a certain transmission scheme, the enhanced receiver techniques can also reduce the performance degradation at the receiver during simultaneous transmissions, improving the SOP performance.

This section applies the SOP test procedure to the TH-PPM systems introduced in Section 5.3 using both the analog receiver and the DCMF-based receivers as well as compares their corresponding SOP performances.

6.5.1 Simultaneously Operating Piconets

This section recalls some definitions related with the SOP analysis and describes the test procedure of the separation distance in the single co-channel case [RE04].

6.5.1.1 Some Definitions

Payload Bit Rate and Error Rate

The payload bit rate is the instantaneous bit rate at Physical Layer Service Access Point (PHY-SAP) level during a peer-to-peer Presentation Service Data Unit (PSDU) transfer. It refers to the net amount of data, after removing the effect of channel coding or other form of redundancy. The data packets are generally using a 32 octet PSDU and the nominal PHY preamble.

The error rate is referred to as the maximum Packet Error Rate (PER) for a specified packet length. The packet error rate is for the 32 octet PSDU.

Receiver Sensitivity Level

The receiver sensitivity is defined as the power level of a signal in dBm at the input of the receiver, when the error rate criteria are achieved in AWGN at a specified bit rate. It is assumed that the antenna gain is 0 dBi with a loss factor 3 dB. The minimum receiver sensitivity is the minimum required average receive power for a received symbol in AWGN. It results in a PER equal to or less than 1 % for 32 octet PSDU when a transmitted signal (with a specified data rate) that is compliant with regulatory emission levels is received.

Link Budget and Calculation of the Range

The link budget can be calculated according to Table 6.1. Given a link margin, the range d can be obtained by

$$d = 10^{\left(\frac{P_T - \mathrm{PL}_0 - P_N - S - I - M}{10 \cdot n}\right)}, \tag{6.23}$$

Tab. 6.1: Link Budget Calculation

Parameter	**Value**
Payload bit rate (R_b)	kb/s
Average transmit power [a] (P_T)	EIRP·B (dBm)
Transmit antenna gain (G_T)	0 dBi
Path loss at 1 meter (PL_0)	dB
Path loss at d meters (PL_d)	$\mathrm{PL}_d = 10 \cdot n \cdot \log_{10} d$ (dB)
Receiver antenna gain (G_R)	0 dBi
Receive power (P_R)	$P_R = P_T + G_T + G_R - \mathrm{PL}_0 - \mathrm{PL}_d$ (dBm)
Average noise power per bit (N_b)	$N_b = -174 + 10 \cdot \log_{10} R_b$ (dBm)
Receive noise figure (N_F)	7 dB
Average noise power per bit (P_N)	$P_N = N_b + N_F$ (dBm)
Required E_b/N_0 (S)	dB at PER = 1 % in AWGN
Implementation loss [b] (I)	5 dB
Link margin (M)	$M = P_R - P_N - S - I$ (dB)
Minimum receiver sensitivity	$P_R - M = P_N + S + I$ (dBm)

[a] The Effective Isotropic Radiated Power (EIRP) required for UWB is at most -41.3 dBm/MHz.
[b] The implementation loss is defined in [RE04] only for the AWGN channel and may include impairments such as filter distortion, phase noise, frequency error, etc.. Here we use a typical value of 5 dB.

where the path loss exponent n depends on the environment [MBC+05].

6.5.1.2 Test Procedure

The geometry of the SOP test scenario is shown in Figure 6.12, where a single co-channel interference is considered. The receiver is located at a fixed distance d_{ref} from the desired or reference piconet 1. The transmitter of an uncoordinated piconet operates at the same power as the reference piconet with a distance d_{int} from the receiver, simultaneously transmitting a co-channel signal (interference).

Test Procedure of the Single Co-channel Separation Distance

1. The reference distance d_{ref} makes sure that the receiver power is 6 dB above the receiver sensitivity level, i.e., the link margin M = 6 dB. Data packets are sent to the test receiver using the reference channel realizations as defined in [MBC+05]. The multipath energy of each channel realization is normalized.

2. Verify the PER at the test receiver.

3. The interference signal is received at the test receiver from a single co-channel transmitter. The channel impulse responses are obtained by the channel models described in [MBC+05].

4. Continue verifying the PER at the test receiver.

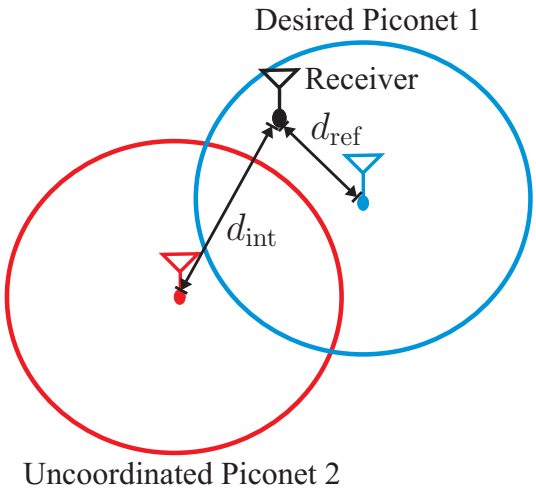

Fig. 6.12: The SOP test geometry with a single co-channel interference.

5. By moving the interfering transmitter towards the test receiver, the distance ratios $d_{\text{int}}/d_{\text{ref}}$ should be indicated when the PER degrades to 1 %.

6.5.2 Simulations and Discussions

This section evaluates the SOP performance for both the analog receiver and the DCMF-based receivers with full-resolution as well as one-bit ADCs.

In contrast to the transmission system discussed in Figure 5.1, forward error correction is applied before the TH encoder and the PPM modulation. In our simulations, we consider the Reed-Solomon codes (63, 55). The data packets use a 32 octet PSDU and the packet length is 256. The random TH codes of $N_s = 10, N_h = 8$ are chosen for both the desired signal and the interference. The Root Raised Cosine (RRC) pulse with a roll-off factor $\beta = 0.3$ and the total bandwidth $B = 1$ GHz is considered as the pulse waveform. We apply the IEEE 802.15.4a channel model with numbers CM1, CM2, CM3, and CM4 (cf. Section 2.3). The parameters such as the path loss exponent n and the reference path loss (at 1 m) are depicted in Table 6.2.

Tab. 6.2: Parameters of IEEE 802.15.4a channels

Channel Number	n	PL_0 (dB)
CM1	1.79	43.9
CM2	4.58	48.7
CM3	1.63	36.6
CM4	3.07	51.4

6.5.2.1 Receiver Sensitivity and Range

According to Section 6.5.1, the first step of the SOP test is to calculate the reference distance d_{ref}, which is determined by the receiver sensitivity, where the minimum E_b/N_0 (S) is obtained at PER = 1 % in AWGN and the link margin of 6 dB is required. In multipath, to calculate the range, S should be specified at PER = 1 % using multipath channels.

Figure 6.13 shows the PER as a function of E_b/N_0 for the analog receiver, the full-resolution and one-bit DCMF-based receivers, respectively. We summarize the parameters and the results such as the maximum channel excess delay $\tau_{\max}$, integration window size T_{i}, the data rate R_b, d_{ref}, S, the receiver sensitivity, and the range d in Table 6.4. The chip duration of the TH-PPM signal is assumed such that $T_c = \tau_{\max}$. As a result, different data rates are tailored for different scenarios.

6.5.2.2 SOP Analysis

Based on the SOP test procedure and the above parameters, the PER as a function of the ratio $d_{\text{int}}/d_{\text{ref}}$ is shown in Figure 6.14. Table 6.3 records the ratios with respect to the piconet separation distances for different receivers when the PER reduces to 1 %. It can be observed that the DCMF-based receivers provide a better piconet separation than the analog counterpart. In accordance with the analysis in Section 6.4.3, the one-bit receiver, which is able to suppress the strong co-channel interference, exhibits a superior performance under the SOP situations, i.e., it is more robust agianst the interference from other piconets/users.

Tab. 6.3: $d_{\text{int}}/d_{\text{ref}}$ at an average 1 % PER for SOP tests

Channels	Analog	DCMF (full)	DCMF (1-b)
CM1	2.15	0.95	0.70
CM2	1.08	0.82	0.64
CM3	1.53	0.65	0.32
CM4	1.05	0.71	0.45

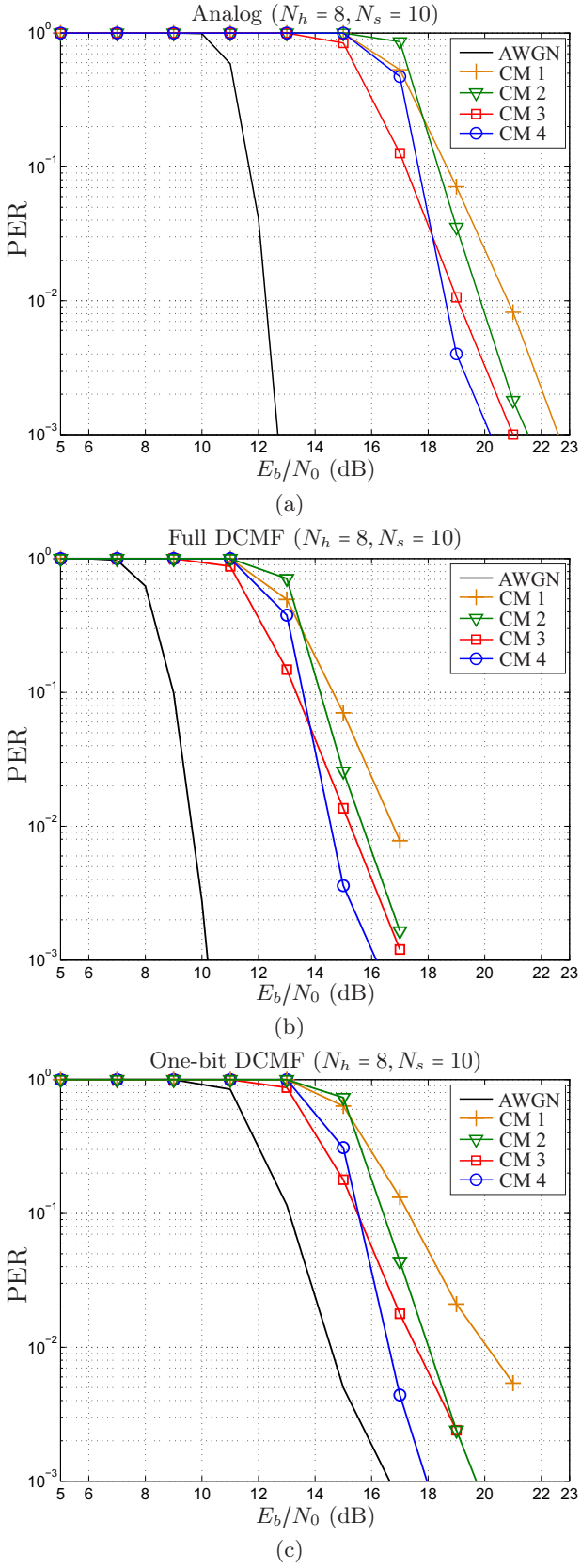

Fig. 6.13: PER of (a) the analog receiver as well as (b) the DCMF-based receivers using full-resolution and (c) one-bit ADCs in AWGN and multipath channels.

Tab. 6.4: Receiver Sensitivity and Range for SOP Tests.

				d_{ref} (m)			Receiver Sensitivity (dBm)			S at PER = 1 % (dB)			d (m)		
Channel	$\tau_{\max}$ (ns)	T_{i} (ns)	R_b (kbps)	Analog	Full	1-bit	Analog	Full	1-bit	Analog	Full	1-bit	Analog	Full	1-bit
CM1	65	24	96	144	202	108	-99.87	-102.47	-97.57	20.8	16.8	20.1	114	200	130
CM2	92	42	68	6	7	5	-101.38	-103.98	-99.08	19.6	15.7	18	5.8	7	6.3
CM3	45	13	139	527	762	381	-98.27	-100.87	-95.97	19.05	15.2	17.6	547	940	670
CM4	60	30	104	10	12	8	-99.52	-102.12	-97.22	18.6	14.6	16.6	11	14	12
AWGN	–	–	–	–	–	–	–	–	–	12.3	9.7	14.6	–	–	–

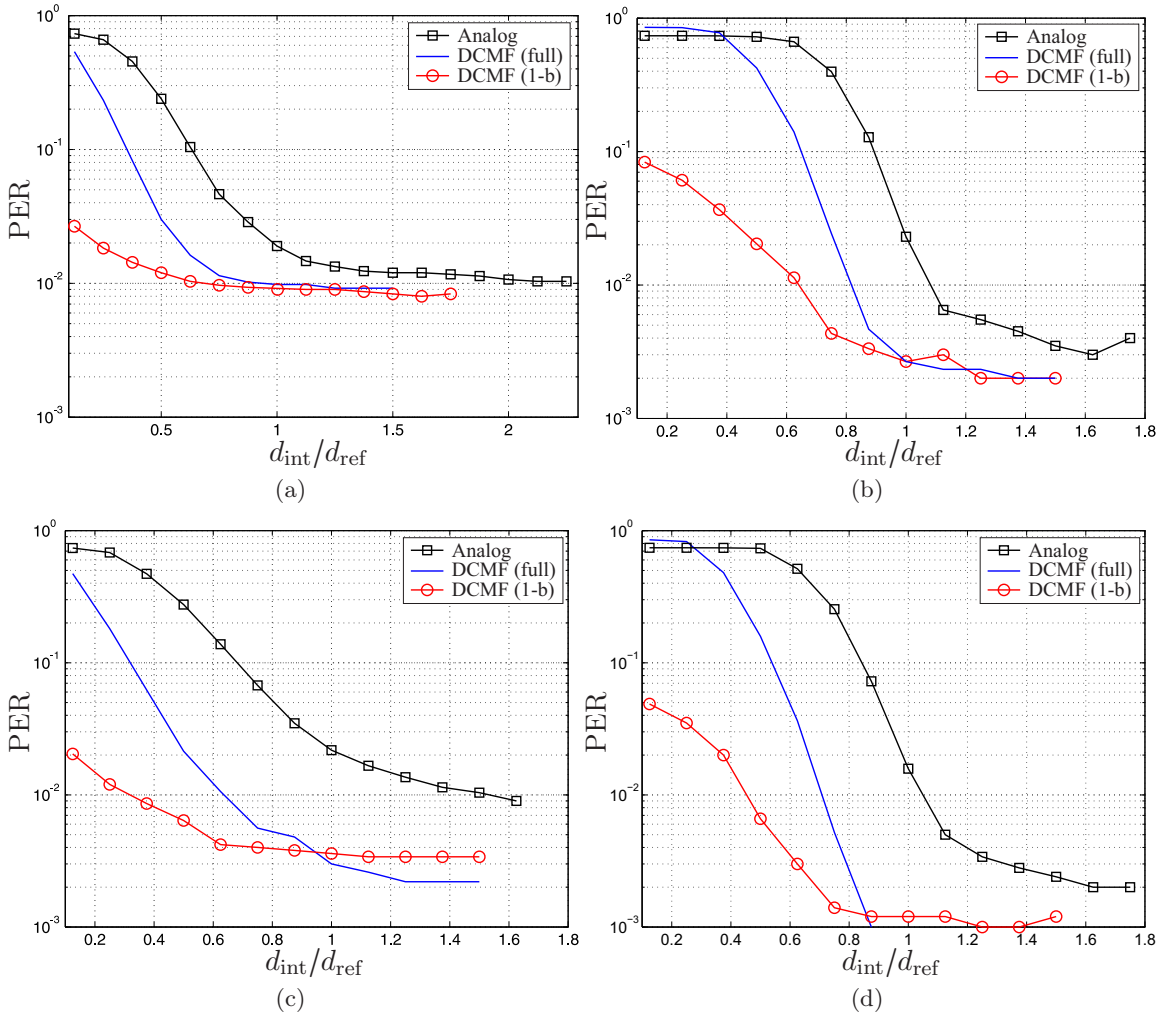

Fig. 6.14: SOP performance for CM1, CM2, CM3, and CM4.

6.6 Narrowband Interference Suppression

6.6.1 Introduction

The IEEE 802.11a standard Wireless Local Area Network (WLAN) operates at around 5.22 GHz, which is overlapping with the frequency band of UWB signals regulated by the US FCC [Fed02]. The IEEE 802.11a WLAN signal based on OFDM [wla99] has a much higher emission power than the UWB signal and is treated as Narrowband Interference (NBI). Non-coherent UWB receivers greatly suffer from the NBI, which calls for NBI mitigation techniques (summarized in [WLJ+09]).

In the DCMF-based receiver which largely relies on digital processing, the NBI problem is serious since the UWB impulse signal together with the additional strong NBI results in a higher dynamic range. This either requires high-resolution ADCs or causes severe saturations. Furthermore, there will also be a significant performance loss due to the quantization of the signal with a large variation. Therefore, the NBI needs to be suppressed before ADCs are employed. In [DM03], a NBI suppression scheme using a feedforward structure, consisting of a hard limiter and an adaptive amplifier gain, is proposed for the Binary Phase Shift Keying (BPSK)-modulated UWB system with coherent detection. Because of the impulsiveness of the IR-UWB signal [DK06], in the presence of the strong NBI, the desired UWB signal can be regarded as the "impulsive noise" to the NBI "signal". The hard limiter is used to suppress the UWB impulse and to boost the NBI. The boosted NBI can then be subtracted from the received signal via a feedforward structure. The non-linear soft limiter is widely used in the presence of impulsive noise. A soft limiter receiver is proposed in [BH08] for a TH-BPSK UWB system to mitigate MUI. Compared to the hard limiter, the soft limiter is more effective at suppressing the impulse-like signal [BH08].

In this section, we propose a NBI suppression scheme using a soft limiter for a digital non-coherent UWB receiver. Both a single-tone interference and the OFDM interference from an IEEE 802.11a WLAN are considered as NBI. We investigate the suitability of the proposed receiver using a soft limiter to mitigate the strong NBI by simulations and the corresponding performance is compared to the hard limiter case. The threshold selection required by both limiters is discussed for full-resolution as well as b-bit ADCs. When $b \neq 1$, the adjustment of the input signal level is required in conjunction with the threshold selection. A block-based threshold adaptive NBI suppression scheme is proposed especially in the presence of the strong OFDM NBI. Finally, we also evaluate the performance of the frequency-dependency arising from the TH-based DCMF.

6.6.2 System Description

We consider a TH-PPM UWB system using the DCMF-based non-coherent receiver discussed in Section 6.2. A NBI suppression block using a feedforward soft limiter is shown in Figure 6.15, where $r_S(t)$ is the output of the soft limiter and $r(t)$ is the signal after suppression.

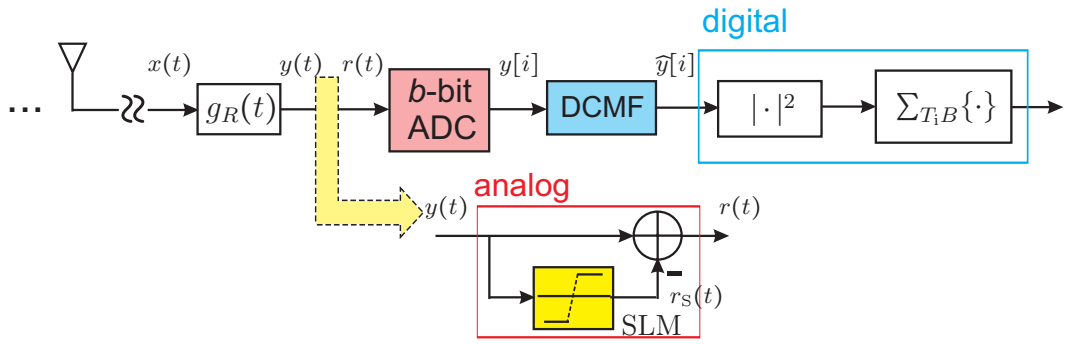

Fig. 6.15: A NBI mitigation structure using a soft limiter ("SLM") for the b-bit non-coherent receiver. The receiver is shown in the complex baseband.

6.6.2.1 System Model

The single-user case in AWGN is assumed. Even though the problem is formulated in AWGN for simplicity, without loss of generality, the NBI suppression concept is also feasible in the multipath case. The difference is that in multipath there is a higher non-coherent combining loss with respect to the E_b/N_0, depending on the number of combined paths or the time-bandwidth product (cf. Section 4.2). Since the multipath arrivals are non-coherently combined, the UWB channels do not have a significant impact on the proposed NBI suppression receiver.

We represent the transmitted signal by equation (5.1) and the received signal can be expressed as

$$y(t) = \underbrace{\sum_{i=0}^{N_s-1} \sqrt{\frac{E_b}{N_s}} \tilde{g}(t - iT_f - C_i T_c - a_0 \Delta)}_{\tilde{s}(t)} + J(t) + n(t), \tag{6.24}$$

where the first term corresponds to the desired signal $\tilde{s}(t)$, $\tilde{g}(t) = g(t) * g_R(t)$, $J(t) = \widehat{J}(t) * g_R(t)$, and $n(t) = \widehat{n}(t) * g_R(t)$ are the filtered pulse, NBI, and noise, respectively. Zero-mean, complex-baseband AWGN $\widehat{n}(t)$ has a power spectral density N_0.

In the simplest case, the NBI $\widehat{J}(t)$ can be modeled as an unmodulated single-tone signal (complex baseband):

$$\widehat{J}(t) = \sqrt{P_J} e^{j(2\pi f_J t + \theta)}, \tag{6.25}$$

where P_J is the NBI power, f_J is the frequency difference between the NBI and the carrier frequency of the UWB signal, and the random phase θ is uniformly distributed in $[0, \pi)$. The signal to NBI ratio can be computed as $\mathrm{SIR} = E_b/(P_J T_s)$.

For an IEEE 802.11a WLAN system, the NBI is represented by an OFDM signal as

$$\widehat{J}(t) = \sqrt{\frac{P_J}{N_c}} \sum_{n=0}^{N_c-1} x_n e^{j(2\pi(f_J + n\cdot\Delta f)t + \theta)}, \tag{6.26}$$

where N_c is the number of sub-carriers, Δf denotes the sub-carrier frequency spacing, and

$x_n \in \{\pm 1\}$ is a BPSK-modulated symbol.

6.6.2.2 Narrowband Interference Suppression Receiver

The idea of the NBI Suppression is elaborated as follows. The received signal consists of the desired TH-PPM signal with an impulsive behavior [DK06] and the unwanted NBI which is either a single sinusoid or a sum of multiple sinusoids. Conversely speaking, the TH-PPM signal in the presence of strong NBI can be treated as the impulsive "noise" to the NBI "signal". Therefore, the non-linear soft limiter suitable for mitigating the impulsive noise can be designed to suppress the TH-PPM "noise" and to extract the NBI. By applying a feedforward structure, the soft limiter output which mainly contains the acquired NBI can thus be subtracted from the received signal.

Figure 6.15 shows the analog feedforward NBI suppression structure for the digital non-coherent receiver. The feedforward branch consists of a soft limiter with adaptable thresholds, which can even be used for turning on/off the NBI mitigation. If the signals before and after the soft limiter are represented by $y(t)$ and $r_S(t)$, the soft limiter will operate as follows

$$r_{S,p}(t) = \begin{cases} \sqrt{P_J}\delta, & \text{if } y_p(t) \geq \sqrt{P_J}\delta \\ y_p(t), & \text{if } -\sqrt{P_J}\delta < y_p(t) < \sqrt{P_J}\delta \\ -\sqrt{P_J}\delta, & \text{if } y_p(t) \leq -\sqrt{P_J}\delta \end{cases}, \tag{6.27}$$

where δ is the threshold factor and $p \in \{R, I\}$ represents the real or the imaginary part of the signal. If the threshold goes to zero, the soft limiter will turn into the hard limiter with the clipping values $\pm\sqrt{P_J}\delta$ as outputs, i.e., a hard-decision device, operating as

$$r_{H,p}(t) = \begin{cases} \sqrt{P_J}\delta, & \text{if } y_p(t) \geq 0 \\ -\sqrt{P_J}\delta, & \text{if } y_p(t) < 0 \end{cases}. \tag{6.28}$$

The advantage of the soft limiter over the hard limiter is that there is a linear operation region that can maintain the weak signal. Since the soft limiter also clips the input signal which has a high power (the clipping operation region), the resulting signal after the NBI suppression will have a smaller dynamic range.

After NBI suppression, $r(t)$ can be written as

$$r(t) = \tilde{s}(t) + J(t) + n(t) - r_S(t), \tag{6.29}$$

where the first three terms are defined in equation (6.24) and $r_S(t) = r_{S,R}(t) + j \cdot r_{S,I}(t)$ in equation (6.27). The output samples of the ADC are given by

$$\begin{cases} y[i] = \tilde{s}[i] + J[i] + n[i] - r_S[i], & \text{full-resolution} \\ y_{1b}[i] = \text{sign}\{y_R[i]\} + j \cdot \text{sign}\{y_I[i]\}, & \text{1-bit.} \end{cases}$$

When $b \neq 1$, the adjustment of the input signal level is required to scale the normalized received

signal samples for proper quantization (cf. Section 6.4.1). The DCMF has an impulse response $f_{\mathrm{DCMF}}(n)$ given by equation (6.3). The corresponding transfer function is

$$H_{\mathrm{DCMF}}(f) = \frac{1}{\sqrt{N_s}} \sum_{n=0}^{N_s-1} e^{-\mathrm{j}2\pi(nN_h+C_n)T_c \cdot f}. \tag{6.30}$$

The DCMF output is denoted by $\widehat{y}[i] = y[i] * f_{\mathrm{DCMF}}[i]$.

If we only consider the full-resolution case in the presence of a single-tone NBI (equation (6.25)) and assume that "0" is transmitted, in the first PPM time slot $\widehat{y}[i]$ can be expressed for the hard limiter and the soft limiter as

$$\begin{aligned} \widehat{y}_{\mathrm{H},0}[i] &= \sqrt{E_b} + \sum_{i=1}^{N_s} \frac{n_0[i]}{\sqrt{N_s}} + \sqrt{P_J} H_{\mathrm{DCMF}}(f_J) e^{j\theta} - (N_+ - N_-)\sqrt{N_s P_J}\delta \\ \widehat{y}_{\mathrm{S},0}[i] &= \frac{N_+ + N_-}{N_s}\sqrt{E_b} + \sum_{i=1}^{N_+ + N_-} \frac{n_0[i]}{\sqrt{N_s}} + \sqrt{P_J}\left[H_{\mathrm{DCMF}}(f_J) - \gamma(f_J)\right] e^{j\theta} \\ &\quad -(N_+ - N_-)\sqrt{N_s P_J}\delta, \end{aligned} \tag{6.31}$$

where N_+ and N_- are the number of samples taking values in $[0, +\infty), (-\infty, 0)$ for hard limiter and $[\sqrt{P_J}\delta, +\infty), (-\infty, -\sqrt{P_J}\delta]$ for soft limiter, respectively, and $\gamma(f_J)$ as a function of f_J scales the NBI part coming from the linear operation region of the limiter $\left(-\sqrt{P_J}\delta, \sqrt{P_J}\delta\right)$. By adjusting the threshold factor δ in equation (6.31), the resulting change of N_+, N_- gives rise to a trade-off among the collected signal energy, the combined AWGN, and the residue NBI. Compared to hard limiter in equation (6.31), the soft limiter provides more degrees of freedom to suppress the NBI. The frequency response of the TH code at the NBI frequency $H_{\mathrm{DCMF}}(f_J)$ also influences the performance and will be discussed in Section 6.6.5.

6.6.3 Simulations and Performance Evaluation

In this section, we will evaluate the performance of the proposed NBI suppression scheme for the digital non-coherent receiver in AWGN, where perfect synchronization is assumed at the receiver side. The chosen pseudo-random TH codes have the parameters $N_h = 5, N_s = 23$.

6.6.4 Threshold Selection

The threshold factor δ of the soft or hard limiter determines the corresponding output signal, which largely influences the NBI suppression performance. An appropriate δ is selected to minimize the BER via a computer search. In general, the threshold δ can be simulated beforehand and stored in a look-up table.

6.6.4.1 Single-tone NBI

We first consider the NBI modeled as the unmodulated single-tone signal introduced in equation (6.25), where the frequency $f_J = 23$ MHz.

Full-resolution and One-bit Cases

Figure 6.16 shows the δ-dependent BER using the soft limiter and the hard limiter for both full-resolution and one-bit receivers. Combined with equation (6.31), the following observation of two extreme cases can be made. When δ is close to zero, no suppression is performed for the soft/hard limiters. When δ is very large, the soft limiter operates in the linear region and the signal will go through the limiter without significant distortion. After the subtraction, most of the signal is lost, yielding a poor performance. In the case of the hard limiter, a large δ does not help at all to clip the strong interference but even augments the interference that lies within the range $(-\sqrt{P_J}\delta, \sqrt{P_J}\delta)$. The "optimal" threshold value at E_b/N_0 or SNR = 16 dB and SIR = -18 dB attained from Figure 6.16 is δ = 0.25 for the hard limiter and δ = 0.5 for the soft limiter using full-resolution ADCs as well as δ = 0.6 for the hard limiter and δ = 0.8 for the soft limiter using one-bit ADCs. In the case of SIR = -22 dB, the best threshold factor is slightly changed, i.e., for the hard and soft limiter, respectively, δ = 0.3 and δ = 0.75 when using full-resolution ADCs as well as δ = 0.8 and δ = 0.9 with one-bit ADCs. By choosing a proper threshold factor δ, our proposed receiver can effectively suppress the NBI. The BER as a function of the SNR is plotted in Figure 6.18(a), where the above threshold factors for SIR = -18 dB are used. It is shown that the soft limiter performs much better than the hard limiter especially when one-bit ADCs are applied.

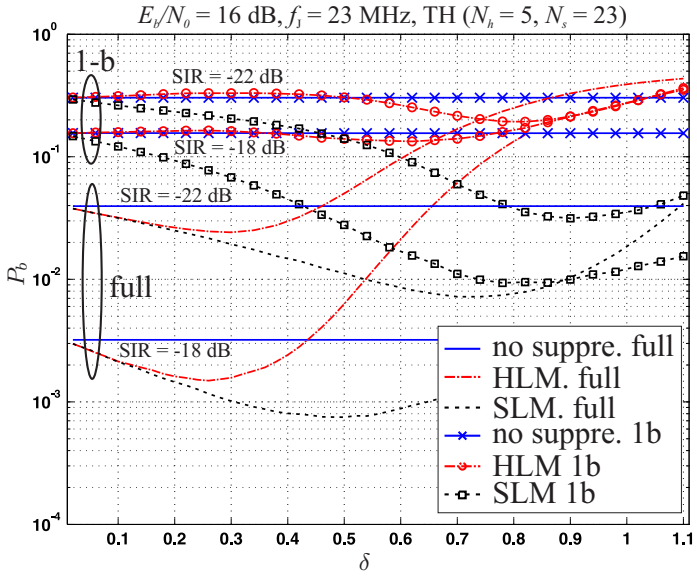

Fig. 6.16: BER versus the threshold factor δ for the proposed full-resolution and one-bit NBI suppression receivers using both the soft limiter ("SLM") and the hard limiter ("HLM").

b-bit Case

When $b \neq 1$, the input signal level or gain G is required for a proper quantization. Thus, besides the impact from the threshold factor δ of the analog limiter on the receiver performance, the choice of G also determines the performance trade-off. Suitable values of δ and G

can be selected jointly to minimize the BER using computer simulations. According to the simulation results as shown in Figure 6.17, the best performance is achieved with 2-bit ADCs $\delta = 0.22$ and $G = 1.51$ for the hard limiter and $\delta = 0.46$ and $G = 1.51$ for the soft limiter, as well as with 4-bit ADCs $\delta = 0.22$ and $G = 1.01$ for the hard limiter and $\delta = 0.42$ and $G = 1.01$ for the soft limiter. The input gain G is determined by the ADC resolution b and does not depend on whether the hard limiter or the soft limiter is employed. Figure 6.18(b) shows that increasing b ($b \leq 4$) leads to an improved performance but at the cost of a higher complexity due to a joint selection of δ and G.

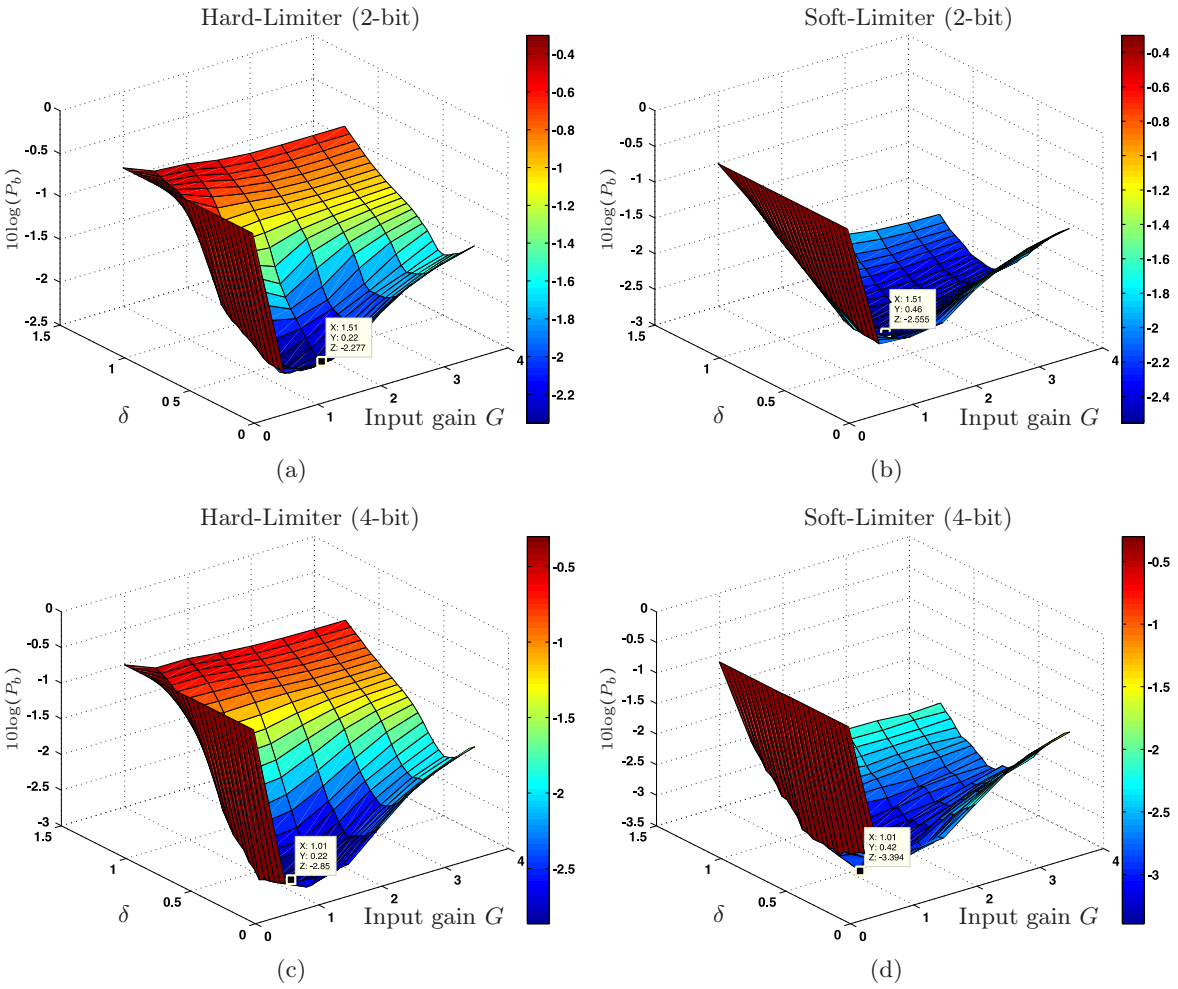

Fig. 6.17: BER as a function of δ, G for b-bit receivers using the hard limiter and the soft limiter, where $E_b/N_0 = 16$ dB and $f_J = 23$ MHz.

Threshold Control and Adaptation

Similarly to [BH08], the threshold factor δ depends on both the SNR and the SIR as shown in Figure 6.16. Even though the threshold δ increases with the decreasing SIR, for a fixed SIR the curve is relatively flat within the range where the BER approaches the lowest point and thus the performance is not that sensitive to the threshold. The proposed NBI

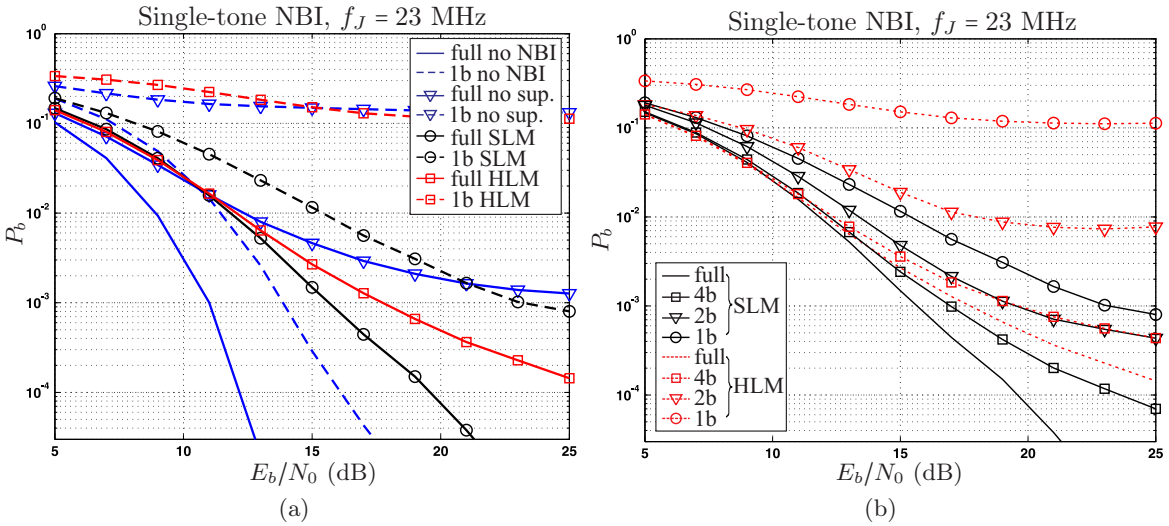

Fig. 6.18: BER versus SNR for the proposed NBI suppression schemes in the presence of the single-tone NBI. SIR = -18 dB and TH code is (N_h = 5, N_s = 23). "HLM" and "SLM" are short for hard limiter and soft limiter, respectively.

suppression scheme utilizing the soft limiter with a fixed δ still performs well (cf. Figure 6.18(a)). However, for a small SNR, the performance without NBI suppression is even better than that with the soft limiter or the hard limiter. The soft limiter is especially designed for impulsive noise rather than AWGN. The superior performance of using the soft limiter is thus lost when AWGN is dominant. Therefore, it is of prime importance to adaptively employ the soft limiter for controlling whether the NBI mitigation is switched on ($\delta \neq 0$) or off ($\delta = 0$) according to whether the NBI or the AWGN is dominant. This decision is made based on the following rule

$$\delta : \begin{cases} = 0, N_0 \geq P_J/B & \rightarrow \text{ AWGN is dominant} \\ \neq 0, N_0 < P_J/B & \rightarrow \text{ NBI is dominant} \end{cases}, \tag{6.32}$$

where B is the total bandwidth of the signal. The adaptation of switching on/off the soft limiter affects the performance and is necessary. When the soft limiter is turned on, δ can be either fixed or adaptively determined under different SNR/SIR situations. Due to the insensitivity of the threshold-dependent performance, the proposed scheme is tolerant to a certain estimation error. Only a rough knowledge of the SNR/SIR is required for the adaptation. In a multipath environment, the threshold selection can also be made by searching a pre-simulated look-up table according to the estimated SNR/SIR. The corresponding estimation methods proposed in [CB07] can be applied.

6.6.4.2 OFDM Interference (Block-based Threshold Adaptive Soft Limiter)

The parameters of the OFDM interference used for the simulations are shown in Table 6.5, where the cyclic prefix and the guard interval are not considered and the OFDM symbol period $T_{s_{\text{OFDM}}}$ is larger than the symbol duration. Figure 6.19 plots the corresponding OFDM interference. It is known that the OFDM signal with multiple carriers has a high Peak-to-

Average Power Ratio (PAPR), resulting in a much larger dynamic range of the received signal compared to in the case with only a single-tone interferer. As a result, a fixed threshold for the whole transmission time will not guarantee an effective NBI mitigation. However, if the whole transmission period is divided into different blocks as shown in Figure 6.19, the instantaneous dynamic range within one block can be smaller. Therefore, the threshold adaptation can be carried out block-by-block according to the instantaneous SNR/SIR within the current block, i.e., a block-based threshold adaptive soft limiter. The look-up table of the pre-simulated thresholds can be built by using the single-tone NBI model.

Tab. 6.5: Parameters for IEEE 802.11a OFDM signal

modulation	f_{OFDM}	N_c	Δf	$T_{s_{\text{OFDM}}}$
BPSK	5.22 GHz	48	312.5 KHz	4 μs

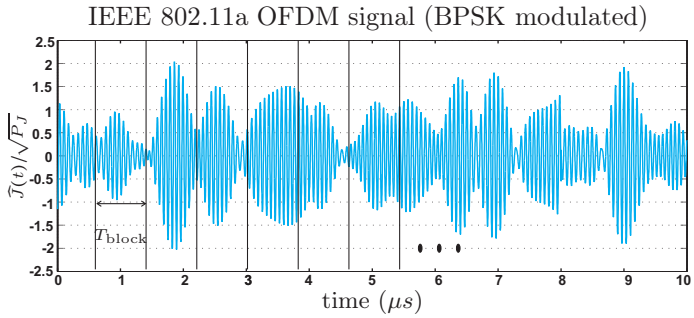

Fig. 6.19: OFDM interference signal with block separation.

Figure 6.20 shows the BER performance of the proposed full-resolution as well as the one-bit receiver in the presence of the OFDM interference when different NBI suppression schemes are applied. For simplicity, we choose a block duration with a constant size, even though the adaptive block size may yield a better performance. In Figure 6.20, it shows that except for the hard limiter using the one-bit ADC, all the other NBI suppression schemes provide performance improvements compared to the case without mitigation. However, when the non-adapted soft limiter or hard limiter is employed, i.e., with the fixed threshold factor δ, an error floor always occurs in the high SNR region due to the high PAPR. The block-based threshold adaptive scheme is able to reduce the error floor, indicating a higher NBI mitigation capability.

6.6.5 Frequency Dependency

The frequency-dependent performance of the proposed NBI suppression scheme in the presence of the single-tone NBI is also evaluated in terms of f_J as illustrated in Figure 6.21(b). It is observed that the BER performance largely depends on the NBI frequency f_J, exhibiting exactly the same behavior as the transfer function of the DCMF in Figure 6.21(a). This transfer function is obviously frequency selective within the range when f_J is less than the cut-off frequency of the pulse filter $g_R(t)$. When there is a deep "fade", e.g., at f_J = 9 MHz,

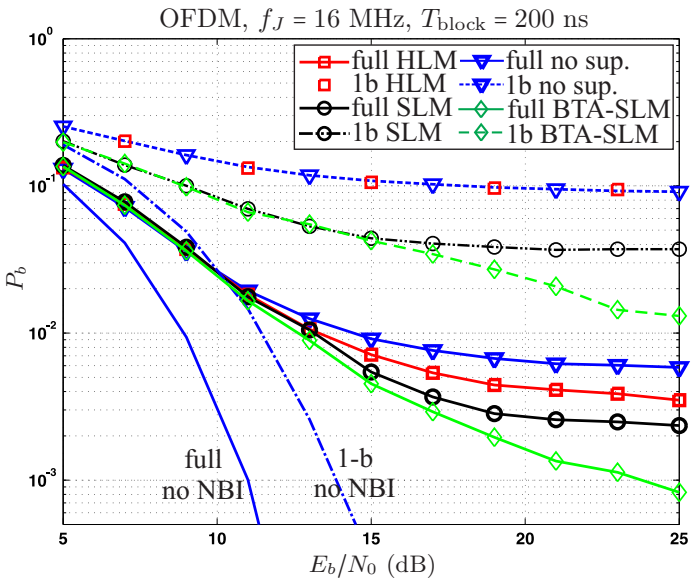

Fig. 6.20: BER versus SNR for the proposed NBI suppression schemes in the presence of the OFDM NBI. In all cases, SIR = -18 dB and TH code is (N_s = 23, N_h = 5). "HLM" and "SLM" are short for hard limiter and soft limiter, respectively. "BTA-SLM" represents the block-based threshold adaptive soft limiter method.

the NBI is suppressed significantly. In the range of $f_J < 5$ MHz, the constructive effect of the DCMF enhances the NBI, greatly deteriorating the receiver performance. At any given NBI frequency, it is shown in Figure 6.21(b) that the soft limiter can achieve performance improvements compared to the hard limiter and the case without suppression.

6.6.6 Conclusions

We propose a novel NBI suppression scheme using a soft limiter carried out in front of a digital non-coherent receiver for low data rate TH-PPM UWB communications. The NBI suppression relies on a feedforward structure with an analog soft limiter to "suppress" the TH-PPM signal and "isolate" the NBI. The soft limiter with adaptable thresholds can be applied under various situations, especially for switching on/off the mitigation procedure according to whether the NBI or the AWGN is dominant or not. The performance of the proposed full-resolution as well as b-bit receivers ($1 \le b \le 4$) is analyzed in the presence of AWGN and strong NBI, where both an unmodulated single-tone NBI and the OFDM NBI from an IEEE 802.11a WLAN are considered. Even though the performance is analyzed in AWGN, the proposed NBI suppression concept is also applicable to UWB multipath channels.

The suitability of the NBI suppression receiver using the soft limiter is investigated in terms of the threshold selection and adaptation as well as the frequency dependency. It is shown that the proposed receiver can effectively mitigate the NBI by appropriately choosing the threshold factor δ. Since the soft limiter operates in both linear and clipping regions, it outperforms the hard limiter counterpart (a special case of the soft limiter) especially when the ADC resolution b is small. When $b \neq 1$, a joint selection of δ and the input gain of the

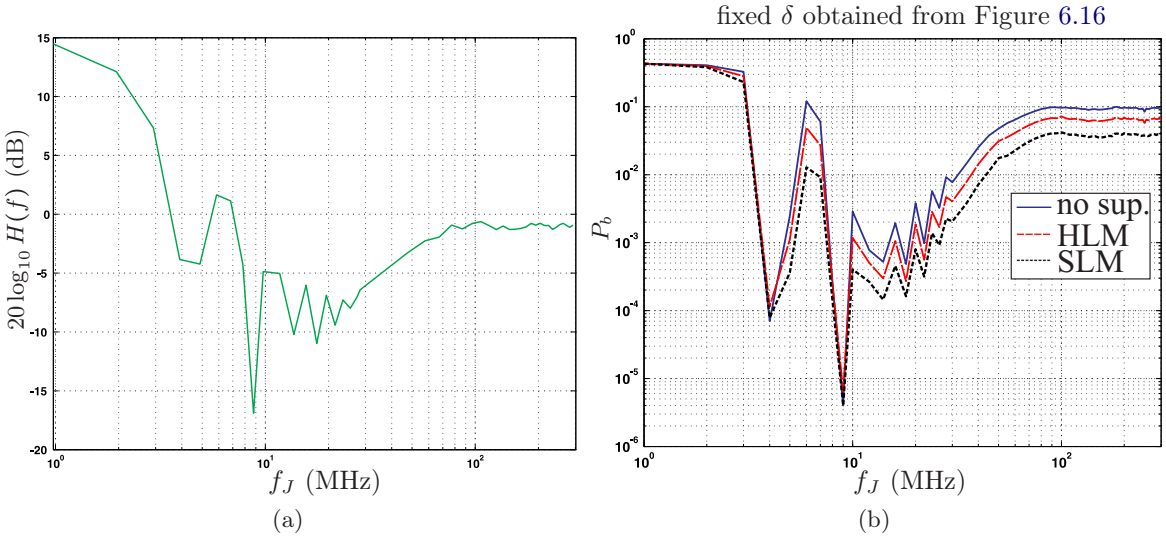

Fig. 6.21: (a) The transfer function of the random TH code (5, 23). (b) BER versus f_J with single-tone NBI in AWGN (full-resolution, E_b/N_0 = 16 dB, SIR = -18 dB). "HLM" and "SLM" are short for hard limiter and soft limiter, respectively.

ADC G is required. This gain G is determined by the resolution b but does not depend on whether the hard limiter or the soft limiter is utilized. The performance of the proposed NBI suppression receiver improves with increasing b (b is kept small) but at the expense of a higher complexity.

In the presence of the strong OFDM interference, the NBI mitigation based on the threshold adaptive soft limiter is proposed, which instantaneously carries out the block-by-block adaptation of the soft limiter threshold. This scheme provides a higher NBI suppression capability than the soft limiter method with a fixed δ. The receiver performance is also affected by the DCMF that is matched to the corresponding TH code, because the frequency response of the random TH sequence is frequency selective. The frequency-dependent performance using the soft limiter/hard limiter is observed. Even with the strong NBI at any given frequency, the soft limiter still has an improved performance compared to the case without NBI suppression and also exhibits a higher robustness than that of the hard limiter.

6.7 Advanced Orthogonal Modulation Schemes for Digital Non-Coherent Receivers

6.7.1 Introduction

Due to the sparse feature of the TH codes and accordingly the reduced receiver complexity (compared to the Direct Sequence Spread Spectrum (DSSS)), we have considered the TH Binary Pulse Position Modulation (2-PPM) transmission scheme in previous sections. In Section 6.4, we propose a DCMF-based non-coherent receiver in order to reduce the NC-CL. The DCMF follows after a high-speed and low-resolution ADC and restricts the non-coherent combining only to the multipath arrivals. It is shown that the proposed digital non-coherent receiver is robust to the MUI, even with a one-bit ADC.

If the modulation order increases, the power efficiency of the system will be further improved. Increasing M of such orthogonal schemes will also provide a higher robustness to the MUI than the binary case. Thus, it calls for utilizing M-ary orthogonal modulation for non-coherent UWB communications. There are some M-ary modulation schemes proposed for TH Impulse Radio (IR) UWB systems, such as M-PPM [ZL08, SUCH10], M-Walsh [EHO+02], or On-Off Keying (OOK) combined with M-ary Pulse Shape Modulation (PSM) [MMPR08]. Most of these discussions and performance evaluations for those proposed M-ary schemes either focus on the coherent detection or do not deal with the interference. Compared with PPM and Walsh, the PSM signaling scheme requires M different analog pulse matched filters in parallel, imposing an even higher complexity on the receiver especially when M is large.

Therefore, in order to achieve an improved power efficiency, we propose to employ TH M-ary Walsh transmission schemes for one-bit non-coherent receivers. Section 6.7.2 investigates the TH M-Walsh method and compares it with TH M-PPM by considering the impact from the receiver implementation, the one-bit quantization, and the multiple access. We will show the suitability and the superior performance of the proposed TH M-Walsh scheme using a digital non-coherent receiver. Section 6.7.3 specifies two TH M-Walsh signaling schemes, namely Repeated Walsh (R-Walsh) and Spread Walsh (S-Walsh). To achieve both power efficiency and bandwidth efficiency, we evaluate both schemes in terms of the robustness against the MUI and the multipath-induced interference. By trading off the signaling parameters, a system design criterion is derived on how to select appropriate transmission schemes according to specified requirements.

6.7.2 Comparison of TH M-PPM and TH M-Walsh

6.7.2.1 System Description

The block diagram of the TH M-Walsh system is shown in Figure 6.22. The sequential input bits are firstly converted from series to parallel and then mapped into Walsh symbols. After each Walsh symbol is encoded by a TH sequence, the pulse shaping $g(t)$ is applied to generate

the transmitted signal $s(t)$. At the receiver, the received signal $x(t)$ goes through a pulse matched filter $g_R(t)$ to obtain a filtered signal $y(t)$. The DCMF matched to the TH code follows after an ADC. The resulting signal samples will be fed to parallel block delays and the Fast Walsh Hadamard Transformation (FWHT) is carried out. The details of the Walsh codes and the FWHT are described to Appendix C. A set of correlators can also be realized but has a higher computational complexity of order $O\left(M^2\right)$ compared to the FWHT with complexity of order $O\left(M \cdot \log_2 M\right)$ [Kam96]. In each branch, a square-law device and a digital accumulator are applied in order to collect the multipath energy for each Walsh chip. Based on the maximum likelihood criterion, the variable Z_m with the largest value is selected and converted into estimated bits.

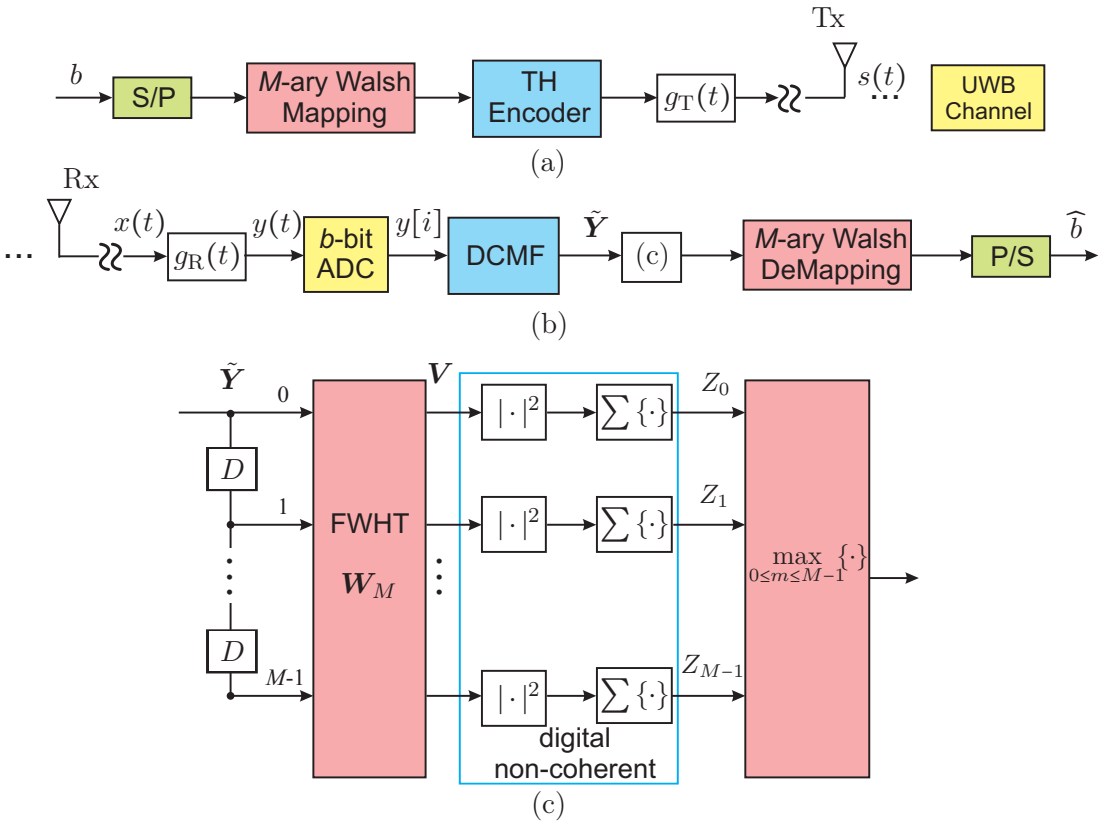

Fig. 6.22: (a) The transmitter for the proposed TH M-Walsh scheme. (b) The proposed digital non-coherent receiver (in complex baseband). (c) The structure of the Walsh demodulator.

Signal Model

The transmitted signal for symbol m in the interval $0 \le t \le T_s$ in Figure 6.22 is given by

$$s_m(t) = \sqrt{\frac{E_s}{N_s}} \sum_{\nu=0}^{M-1} \sum_{i=0}^{N_s-1} w_{m,\nu} g\left(t - iT_f - C_i T_c - \nu\Delta\right), \quad m \in \{0, \ldots, M-1\} \tag{6.33}$$

where

- $E_s = E_b \log_2 M$ is the symbol energy;

- each Walsh chip is denoted by $w_{m,\nu} \in \{\pm 1/\sqrt{M}\}$, which is the ν-th element of the m-th Walsh Hadamard sequence $\boldsymbol{w}_m = [w_{m,0}, \ldots, w_{m,M-1}]^T$. The Walsh Hadamard matrix of size $M \times M$ can be denoted by $\boldsymbol{W}_M = [\boldsymbol{w}_0, \boldsymbol{w}_1, \ldots, \boldsymbol{w}_{M-1}]$;
- TH codes are determined by the number of pulse repetitions N_s and the number of hopping positions N_h, where the repetition period and hopping duration are T_f and T_c, respectively. Each symbol is repeated and transmitted at different hopping positions according to $C_i \in \{0, \ldots, N_h - 1\}$. The modulation interval is denoted by $\Delta = T_c/M$.

We use the tapped-delay line channel model as shown in Chapter 2. At the receiver, the filtered received signal $y(t)$ is represented by

$$y_m(t) = \sqrt{\frac{E_s}{N_s}} \sum_{l=0}^{L-1} \sum_{\nu=0}^{M-1} \sum_{i=0}^{N_s-1} \alpha_l w_{m,\nu} \tilde{g}\left(t - iT_f - C_i T_c - \nu\Delta - l/B\right) + n(t), \tag{6.34}$$

where $\tilde{g}(t) = g(t) * g_R(t)$ and $n(t) = \widehat{n}(t) * g_R(t)$ are filtered (convolved) pulse and noise, respectively. The zero-mean, complex-baseband AWGN $\widehat{n}(t)$ has the PSD N_0.

Decoding and Demodulation

The block signal after the DCMF is collected in an $L_\mathrm{i} \times M$ matrix as $\tilde{\boldsymbol{Y}}_m$. If the one-bit ADC is employed, each element of $\tilde{\boldsymbol{Y}}_m$ is given by $\tilde{y}_m[l,\nu] = \dfrac{1}{\sqrt{N_s}} \sum_{i=1}^{N_s} y_m[l,\nu,i]$, where the one-bit quantized sample is expressed as

$$y_m[l,\nu,i] = \mathrm{sign}\{\widehat{y}_{R,m}[l,\nu,i]\} + j \cdot \mathrm{sign}\{\widehat{y}_{I,m}[l,\nu,i]\} \tag{6.35}$$

with $\widehat{y}_{p,m}[l,\nu,i]$ being the samples of the filtered signal $y_m(t)$ and $p \in \{R, I\}$ representing the real and imaginary parts. Each entry of $\tilde{\boldsymbol{Y}}_m$, i.e., the l-th row and ν-th column element is

$$\tilde{y}_m[l,\nu] = \sqrt{E_s}\alpha_l w_{m,\nu} + \sum_{i=1}^{N_s} \frac{n_m[l,\nu,i]}{\sqrt{N_s}}, l \in \mathfrak{L}_\mathrm{i}, \nu \in \{0,1,\ldots,M-1\}, \tag{6.36}$$

where $n_m, m \in \{0,1,\ldots,M-1\}$ are complex AWGN samples with zero mean and PSD N_0. The set of L_i taps that are included in the integration window is denoted by $\mathfrak{L}_\mathrm{i}$.

The output of FWHT can be written as

$$\boldsymbol{V} = \tilde{\boldsymbol{Y}}_m \boldsymbol{W}_M = \left[\tilde{\boldsymbol{Y}}_m \boldsymbol{w}_0, \ldots, \tilde{\boldsymbol{Y}}_m \boldsymbol{w}_{M-1}\right] \stackrel{!}{=} [\boldsymbol{v}_0, \ldots, \boldsymbol{v}_{M-1}]. \tag{6.37}$$

The decision variables obtained after the square-law multipath combining are represented as $Z_m = \boldsymbol{v}_m^H \boldsymbol{v}_m$ and the detected symbol is $\max\limits_{0 \le m \le M-1} \{Z_m\}$.

M-PPM and M-Walsh

M-ary PPM can also be applied for TH UWB communications but has some disadvantages compared to M-Walsh.

- M-PPM may cause a higher PAPR than M-Walsh. For the M-Walsh modulation, a sequence of pulses modulated by a bipolar Walsh code is transmitted as a Walsh symbol. However, each M-PPM symbol $\boldsymbol{w}_m$ contains only one pulse, i.e., in equation (6.33) $w_{m,\nu}$ takes values in $\{0,1\}$, where 1 determines the pulse position. If the same data rate is assumed, the energy per pulse for M-PPM is $E_b \log_2 \frac{M}{N_s}$, which is higher than that for M-Walsh, i.e., $E_b \log_2 \frac{M}{MN_s}$.

- The receiver structure for M-PPM is more complex than for M-Walsh. If M-PPM is applied, a branch of parallel correlators is required for demodulation, which exhibits a higher complexity $O(M^2)$ than the implementation of the FWHT $O(M \log_2 M)$.

6.7.2.2 Analytical Performance of M-Walsh and M-PPM using One-Bit Non-Coherent Receiver

This section analyzes the BER performance of M-Walsh and M-PPM using one-bit non-coherent receivers [3]. For M-ary orthogonal modulation schemes (Walsh and PPM), the symbol demodulation is based on $\max_{0\le m\le M-1}\{Z_m\}$. Assuming "0" is transmitted, i.e., $m = 0$ is desired, it follows that the probability of correct decision P_c is simply the probability that $Z_0 > Z_1, Z_0 > Z_2, \ldots, Z_0 > Z_{M-1}$, given by

$$\begin{aligned} P_c &= \Pr\{Z_0 > Z_1, \ldots, Z_0 > Z_{M-1}\} \\ &= \int_{-\infty}^{\infty} \Pr\{Z_0 > Z_1, \ldots, Z_0 > Z_{M-1} | Z_0 = x\} f_{Z_0}(x) dx, \end{aligned} \tag{6.38}$$

where $f_{Z_m}(x)$ is the PDF of Z_m. Since the decision variables Z_m are independent and identically-distributed, the joint probability in equation (6.38) can be simplified as

$$P_c = \int_{-\infty}^{\infty} [1 - P_2(x)]^{M-1} f_{Z_0}(x) dx, \tag{6.39}$$

where

$$P_2(x) = \Pr\{Z_0 < Z_1 | Z_0 = x\} = \int_x^{\infty} f_{Z_1}(y) dy. \tag{6.40}$$

The averaged BER is given by [Pro01]

$$P_b = \frac{M/2}{M-1} P_M = \frac{M/2}{M-1}(1 - P_c), \tag{6.41}$$

where $P_M = 1 - P_c$ the probability of symbol error.

If the PDFs of the decision variables Z_m are unknown, a BER bound can be calculated in terms of the averaged BER for $M = 2$, i.e., $P_2 = \int_{-\infty}^{\infty} \Pr\{Z_0 < Z_1 | Z_0 = x\} f_{Z_0}(x) dx$. Similar to equation (5.8), using the central limit theorem and the Gaussian approximation for Z_0 and

[3] It is assumed that no interference exists.

Z_1, we can obtain

$$P_2 \approx \mathrm{Q}\left(\frac{\mathbb{E}\{Z\}}{\sqrt{\mathbb{V}\{Z\}}}\right), \quad Z = Z_0 - Z_1. \tag{6.42}$$

The BER bound can thus be computed as [Pro01]

$$P_b \le \frac{M/2}{M-1}\left[1-(1-P_2)^{M-1}\right]. \tag{6.43}$$

When E_b/N_0 is large, this bound will approach the exact BER.

Full-Resolution Performance of M-Walsh and M-PPM

For the full-resolution case, the performance of M-ary orthogonal modulation schemes (M-Walsh and M-PPM) is the same.

- ***Exact BER***

Assuming $m = 0$ is transmitted, the decision variables can be written as

$$\begin{aligned} Z_0 &= \boldsymbol{v}_0^H \boldsymbol{v}_0 = \sum_{l\in\mathfrak{L}_\mathrm{i}} \left|\sqrt{E_s}\alpha_l + n_0[l]\right|^2 \\ Z_m &= \boldsymbol{v}_m^H \boldsymbol{v}_m = \sum_{l\in\mathfrak{L}_\mathrm{i}} |n_m[l]|^2, 0 < m \le M-1. \end{aligned} \tag{6.44}$$

It is obvious that Z_0 is a sum of $2L_\mathrm{i}$ squared Gaussian random variables (real-valued) each with variance $N_0/2$, exhibiting a non-central χ^2-distribution with $2L_\mathrm{i}$ degrees of freedom and with a non-centrality parameter $\mu_0 = E_s \sum_{l\in\mathfrak{L}_\mathrm{i}} \Omega_l$. The second-order moment of the channel taps is given by $\Omega_l = \mathbb{E}\left\{|\alpha_l|^2\right\}$, $l \in \mathfrak{L}_\mathrm{i}$. Similarly, Z_m ($m \ne 0$) has a central χ^2-distribution with $2L_\mathrm{i}$ degrees of freedom. The probability of correct detection can be represented by [Pro01]

$$P_c = \int_{-\infty}^{\infty} [1-P_2(x)]^{M-1} \frac{1}{N_0}\left(\frac{x}{\mu_0}\right)^{\frac{L_\mathrm{i}-1}{2}} \exp\left(-\frac{x+\mu_0}{N_0}\right) I_{L_\mathrm{i}-1}\left(\frac{2\sqrt{\mu_0 x}}{N_0}\right) dx, \tag{6.45}$$

where

$$P_2(x) = \frac{\exp\left(-\frac{x}{N_0}\right)\sum_{k=0}^{L_\mathrm{i}-1}\left(\frac{x}{N_0}\right)^k}{k!} \tag{6.46}$$

and $I_n(x)$ is the nth-order modified Bessel function of the first kind. The exact BER for the full-resolution case can be calculated numerically by substituting P_c in equation (6.45) into equation (6.41).

- ***BER Bound***

It has been shown in Section 6.4 that the BER for the 2-PPM non-coherent receiver in multipath channels can be calculated by the Gaussian approximation. For M-ary modulation,

P_2 in equation (6.42) is estimated according to

$$\begin{aligned}\mathbb{E}\{Z\} &= E_s \sum_{l\in\mathfrak{L}_\mathrm{i}} \Omega_l \\ \mathbb{V}\{Z\} &= 2E_s N_0 \sum_{l\in\mathfrak{L}_\mathrm{i}} \Omega_l + 2L_\mathrm{i} N_0^2.\end{aligned} \tag{6.47}$$

Thus, we can obtain the BER bound for M-ary modulation in the full-resolution case from equation (6.43).

One-bit Performance (BER bound)

Since it is difficult to determine the distribution of Z_m when a one-bit ADC is applied, we will only analyze the BER bound. The performance evaluation using one-bit ADCs is different for M-Walsh and M-PPM due to the different decorrelating sequences $\boldsymbol{w}_m$.

- ***M-Walsh***

By assuming $m = 0$ is the desired symbol, the decision variables can be simplified as

$$Z_m = \sum_{p\in\{R,I\}} \sum_{l\in\mathfrak{L}_\mathrm{i}} |v_{m,p}[l]|^2, \tag{6.48}$$

where

$$v_{m,p}[l] = \frac{1}{\sqrt{N_s}} \sum_{\nu=1}^{M} \sum_{i=1}^{N_s} y_{p,0}[l,\nu,i] w_{m,\nu}, \ m \in \{0,1,\ldots,M-1\} \tag{6.49}$$

Each output sample of the one-bit ADC $y_{p,0}[l,\nu,i]$ takes values in $\{-1,+1\}$ with corresponding probability $p_l = \mathrm{Q}\left(\sqrt{\frac{E_b \log_2 M \cdot \sum_{l\in\mathfrak{L}_\mathrm{i}} \Omega_l}{MN_sN_0}}\right)$ and $1-p_l$, respectively. If MN_s is large, according to the central limit theorem, $v_{0,p}[l]$ (and $v_{m,p}[l], m \neq 0$) are approximated by Gaussian distributions with mean $\sqrt{MN_s}(1-2p_l)$ (and $0, m \neq 0$) and variance $4p_l(1-p_l)$, where the calculation of the mean and the variance can be found in Appendix A.2.1. Therefore, Z_0 ($Z_m, m \neq 0$) are the sum of L_i non-central (central) χ^2-distributed random variables each with 2 degrees of freedom. Therefore, P_2 in equation (6.42) can be analyzed by using

$$\begin{aligned}\mathbb{E}\{Z\} &= MN_s \sum_{l\in\mathfrak{L}_\mathrm{i}} (1-2p_l)^2 \\ \mathbb{V}\{Z\} &= 2(1-MN_s) \sum_{l\in\mathfrak{L}_\mathrm{i}} (1-2p_l)^4 + (2MN_s-1) \sum_{l\in\mathfrak{L}_\mathrm{i}} (1-2p_l)^2 + 2L_\mathrm{i}.\end{aligned} \tag{6.50}$$

By increasing M and/or N_s, p_l also increases, which influences P_2 accordingly.

- ***M-PPM***

For M-PPM using a one-bit non-coherent receiver, P_2 can be computed by

$$\begin{aligned}\mathbb{E}\{Z\} &= (N_s-1) \sum_{l\in\mathfrak{L}_\mathrm{i}} (1-2p_l)^2 \\ \mathbb{V}\{Z\} &= (1-2N_s) \sum_{l\in\mathfrak{L}_\mathrm{i}} (1-2p_l)^4 + 2(N_s-1) \sum_{l\in\mathfrak{L}_\mathrm{i}} (1-2p_l)^2 + 2L_\mathrm{i},\end{aligned} \tag{6.51}$$

where $p_l = \mathrm{Q}\left(\sqrt{\frac{E_b \log_2 M \cdot \sum_{l\epsilon\mathfrak{L}_i} \Omega_l}{N_s N_0}}\right)$. In contrast to the case of M-Walsh, when M gets larger, p_l decreases. This will account for the performance of the M-PPM scheme under the one-bit quantization effect, which will be discussed in Section 6.7.2.3.

6.7.2.3 Simulation Results and Discussions

In this section, we will show the performance of the proposed TH M-Walsh scheme compared with the TH M-PPM using a digital non-coherent receiver in multipath channels. The quantization effect due to a one-bit ADC on the performance of the two schemes is firstly discussed. We also evaluate the multiple access performance via Monte Carlo simulations, considering both perfect and imperfect power control. For multipath channels, we use UWB channels measured in a NLOS office scenario by IMST as described in Section 2.3.

Quantization Effect

When the full-resolution receiver is applied (no MUI), the performance of M-Walsh and M-PPM is the same. Figure 6.23(a) depicts the corresponding simulation results to validate the analytical ones, i.e., the exact BER obtained according to equations (6.41), (6.45) and the BER bound estimated by (6.42), (6.43), (6.46), and (6.47). It can be observed that for each M the exact BER provides an accurate performance analysis and the BER bound is quite close to the simulated performance for a large E_b/N_0. The performance of both schemes for $N_s = 10$ using the one-bit receiver is shown in Figure 6.23(b) and 6.23(c), which can be well estimated by the BER bound calculated via (6.50) and (6.51). In both the full-resolution and the one-bit resolution cases, a larger modulation order M leads to a higher power efficiency.

The equations (6.50) and (6.51) show that the one-bit performance depends on the number of repetitions N_s. According to the analytical performance bound, the one-bit quantization loss at BER = 10^{-3} is plotted as a function of the number of repetitions N_s in Figure 6.24 for both M-Walsh and M-PPM. When N_s is very small, M-PPM suffers greatly from the quantization and the loss is higher with a larger M. However, the quantization loss of M-Walsh only has a small variation with changing N_s and/or M ($M > 2$). This is due to the correlation characteristics of the Walsh codes. The output samples of the one-bit ADC are linearly combined and demodulated by the bipolar Walsh codes in a maximum likelihood sense, which actually decreases the variance of the resulting signal. The M-PPM sequence only consists of a single "1" and the other bits are "0". As a result, the decoding performance is much worse compared to the Walsh sequence. Furthermore, the significant quantization loss is also caused by the higher PAPR of M-PPM. In order to reduce this loss for M-PPM, a large number of repetitions is required but at the expense of lower data rates and a higher computational complexity.

Multiple Access Performance (Perfect Power Control)

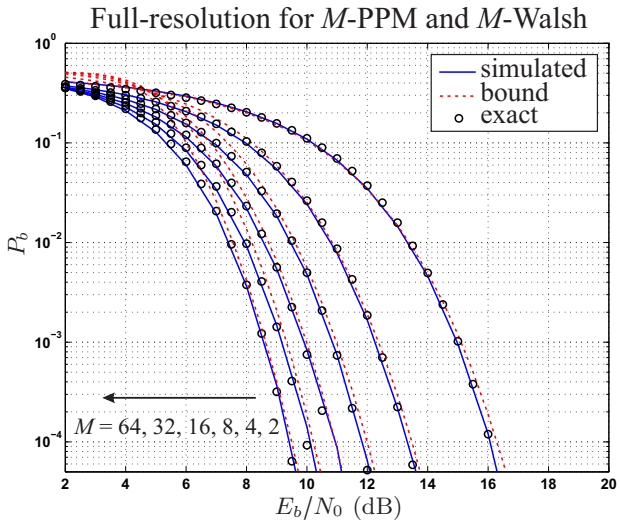

(a) Simulations, the exact BERs, and BER bounds

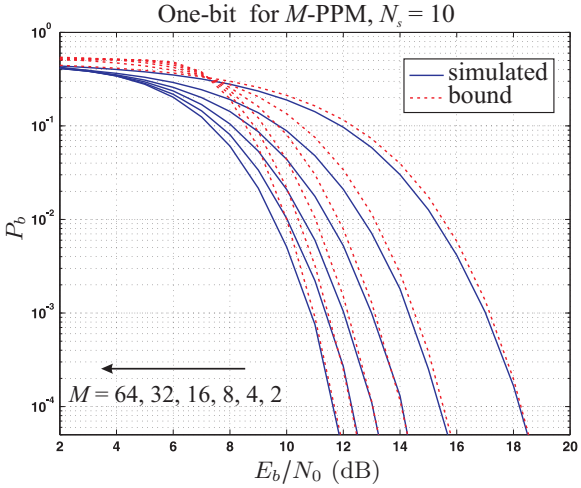

(b) Simulations and BER bounds

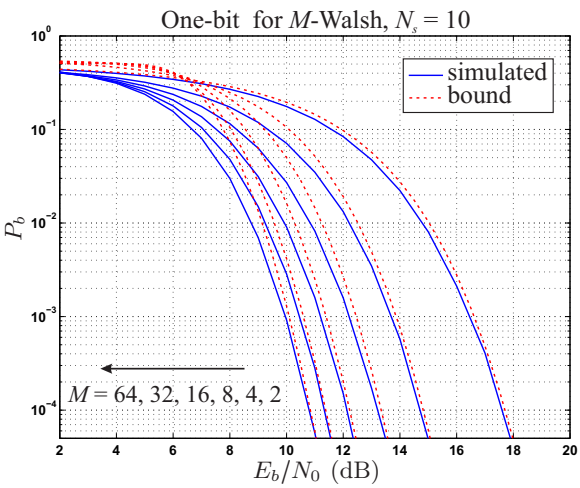

(c) Simulations and BER bounds

Fig. 6.23: Validation of the analytical BERs for M-Walsh and M-PPM using non-coherent detection in multipath. The integration window $T_{\mathrm{i}} = 32$ ns.

We compare the multiple access performance of the proposed TH M-Walsh scheme with the TH M-PPM scheme as shown in Figure 6.25(a) for the full-resolution receiver and in Figure 6.25(b) for the one-bit receiver. It can be observed that increasing M provides a higher power efficiency in the presence of MUI. Unlike decoding the unipolar PPM sequence, the Walsh demodulation can reduce the variance of the input signal (including MUI). As a result, the TH-M-Walsh exhibits a better MUI resistance than TH M-PPM in both full-resolution and one-bit cases.

Near-Far Problem (Imperfect Power Control)

Figure 6.26 shows the performance of TH M-PPM and TH M-Walsh with imperfect power control for the two-user case, where the Signal to MUI ratio (SIR) is defined as $\mathrm{SIR} = \log_{10}(E_b^{(1)}/E_b^{(2)})$ dB with superscript "(1)" corresponding to the desired user and "(2)" to the interferer. It can be observed that under the near-far effect especially when the SIR is

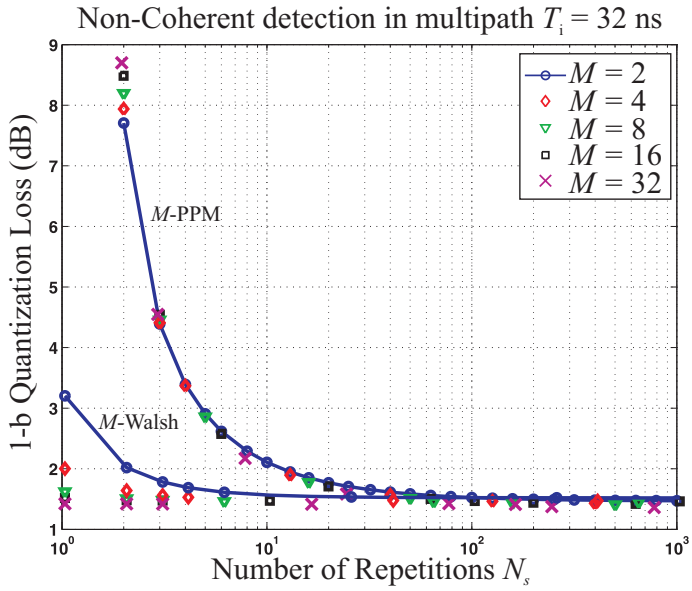

Fig. 6.24: Quantization loss due to a one-bit ADC versus the number of repetitions N_s at BER $= 10^{-3}$ for M-Walsh and M-PPM in multipath channels (analytical estimation).

very low, TH M-PPM outperforms TH M-Walsh when the one-bit receiver is employed. This can be explained by the hard operation property of the one-bit ADC. With a low SIR, the MUI for M-PPM is much stronger than for M-Walsh, leading to a larger PAPR (or dynamic range) of the received signal. The one-bit ADC is able to clip the strong MUI and thus PPM provides a higher near-far robustness compared to Walsh.

6.7.2.4 Summary

At the receiver, an FWHT structure is carried out after the one-bit ADC and the TH DCMF, which has a lower complexity compared to the parallel correlators used in the M-PPM scheme. We discuss the one-bit quantization loss by deriving the BER bounds for both M-Walsh and M-PPM in multipath channels. Because of the superior property of the Walsh codes combined with the maximum likelihood demodulation, when N_s is small the quantization loss for M-PPM is significantly higher than that for M-Walsh. The M-Walsh scheme only has a loss around 1.5 dB at BER = 10^{-3} even with changing N_s and/or M ($M > 2$). We also evaluate the multiple access performance of the two schemes considering perfect and imperfect power control. It is shown that a larger M provides a higher MUI robustness. In the case of perfect power control, the TH M-Walsh scheme outperforms the TH M-PPM when both full-resolution and one-bit receivers are employed. This can be interpreted by different distributions of the MUI due to different code properties of M-PPM and M-Walsh. With imperfect power control (near-far scenario), a strong MUI (a low SIR) leads to an even larger PAPR for PPM. The hard clipping operation of the one-bit ADC can effectively suppress the strong MUI, which shows that PPM has a better near-far resistance than Walsh.

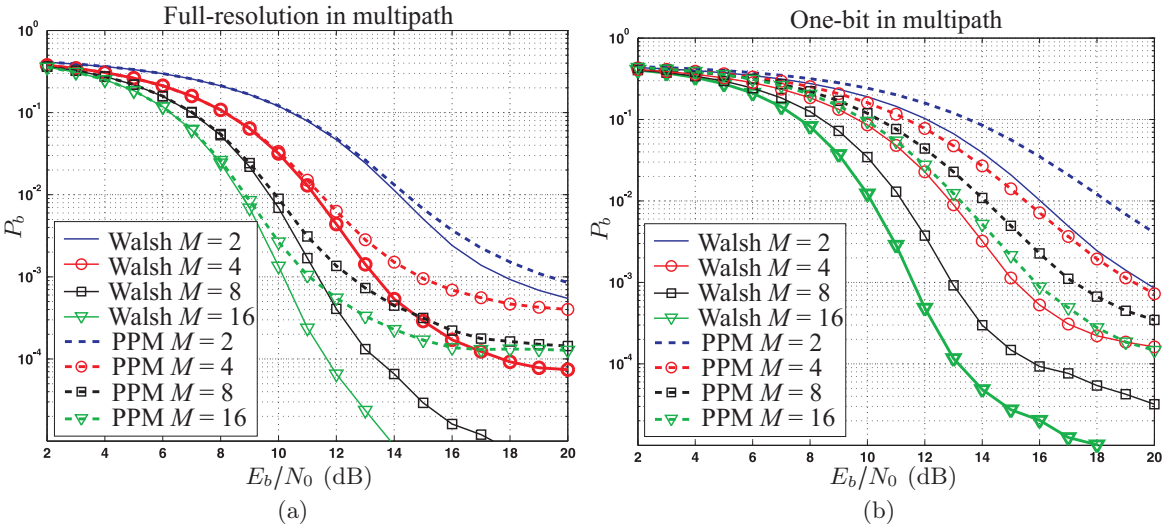

Fig. 6.25: Multiple access performance of TH M-Walsh and TH M-PPM using both full-resolution and one-bit receivers in multipath channels for the perfect power control case. TH code of parameters $(N_h = 12, N_s = 3)$ and the number of users $N_u = 6$ are chosen.

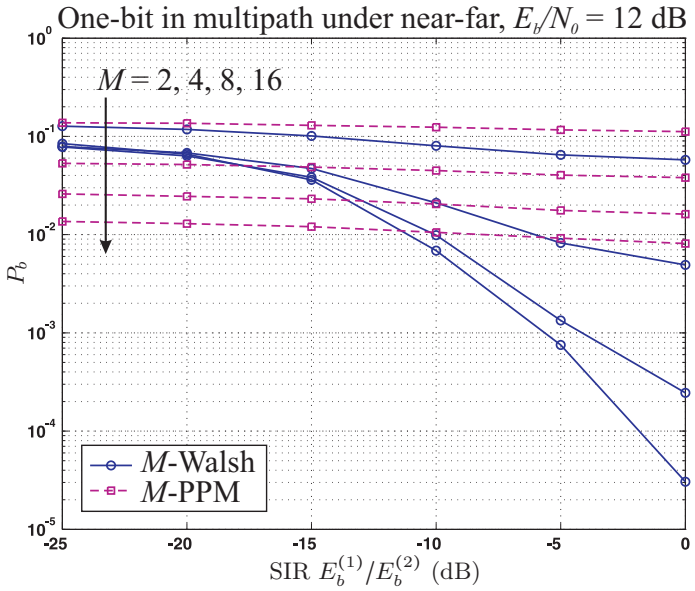

Fig. 6.26: Multiple access performance of TH M-Walsh and TH M-PPM using the one-bit receiver in multipath channels under the near-far effect. TH code of parameters $(N_h = 12, N_s = 3)$ is chosen and $N_u = 2$. The energy per bit for user 1 and 2 is denoted by $E_b^{(1)}$ and $E_b^{(2)}$.

6.7.3 TH M-ary Walsh Transmission Schemes

The TH M-Walsh scheme discussed in Section 6.7.2.1 is based on repeating each Walsh symbol and assigning them in specified hopping positions according to the TH code. We refer to this approach as Repeated Walsh (R-Walsh). Alternatively, each Walsh symbol comprises a sequence of bipolar chips. We can thus spread the chips into different TH frames and each chip is transmitted in a hopping position which is determined by the TH code. This signaling scheme is named as Spread Walsh (S-Walsh).

This section deals with these two TH M-Walsh transmission strategies. In order to achieve both power efficiency and bandwidth efficiency, the signaling parameters such as the modulation order M as well as the TH parameters (N_h, N_s) have to be carefully chosen. We will discuss the selection of these parameters and the schemes for the system design in different data rate applications.

6.7.3.1 System Description

The signaling representations of R-Walsh and S-Walsh are illustrated in Figure 6.27(a) and Figure 6.27(b), respectively. Similar to the TH PPM scheme (cf. Figure 5.2), the overall transmitted symbol of duration T_s contains N_s TH frames each of length T_f. One frame consists of N_h hopping positions or TH chips and the duration of each TH chip is T_c. We denote Δ as the modulation interval, which is also the period of the Walsh chip. If the pulse interval is T_g, we can obtain $\Delta = LT_g$, where L is an integer corresponding to the inverse of the duty cycle. For S-Walsh, $N_s = M$ holds.

Processing Factor

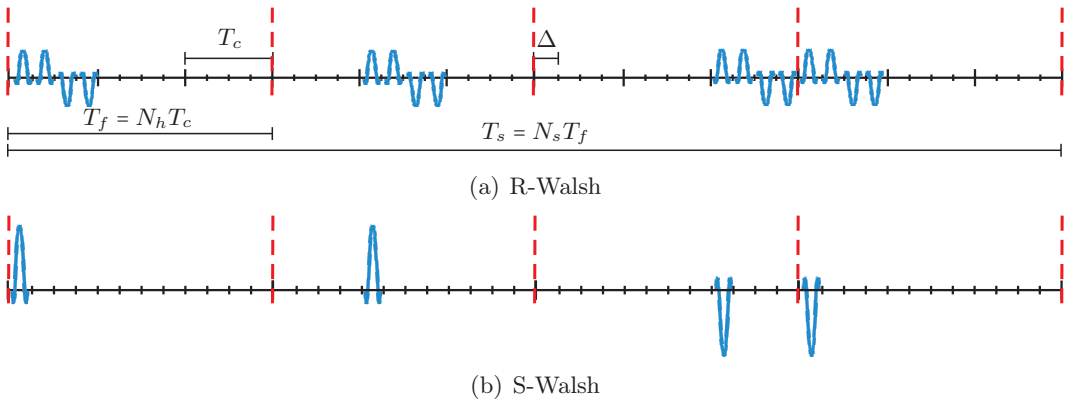

(a) R-Walsh

(b) S-Walsh

Fig. 6.27: Representations of R-Walsh and S-Walsh schemes using the Walsh symbol $(1, 1, -1, -1)$. (a) $M = 4, N_h = 3, N_s = 4$ with TH positions $(0, 1, 2, 0)$; (b) $M = N_s = 4, N_h = 12$ with TH positions $(0, 4, 8, 0)$. In this example, $L = 1$ is shown.

Let us define the processing factor [4] of two TH M-Walsh schemes as

$$N = \frac{T_s}{T_g} = \frac{B}{R_b} = \begin{cases} \dfrac{M}{\log_2 M} \cdot N_s N_h L, & \text{R-Walsh} \\ \dfrac{M}{\log_2 M} \cdot N_h L, & \text{S-Walsh} \end{cases}, \tag{6.52}$$

where B is the total bandwidth of the pulse and R_b represents the data rate. Figure 6.27 illustrates the signal representations of both schemes with the same processing factor $N = 24$.

Receiver

The block diagram of the transmitter shown in 6.22 (a) applies to both schemes. The receiver of R-Walsh has been shown in Figure 6.22 (b)(c). The S-Walsh method has a slightly different receiving structure since the Walsh chips are interleaved with the TH code. We depict the digital non-coherent receiver for S-Walsh in Figure 6.28. The DCMF is applied across M parallel branches, which correspond to M Walsh chips in one symbol.

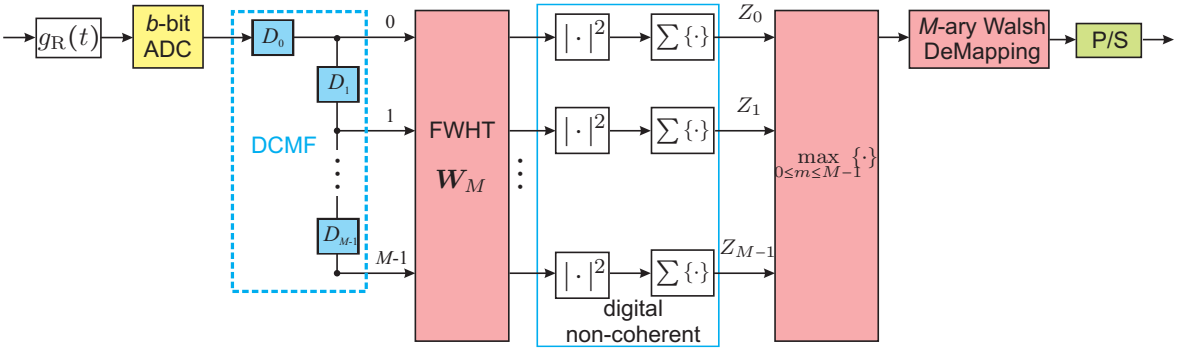

Fig. 6.28: Block diagram of the digital non-coherent receiver for S-Walsh.

Discussions on the System Parameters

It is known that a larger M provides a higher power efficiency. From equation (6.52), we distinguish the following two cases in terms of the MUI and the multipath-induced interference.

- **MUI:** For simplicity, it is assumed that only AWGN is present, i.e., $L = 1$. With a fixed processing factor N, increasing M leads to a reduced $N_s N_h$ for R-Walsh or a reduced N_h for S-Walsh. The smaller these TH parameters are, the more vulnerable to the MUI the system becomes. There exists a trade-off on the selection of parameters M and $N_s N_h$ or N_h for the system design.

[4] This is different from the one discussed in Chapter 5 and Section 6.4, which is exclusively referred to as the length of a TH code, i.e., $L_m = N_h N_s$. We use the term "processing factor" here instead of the "processing gain" due to the fact that it contains the number of resolvable multipath components L, which are non-coherently combined, leading to a NC-CL.

- **Multipath-induced Interference:** We consider the R-Walsh scheme in the single-user case [5], i.e., assuming the simplest $N_h = N_s = 1$. The equation (6.52) can thus be simplified to $N = \frac{M}{\log_2 M} \cdot L$. With a fixed N, increasing M gives rise to a smaller L; if N is decreased in order to achieve a higher data rate, a larger M yields a even smaller L. A reduced L indicates that the interference due to the multipath occurs among the Walsh chips. Due to the fact that Walsh codes have a poor auto-correlation property, the multipath-induced interference may cause a significant performance degradation. We propose to use additional Direct Sequence (DS) codes such as m-sequences on the Walsh codes. The length of the m-sequence, which determines the capability of resolving the multipath-induced interference, depends on M. However, a longer sequence results in a smaller L and consequently the more severe multipath-induced interference. Thus, there is another trade-off on how to choose M.

Furthermore, a greater M also implies a higher complexity at the receiver side.

In what follows, we will derive a system design rule for TH M-Walsh transmission schemes by considering the above trade-offs.

6.7.3.2 Multiple Access Performance in AWGN

Figures 6.29 and 6.30 show the BER performance of both R-Walsh and S-Walsh for various fixed processing factor N in AWGN, where $N_u = 6$ and the random TH codes (cf. Section 5.4.1) are chosen.

In the case of R-Walsh as shown in Figure 6.29, the best combination of the TH codes for each M is summarized in Table 6.6. We can observe that with a fixed N, a higher power efficiency can be obtained by increasing M. While due to the trade-off between the power efficiency and the MUI robustness, the performance degrades by further enlarging M, e.g., $M = 32$. In our considered scenario, for $N = 96, 128$, the best performance for R-Walsh is achieved with $M = 8, 16$. The TH codes selection is based on the rule that

- N_h should not be very small in order to accommodate enough users, and
- $N_h > N_s$ and $N_s > 2$ hold.

Tab. 6.6: The best combination of the TH code (N_h, N_s) for R-Walsh.

M	2	4	**8**	**16**	32
$N = 128$	(16,4)	(16,4)	**(12,4)**	**(8,4)**	(5,4)
$N = 96$	(16,3)	(16,3) or (12,4)	**(12,3) or (9,4)**	**(8,3)**	(5,3)

[5] The duty cycle of the TH S-Walsh is inherently low, we assume no multipath interference occurs.

In the case of S-Walsh as shown in Figure 6.30 for any fixed N, increasing M provides an improved power efficiency as well as a higher MUI robustness, since the TH parameter depends on N_s and $N_s = M$.

We plot the required E_b/N_0 in dB at $P_b = 10^{-3}$ as a function of the modulation order M for the best cases using both R-Walsh and S-Walsh in Figure 6.31. We can see that for the same N and with a larger M, S-Walsh outperforms R-Walsh with around $3-6$ dB performance improvement. It also indicates that S-Walsh is more appropriate than R-Walsh when M is large, e.g., $M \geq 32$. With $N = 96$ or 64, S-Walsh also exhibits a better performance as compared to R-Walsh with $N = 128$ or 96, implying its suitability to higher data rate applications.

From the complexity point of view, S-Walsh is more complex than R-Walsh due to a larger M and a higher number of delay elements that are determined by N_h.

6.7.3.3 Bandwidth Efficiency

The bandwidth efficiency is often defined as the ratio of the data rate and the total bandwidth, i.e., R_b/B [Pro01]. In the case of multipath, we use the UWB channels measured in the NLOS scenario (cf. Section 2.3). The reference performance is obtained when no multipath-induced interference exits, i.e., for $M = 2, 4$ with the corresponding data rate denoted by R_b. When M gets larger, multipath interference occurs even with the data rate R_b. Figure 6.32 depicts the BER performance of the M-ary R-Walsh scheme for the single-user case with increasing data rates. It can be observed that by increasing the data rate from R_b to $\log_2 M \cdot R_b$, the performance difference becomes larger with a greater M (e.g., $M \geq 8$). For R-Walsh, $M \geq 8$ can be considered as an appropriate modulation order in terms of the multipath interference robustness.

Tab. 6.7: Required E_b/N_0 (dB) of R-Walsh at $P_b = 10^{-3}$ for different M with various data rates.

M	2	4		8		16		32		64	
Data Rate	R_b	R_b	$2R_b$	R_b	$3R_b$	R_b	$4R_b$	R_b	$5R_b$	R_b	$6R_b$
E_b/N_0(dB)	15.05	12.2	12.7	11.2	11.75	10.2	12.12	9.55	11.48	9.1	11.48

6.7.3.4 Comparison of two Walsh Schemes and System Design Rule

To summarize, we compare the TH M-ary R-Walsh and the TH M-ary S-Walsh schemes in Table 6.8 in terms of the MUI robustness, the applied data rates, the suitable modulation order M, and the complexity. The data rate is calculated by considering the appropriate selection of the signaling parameters M, N_h, N_s (cf. Section 6.7.3.2) as well as the multpath propagation [6]. The R-Walsh scheme is more suitable for lower data rate applications, i.e.,

[6] The multipath-induced interference is taken into account for R-Walsh, where additional DS codes are required. For S-Walsh, it is assumed that no significant multipath-induced interference exists.

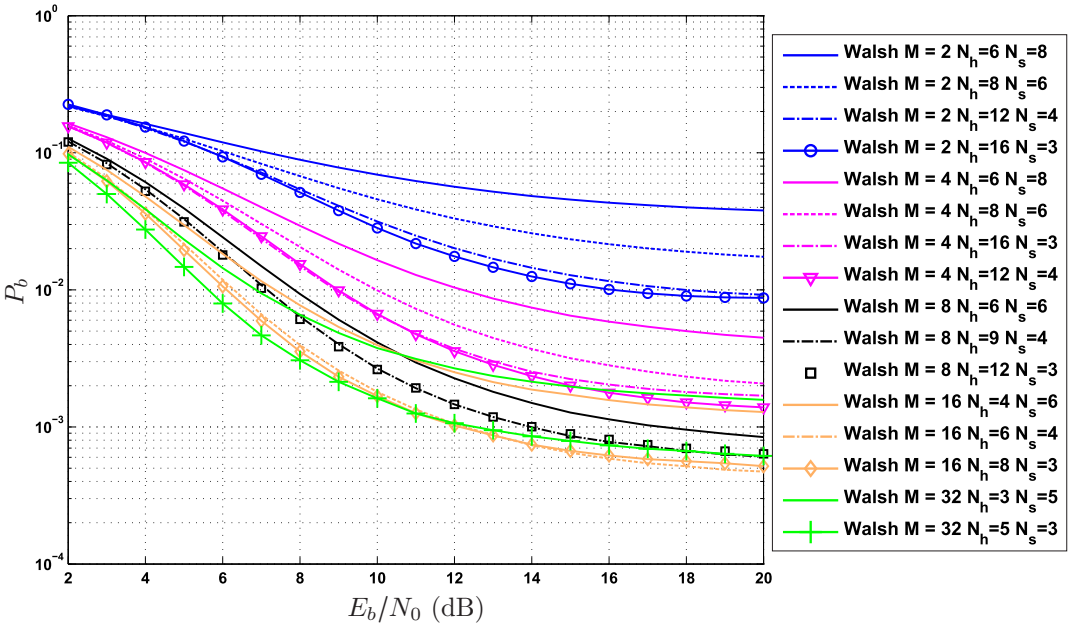

(a) $N = 96, N_u = 6$

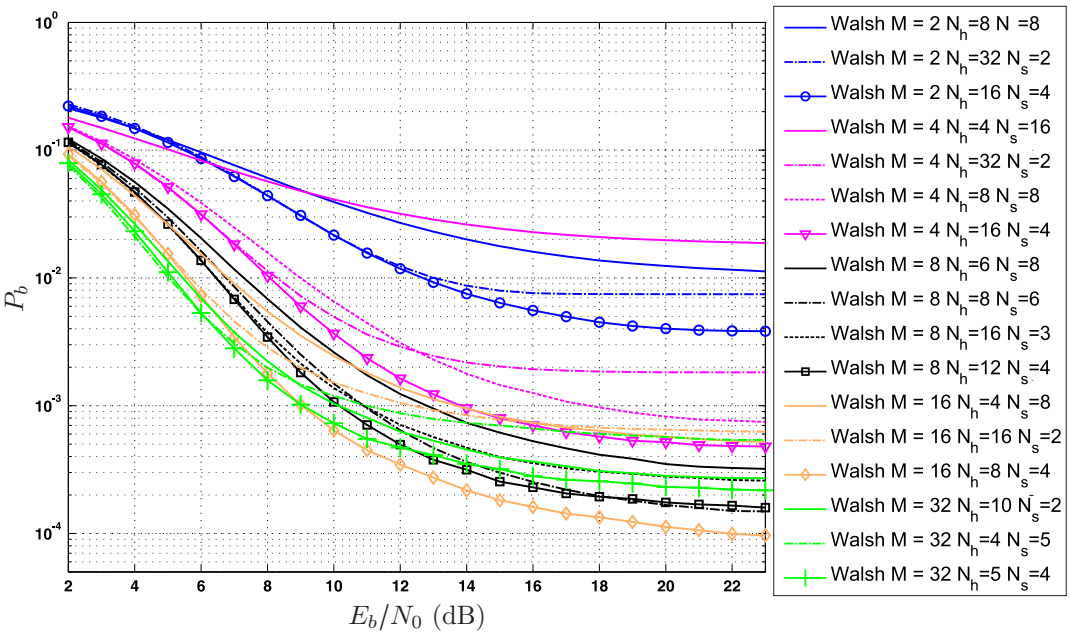

(b) $N = 128, N_u = 6$

Fig. 6.29: BER of the TH M-ary R-Walsh scheme in AWGN.

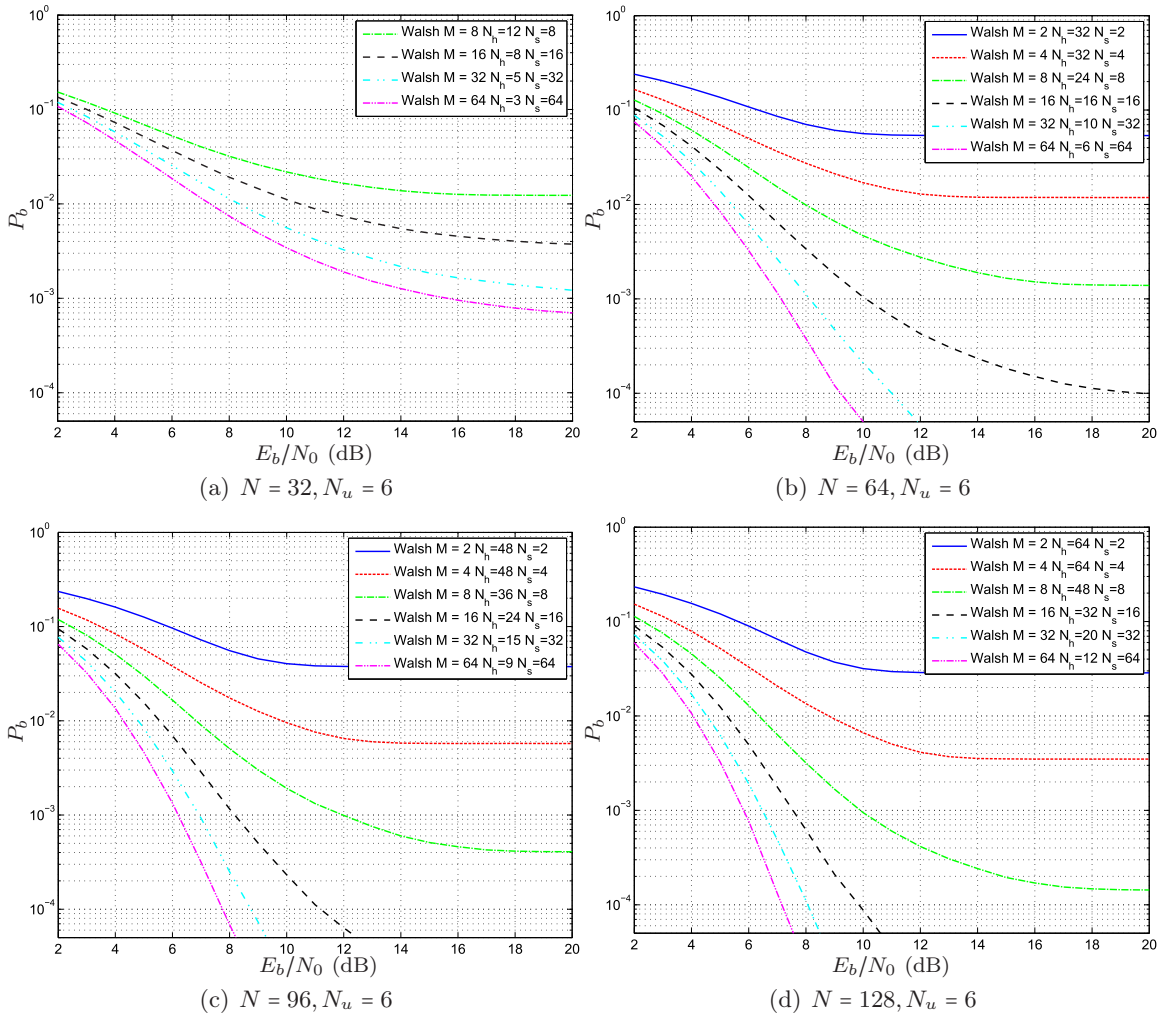

(a) $N = 32, N_u = 6$ (b) $N = 64, N_u = 6$

(c) $N = 96, N_u = 6$ (d) $N = 128, N_u = 6$

Fig. 6.30: BER of the TH M-ary S-Walsh scheme in AWGN.

$R_b < 180$ kbps. The modulation orders of 8 and 16 are suggested. The S-Walsh approach is more robust to MUI but has a higher computational complexity. It is more appropriate to use $M \geq 32$ in the applications with $R_b > 120$ kbps.

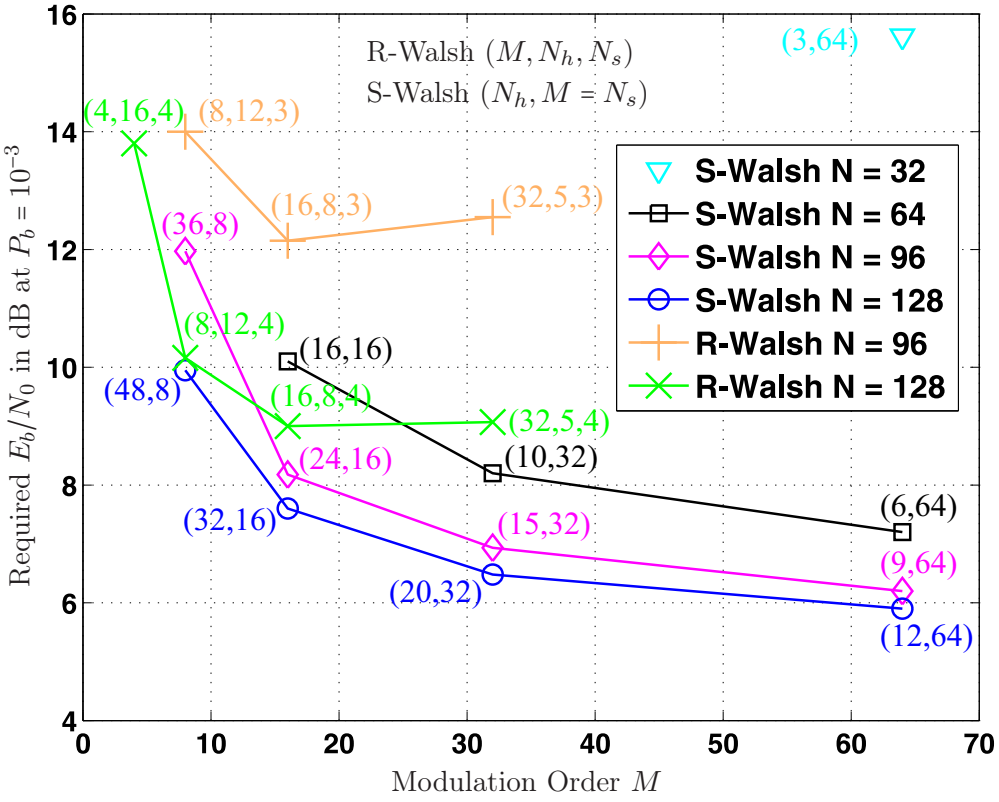

Fig. 6.31: The required E_b/N_0 in dB of both R-Walsh and S-Walsh schemes at $P_b = 10^{-3}$ using different signaling parameters in AWGN.

Tab. 6.8: Comparison of R-Walsh and S-Walsh

	R-Walsh	S-Walsh
MUI Robustness	–	+
Data Rate	30-180 kbps	60-250 kbps
Modulation Order M	8 or 16	≥ 32
Complexity	lower	higher

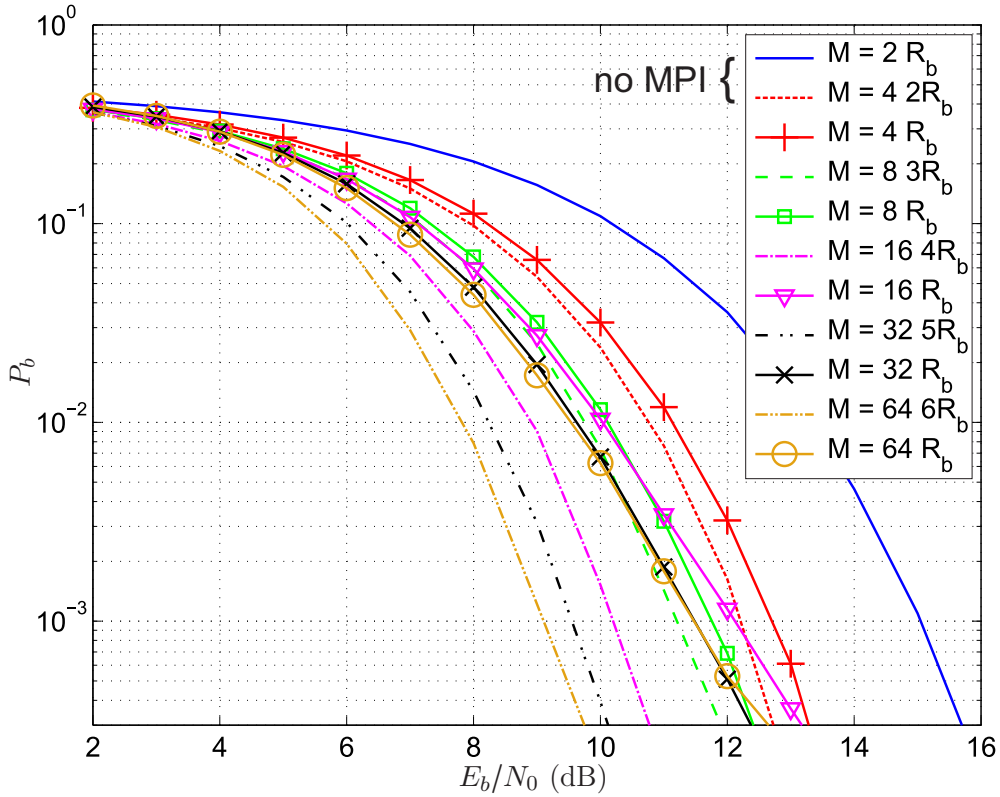

Fig. 6.32: BER versus E_b/N_0 (dB) in the presence of multipath-induced interference (MPI) for M-ary R-Walsh in the single-user case. The maximum channel excess delay is $\tau_{\max} = 128$ ns and the integration window for SinW-C is chosen as $T_{\mathrm{i}} = 32$ ns. The TH code is $N_h = 1, N_s = 1$.

6.8 A One-Bit Sigma-Delta Analog-to-Digital Converter based Non-Coherent Receiver

6.8.1 Introduction

As we discussed before, the concept of applying fully digital solutions to non-coherent UWB receivers becomes quite promising [HSA05, TXS07, FM07]. Such digital receivers are based on high-speed but very low-resolution ADCs. One major attraction is that the broadband analog delays which are required in some preprocessing schemes can be avoided [TGM06, DM05]. Digital receivers can also facilitate flexible designs of various signal processing algorithms. Compared to the analog counterpart, their robustness to the noise as well as to the interference can also be enhanced (cf. Section 6.4).

A key component in the digital receiver is the ADC. The power dissipation (in Watt) of an ideal ADC can be estimated by $P_{\mathrm{ADC}} = \gamma \cdot f_s \cdot 2^{2b}$, where f_s is the sampling rate, b is the ADC resolution, and γ is a constant [LRRB05]. To maintain a low power consumption, one idea is to apply the Nyquist sampling rate ADC with a very limited resolution [HSA05, TXS07, FM07], as we have investigated in previous sections. Performance improvements can be achieved by a larger b but require the automatic gain control [Nam01].

Nevertheless, since the power dissipation increases linearly with f_s while exponentially with b, oversampling seems more promising than increasing the the resolution. Compared to the Nyquist rate ADCs, the $\Sigma\Delta$ ADCs which employ both oversampling and noise shaping can enhance the signal-to-noise ratio [AS96]. The stringent requirements on the sampling clock synchronization can also be alleviated by the oversampling [Gra87]. The rapid advances in nm-CMOS technology have shown the availability and potential of implementing the high-speed $\Sigma\Delta$ ADCs [BBM08]. Only in [HSA05], a one-bit oversampling $\Sigma\Delta$ ADC is analyzed for a non-coherent UWB system based on the transmitted-reference signaling scheme. However, it has not been investigated but of great interest is how to characterize the quantization loss due to the $\Sigma\Delta$ ADCs as well as their impact on the modulation schemes and signaling parameters.

In this section, we propose a digital non-coherent detector based on a one-bit oversampling $\Sigma\Delta$ ADC for low data rate TH UWB communication systems, where both M-ary PPM and M-ary Walsh modulation schemes are investigated. By deriving the BER bounds, we discuss the quantization effect of the $\Sigma\Delta$ ADCs in conjunction with modulation schemes and signaling parameters on the receiver performance. Finally, a generalized system design rule is suggested for low-power and low-complexity non-coherent UWB communications.

6.8.2 System Description

6.8.2.1 Signal Model and Digital Non-Coherent Receiver

The block diagram of the proposed digital non-coherent receiver is shown in Figure 6.33(a). We employ a ΣΔ ADC after the receive filter to obtain the received samples. The block diagram of the first-order ΣΔ ADC and its equivalent one-bit model are depicted in Figure 6.33(b)(c). Then a digital code matched filter that is matched to the TH code is applied before the demodulation and the non-coherent detector. The major advantage is that it coherently combines part of the signal energy that is spread by the TH code at the transmitter and restricts the non-coherent combining only to the multipath arrivals. The M-ary demodulation and the non-coherent detection are performed afterwards with respect to the m-th branch, which is similarly illustrated in Figure 6.22(c).

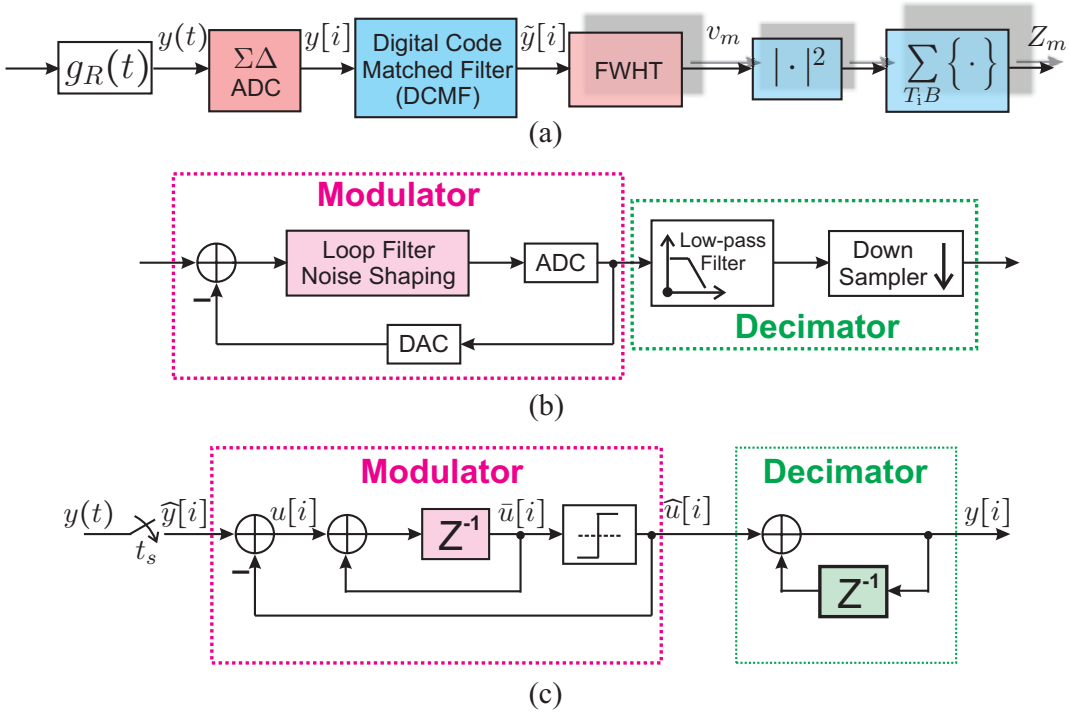

Fig. 6.33: (a) The proposed digital non-coherent receiver using a ΣΔ ADC (in complex baseband). (b) Block diagram of the first-order ΣΔ ADC. (c) Equivalent model of the first-order one-bit ΣΔ ADC [Gra87].

We consider two M-ary modulation schemes, i.e., PPM and R-Walsh [7], for a TH UWB system. In both cases, the received signal for the m-th symbol after the pulse matched filter $g_R(t)$ is given by equation (6.34), where the ν-th element of the m-th modulation sequence $\boldsymbol{w}_m = [w_{m,0}, \ldots, w_{m,M-1}]^T$ is denoted by $w_{m,\nu}$. For the Walsh modulation, $w_{m,\nu} \in \{\pm 1/\sqrt{M}\}$ and $\boldsymbol{w}_m$ is the Walsh Hadamard code. For PPM, $w_{m,\nu} \in \{0, 1\}$ and $\boldsymbol{w}_m$ contains only a single "1" that determines the pulse position.

[7] In this section, only the R-Walsh is employed and we simply denote it as Walsh during this section.

The output of the ΣΔ ADC is denoted as $y[i]$. After the code matched filter, the sample for one symbol can be written as $\tilde{y}[l,\nu] = \frac{1}{\sqrt{N_s}} \sum_{i=1}^{N_s} y[l,\nu,i], l \in \mathfrak{L}_\mathrm{i}, \nu \in \{0,1,\ldots,M-1\}$, where $\mathfrak{L}_\mathrm{i}$ represents the set of L_i taps included in the integration window. The demodulator consists of parallel correlators each of which corresponds to the code sequence $\boldsymbol{w}_m$. The resulting sample at the m-th branch is expressed as $v_m[l] = \sum_{\nu=1}^{M} \tilde{y}[l,\nu] w_{m,\nu}$. Alternatively, in the case of Walsh modulation, a FWHT can be applied, which has a lower complexity than using correlator banks [Kam96]. The decision variable is obtained after the digital non-coherent multipath combining as $Z_m = \boldsymbol{v}_m^H \boldsymbol{v}_m, \boldsymbol{v}_m = [v_m[0], v_m[1], \ldots, v_m[L_\mathrm{i}-1]]^T$ and the decision is made according to $\max_{0 \le m \le M-1} \{Z_m\}$.

6.8.2.2 First-Order One-Bit Sigma-Delta ADC

Figure 6.33(b) illustrates the model of the simplest first-order one-bit ΣΔ ADC, including a ΣΔ modulator followed by a digital decimator. The ΣΔ modulator consists of a noise shaping filter, an ADC, and a Digital-to-Analog Converter (DAC) used in a feedback loop. Let us define the oversampling rate as $N_{os} = 1/(t_s B)$, where $1/t_s$ is the sampling frequency and the Nyquist sampling rate equals to the total signal bandwidth B. If $N_{os} > 1$, the continuous-time signal $y(t)$ is oversampled. Oversampling spreads the quantization noise power over a bandwidth larger than the signal band. The resulting samples $\widehat{y}[i]$ go through a noise shaping filter, which further attenuates the in-band quantization noise and amplifies it outside of the signal band. The noise shaping filter can be modeled as an integrator [Gra87]. The out-of-band quantization noise can then be filtered out by a low-pass filter. The low-pass filter and the following down sampler compose a decimator, simply modeled by an accumulator (or a comb filter) [Gra87]. We consider the simplest one-bit ΣΔ ADC (c.f. Figure 6.33(c)). Thus, the one-bit DAC can be removed since for the output of the one-bit ADC, $\widehat{u}[i] \in \{\pm 1\}$ holds.

The oversampled signal is written as

$$\widehat{y}_p[l,\nu,i] = \sqrt{\frac{E_s}{N_s}} \widehat{\alpha}_{l,p}[i] w_{m,\nu}[i] + n_p[i], p \in \{R, I\}, \tag{6.53}$$

where $\widehat{\alpha}_{l,p}[i] = \alpha_{l,p} \tilde{g}(it_s - l/B), n_p[i] = n_p(it_s)$, and R, I stand for the real and imaginary parts of the signal. For convenient analysis, we drop the indices p, l, ν of $\widehat{y}$. According to Figure 6.33(b), we obtain the following expressions for either R or I samples as

$$\begin{aligned} \bar{u}[i] &= \widehat{y}[i-1] + \bar{u}[i-1] - \widehat{u}[i-1], \qquad \bar{u}[i] = \mathrm{sign}\{\widehat{u}[i]\} \\ &= \widehat{y}[i-1] - q[i-1], \end{aligned} \tag{6.54}$$

where $q[i] = \widehat{u}[i] - \bar{u}[i]$ is the quantization noise. Consequently, the ΣΔ modulated signal $\widehat{u}[i]$ can be written as

$$\widehat{u}[i] = \widehat{y}[i-1] + q[i] - q[i-1]. \tag{6.55}$$

The output of the ΣΔ ADC is calculated as $y[i] = \frac{1}{\sqrt{N_{os}}} \sum_{n=1}^{N_{os}} \widehat{u}[i-n]$.

6.8.3 Bit Error Rate Analysis for One-Bit ΣΔ ADC-based Non-Coherent Receiver

In this section, we derive the BER bounds for the one-bit ΣΔ ADC-based non-coherent detector in the single-user case, where no multipath-induced interference is assumed. According to the analysis in Section 6.7.2.2, we can use equations (6.42) and (6.43) to obtain the BER bound of the M-ary orthogonal modulation schemes (PPM/Walsh).

Performance using the One-Bit ΣΔ ADC

Let us assume the symbol with $m = 0$ is the desired signal and rewrite the decision variable for $M = 2$ as

$$Z_m = \sum_{p\in\{R,I\}} \sum_{l\in\mathfrak{L}_i} |v_{m,p}[l]|^2, \quad m = \{0,1\}, \tag{6.56}$$

where

$$v_{m,p}[l] = \sum_{\nu=1}^{M} \underbrace{\left(\sum_{i=1}^{N_s} \underbrace{\frac{1}{\sqrt{N_{os}}} \sum_{n=1}^{N_{os}} \widehat{u}_{m,p}[l,\nu,i-n]}_{y_{p[l,\nu,i]}} \right)}_{\tilde{y}[l,\nu]} w_{m,\nu}. \tag{6.57}$$

The statistical distribution of $v_{m,p}[l]$ is required to calculate P_2 which is shown in equation (6.42).

Without loss of generality, we assume that the quantization noise $q[i]$ of the ΣΔ ADC is uncorrelated and white with covariance $\frac{d^2\pi^2}{36N_{os}^3}$, where d is the quantization step size and $d = 2$ for the one-bit quantization [AS96]. The output of the ΣΔ modulator $\widehat{u}_{0,p}[i]$ described in (6.55) takes values in $\{-1,+1\}$ with the corresponding probability p_l and $1-p_l$, where the probability of $\widehat{u}_{0,p}[i]$ being -1 can be approximated by

$$p_l \approx \frac{1}{N_{os}} \sum_{n=1}^{N_{os}} p_l[n] \tag{6.58}$$

with

$$p_l[n] \approx \mathrm{Q}\left(\sqrt{\frac{E_s \tilde{\Omega}_l(n)}{kN_s\left(\tilde{N}_0(n) + \frac{2\pi^2}{9N_{os}^3}\right)}} \right), \tag{6.59}$$

with $k = 1$ for PPM and $k = M$ for Walsh. Specifically, we have the statistics of the oversampled channel and the noise determined by $\tilde{\Omega}_l(n) = \mathbb{E}\left\{|\alpha_l|^2 \tilde{g}(t)\tilde{g}(t-nt_s)\right\}$ and $\tilde{N}_0(n) = N_0\mathbb{E}\{g(t)g(t-nt_s)\}$, respectively. For PPM, the oversampled signal $\widehat{y}_p[l,\nu,i]$ contains only AWGN and thus $\widehat{u}_{1,p}[i] \in \{\pm 1\}$ have an equal probability of 0.5. In contrast, for Walsh, the sample $\widehat{u}_{1,p}[i]$ which takes values in $\{\pm 1\}$ has the same probability as $\widehat{u}_{0,p}[i]$.

In the case of PPM, if $N_s N_{os}$ is large, according to the central limit theorem $v_{m,p}[l]$ is approximated by Gaussian distributions with mean $\sqrt{N_s N_{os}}(1-2p_l)$ for $m=0$ (and 0 for $m=1$) and variance 1 (for $m=0,1$). Therefore, Z_0 and Z_1 are the sum of L_i non-central and central χ^2-distributed random variables each with 2 degrees of freedom, respectively. From equation (6.42), P_2 can be analyzed by

$$\begin{aligned}\mathbb{E}\{Z\} &= (N_s N_{os}-1)\sum_{l\in\mathfrak{L}_\mathrm{i}}(1-2p_l)^2 \\ \mathbb{V}\{Z\} &= (1-2N_s N_{os})\sum_{l\in\mathfrak{L}_\mathrm{i}}(1-2p_l)^4 + 2(N_s N_{os}-1)\sum_{l\in\mathfrak{L}_\mathrm{i}}(1-2p_l)^2 + 2L_\mathrm{i}. \end{aligned} \quad (6.60)$$

When M gets larger, p_l decreases.

Similarly, in the case of Walsh if MN_sN_{os} is large, $v_{m,p}[l]$ is approximately Gaussian distributed with mean $\sqrt{MN_sN_{os}}(1-2p_l)$ for $m=0$ (and 0 for $m=1$) and variance $4p_l(1-p_l)$ (for $m=0,1$). We can estimate P_2 shown in equation (6.42) by

$$\begin{aligned}\mathbb{E}\{Z\} &= MN_sN_{os}\sum_{l\in\mathfrak{L}_\mathrm{i}}(1-2p_l)^2 \\ \mathbb{V}\{Z\} &= 2(1-MN_sN_{os})\sum_{l\in\mathfrak{L}_\mathrm{i}}(1-2p_l)^4 + (2MN_sN_{os}-1)\sum_{l\in\mathfrak{L}_\mathrm{i}}(1-2p_l)^2 + 2L_\mathrm{i}. \end{aligned} \quad (6.61)$$

In contrast to the case of M-PPM, by increasing M and/or N_s, p_l also increases, which influences P_2 accordingly.

6.8.4 Simulation Results

In this section, we provide the numerical results to show the effect due to the one-bit ΣΔ ADC on the digital non-coherent receiver using both the M-PPM and M-Walsh schemes. The transmitted pulse $g(t)$ is the RRC pulse and assumed to have a roll-off factor $\beta=0.3$ and the bandwidth $B_3=500$ MHz. we use the UWB channels measured in the NLOS scenario (cf. Chapter 2). The corresponding maximum channel excess delay is 128 ns and the time resolution of the channel tap is 1 ns. The integration window for non-coherent detection of length 32 ns is chosen.

Figure 6.34 depicts the simulation results to validate the derived BER bounds of TH M-PPM/M-Walsh schemes using the one-bit ΣΔ ADC-based non-coherent detector in the single-user case, where the full-resolution performance is also included as a reference. We can observe that the BER bound is quite close to the simulated performance for a large E_b/N_0 [8]. The results show that with $N_{os}=4$ a significant performance improvement can be achieved and almost no further gain can be made with $N_{os}=5$. For the case in Figure 6.34, the M-Walsh outperforms the M-PPM, which is due to the different quantization effect of the one-bit ΣΔ ADC on modulation schemes.

[8] When $M>2$ for the low E_b/N_0, the inaccuracy of the analytical results is due to the approximation shown in the upper bound (6.43).

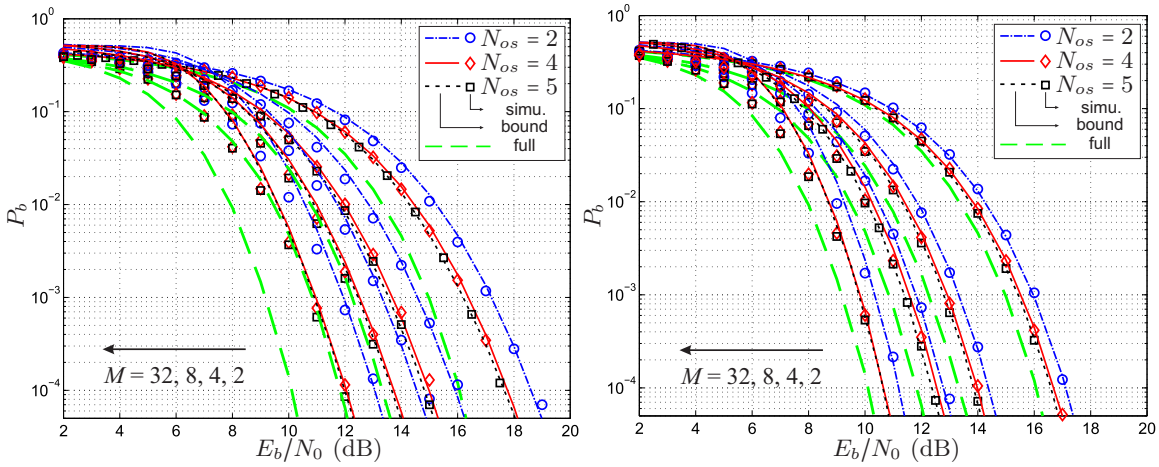

(a) M-PPM with $N_s = 2$ (b) M-PPM with $N_s = 6$

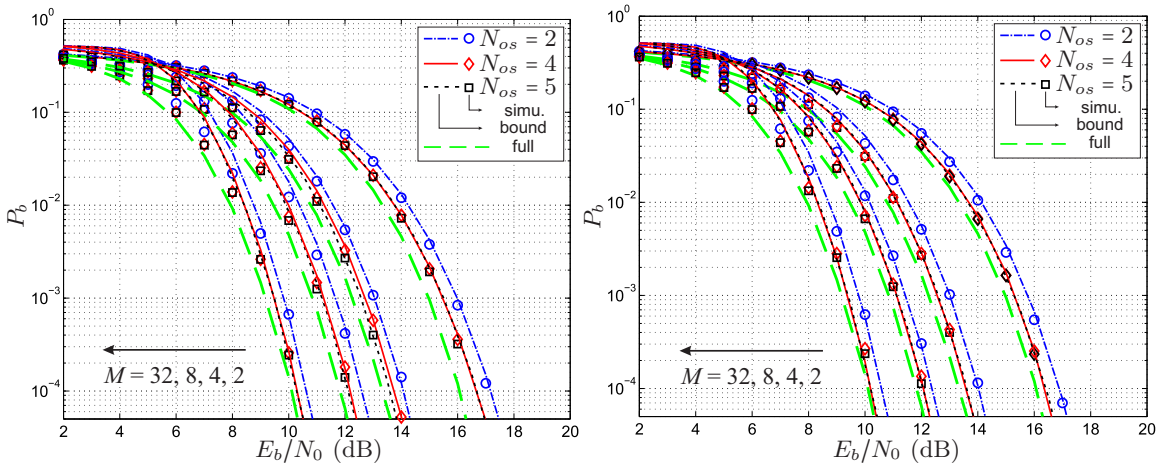

(c) M-Walsh with $N_s = 2$ (d) M-Walsh with $N_s = 6$

Fig. 6.34: Validation of the BER bounds for M-PPM and M-Walsh using non-coherent detection in multipath. The integration window $T_{\text{i}} = 32$ ns.

As shown in (6.60) and (6.61), the BER performance depends on the number of repetitions N_s. According to the analytical performance bound, the quantization loss due to the one-bit ΣΔ ADC at BER = 10^{-3} is plotted as a function of the number of repetitions N_s in Figure 6.35 for M-PPM and M-Walsh, where different oversampling rates are considered. The following observations can be made.

- From Figure 6.35(a) with $N_{os} = 2$, for a small N_s (e.g., $N_s < 10$), M-PPM exhibits a higher quantization loss compared to M-Walsh and the loss increases as M becomes larger. In contrast to this, the loss of M-Walsh does not vary much with N_s and increasing M leads to a better performance. The advantage of M-Walsh can be interpreted by the correlation characteristics of the Walsh codes (cf. Section 6.7.2.3). The output samples of the one-bit ΣΔ ADC are linearly combined and demodulated by the bipolar Walsh codes in a maximum likelihood sense, which actually decreases the variance of the resulting signal. The M-PPM sequence only consists of a single "1" and the other code bits are "0". Thereby, its decoding performance is much worse than that of the

Walsh sequence. For the case of $N_{os} = 4$ shown in Figure 6.35(b), it also shows that M-Walsh is more robust to the quantization than M-PPM.

- With the oversampling rate of $N_{os} = 4$ (cf. Figure 6.35(b)), the performance is just $0.2 - 0.3$ dB away from the full-resolution case. To approach the full-resolution performance, M-Walsh only needs to satisfy either $N_s < 10$ or $M \geq 8$ while for M-PPM a larger number of pulse repetitions is required (e.g., $N_s \geq 30$) at the expense of a higher computational complexity.

6.8.5 Discussions

This section considers a digital energy detector based on a one-bit ΣΔ ADC, where TH M-ary PPM and TH M-ary Walsh modulation are employed. We characterize the quantization loss due to such ADCs as well as evaluate their impact on the selection of the modulation schemes and the signaling parameters. The analysis indicates that with a ΣΔ ADC, the TH M-Walsh modulation is much more robust against the quantization loss than the TH M-PPM. With an oversampling rate of 4, the quantization loss can be only $0.2 - 0.3$ dB at BER $= 10^{-3}$. However, to approach the full-resolution performance, a sufficient number of pulse repetitions, e.g., $N_s \geq 30$, is required for the TH M-PPM.

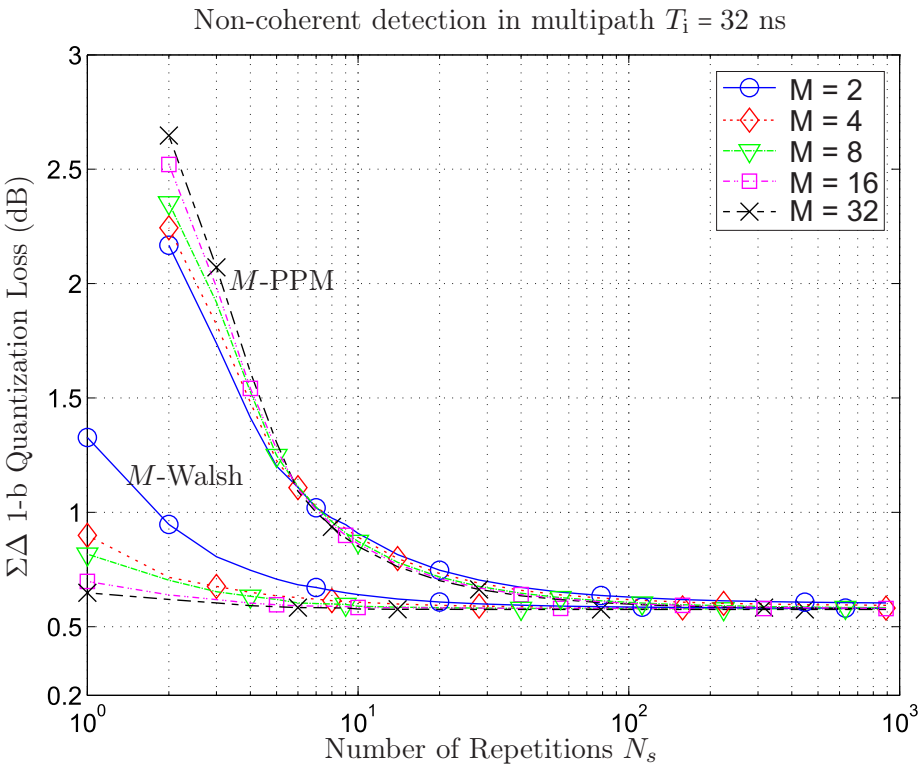

(a) N_{os} = 2

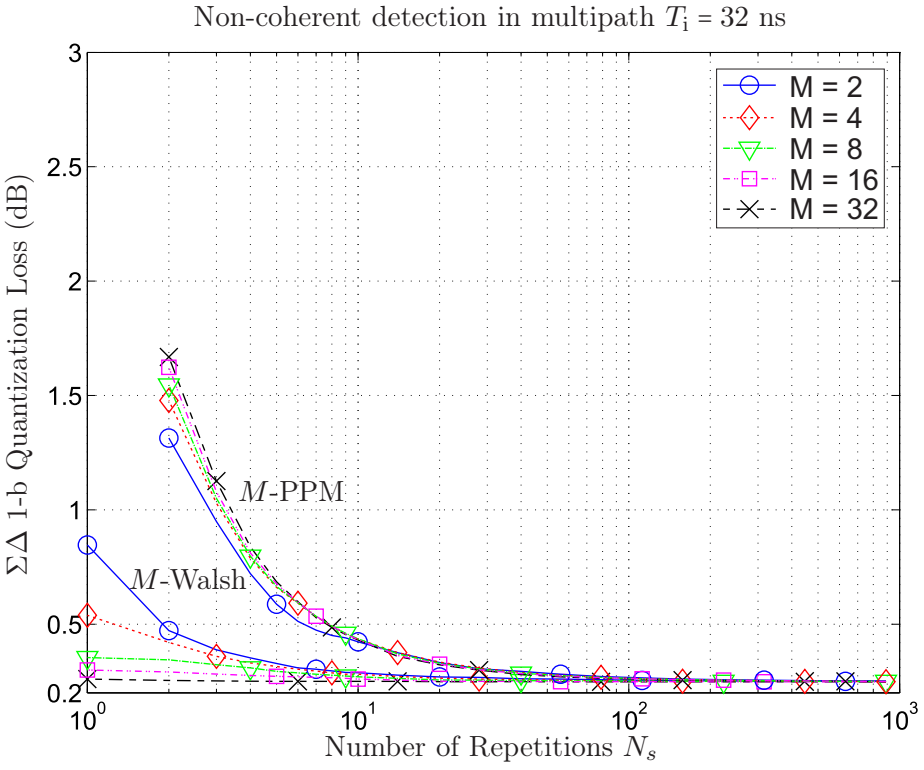

(b) N_{os} = 4

Fig. 6.35: Quantization loss due to the 1-bit ΣΔ ADC versus the number of repetitions N_s at BER = 10^{-3}.

6.9 Summary and Discussions

This chapter presents some of the most important achievements of our work, i.e., the fully ***digital*** solutions for non-coherent UWB communication systems. We summarize the key results of this chapter as follows.

Digital Solutions:

In this section, we propose a Digital Code Matched Filter (DCMF)-based non-coherent receiver for Time Hopping (TH)-UWB communications. It is based on a high-speed but very-low resolution time-domain Analog-to-Digital Converter (ADC), taking advantage of the trade-off between the sampling rate and the number of bits per sample (or resolution). The major advantages (A1-A3) of using such ***digital*** solutions are given.

A1 The DCMF, which coherently decodes the user-specific code, follows after the ADC. It restricts the non-coherent combining only to the multipath arrivals in the fully digital domain. In this sense, as compared to the analog counterpart, the code-induced Non-Coherent Combining Loss (NC-CL) is completely removed.

A2 Due to the coherent decoding of the user-specific code, the proposed digital receiver shows a higher robustness against Multi-User Interference (MUI) and Inter-/Intra-Symbol Interference (ISI) than the analog receiver.

A3 Since the non-coherent combining is performed digitally, it overcomes the difficulty of implementing long analog delay lines and makes differential UWB receivers possible. The completely digital implementations also facilitate the development of other digital signal processing techniques such as multi-user detection, interference suppression, equalization, etc..

Quantization Effect

We analyze the quantization loss due to both the b-bit Nyquist rate ADC as well as the one-bit Sigma-Delta ($\Sigma\Delta$) ADC. The main conclusions (C1-C3) are summarized.

C1 **1-bit Nyquist rate ADC:** The quantization loss due to the one-bit Nyquist rate ADC at a BER = 10^{-3} for the TH Binary Pulse Position Modulation (2-PPM) using non-coherent detection is only $1.5 - 2$ dB, if the number of pulse repetitions $N_s \geq 8$.

C2 **b-bit Nyquist rate ADC ($b > 1$):** With $b = 2$ a great performance improvement can be achieved and the full-resolution performance can almost be approached when $b = 4$. In the b-bit case ($b > 1$), an appropriate gain G of the ADC is required to adjust the input signal level.

C3 **1-bit $\Sigma\Delta$ ADC:** With the oversampling rate of $N_{os} = 4$, the resulting performance at a BER = 10^{-3} for both the TH M-Pulse Position Modulation (PPM) and the TH M-Walsh can be only $0.2 - 0.3$ dB away from the full-resolution case.

Multiple Access Performance

C4 **TH 2-PPM:** The proposed digital receiver exhibits a better performance than its analog counterpart in the presence of MUI, even with a one-bit ADC. Under near-far conditions, the one-bit receiver can effectively suppress the strong MUI due to its hard-clipping operation, outperforming the b-bit ($b > 1$) case.

C5 **Simultaneously Operating Piconets (Simultaneously Operating Piconets (SOP)):** In accordance with C4, the SOP analysis shows that the one-bit receiver provides a much higher capability of separating piconets than both the full-resolution and the analog ones.

System Design Rule

A system design rule, in terms of the selection of the signaling parameters as well as the modulation schemes, is proposed for the TH UWB systems using digital non-coherent detection. The conclusions (C6-C8) are listed as follows.

C6 **TH M-PPM:** To ensure a smaller loss arising from both MUI and quantization, the selection of TH parameters should follow that, for a fixed length of the TH code

- the number of pulse repetitions N_s and the number of hopping positions N_h should be not be small and
- $N_h \approx N_s$ with N_h is slightly larger than N_s.

When the length of the TH code $L_m = N_s N_h$ gets larger, the multiple access performance becomes better. The TH M-PPM has a higher Peak-to-Average Power Ratio (PAPR) and a sufficiently large number of pulse repetitions N_s is required, e.g., with $N_{os} = 4$ for the one-bit $\Sigma\Delta$ ADC, $N_s \geq 30$ should hold to approach the full-resolution performance.

C7 **TH M-Walsh:** As compared to M-PPM, M-Walsh is more robust to the quantization loss without any strict requirements on N_s and/or M ($M > 2$). The TH selection follows that N_h should not be small and $N_h > N_s, N_s > 2$. With the same TH parameters, its multiple access performance is better with perfect power control but PPM shows a higher near-far resistance especially using one-bit ADCs. The receiver implementation of the TH M-Walsh, which is based on the Fast Walsh Hadamard Transformation (FWHT), is more efficient than M-PPM.

C8 **R-Walsh and S-Walsh:** The TH Repeated Walsh (R-Walsh) is more suitable with $M = 8$ or 16 in the applications where $R_b < 180$ kbps. The TH Spread Walsh (S-Walsh) shows a great advantage with $M \geq 32$ and is more appropriate to be applied in the case of $R_b > 120$ kbps.

NBI using Soft Limiter

Due to the effectiveness of the soft limiter in suppressing the impulsive noise, the proposed Narrowband Interference (NBI) suppression scheme applies the soft limiter in a feedforward structure to "isolate" the NBI from the "suppressed" impulsive TH-PPM signal. The NBI suppression is performed before the ADC of the digital non-coherent receiver. It is shown that

C9 the soft limiter can effectively mitigate the strong NBI by appropriately choosing the threshold factor and outperforms its hard limiter counterpart. In the case of the strong Orthogonal Frequency Division Multiplexing (OFDM) interference, the soft limiter threshold can be adapted in a block-by-block fashion to provide a higher NBI suppression capability.

To summarize, the proposed DCMF-based non-coherent receiver is able to approach the full-resolution performance with either a very low ADC resolution $b = 4$ or a slightly higher oversampling rate $N_{os} = 4$. It also shows a significantly improved performance in the presence of MUI as compared to its analog counterpart. Especially, the simplest one-bit receiver is near-far resistant. Advanced modulation schemes, e.g., TH M-Walsh, are quite suitable for such UWB systems in order to further increase the power efficiency.

7. LOW-COMPLEXITY FREQUENCY HOPPING ULTRA WIDEBAND SYSTEM

7.1 Introduction

As elaborated in Section 4.2, the Non-Coherent Combining Loss (NC-CL) is determined by the product of the integration interval and the signal bandwidth $T_{\mathrm{i}}B$. Besides the reduction of T_{i}, the NC-CL can also be reduced by decreasing the signal bandwidth B. However, the decrease in B leads to a lower fading resistance at the receiver input, which increases the required fading margin [WGH05]. Therefore, it is of key importance to choose an "appropriate" value for B which guarantees a good trade-off between the fading resistance and the NC-CL. The goal of Section 7.2 is to find an appropriate bandwidth that ensures a reliable non-coherent UWB system for a given BER, so that the required E_b/N_0 is the lowest. Section 7.2.1 analyzes the robustness of UWB signals to the small scale fading. To evaluate the system performance, in Section 7.2.2 we employ the fading margin calculation [MGS+08] for non-coherent UWB systems instead of using the averaged BER analysis, which requires the exact distribution of the channel gains.

Defined by the FCC in 2002 [Fed02], an UWB signal should have a bandwidth of at least 500 MHz. With the UWB regulation changing and being modified [FCC05, ECC07, Com08], various UWB techniques can be flexibly utilized. Multi-Band Orthogonal Frequency Division Multiplexing (MB-OFDM) [Bat01] and Direct Sequence (DS)-UWB [OSR+04] are designed for high data rate communications, whereas the IEEE 802.15.4a UWB physical layer specifies a Time Hopping (TH) Impulse Radio (IR) UWB system for low data rate wireless sensor networks. Other techniques such as chirp and Frequency Hopping (FH)-DS [IHQ04, Eur06] are also appealing alternatives for UWB communications. According to the results on the useful bandwidths in Section 7.2, Section 7.3 proposes a novel UWB system concept based on the FH technique. The major advantage is that the baseband bandwidth can be reduced to values that are much lower than 500 MHz. This opens up new opportunities for power efficient transceivers. Section 7.3.2 analyzes the impact of the bandwidth on the BER performance of a low-complexity FH-Pulse Position Modulation (PPM) scheme. The summary of this chapter and the future perspectives on the generic FH-UWB system are provided in Section 7.4.

7.2 Bandwidth Selection for Non-Coherent Ultra Wideband Systems

7.2.1 Robustness to the Small Scale Fading

We represent the impulse response of the m-th channel realization $h_m(t)$ with a tapped-delay-line model as in equation (2.3). Given the signal bandwidth B, the Mean Power Gain (MPG) Γ_m of a certain channel realization $h_m(t)$ is defined in [RK03, WGH05] as

$$\Gamma_m = 10\log_{10}\left\{\frac{1}{B}\int_{-B/2}^{+B/2}|H_m(f)|^2\,\mathrm{d}f\right\} = 10\log_{10}\left\{\frac{1}{B^2}\sum_{l=0}^{L-1}\left|h_m(l\cdot\frac{1}{B})\right|^2\right\} \quad \text{(dB)}, \tag{7.1}$$

where $H_m(f)$ denotes the complex transfer function of $h_m(t)$. The MPG describes the maximum received energy $E_{\mathrm{rx}} = E_{\mathrm{tx}} + \Gamma_m$ (in dB) for a single transmitted symbol with a total transmit energy E_{tx} uniformly distributed in $[f_c - B/2, f_c + B/2]$. It is proportional to the received signal power and thus can be used to evaluate the error performance. The MPG is able to measure the signal quality. Figure 7.1 shows the MPG of a signal with $B = 50$ MHz and 500 MHz at the center frequency $f_c = 4$ GHz as a function of the receiver positions. The channels are calculated based on the measurement data in the Non-Line-Of-Sight (NLOS) scenario (cf. Section 2.3). We can observe that when $B = 50$ MHz, the MPG varies significantly, with the difference between the largest and the smallest values of Γ_m being around 22 dB. When $B = 500$ MHz, the variation of the MPG is only 7 dB.

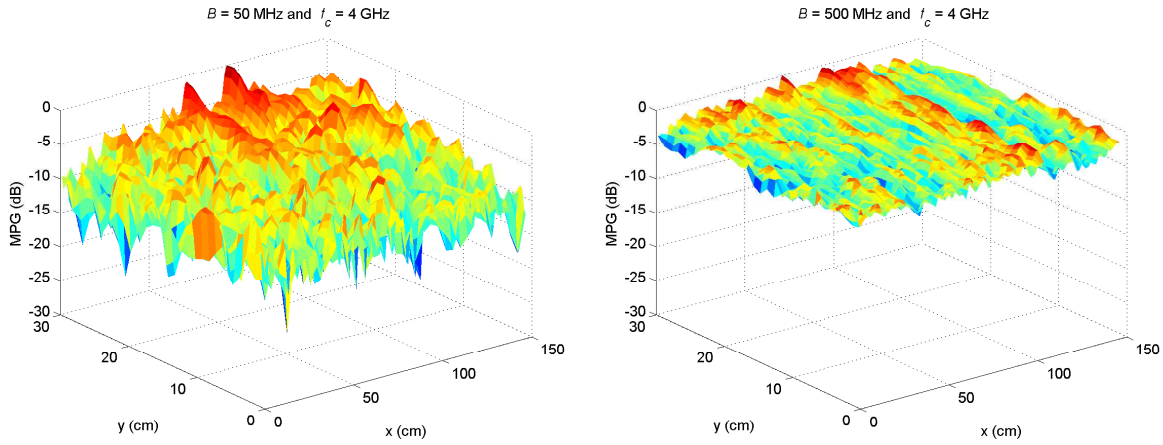

(a) $B = 50$ MHz (b) $B = 500$ MHz

Fig. 7.1: The MPG of signals with $B = 50, 500$ MHz using the IMST measured channels in the NLOS scenario. The receiver positions are represented by x, y in cm.

The smaller the variation of the MPG is, the more robust becomes the signal against the small scale fading. Accordingly, the Cumulative Density Function (CDF) of the MPG can also be related to the signal robustness. This can be revealed by the steepness of the CDF. Figure 7.2 illustrates the CDFs of the MPG for different bandwidths using the measured channels by IMST (office Line-Of-Sight (LOS), office NLOS) and the IEEE 802.15.4a channel model (CM1 residential LOS, CM2 residential NLOS, CM5 outdoor LOS, and CM6 outdoor NLOS) (cf.

Section 2.3). We can observe that by increasing the bandwidth a higher robustness against the small scale fading is achieved.

7.2.2 Fading Margin Analysis

The averaged BER in a multipath fading channel can be computed by averaging over the probability density function of the channel gains (or the fading distribution). However, when the distribution of the received energy is not available or the averaged BER is difficult to obtain, a fading margin analysis [MGS+08] can be employed to evaluate the quality of the system instead of the averaged BER performance. As illustrated in Figure 7.3, the Fading Depth (FD) is defined by

$$\mathrm{FD} = \bar{\Gamma}_m - \Gamma_m, \tag{7.2}$$

where $\bar{\Gamma}_m$ is the average MPG. Since the MPG is proportional to the received energy, the Fading Margin (FM) can be expressed as

$$\mathrm{FM} = \frac{E_b}{N_0} - \frac{E_{\min}}{N_0}, \tag{7.3}$$

where E_b is the received energy per bit and $E_{\min}$ is the minimum received energy required for a certain instantaneous BER, which can be calculated according to equation (4.7) or (4.8). Whether a communication link is available or not is determined according to the following rule:

$$\begin{cases} \text{available}, & \text{if} \quad \mathrm{FD} \le \mathrm{FM} \\ \text{unavailable}, & \text{if} \quad \mathrm{FD} > \mathrm{FM} \end{cases} \tag{7.4}$$

The availability A is then defined as

$$A = \Pr\left\{ \frac{E_b}{N_0} \ge \frac{E_{\min}}{N_0} + \mathrm{FD} \right\}. \tag{7.5}$$

Figure 7.4 shows the CDF of E_b/N_0 in various scenarios. The path loss effect is removed. We assume that no interference is presence. The required E_b/N_0 for a specified availability can be obtained, and the results are summarized in Table 7.1. It can be concluded that at an availability of 99 % and a maximum BER $= 10^{-3}$, a bandwidth $B > 200$ MHz is not desirable for UWB communications using non-coherent detection.

7.3 Frequency Hopping for Ultra Wideband Communications

7.3.1 A Generic FH-UWB System Concept

According to the results from the previous section, a bandwidth of $B > 200$ MHz is NOT desirable for UWB communications based on non-coherent detection. With a smaller bandwidth, the Analog-to-Digital Converter (ADC)s and the corresponding signal processing will perform at a much lower speed. This considerably reduces the power consumption at the receiver. It

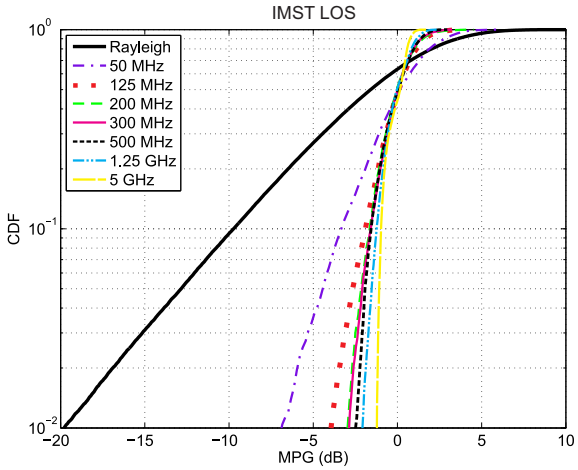

(a) IMST office LOS

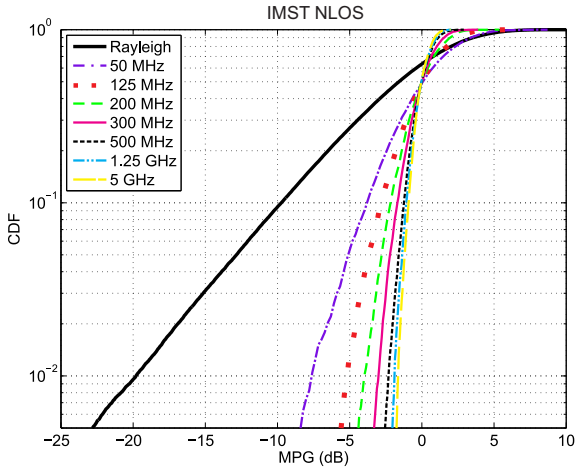

(b) IMST office NLOS

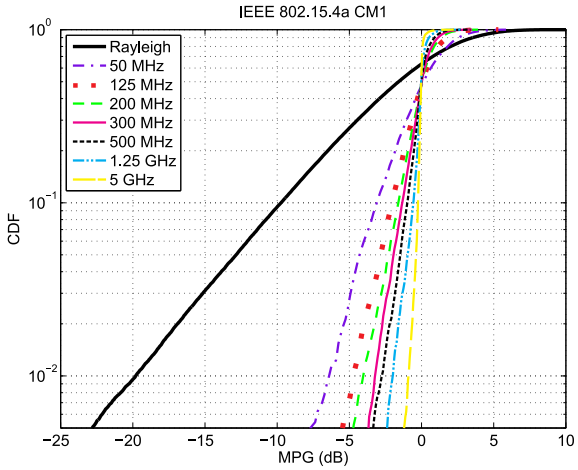

(c) IEEE 802.15.4a CM1

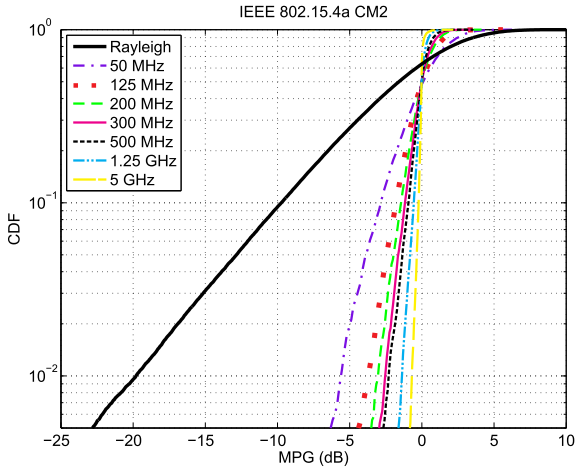

(d) IEEE 802.15.4a CM2

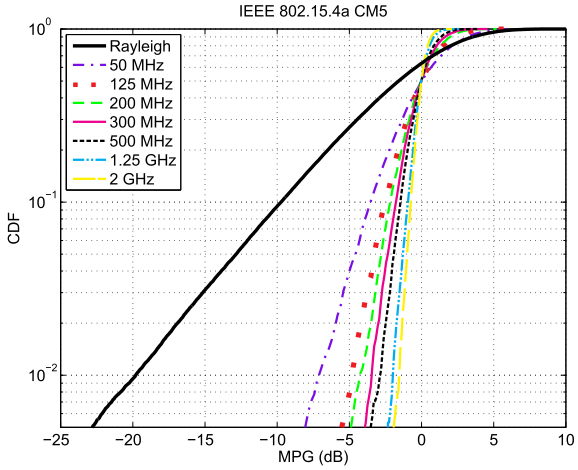

(e) IEEE 802.15.4a CM5

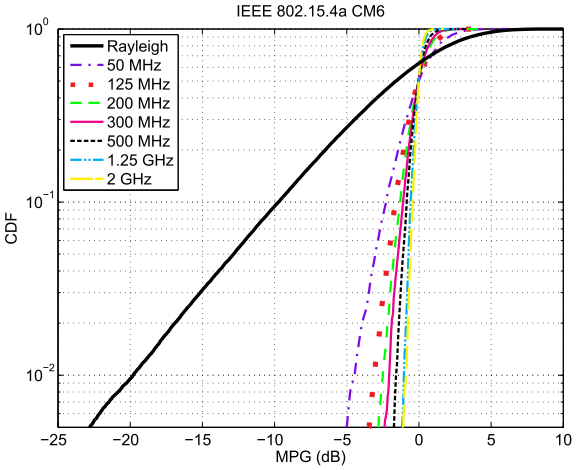

(f) IEEE 802.15.4a CM6

Fig. 7.2: The CDF of the MPG in dB for various bandwidths.

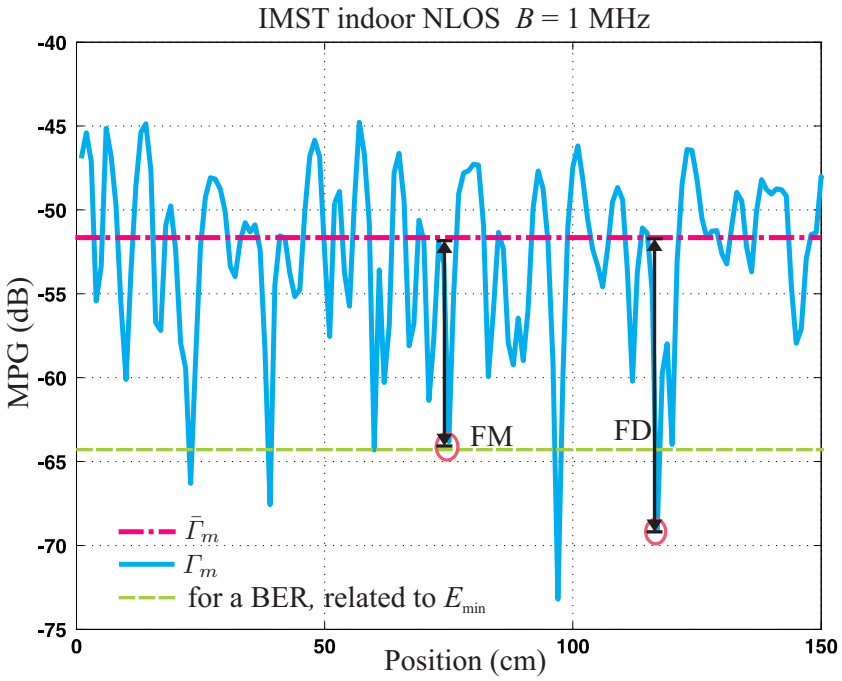

Fig. 7.3: The illustration of the FD and the FM.

Tab. 7.1: Required E_b/N_0 dB of non-coherent detection obtained by fading margin analysis at BER $= 10^{-3}$ and availability $A = 99$ % for various channels

Bandwidth	IMST LOS	IMST NLOS	CM1	CM2	CM5	CM6
5 GHz	18.57	20.22	18.17	19.25	–	–
2 GHz	–	–	–	–	17.46	17.9
1.25 GHz	17.31	18.1	17.15	17.68	17.14	17.29
500 MHz	16.7	**17.25**	16.9	17.08	17.04	16.63
300 MHz	**15.7**	**17.4**	**16.13**	16.98	**16.3**	16.6
200 MHz	**15.3**	**17.7**	**16**	**16.31**	**16.25**	**15.73**
125 MHz	**16**	**17.8**	**16.4**	**16.36**	**16.78**	**15.62**
50 MHz	17.8	19	17.3	17.26	17.05	**15.96**

also facilitates the implementation of the Digital Code Matched Filter (DCMF)-based receiver that relies on the operation at the Nyquist rate.

From the regulation point of view, the FCC waiver in 2005 [FCC05] indicates that the compliance measurement procedure is independent from the techniques that are utilized. It is thus more flexible to design UWB systems subject to a few regulation parameters. If the power spectral density of an UWB emission measured within a maximum average time of 1 ms does not exceed -41.3 dBm/Hz, it is FCC compliant with respect to the average power limit. Our main consideration in the previous chapters is that the UWB waveform is obtained by single-carrier modulation schemes with a bandwidth of at least 500 MHz. With the evolution of the UWB regulations discussed above, this is no longer required.

Therefore, based on the discussions of the useful bandwidth, FH is quite promising to be applied in UWB systems. An illustration of the FH scheme is presented in Figure 7.5. There

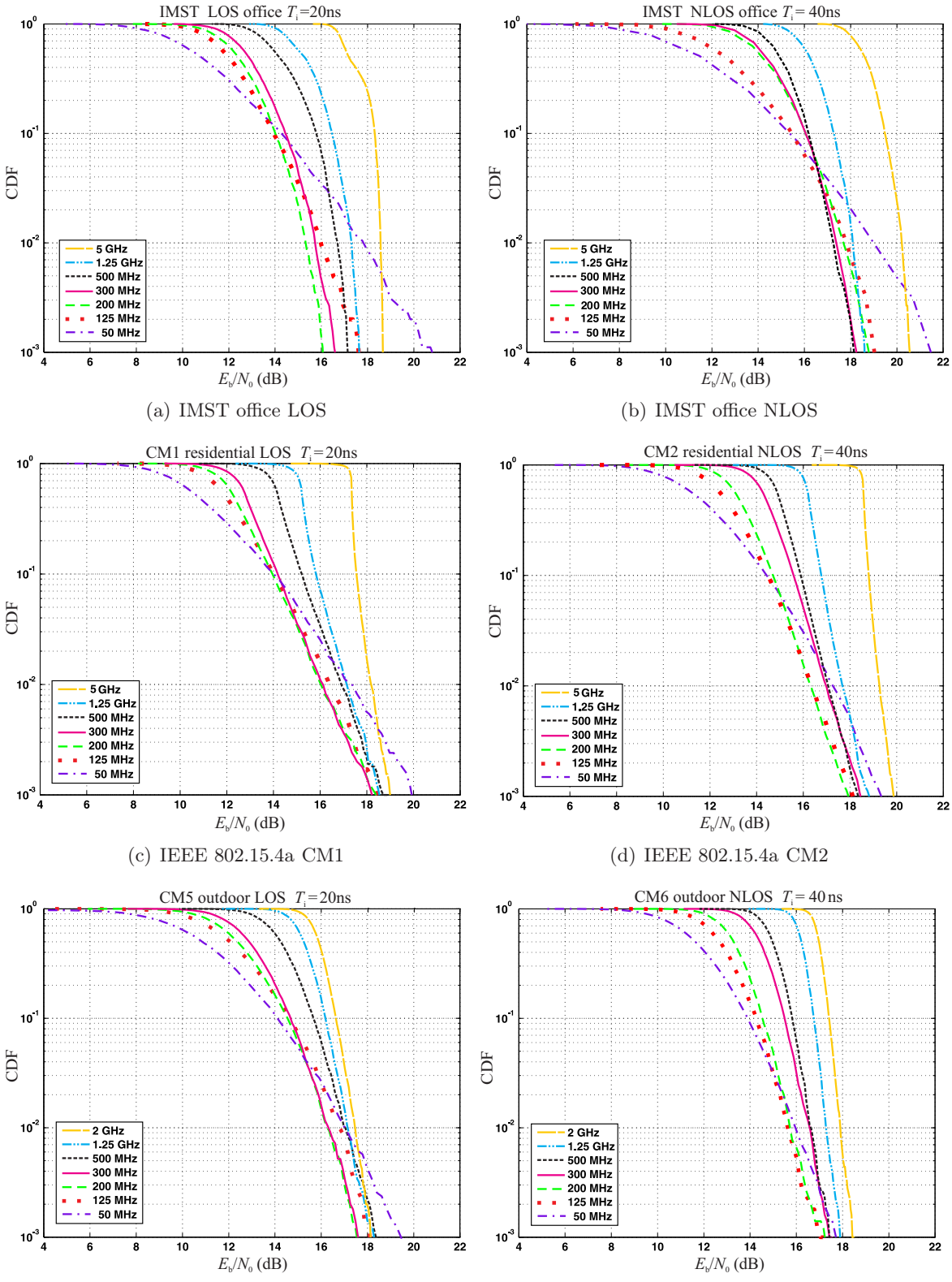

(a) IMST office LOS

(b) IMST office NLOS

(c) IEEE 802.15.4a CM1

(d) IEEE 802.15.4a CM2

(e) IEEE 802.15.4a CM5

(f) IEEE 802.15.4a CM6

Fig. 7.4: The CDF of the required E_b/N_0 (dB) for various bandwidths. The target BER = 10^{-3} and the integration interval T_i is 20 ns for LOS and 40 ns for NLOS, respectively.

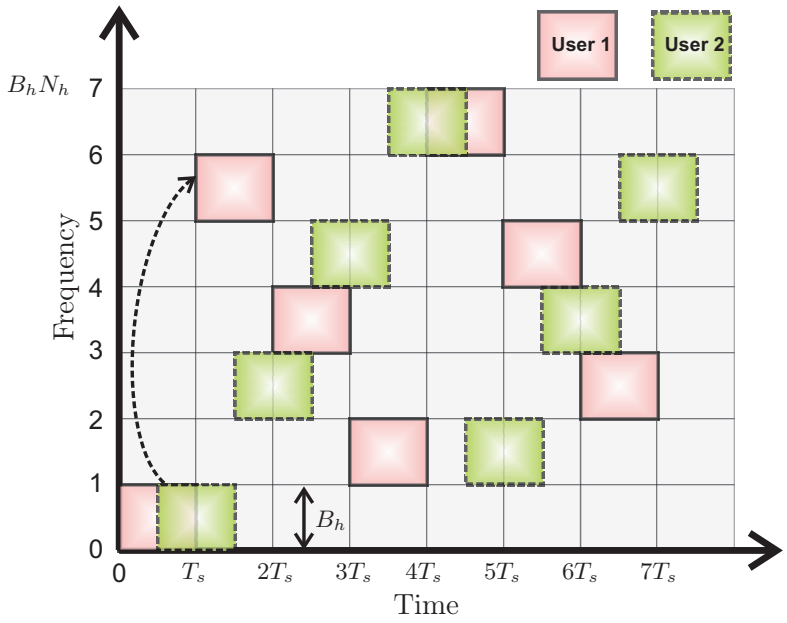

Fig. 7.5: The illustration of the FH scheme for the two-user case. The symbol duration is denoted by T_s.

are N_h non-overlapping channels and the transmit power is determined by the total bandwidth $B = B_h N_h$ covered by all the hops within 1 ms, where B_h is the bandwidth per hop. To meet the UWB requirement, $B \geq 500$ MHz should be satisfied. We propose a FH-UWB system concept, where a non-UWB waveform with a bandwidth $B_h < 500$ MHz represents one data symbol (or a block of symbols) and is modulated on a certain frequency band according to the FH pattern. The block diagram is shown in Figure 7.6. To be specific, a hybrid spreading is utilized in the system concept. Each data symbol is modulated by a Pseudo-Noise (PN) Direct Sequence Spread Spectrum (DSSS) code. This is achieved in the digital domain. The corresponding bandwidth of the waveform $B_h < 500$ MHz. Then the signal is coherently up-converted to N_h frequencies in the analog domain. The total bandwidth $B \geq 500$ MHz is obtained. By changing the number of hops N_h, the per-hop bandwidth B_h varies, leading to different fading situations.

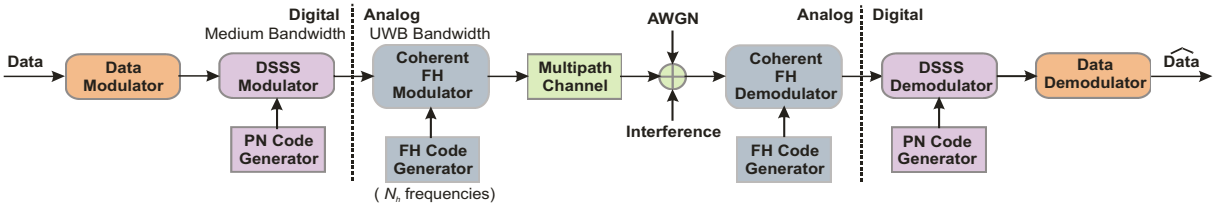

Fig. 7.6: The block diagram of the proposed FH-UWB system.

Several advantages of the FH-UWB system concept can be observed in the following.

- The baseband bandwidth is reduced to the values that are much lower than 500 MHz.

This ensures the ADCs and the fully digital signal processing to operate at a much lower speed, considerably reducing the power consumption. It is suitable for both coherent and non-coherent receivers.

- The system still benefits from the large total bandwidth. In the European project "Emergency Ultrawideband RadiO for Positioning and COMmunications" [Eur06], an UWB FH system using the FH-DS scheme is investigated for the application of indoor personnel tracking. It shows in [IHQ04] that a localization accuracy of 10 cm can be achieved in the free space.
  Assisted by the forward error correction codes, the full frequency diversity can also be exploited.

- It is very flexible to combine FH with other transmission schemes such as DSSS or Orthogonal Frequency Division Multiplexing (OFDM) to support various data rate applications.

- FH promises a very good piconet separation and interference (from non-FH networks) rejection capability.

7.3.2 Frequency Hopping Pulse Position Modulation Scheme

The main purpose of this section is to analyze the impact of the number of hops on the uncoded BER performance of an FH-UWB system, given a fixed total bandwidth.

7.3.2.1 System Description

As an example, we investigate the FH technique combined with PPM for non-coherent detection. The first-stage spreading (DSSS) is neglected for simplicity. The corresponding block diagram is shown in Figure 7.7.

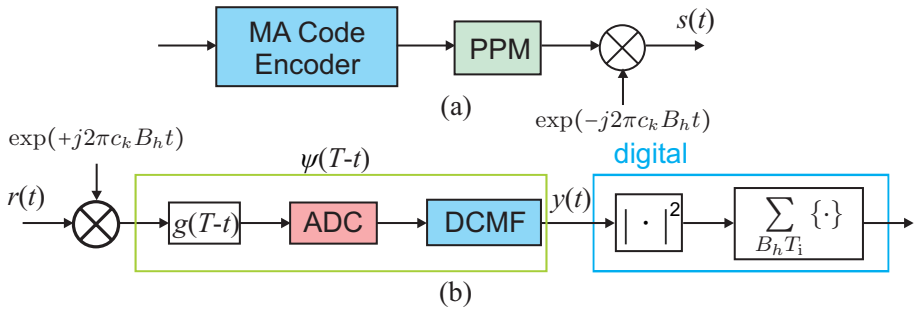

Fig. 7.7: The transmitter (a) and the non-coherent receiver (b) for the FH-PPM system shown in the complex baseband. "MA" is short for multiple access.

For the binary modulation case (FH-Binary Pulse Position Modulation (2-PPM)), the

transmitted signal can be represented by

$$s(t) = \sum_{i=-\infty}^{\infty} \sqrt{E_b}\psi(t - iT_b - \Delta \cdot a_i) \cdot \exp(-j2\pi c_k B_h t), \tag{7.6}$$

where E_b is the energy per bit, $\psi(t)$ is the basis function with unit energy and a bandwidth B_h, $a_i \in \{0,1\}$ is the information bit, T_b is the bit duration, and the modulation index $\Delta = T_b/2$. The FH code is denoted by c_k that takes values in $\{0,1,\cdots,N_h-1\}$, $k = \lfloor t/T_b \rfloor$, and B_h is the bandwidth of each sub-band computed as $B_h = B/N_h$ (B is the total bandwidth of the FH span). The floor operator $\lfloor x \rfloor$ rounds the argument x down to the closest integer that is less and equal to x. The waveform $\psi(t)$ can be either a single pulse $g(t)$ or a burst (or a sequence) of pulses $g(t)$ with polarity scrambling and/or multiple access code encoding [IEE07]. For the latter case, the DCMF-based non-coherent receiver as described in Section 6.2 can be easily implemented.

The received signal after the multipath channel is given by $r(t) = s(t) * h(t) + n(t)$, where, $*$ denotes the convolution operator, $h(t)$ is the UWB channel described in Chapter 2 and $n(t)$ is the Additive White Gaussian Noise (AWGN) with the Power Spectral Density (PSD) N_0. After the down conversion, the signal $y(t)$ will be fed into a filter that is matched to the basis function $\psi(t)$ so that the non-coherent processing is restricted to the multipath combining only. The digital implementation of the matched filter $\psi(T-t)$ as shown in Figure 7.7 consists of a pulse matched filter $g(T-t)$, an ADC, and a DCMF that is matched to the multiple access code. The resulting signal $y(t)$ can be written as

$$y(t) = r(t) * \psi(T-t) \cdot \exp(j2\pi c_k B_h t). \tag{7.7}$$

The square-law detection is therefore performed with respect to the multipath propagation. The decision variables can be calculated by

$$Z_m(i) = \int_{iT_b+m\Delta}^{iT_b+m\Delta+T_i} |y(t)|^2 \, \mathrm{d}t, \qquad m \in \{0,1\}, \tag{7.8}$$

where m represents the position of the decision variable, i.e., the energy collected in the first PPM time slot "0" or in the second "1" (cf. Section 3.2.1.1). The decision to estimate the information bit $\widehat{a}_i$ will be made based on the sign of $Z_0(i) - Z_1(i)$ as

$$\widehat{a}_i = \begin{cases} 0, & \text{if } Z_0(i) - Z_1(i) \geq 0 \\ 1, & \text{if } Z_0(i) - Z_1(i) < 0 \end{cases}. \tag{7.9}$$

7.3.2.2 BER Performance Analysis for FH-PPM

For simplicity, we choose the Root Raised Cosine (RRC) pulse as $\psi(t) = g(t)$ with a roll-off factor $\beta = 0.3$. No interference is taken into account. The measured channels in both LOS and NLOS office scenarios (by IMST) are used for the simulations. The BER is obtained by averaging over many channel realizations. Figure 7.8 shows the BER of the FH-PPM system

as a function of E_b/N_0 for different bandwidths of the sub-bands B_h or for different number of frequency hops N_h, where we fix the total bandwidth as 1 GHz, i.e., $B = B_h N_h = 1$ GHz. All the energy spread over time is non-coherently collected at the receiver. The analytical performance of 2-PPM non-coherent detection in the Rayleigh fading channel is given by $P_b = 1/(2 + E_b/N_0)$ [Hay01], which can be considered as the worst performance. In the multipath propagation scenario, a wider bandwidth leads to a larger number of resolvable paths at the receiver. For a signal with a very narrow bandwidth, no multipath can be resolved and subsequently it will suffer from the deep fade.

Figure 7.8 indicates that if $B_h = B = 1$ GHz is utilized, a great performance degradation arising from the NC-CL is observed, whereas if the bandwidth is quite small, the fading effect is dominant. The best performance still lies in the cases when $B_h = 200$ MHz for the NLOS scenario and $B_h = 100$ MHz for LOS.

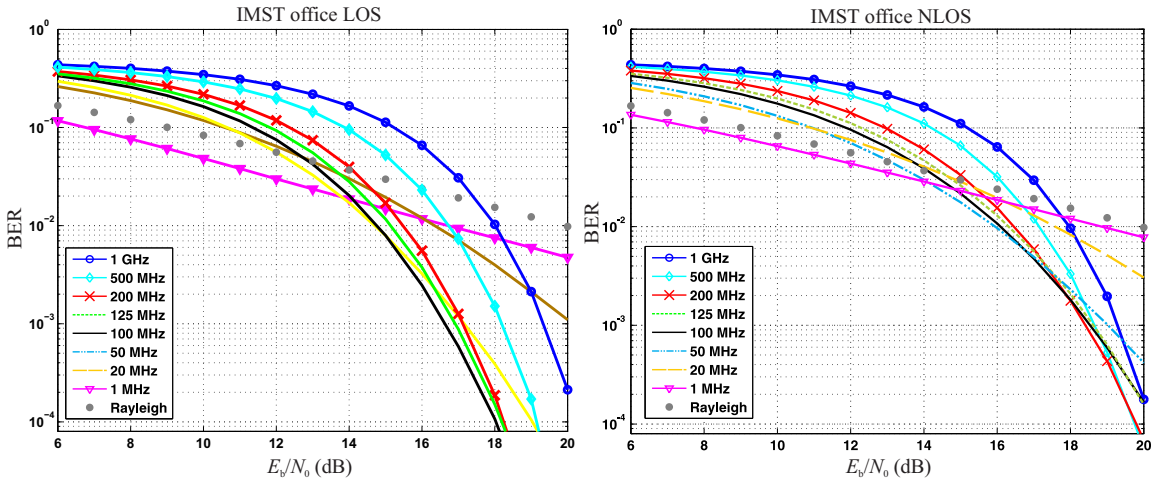

Fig. 7.8: BER versus SNR for the FH-PPM scheme using different sub-band bandwidths (B_h) in LOS (a) and NLOS (b) office scenarios. $B = 1$ GHz.

7.4 Summary and Discussions

A good small scale fading resistance requires a certain bandwidth B to resolve the propagation paths in the time domain. On the contrary, if a receiver adds up the multipath components so that they interfere with each other, deep fades may occur. Therefore, a good single-carrier system design needs to choose an "appropriate" bandwidth B which trades off the small scale fading resistance and the NC-CL. Our analysis in Section 7.2 shows that a signal bandwidth of $B > 200$ MHz is NOT desirable from the required E_b/N_0 perspective. For the LOS scenarios, a well suited B is even smaller.

According to the selection of the useful bandwidth and the recent UWB regulations, Section 7.3.1 presents a generic FH-UWB system concept, where both coherent and non-coherent receivers can be applied. The main advantage of such a system is that the baseband

bandwidth can be brought down to the values that are much lower than 500 MHz. This enables low-cost ADCs and low-complexity digital signal processing techniques. Nevertheless, such a FH-UWB system benefits from the total analog bandwidth, which is still "ultra wide". The FH technique is able to provide a good piconet operation and interference resistance by applying either fixed FH or even adaptive FH strategies [PYP06]. It is also very flexible with respect to the data rate.

In Section 7.3.2, we investigate the FH-PPM scheme for non-coherent detection in the single-user case. With a total bandwidth of 1 GHz, the corresponding performance is analyzed when the per-hop bandwidth or the number of frequency hops varies. The results show that the best (uncoded) BER performance averaged over all sub-carriers can be achieved if the per-hop bandwidth lies in the range of 50 – 200 MHz, depending on different scenarios.

To develop and evaluate such an FH-UWB system, the analysis of the simple FH-PPM scheme is only a starting point. Advanced modulation schemes combined with the hybrid spreading can be adopted. Figure 7.9 takes one hybrid FH-DS UWB signal using the 4-ary Walsh modulation as an example. The first spreading is achieved by multiplying each Walsh waveform with the DS codes. One FH block comprises two Walsh chips with a duration $2T$. Each block is up-converted to a certain frequency according to the specific FH pattern, accomplishing the second spreading. For such a hybrid FH-DS system, there are several potential topics for future research (with the major emphasis on the communication aspects):

- efficient modulation schemes for various data rate applications, e.g., M-ary Walsh modulation for non-coherent detection (or PSK for coherent detection),
- interference rejection and piconet separation capabilities,
- efficient and robust encoding and decoding techniques, and
- receiver synchronization.

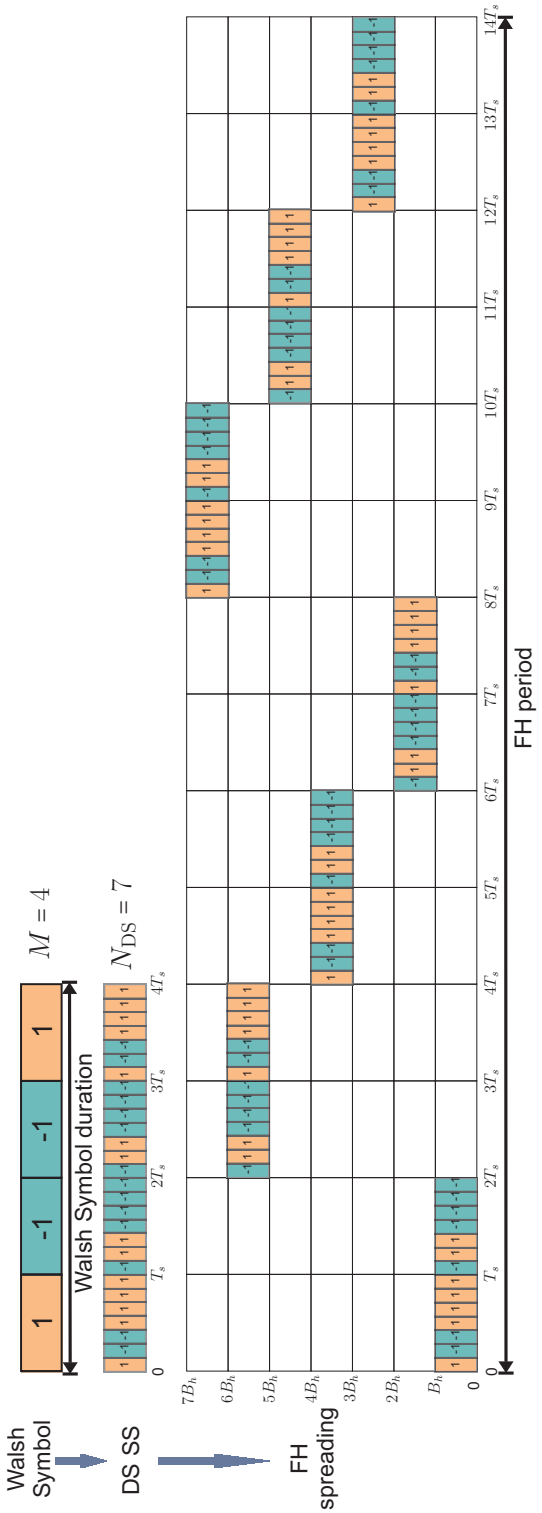

Fig. 7.9: One example of the hybrid FH-DS UWB signal using the Walsh modulation. Modulation order $M = 4$; length of DS code $N_{\mathrm{DS}} = 7$; one block consisting of 2 Walsh chips of duration $2T_s$ is transmitted per hop; the linear congruence code (cf. [SD84]) is used as the FH pattern.

PART II: ADVANCED SIGNAL PROCESSING FOR HIGH DATA RATE ULTRA WIDEBAND SYSTEMS

8. INTERFERENCE SUPPRESSION FOR HIGH DATA RATE ULTRA WIDEBAND COMMUNICATIONS

Motivation and the state of the art:

Complex-valued signals have been widely used in various fields such as mobile communications, smart antennas, radar, biomedicine, optics and seismics, etc.. Complex-domain representations are quite convenient to physically characterize the signals in practice [AH10, SS10, MG09]. Most parameter estimation and filtering techniques for complex-valued signals, whose samples are often organized in a vector $\boldsymbol{r}$, are based on their second-order statistics. It is often assumed that the signal $\boldsymbol{r}$ is second-order circular (or proper). As a result, only the covariance matrix $\boldsymbol{R} = \mathbb{E}\left\{\boldsymbol{r}\boldsymbol{r}^H\right\}$ is utilized for signal processing. However, it is shown that in many applications when $\boldsymbol{r}$ is non-circular or improper, the second-order behavior should be described by both the covariance matrix $\boldsymbol{R}$ and the pseudo-covariance (also called complementary covariance in [SS10, SS03]) matrix $\check{\boldsymbol{R}} = \mathbb{E}\left\{\boldsymbol{r}\boldsymbol{r}^T\right\}$, where $\check{\boldsymbol{R}}$ is not vanishing [PC95]. The improperness may arise from modulations which employ improper signal constellations such as Binary Phase Shift Keying (BPSK), Amplitude Shift Keying (ASK), bi-orthogonal keying, or the ones that can be interpreted as a real constellation after reformulation such as Offset Quadrature Phase Shift Keying (OQPSK), Minimum Shift Keying (MSK), or Gaussian Minimum Shift Keying (GMSK) [TS00].

Widely Linear (WL) processing, which fully exploits the second-order statistics ($\boldsymbol{R}$ and $\check{\boldsymbol{R}}$) of improper signals, can significantly improve the estimation performance [PC95, SS03, RH07, HR04]. The WL filtering techniques have gained a great popularity in the applications of interference suppression, equalization, and synchronization. Data-aided and blind adaptive WL Minimum Mean Square Error (MMSE) receivers based on Recursive Least Squares (RLS) [BLT01] and Stochastic Gradient (SG) [SGL04] techniques are proposed to achieve interference suppression in BPSK-based Direct Sequence Code Division Multiple Access (DS-CDMA) systems. Different equalization strategies based on WL processing have been developed for DS-CDMA [MPP06] and Direct Sequence Ultra Wideband (DS-UWB) [PLSL07]. The authors of [CP06] provide new insights into the optimum WL array receivers for their applications to single antenna interference cancellation techniques [MGSH06] as well as to synchronization schemes [CPD07] for Global System for Mobile Communications (GSM) systems, considering BPSK, MSK, and GMSK signals in the presence of non-circular interferences. Compared to

the linear processing, these WL receivers exhibit an increased robustness against interferences, and the related adaptive algorithms are able to provide a better convergence performance. One important property is that the WL estimate of the real-valued data from a sequence of complex and improper observations results in a real-valued estimate. This not only produces a smaller estimation error than the linear estimate but may also reduce the receiver complexity since only the real-valued signal is processed [BLT01, MPP06].

In many situations, the observation data used for parameter estimation has a large size due to a high processing gain, a large number of antennas, or numerous multipath components, which requires a long receive filter. However, a filter with a large number of taps requires substantial training, which considerably slows down the convergence speed, and becomes highly sensitive to interference. Thereby, in order to decrease the number of estimated parameters (e.g., filter coefficients), reduced-rank processing can be applied such that the received vector is transformed into a lower dimensional subspace and the filtering optimization is carried out within this subspace. Compared to the full-rank techniques, the reduced-rank methods are able to achieve a faster convergence, an increased robustness against interference, and a lower complexity by estimating a reduced number of parameters. There have been several reduced-rank techniques proposed for interference suppression. Some well-known approaches, for example, based on the Principal Components Analysis (PCA) [WP98, SR99] and the "cross spectral" metric [GR97], exclusively rely on the eigen-decomposition for estimating the signal subspace. This demands huge computational efforts and an often large rank to reach a satisfactory performance [GR97]. A more effective method called Multistage Wiener Filter (MSWF) was proposed in [GRS98, HX01]. In contrast to the eigen-decomposition algorithms, the MSWF does not require the knowledge of the signal subspace but utilizes a successive orthogonal decomposition for parameter estimation. It is capable of attaining an improved convergence with a filter rank which is much smaller than the dimension of the signal subspace [HG02]. Another reduced-rank approach is called Auxiliary Vector Filter (AVF), which iteratively updates the filter weights according to a sequential and conditioned optimization of auxiliary vectors [PK01]. Both the MSWF and the AVF estimators can be combined with different design criteria such as MMSE [QB03], Constrained Minimum Variance (CMV) [dLHSN08], or Constrained Constant Modulus (CCM) [dLHSN08, WdL10]. The AVF outperforms the MSWF but has a higher complexity. In the WL case, both the original received signal $\boldsymbol{r}$ and its complex conjugate $\boldsymbol{r}^*$ have to be considered, which further increases the filter length and thus decelerates the convergence [MG09, Dou09]. Reduced-rank techniques are thus more attractive and efficient in WL signal processing. So far, most of the reduced-rank algorithms are based on linear processing [dLHSN08, dLSN07, dLSN09, dLSN10]. One of the few algorithms that combine both is the WL reduced-rank Wiener filter investigated in [SS03], where the computationally expensive eigen-decomposition is employed. This reduced-rank WL estimator usually requires twice the rank of its linear counterpart.

Interference Suppression for DS-UWB Systems:

In high data rate DS-UWB applications [FKLW05], the system performance may be dete-

riorated by Inter-/Intra-Symbol Interference (ISI), Multi-User Interference (MUI), or even by the interference from other non-UWB systems operating in the same bandwidth (e.g., Narrowband Interference (NBI)). The large bandwidth requires a high sampling rate and leads to a received vector with a large size. The reduced-rank techniques are thus very promising for interference suppression in DS-UWB systems [AY10]. One mandatory modulation scheme for DS-UWB systems is the non-circular BPSK modulation [FKLW05]. Therefore, the combination of the reduced-rank techniques and the WL processing is motivated to ensure a faster convergence and a lower complexity than the full-rank and/or the linear counterparts.

Own Contribution:

This chapter introduces two WL reduced-rank schemes to the receiver design with the aim of suppressing the interference in DS-UWB systems. The receiver consists of a bijective transformation to form an augmented observation vector and a reduced-rank filter that is adjusted by adaptive algorithms. In contrast to the WL reduced-rank Wiener filter based on PCA [SS03], the proposed receiver applies the linear reduced-rank concepts, namely MSWF and AVF, in the WL case. It does not require the eigen-decomposition and thus its computational complexity is considerably reduced.

Section 8.2 details the data model for the DS-UWB system, including the MUI, ISI, and NBI.

Section 8.3 presents the MSWF scheme and characterizes some key properties. Two constructions of the rank-reduction matrix are introduced, namely the Total Widely Linear (TWL) and the Quasi Widely Linear (QWL) designs. For both low-rank WL designs (TWL and QWL), we develop the SG and the RLS adaptive algorithms to compute the MSWF. We analyze the statistical performance in terms of MSE for the adaptive SG and RLS algorithms, including the stability and the convergence performance. The computational complexity of the proposed and the existing schemes is estimated and compared in terms of real additions and multiplications. The proposed TWL/QWL-MSWF schemes are examined under realistic scenarios and compared with the linear MSWF counterparts, linear/WL full-rank schemes, as well as the linear/WL PCA-based methods. We mainly focus on the scenario when both the signal and the interference (MUI and NBI) are non-circular. We also show the suitability of the proposed methods applied in the case when the desired signal is strictly circular but the interference (MUI or NBI) is non-circular.

In Section 8.4, we propose the WL-AVF scheme and develop a training-based adaptive algorithm. Its key properties are specified and the performance is shown in comparison with the linear AVF. In the summary (cf. Section 8.5), we also discuss the WL-AVF scheme and a proposed WL-Joint Iterative Optimization (JIO) algorithm in the beamforming applications.

Notation in Sections 8.3 and 8.4: We use a as the subscript to denote the associated augmented quantities. The reduced-rank quantities are symbolized with a "bar". The Hadamard (element-wise) product is denoted by $\odot$. The expectation and the trace operations are expressed by $\mathbb{E}\{\cdot\}$ and $\mathrm{tr}\{\cdot\}$. The floor/ceiling operator $\lfloor x \rfloor / \lceil x \rceil$ rounds the argument x down/up

to the closest integer that is less/greater than or equal to x. The operation $\Re\{\cdot\}$ is to take the real part of a variable. We use the bold capital letters to represent matrices and the bold small letters for vectors.

8.1 Preliminaries on Non-Circular Signals

This section introduces the fundamentals of complex random signals and characterizes the corresponding second-order statistics. We also present the definition of non-circularity and show some examples of non-circular signals. Finally, a brief discussion is made to point out our considerations for the remainder of this chapter. Please note that the circularity we consider here is only with respect to the second order.

8.1.1 Complex Signals and Second-Order Statistics

We denote a random complex vector by $\boldsymbol{z} = \boldsymbol{x} + j \cdot \boldsymbol{y} \in \mathbb{C}^M$, where $\boldsymbol{x}, \boldsymbol{y} \in \mathbb{R}^M$ are real zero-mean random vectors.

8.1.1.1 Vector-Concatenation Mapping

To analyze the complex vectors, two vector-concatenation mappings are introduced in the following [AH10].

- **Complex-to-Real Mapping**: this mapping has a very simple form and is written as

$$\tilde{\boldsymbol{z}}_R = \left[\begin{array}{cc} \boldsymbol{x}^T, & \boldsymbol{y}^T \end{array} \right]^T \in \mathbb{R}^{2M}. \tag{8.1}$$

  It is a practical way to reformulate the complex data vector for deviations in the complex domain [Goo63, CA06].

- **Complex-to-Complex Mapping**: it is obtained by the concatenation of the complex vector and its complex conjugate as

$$\tilde{\boldsymbol{z}}_C = \left[\begin{array}{cc} \boldsymbol{z}^T, & \boldsymbol{z}^H \end{array} \right]^T \in \mathbb{C}^{2M}. \tag{8.2}$$

  The presentation of this complex *augmented vector* preserves the nature of the complex signals. It is a smart and convenient way to take advantage of the Wirtinger calculus, leading to simplified expressions [vdB94]. More importantly, in the following we will show that this mapping is quite useful to characterize the WL transformation and to easily obtain the full second-order statistics of the complex vector.

The relationship between the above two mappings is given by

$$\tilde{\boldsymbol{z}}_C = \boldsymbol{T}_M \tilde{\boldsymbol{z}}_R, \tag{8.3}$$

where the unitary transformation matrix $\boldsymbol{T}_M$ is denoted as

$$\boldsymbol{T}_M = \frac{1}{\sqrt{2}} \begin{bmatrix} \boldsymbol{I}_M & j\boldsymbol{I}_M \\ \boldsymbol{I}_M & -j\boldsymbol{I}_M \end{bmatrix} \in \mathbb{C}^{2M \times 2M}, \quad \boldsymbol{T}_M^H \boldsymbol{T}_M = \boldsymbol{T}_M \boldsymbol{T}_M^H = \boldsymbol{I}_{2M}. \tag{8.4}$$

8.1.1.2 Widely-Linear Transformation

Based on the analysis in [SS03], we apply a real linear transformation $\boldsymbol{H} \in \mathbb{R}^{2N \times 2M}$ to $\tilde{\boldsymbol{z}}_R$ and the resulting real vector $\tilde{\boldsymbol{r}}_R = \left[\boldsymbol{a}^T, \boldsymbol{b}^T\right]^T \in \mathbb{R}^{2N}$ with $\boldsymbol{r} = \boldsymbol{a} + j\boldsymbol{b}$ is expressed as

$$\tilde{\boldsymbol{r}}_R = \begin{bmatrix} \boldsymbol{H}_{11} & \boldsymbol{H}_{12} \\ \boldsymbol{H}_{21} & \boldsymbol{H}_{22} \end{bmatrix} \begin{bmatrix} \boldsymbol{x} \\ \boldsymbol{y} \end{bmatrix}, \tag{8.5}$$

where $\boldsymbol{H}_{nm} \in \mathbb{R}^{N \times M}$, $n, m \in \{1, 2\}$. Using the unitary transformation $\boldsymbol{T}_N$ (cf. equation (8.3)), the complex vector is given by

$$\tilde{\boldsymbol{r}}_C = \begin{bmatrix} \boldsymbol{r} \\ \boldsymbol{r}^* \end{bmatrix} = \boldsymbol{T}_N \tilde{\boldsymbol{r}}_R = \left(\boldsymbol{T}_N \begin{bmatrix} \boldsymbol{H}_{11} & \boldsymbol{H}_{12} \\ \boldsymbol{H}_{21} & \boldsymbol{H}_{22} \end{bmatrix} \boldsymbol{T}_M^H \right) (\boldsymbol{T}_M \tilde{\boldsymbol{z}}_R) = \begin{bmatrix} \boldsymbol{F}_{11} & \boldsymbol{F}_{12} \\ \boldsymbol{F}_{21} & \boldsymbol{F}_{22} \end{bmatrix} \tilde{\boldsymbol{z}}_C = \boldsymbol{F} \begin{bmatrix} \boldsymbol{z} \\ \boldsymbol{z}^* \end{bmatrix}. \tag{8.6}$$

If and only if $\boldsymbol{H}_{11} = \boldsymbol{H}_{22}$ and $\boldsymbol{H}_{12} = -\boldsymbol{H}_{21}$, the transformation on $\mathbb{R}^{2N \times 2M}$ as shown in equation (8.5) is equivalent to the linear transformation on $\mathbb{C}^{N \times M}$ represented by $\boldsymbol{r} = \boldsymbol{F}_{11}\boldsymbol{z}$. In most general cases, where $\boldsymbol{H}_{11} \neq \boldsymbol{H}_{22}$ and $\boldsymbol{H}_{12} \neq -\boldsymbol{H}_{21}$, the transformation $\boldsymbol{F}$ is *widely linear* in $\boldsymbol{z}$ and linear in $\tilde{\boldsymbol{z}}_C$.

8.1.1.3 Second-Order Statistics

To characterize the second-order statistics of a random vector $\boldsymbol{z}$, we can calculate the corresponding covariance matrix of the real concatenation vector $\tilde{\boldsymbol{z}}_R$ as

$$\boldsymbol{\Gamma}_{zz} = \mathbb{E}\left\{\tilde{\boldsymbol{z}}_R \tilde{\boldsymbol{z}}_R^T\right\} = \begin{bmatrix} \mathbb{E}\left\{\boldsymbol{x}\boldsymbol{x}^T\right\} & \mathbb{E}\left\{\boldsymbol{x}\boldsymbol{y}^T\right\} \\ \mathbb{E}\left\{\boldsymbol{y}\boldsymbol{x}^T\right\} & \mathbb{E}\left\{\boldsymbol{y}\boldsymbol{y}^T\right\} \end{bmatrix} = \begin{bmatrix} \boldsymbol{\Gamma}_{xx} & \boldsymbol{\Gamma}_{xy} \\ \boldsymbol{\Gamma}_{xy}^T & \boldsymbol{\Gamma}_{yy} \end{bmatrix} \in \mathbb{R}^{2M \times 2M}. \tag{8.7}$$

Alternatively, we can also obtain the *augmented covariance matrix* for $\tilde{\boldsymbol{z}}_C$ by

$$\boldsymbol{R}_a = \mathbb{E}\left\{\tilde{\boldsymbol{z}}_C \tilde{\boldsymbol{z}}_C^H\right\} = \begin{bmatrix} \mathbb{E}\left\{\boldsymbol{z}\boldsymbol{z}^H\right\} & \mathbb{E}\left\{\boldsymbol{z}\boldsymbol{z}^T\right\} \\ \mathbb{E}\left\{\boldsymbol{z}^*\boldsymbol{z}^H\right\} & \mathbb{E}\left\{\boldsymbol{z}^*\boldsymbol{z}^T\right\} \end{bmatrix} = \begin{bmatrix} \boldsymbol{R} & \check{\boldsymbol{R}} \\ \check{\boldsymbol{R}}^* & \boldsymbol{R}^* \end{bmatrix} \in \mathbb{C}^{2M \times 2M}, \tag{8.8}$$

where $\boldsymbol{R}$ is the covariance matrix and $\check{\boldsymbol{R}}$ is the *complementary covariance matrix* of the vector $\boldsymbol{z}$ [SS10]. It is also referred to as the *pseudo-covariance matrix*. The augmented covariance matrix $\boldsymbol{R}_a$ is related to $\boldsymbol{\Gamma}_{zz}$ as

$$\boldsymbol{R}_a = \boldsymbol{T}_M \boldsymbol{\Gamma}_{zz} \boldsymbol{T}_M^H, \tag{8.9}$$

where

$$\boldsymbol{R} = \frac{1}{2}\left[\boldsymbol{\Gamma}_{xx} + \boldsymbol{\Gamma}_{yy} + j\left(\boldsymbol{\Gamma}_{xy}^T - \boldsymbol{\Gamma}_{xy}\right)\right] = \boldsymbol{R}^H \tag{8.10}$$

and

$$\check{\boldsymbol{R}} = \frac{1}{2}\left[\boldsymbol{\Gamma}_{xx} - \boldsymbol{\Gamma}_{yy} + j\left(\boldsymbol{\Gamma}_{xy}^T + \boldsymbol{\Gamma}_{xy}\right)\right] = \check{\boldsymbol{R}}^T \tag{8.11}$$

To fully interpret the second-order behavior of a random complex vector, both $\boldsymbol{R}$ and $\check{\boldsymbol{R}}$ are required.

Some key properties of the augmented covariance matrix $\boldsymbol{R}_a$ are listed as follows [SS10].

- $\boldsymbol{R}_a$ has a block structure, consisting of the covariance matrix $\boldsymbol{R}$ and the complementary covariance matrix $\check{\boldsymbol{R}}$.
- $\boldsymbol{R}_a$ is Hermitian and positive semidefinite.
- The complementary covariance matrix is symmetric, i.e., $\check{\boldsymbol{R}} = \check{\boldsymbol{R}}^T$.
- The Schur complement of the augmented covariance matrix, $\boldsymbol{R}^* - \check{\boldsymbol{R}}^* \boldsymbol{R}^{-1} \check{\boldsymbol{R}}$, is positive semidefinite to ensure that $\boldsymbol{R}_a$ is positive semidefinite.

These properties indicate that using the augmented vector may facilitate the second-order analysis. We will also apply these properties to some analyses in the following sections.

8.1.2 Non-Circularity

Definition 8.1.1. *A complex random vector $\boldsymbol{z} = \boldsymbol{x} + j \cdot \boldsymbol{y} \in \mathbb{C}^M$, where $\boldsymbol{x}, \boldsymbol{y} \in \mathbb{R}^M$ are zero-mean, is second-order circular or proper if $\check{\boldsymbol{R}} = \mathbb{E}\left\{\boldsymbol{z}\boldsymbol{z}^T\right\} = \boldsymbol{0}$; otherwise, $\boldsymbol{z}$ is non-circular or improper.*

In one special case when $\check{\boldsymbol{R}}$ vanishes, i.e., $\boldsymbol{z}$ is second-order circular, only $\boldsymbol{R}$ characterizes the second-order statistics. The resulting augmented covariance matrix $\boldsymbol{R}_a$ is block diagonal and from equation (8.11) we have

$$\boldsymbol{\Gamma}_{xx} = \boldsymbol{\Gamma}_{yy}, \quad \boldsymbol{\Gamma}_{xy} = -\boldsymbol{\Gamma}_{xy}^T, \tag{8.12}$$

implying that $\boldsymbol{x}$ and $\boldsymbol{y}$ are uncorrelated. In most cases when $\check{\boldsymbol{R}} \neq \boldsymbol{0}$, i.e., $\boldsymbol{z}$ is non-circular, $\boldsymbol{R}_a$ is able to completely describe the second-order information. Accordingly, $\boldsymbol{z}, \boldsymbol{z}^*$ are correlated and $\boldsymbol{x}, \boldsymbol{y}$ are linearly dependent.

8.1.2.1 Non-Circularity Rate

To measure the degree of the non-circularity of a random variable $z = x + j \cdot y \in \mathbb{C}$, where x, y are real zero-mean random variables, we define the *non-circularity rate* as

$$\rho = \frac{\mathbb{E}\left\{z^2\right\}}{\mathbb{E}\left\{|z|^2\right\}} = |\rho| \, e^{j\phi}. \tag{8.13}$$

We distinguish the following three cases.

1. $\rho = 0$: z is second-order circular;
2. $|\rho| = 1$: z is strictly non-circular;
3. $0 < |\rho| < 1$: z is wide-sense non-circular.

Some examples are shown in Figure 8.1, where the BPSK signals are strictly non-circular, the Quadrature Phase Shift Keying (QPSK) signals and complex Gaussian signals with $\rho = 0$ are second-order circular, and the others are wide-sense non-circular.

8.1.3 Discussions

According to the discussions on vector-concatenation mappings and the widely linear transformation, it seems that the representation of the *augmented* vector is inherently redundant as compared to that of the real vector obtained by the complex-to-real mapping. As a matter of fact, the complex representation preserves the nature of many signals. The expressions involving complex conjugates are quite powerful and convenient for analyzing the second-order statistics of the non-circular signals. The *augmented covariance matrix* $\boldsymbol{R}_a$ exhibits several key properties such as block structure, Hermitian, positive semidefinite, etc.. Therefore, in our work, we utilize the *augmented* representation for the filtering design and the corresponding analysis.

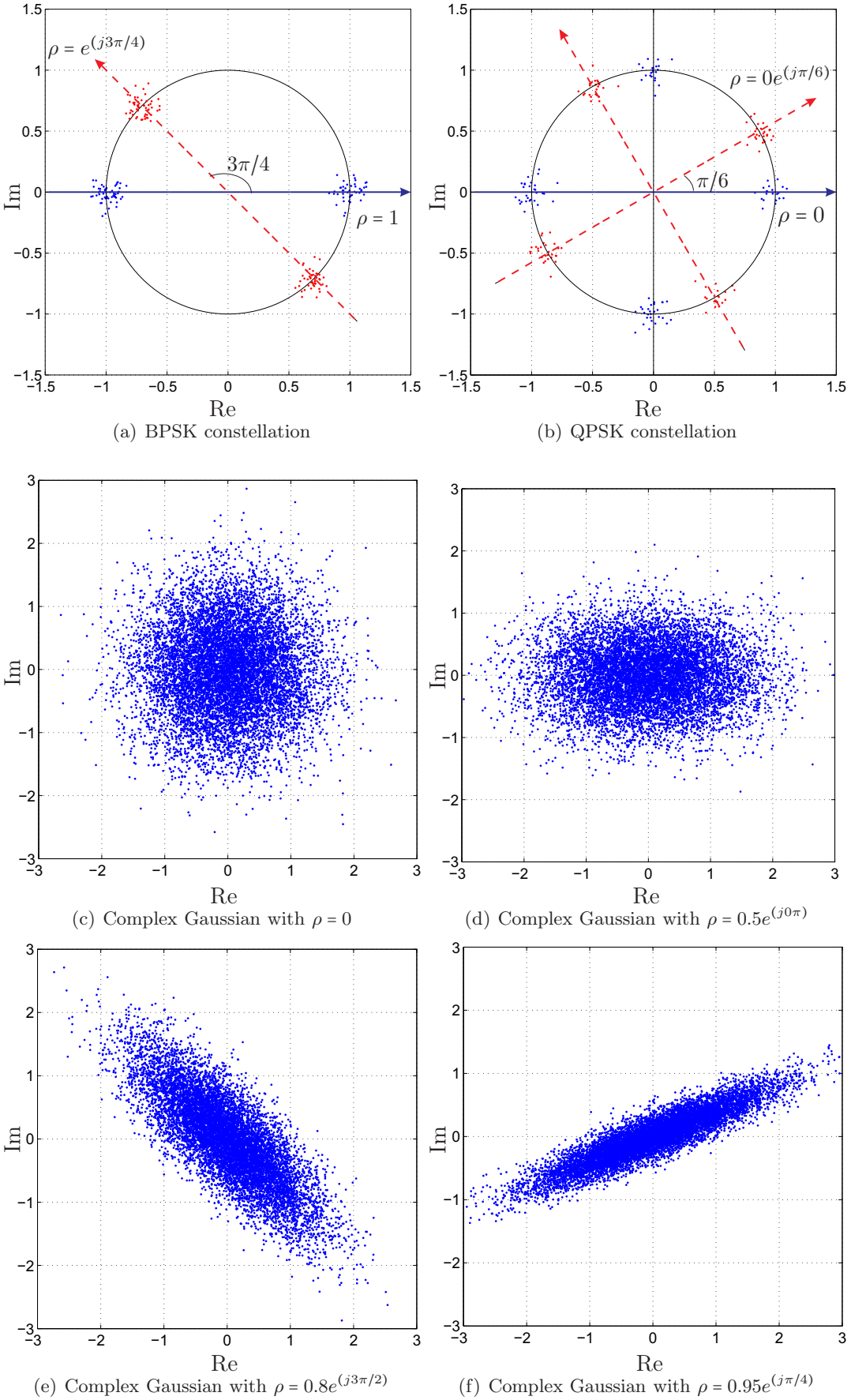

(a) BPSK constellation

(b) QPSK constellation

(c) Complex Gaussian with $\rho = 0$

(d) Complex Gaussian with $\rho = 0.5e^{(j0\pi)}$

(e) Complex Gaussian with $\rho = 0.8e^{(j3\pi/2)}$

(f) Complex Gaussian with $\rho = 0.95e^{(j\pi/4)}$

Fig. 8.1: Scatter plots for BPSK, QPSK, and complex Gaussian signals.

8.2 Direct Sequence Ultra Wideband Data Model

We consider the uplink of a BPSK DS-UWB system with N_u asynchronous users in the presence of NBI. In the complex baseband, the transmitted signal for the k-th user is given by

$$s_k(t) = \sum_{i=-\infty}^{\infty} b_k(i) \sum_{n=0}^{N-1} \sqrt{E_k} c_k(n) g(t - iT_b - nT_c), \tag{8.14}$$

where $b_k(i) \in \{\pm 1\}$ is the i-th BPSK symbol for the user k with unit variance $\sigma_b^2 = \mathbb{E}\left\{|b_1(i)|^2\right\} = 1$, T_b is the bit duration, E_k and $c_k(n) \in \{\pm 1/\sqrt{N}\}$ denote the corresponding energy per bit and the multiple access code with chip interval T_c. The baseband reference pulse $g(t)$ is the impulse response of a Root Raised Cosine (RRC) low pass filter with 30 % excess bandwidth, i.e., the roll-off factor is $\beta = 0.3$. For both the low and high frequency bands, the filter cutoff frequency (-3 dB point) is $\frac{1}{2T_c}$ [FKLW05]. The processing gain N is equal to T_b/T_c.

Since the signal bandwidth is constrained to $B = (\beta + 1)B_3$, the complex-valued impulse response of the multipath UWB channel can be fully described by the discrete response (cf. Chapter 2), i.e., tapped-delay line model written as $h_k(t) = \sum_{l=0}^{L-1} \alpha_k(l)\delta(t - l/B)$, where $\alpha_k(l)$ is the l-th complex channel tap for the k-th user and $\sum_{l=0}^{L-1} |\alpha_k(l)|^2 = 1$. In our case, the channel is assumed to be time-invariant block fading. For UWB communications with $B \geq 500$ MHz, the statistics of the path gains are different from those in narrowband systems. The large bandwidth also results in a significant number of resolvable multipath components and severe ISI.

The received signal at the output of a pulse matched filter with the impulse response $g(T - t)$ can be expressed as

$$y(t) = \sum_{i=-\infty}^{\infty} \sum_{k=1}^{N_u} \sum_{n=0}^{N-1} \sum_{l=0}^{L-1} \sqrt{E_k} b_k \left(i + \left\lfloor \frac{n - q_k}{N} \right\rfloor \right) c_k(n) \alpha_k(l) \tilde{g}\left(t - iT_b - nT_c - \frac{l}{B} - \tau_k \right) + J(t) + n(t), \tag{8.15}$$

where $\tilde{g}(t) = g(t) * g(T - t)$, $J(t) = \widehat{J}(t) * g(T - t)$, and $n(t) = \widehat{n}(t) * g(T - t)$ are the filtered pulse, NBI, and noise, respectively. The zero-mean, complex Additive White Gaussian Noise (AWGN) $\widehat{n}(t)$ is assumed to have a power spectral density N_0. Asynchronous (but chip synchronous) transmission is assumed and the signal of the k-th user has a delay τ_k, satisfying that $\tau_1 - \tau_k = q_k T_c$, where the random variable q_k takes values in $\{0, 1, \ldots, N - 1\}$ with equal probability. Without loss of generality, we assume that the delay of the desired user τ_1 is known and $\tau_1 = 0$ is chosen.

The NBI is often modeled as a single tone as shown in equation (6.25). It is more realistic to consider the Orthogonal Frequency Division Multiplexing (OFDM) signal from the IEEE 802.11a Wireless Local Area Network (WLAN) that overlays the UWB emission spectrum. Such an OFDM signal can be regarded as a sum of multiple single-tone NBIs, given by equation (6.26). The signal to NBI ratio is computed as SIR $= E_s/(P_J T_s)$, where E_s is the signal energy per symbol and $E_s = E_b$ for BPSK. Usually in UWB communications, it is assumed that the duration of a NBI T_J is greater than T_b.

At the receiver, by sampling $y(t)$ at a chip rate $1/T_c$, the resulting received vector of size $N_sN + L - 1$ is given by

$$\boldsymbol{y} = \sum_{k=1}^{N_u} \sqrt{E_k}\boldsymbol{F}_k\boldsymbol{H}_k\boldsymbol{b}_k + \boldsymbol{J} + \boldsymbol{n}, \tag{8.16}$$

where $\boldsymbol{F}_k \in \mathbb{R}^{(N_sN+L-1)\times N_sL}$ illustrated in Figure 8.2 is the code matrix, the channel matrix is represented as $\boldsymbol{H}_k = \boldsymbol{I}_{N_s} \otimes \boldsymbol{h}_k \in \mathbb{C}^{N_sL\times N_s}$ containing the channel information $\boldsymbol{h}_k = [\alpha_k(0), \ldots, \alpha_k(L-1)]^T$, as well as $\boldsymbol{J}$ and $\boldsymbol{n} \in \mathbb{C}^{N_sN+L-1}$ correspond to the NBI and the AWGN vectors, respectively. The structure of the code matrix for the k-th user $\boldsymbol{C}_k \in \mathbb{R}^{M\times L}$ is shown in equation (8.18).

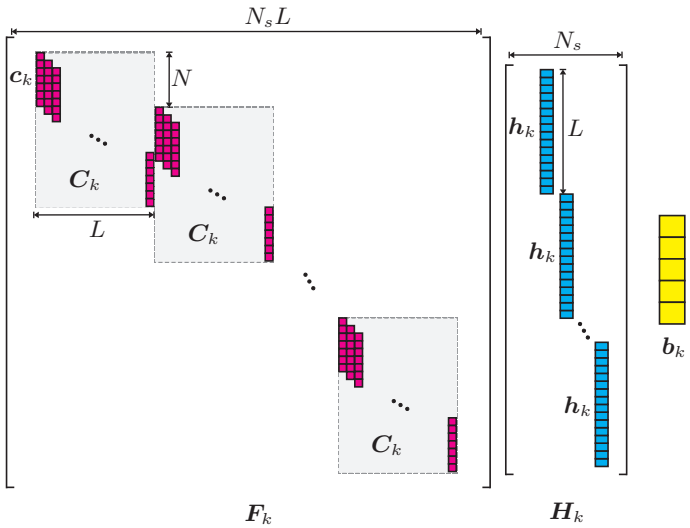

Fig. 8.2: Data model of the signal for a synchronous user k, where $\boldsymbol{c}_k = [c_k(0), \ldots, c_k(N-1)]^T$. Asynchronous transmission can be obtained by shifting down the code matrix $\boldsymbol{F}_k$ with an offset q_k.

For the i-th transmitted bit $i = 0, 1, \ldots, N_s - 1$, the corresponding received vector of length $M = N + L - 1$ can be written as

$$\boldsymbol{r}(i) = \sqrt{E_1}b_1(i)\boldsymbol{C}_1\boldsymbol{h}_1 + \boldsymbol{v}(i) + \boldsymbol{\eta}(i) + \boldsymbol{j}(i) + \boldsymbol{n}(i), \tag{8.17}$$

including the desired user signal, the MUI part $\boldsymbol{v}(i)$, the ISI $\boldsymbol{\eta}(i)$, the NBI vector $\boldsymbol{j}(i)$ observed in the i-th bit, and the AWGN vector $\boldsymbol{n}(i)$. The code matrix for the k-th user $\boldsymbol{C}_k \in \mathbb{R}^{M\times L}$ is a Toeplitz matrix, which can be expressed as

$$\boldsymbol{C}_k = \begin{bmatrix} c_k(0) & 0 & \cdots & 0 \\ c_k(1) & c_k(0) & \cdots & 0 \\ \vdots & \vdots & \ddots & \vdots \\ c_k(N) & c_k(N-1) & \cdots & 0 \\ 0 & c_k(N) & \cdots & 0 \\ \vdots & \vdots & \ddots & \vdots \\ 0 & 0 & \cdots & c_k(N) \end{bmatrix}. \tag{8.18}$$

In what follows, we denote $\boldsymbol{X}(m:n,:)$ as a matrix consisting of the rows in $\boldsymbol{X}$ that are indexed from m to n.

The NBI vector is expressed as

$$\boldsymbol{j}(i) = \sqrt{\frac{P_J}{N_c}} \sum_{n=0}^{N_c-1} \boldsymbol{x}_n(i) \odot e^{j[2\pi(f_J+n\cdot\Delta f)\cdot\boldsymbol{k}T_c+\theta]}, \tag{8.19}$$

where $\boldsymbol{x}_n(i) = \left[x_n\left(\left\lfloor\frac{iNT_c}{T_J}\right\rfloor\right), x_n\left(\left\lfloor\frac{(iN+1)T_c}{T_J}\right\rfloor\right), \ldots, x_n\left(\left\lfloor\frac{(iN+M-1)T_c}{T_J}\right\rfloor\right)\right]^T$, $j=\sqrt{-1}$, and $\boldsymbol{k} = [iN, iN+1, \ldots, iN+M-1]^T$ [1].

We represent the asynchronous MUI each with a delay offset q_k by $\boldsymbol{v}(i) = \sum_{k=2}^{N_u}\sqrt{E_k}b_k(i)\check{\boldsymbol{C}}_k\boldsymbol{h}_k$, where $\check{\boldsymbol{C}}_k \in \mathbb{R}^{M\times L}$, is constructed from a zero matrix and the first $M-q_k$ rows of $\boldsymbol{C}_k$ defined as

$$\check{\boldsymbol{C}}_k = \begin{bmatrix} \boldsymbol{0} \\ \boldsymbol{C}_k(1:M-q_k,:) \end{bmatrix}. \tag{8.20}$$

The ISI is expressed as

$$\boldsymbol{\eta}(i) = \sum_{k=1}^{N_u}\sqrt{E_k}\sum_{j=i-\xi}^{i-1}\tilde{\boldsymbol{C}}_k\boldsymbol{h}_k b_k(j) + \sum_{k=1}^{N_u}\sqrt{E_k}\sum_{j=i+1}^{i+\xi}\widehat{\boldsymbol{C}}_k\boldsymbol{h}_k b_k(j),\ \xi = \left\lceil\frac{L-1+q_k}{N}\right\rceil, \tag{8.21}$$

where the code matrices that contain the information from the previous symbol $\tilde{\boldsymbol{C}}_k$ and from the subsequent symbol $\widehat{\boldsymbol{C}}_k \in \mathbb{R}^{M\times L}$ include the last $M-(i-j)N+q_k$ and the first $M-(j-i)N+q_k$ rows of $\boldsymbol{C}_k$, respectively, given by

$$\begin{aligned} \tilde{\boldsymbol{C}}_k &= \begin{bmatrix} \boldsymbol{C}_k(\tilde{\xi}:M,:) \\ \boldsymbol{0} \end{bmatrix},\ \text{with } \tilde{\xi} = (i-j)N - q_k + 1, \\ \widehat{\boldsymbol{C}}_k &= \begin{bmatrix} \boldsymbol{0} \\ \boldsymbol{C}_k(1:\widehat{\xi},:) \end{bmatrix},\ \text{with } \widehat{\xi} = M-(j-i)N+q_k. \end{aligned} \tag{8.22}$$

8.3 Widely Linear Multi-Stage Wiener Filter Algorithm

This section considers one WL reduced-rank framework which is based on the combination of the WL processing and the MSWF technique.

8.3.1 Linear Reduced-Rank Wiener Filter

We first recall the key concept of linear reduced-rank filters as preliminaries and summarize the major results on the Linear MSWF (L-MSWF) algorithm. The cost function of the linear

[1] For a quantity, either a vector $\boldsymbol{x}$ or a matrix $\boldsymbol{X}$, the expression $e^{\boldsymbol{x}}$ or $e^{\boldsymbol{X}}$ returns the exponential for each element in $\boldsymbol{x}$ or $\boldsymbol{X}$ (MATLAB-like notation).

MMSE filter is given by [2]

$$J = \mathbb{E}\left\{\left|b_1(i) - \boldsymbol{w}^H \boldsymbol{r}(i)\right|^2\right\}. \tag{8.23}$$

The Wiener solution can be obtained as

$$\boldsymbol{w}_o = \boldsymbol{R}^{-1}\boldsymbol{p}, \tag{8.24}$$

where $\boldsymbol{p} = \mathbb{E}\{b_1^*(i)\boldsymbol{r}(i)\}$. The filter weights can be estimated by adaptive algorithms such as SG and RLS [Hay02].

However, when a large amount of data is processed, the conventional full-rank filter $\boldsymbol{w} \in \mathbb{C}^M$ that has the same length as the received vector $\boldsymbol{r}(i) \in \mathbb{C}^M$ exhibits a slow convergence and a high interference sensitivity. The reduced-rank technique is able to exploit the key features of the data and to reduce the number of adaptive parameters. The rank-reduction is achieved by transforming the received vector $\boldsymbol{r}(i)$ onto a D-dimensional subspace with $D \ll M$. Let us denote the rank-reduction matrix as $\boldsymbol{S}_D \in \mathbb{C}^{M\times D}$ and the reduced-rank vector is given by $\bar{\boldsymbol{r}}(i) = \boldsymbol{S}_D^H \boldsymbol{r}(i) \in \mathbb{C}^D$. The weight vector $\bar{\boldsymbol{w}} \in \mathbb{C}^D$ is estimated based on $\bar{\boldsymbol{r}}(i)$ and the filter length can be significantly reduced. The linear reduced-rank Wiener solution can be obtained as $\bar{\boldsymbol{w}}_o = \bar{\boldsymbol{R}}^{-1}\bar{\boldsymbol{p}}$, where the reduced-rank covariance matrix is $\bar{\boldsymbol{R}} = \mathbb{E}\{\bar{\boldsymbol{r}}(i)\bar{\boldsymbol{r}}^H(i)\} = \boldsymbol{S}_D^H \boldsymbol{R}\boldsymbol{S}_D$ and the reduced-rank cross-correlation vector is $\bar{\boldsymbol{p}} = \mathbb{E}\{b_1^*(i)\bar{\boldsymbol{r}}(i)\} = \boldsymbol{S}_D^H\boldsymbol{p}$. Similarly to the solutions of the full-rank MMSE filter, we can then calculate the corresponding MMSE

$$\bar{J}_{\min} = 1 - \bar{\boldsymbol{p}}^H \bar{\boldsymbol{R}}^{-1}\bar{\boldsymbol{p}}, \tag{8.25}$$

and the Signal-to-Interference plus Noise Ratio (SINR)

$$\bar{\text{SINR}} = \frac{\bar{\boldsymbol{p}}^H \bar{\boldsymbol{R}}^{-1}\bar{\boldsymbol{p}}}{1 - \bar{\boldsymbol{p}}^H \bar{\boldsymbol{R}}^{-1}\bar{\boldsymbol{p}}} = \frac{1}{\bar{J}_{\min}} - 1. \tag{8.26}$$

8.3.1.1 Linear MSWF

One method to construct the rank-reduction matrix is to apply the L-MSWF [GRS98, HX01]. It is shown in [HG02] that the rank-reduction matrix for the L-MSWF $\boldsymbol{S}_D$ is spanned by D normalized basis vectors $\boldsymbol{f}_1, \ldots, \boldsymbol{f}_D$, where $\boldsymbol{f}_n = \boldsymbol{R}^{n-1}\boldsymbol{p}$ can be chosen. In other words, the linear reduced-rank filter transforms the received signal into the Krylov subspace represented by

$$\boldsymbol{S}_D = \left[\ \boldsymbol{p},\quad \boldsymbol{R}\boldsymbol{p},\quad \ldots,\quad \boldsymbol{R}^{D-1}\boldsymbol{p}\ \right]. \tag{8.27}$$

The MMSE and the output SINR of the L-MSWF asymptotically converge to the linear full-rank case, i.e., $\bar{J}_{\min} \geq J_{\min}$ and $\bar{\text{SINR}} \leq \text{SINR}$. Another important property is that the rank D required to achieve the full rank performance does not scale significantly with the

[2] In some cases when the observation data vector $\boldsymbol{r}(i)$ is not stationary, e.g., it contains time-varying interference, the cost function shown in equation (8.23) also depends on the time index i [BLT01]. For notaional simplicity, we remove the index i in some cases that are related with non-stationary variables such as $\boldsymbol{R}_a$ and $\check{\boldsymbol{R}}$ shown in (8.29).

system size such as the number of users N_u and and the length of the received vector M. Generally, $D \leq 8$ can be chosen. The analysis in [GRS98, HX01] also indicates that D can be decreased without considerably increasing the Mean Square Error (MSE).

The associated adaptive algorithms based on the powers of $\boldsymbol{R}$ given in (8.27) can be carried out in terms of SG or RLS [dLHSN08]. Compared to the full-rank adaptive algorithms, the adaptive L-MSWF with a small rank D can provide a faster convergence speed and a better steady state performance for a given data record.

8.3.2 Widely Linear Multi-Stage Wiener Filter

The main purpose of this section is to investigate the WL-MSWF techniques and compare them to the linear counterpart.

8.3.2.1 Preprocessing: Augmented Vector Formulation

In order to exploit the information contained in both second-order statistics, i.e., $\boldsymbol{R}$ and $\check{\boldsymbol{R}}$, the received signal $\boldsymbol{r}(i)$ and its complex conjugate $\boldsymbol{r}^*(i)$ are formulated into an augmented vector using a bijective transformation $\mathbb{T}$ [BLT01, SGL04]

$$\boldsymbol{r} \xrightarrow{\mathbb{T}} \boldsymbol{r}_a : \qquad \boldsymbol{r}_a = \frac{1}{\sqrt{2}} \begin{bmatrix} \boldsymbol{r}^T, & \boldsymbol{r}^H \end{bmatrix}^T \in \mathbb{C}^{2M\times 1}, \tag{8.28}$$

where $1/\sqrt{2}$ is a scalar which is introduced to facilitate our analysis in the following sections. The filter with coefficients $\boldsymbol{w}_a$, which is designed according to the augmented received vector $\boldsymbol{r}_a(i)$, is widely linear with $\boldsymbol{r}(i)$. It is thus named as a WL filter.

For example, the solution for a WL Wiener filter has a similar expression as in the linear case shown in Section 8.3.1 but with a subscript "a", denoting the augmented quantities. Let us then analyze the augmented covariance matrix, which can be represented by the covariance matrix $\boldsymbol{R}$ and the pseudo-covariance matrix $\check{\boldsymbol{R}}$ of $\boldsymbol{r}(i)$ as

$$\boldsymbol{R}_a = \frac{1}{2} \begin{bmatrix} \boldsymbol{R} & \check{\boldsymbol{R}} \\ \check{\boldsymbol{R}}^* & \boldsymbol{R}^* \end{bmatrix}, \tag{8.29}$$

where

$$\boldsymbol{R} = \sum_{k=1}^{N_u} E_k \check{\boldsymbol{C}}_k \boldsymbol{h}_k \boldsymbol{h}_k^H \check{\boldsymbol{C}}_k^H + \boldsymbol{R}_{\eta\eta} + \boldsymbol{R}_{jj} + N_0 \boldsymbol{I}_M$$

and

$$\check{\boldsymbol{R}} = \sum_{k=1}^{N_u} E_k \check{\boldsymbol{C}}_k \boldsymbol{h}_k \boldsymbol{h}_k^T \check{\boldsymbol{C}}_k^T + \check{\boldsymbol{R}}_{\eta\eta} + \check{\boldsymbol{R}}_{jj}(i).$$

The covariance and pseudo-covariance matrices of the ISI $\boldsymbol{\eta}(i)$ are denoted by $\boldsymbol{R}_{\eta\eta}$ and $\check{\boldsymbol{R}}_{\eta\eta}$

as

$$\begin{aligned}\boldsymbol{R}_{\eta\eta} &= \sum_{k=1}^{N_u} E_k \left(\sum_{j=i-\xi}^{i-1} \tilde{\boldsymbol{C}}_k \boldsymbol{h}_k \boldsymbol{h}_k^H \tilde{\boldsymbol{C}}_k^H + \sum_{j=i+1}^{i+\xi} \widehat{\boldsymbol{C}}_k \boldsymbol{h}_k \boldsymbol{h}_k^H \widehat{\boldsymbol{C}}_k^H \right), \\ \check{\boldsymbol{R}}_{\eta\eta} &= \sum_{k=1}^{N_u} E_k \left(\sum_{j=i-\xi}^{i-1} \tilde{\boldsymbol{C}}_k \boldsymbol{h}_k \boldsymbol{h}_k^T \tilde{\boldsymbol{C}}_k^T + \sum_{j=i+1}^{i+\xi} \widehat{\boldsymbol{C}}_k \boldsymbol{h}_k \boldsymbol{h}_k^T \widehat{\boldsymbol{C}}_k^T \right).\end{aligned}$$

Since the modulated symbols $\boldsymbol{x}_n(i)$ on different sub-carriers are uncorrelated, the second-order statistics of the BPSK-modulated OFDM NBI vector $\boldsymbol{j}(i)$ can be expressed as

$$\begin{aligned}\boldsymbol{R}_{jj} &= \frac{P_J}{N_c} \sum_{n=0}^{N_c-1} e^{j2\pi(f_J+n\cdot\Delta f)\cdot \boldsymbol{K} T_c} \odot \mathbb{E}\left\{ \boldsymbol{x}_n(i) \boldsymbol{x}_n^H(i) \right\}, \\ \check{\boldsymbol{R}}_{jj}(i) &= \frac{P_J}{N_c} \sum_{n=0}^{N_c-1} e^{j[2\pi(f_J+n\cdot\Delta f)\cdot \check{\boldsymbol{K}}(i) T_c + 2\theta]} \odot \mathbb{E}\left\{ \boldsymbol{x}_n(i) \boldsymbol{x}_n^T(i) \right\},\end{aligned} \tag{8.30}$$

where

$$\boldsymbol{K} = \begin{bmatrix} 0 & 1 & \cdots & M-1 \\ -1 & 0 & \cdots & M-2 \\ \vdots & \vdots & \ddots & \vdots \\ -(M-1) & -(M-2) & \cdots & 0 \end{bmatrix}$$

and

$$\check{\boldsymbol{K}}(i) = \begin{bmatrix} 2iN & 2iN+1 & \cdots & 2iN+M-1 \\ 2iN+1 & 2(iN+1) & \cdots & 2iN+M \\ \vdots & \vdots & \ddots & \vdots \\ 2iN+M-1 & 2iN+M & \cdots & 2(iN+M-1) \end{bmatrix}.$$

In our case where BPSK modulated signals are considered, the improperness of $\boldsymbol{r}$ arises from signals of all users, the ISI, and the NBI. Since $\check{\boldsymbol{R}}$ is non-zero, the WL processing is able to take full advantage of this improper nature.

The WL-MMSE or WL Wiener filter has been discussed in [PC95, BLT01]. In Appendix D.1, we present its optimal solution as well as derive the expressions for MMSE and the corresponding SINR. It is also shown that when the data to be estimated are real, the WL Wiener filter weight vector $\boldsymbol{w}_a$ follows the transformation defined in (8.28) such that $\boldsymbol{w}_a = [\ \check{\boldsymbol{w}}^T,\ \ \check{\boldsymbol{w}}^H\ ]^T/\sqrt{2}$, where $\check{\boldsymbol{w}} \in \mathbb{C}^{M\times 1}$. Therefore, for the real estimated data, a key property of the WL filtering is conjugate symmetry defined by

$$\boldsymbol{w}_a^H \boldsymbol{r}_a(i) = \boldsymbol{r}_a^T(i) \boldsymbol{w}_a^* = \Re\left\{ \check{\boldsymbol{w}}^H \boldsymbol{r}(i) \right\}. \tag{8.31}$$

In contrast to the conventional linear filter whose estimate is generally complex, the WL procedure exploits the statistics of both the covariance matrix and the pseudo-covariance matrix, yielding a real estimate with a smaller error.

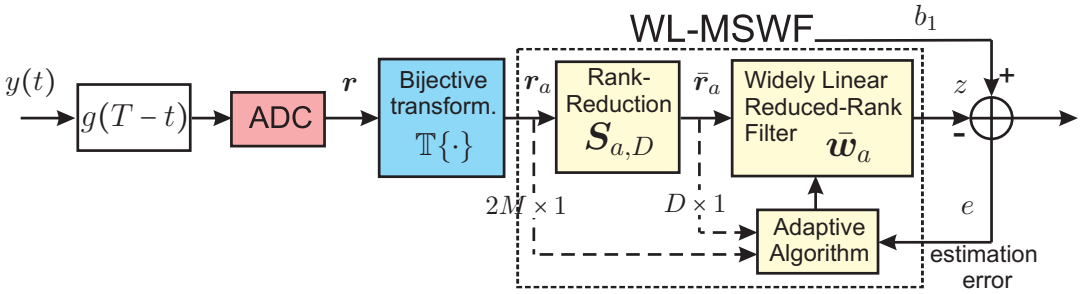

Fig. 8.3: Block diagram of the WL reduced-rank receiver in the complex baseband.

8.3.2.2 Widely Linear Reduced-Rank Filter

In the WL case, the augmented vector with twice the size of the received signal has to be considered. This requires a large number of symbols to reach the steady-state performance and imposes an even higher complexity on the receiver. To this end, the reduced-rank signal processing techniques can be combined with the WL filter to achieve a fast convergence, increased robustness to interference, and a lower complexity.

The principle of the proposed WL reduced-rank receiver is shown in Figure 8.3, where the reduced-rank signal processing and the adaptive receiver design follow after the bijective transformation $\mathbb{T}$. The augmented received signal $\boldsymbol{r}_a$ of dimension $2M$ is then transformed by a rank-reduction matrix $\boldsymbol{S}_{a,D} \in \mathbb{C}^{2M \times D}$ onto a D-dimensional subspace, yielding a reduced-rank vector $\bar{\boldsymbol{r}}_a(i) = \boldsymbol{S}_{a,D}^H \boldsymbol{r}_a(i) \in \mathbb{C}^D$. The WL reduced-rank Wiener solution is written as

$$\bar{\boldsymbol{w}}_{a,o} = \bar{\boldsymbol{R}}_a^{-1} \bar{\boldsymbol{p}}_a, \tag{8.32}$$

where the reduced-rank augmented covariance matrix and the reduced-rank augmented cross-correlation vector are expressed by $\bar{\boldsymbol{R}}_a = \mathbb{E}\left\{\bar{\boldsymbol{r}}_a(i)\bar{\boldsymbol{r}}_a^H(i)\right\} = \boldsymbol{S}_{a,D}^H \boldsymbol{R}_a \boldsymbol{S}_{a,D}$ and $\bar{\boldsymbol{p}}_a = \mathbb{E}\left\{b_1^*(i)\bar{\boldsymbol{r}}_a(i)\right\} = \boldsymbol{S}_{a,D}^H \mathbb{E}\left\{b_1^*(i)\boldsymbol{r}_a(i)\right\} \triangleq \boldsymbol{S}_{a,D}^H \boldsymbol{p}_a$. Using augmented notations, the resulting MMSE and SINR can also be represented in the same fashion as (8.25) and (8.26) by

$$\bar{J}_{a,\min} = 1 - \bar{\boldsymbol{p}}_a^H \bar{\boldsymbol{R}}_a^{-1} \bar{\boldsymbol{p}}_a, \tag{8.33}$$

and

$$\overline{\mathrm{SINR}}_a = \frac{\bar{\boldsymbol{p}}_a^H \bar{\boldsymbol{R}}_a^{-1} \bar{\boldsymbol{p}}_a}{1 - \bar{\boldsymbol{p}}_a^H \bar{\boldsymbol{R}}_a^{-1} \bar{\boldsymbol{p}}_a} = \frac{1}{\bar{J}_{a,\min}} - 1, \tag{8.34}$$

respectively.

It is worth mentioning that if the received signal is second-order circular, the WL solutions become equivalent to the linear case. Therefore, the proposed WL reduced-rank receiver, which additionally requires a bijective transformation before the filtering implementation, can be regarded as a generalized framework.

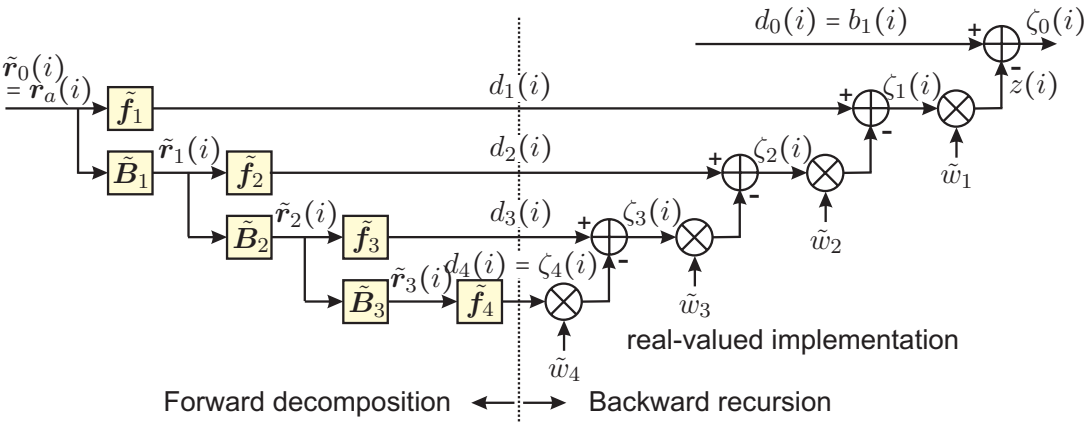

Fig. 8.4: The structure of a 4-stage WL-MSWF.

8.3.2.3 The WL-MSWF Strategies

Total-WL Construction (TWL)

One way to construct the rank-reduction matrix $\boldsymbol{S}_{a,D}$ is to extend the L-MSWF to the widely linear case. Figure 8.4 represents the four-stage MSWF, which consists of several nested filters $\tilde{\boldsymbol{f}}_1, \ldots, \tilde{\boldsymbol{f}}_D \in \mathbb{C}^{2M\times 1}$ and a combining procedure via the weighting coefficients $\tilde{w}_1, \ldots, \tilde{w}_D$. The "observation" data $\tilde{\boldsymbol{r}}_{n-1}(i)$ is successively decomposed by the filters $\tilde{\boldsymbol{f}}_n$ into one direction of the cross-correlation vector and the other subspace orthogonal to this direction by a blocking matrix $\tilde{\boldsymbol{B}}_n$. This matrix satisfies $\tilde{\boldsymbol{B}}_n^H \tilde{\boldsymbol{f}}_n = \boldsymbol{0}$ and can be chosen as the $2M \times 2M$-dimensional matrix $\tilde{\boldsymbol{B}}_n = \boldsymbol{I}_{2M} - \tilde{\boldsymbol{f}}_n \tilde{\boldsymbol{f}}_n^H$. In Figure 8.4, $d_n(i)$ denotes the output of the filter $\tilde{\boldsymbol{f}}_n$ and $\tilde{\boldsymbol{r}}_n(i)$ is the output of $\tilde{\boldsymbol{B}}_n$. When $n = 0$, $d_0(i) = b_1(i)$ is the desired signal and $\tilde{\boldsymbol{r}}_0(i) = \boldsymbol{r}_a(i)$ is the augmented vector of the received signal. At the n-th stage, the filter $\tilde{\boldsymbol{f}}_n$ is calculated according to the cross-correlation between the "desired" data $d_{n-1}(i)$ and the "observation" data vector $\tilde{\boldsymbol{r}}_{n-1}(i)$ from the previous stage

$$\tilde{\boldsymbol{f}}_n = \mathbb{E}\left\{d_{n-1}^*(i)\tilde{\boldsymbol{r}}_{n-1}(i)\right\}, \ \|\tilde{\boldsymbol{f}}_n(i)\| = 1, \ n = 1, \ldots D. \tag{8.35}$$

Then the forward recursion can be continued by

$$d_n(i) = \tilde{\boldsymbol{f}}_n^H \tilde{\boldsymbol{r}}_{n-1}(i), \ n = 1, \ldots, D, \tag{8.36}$$

$$\tilde{\boldsymbol{r}}_n(i) = \tilde{\boldsymbol{B}}_n^H \tilde{\boldsymbol{r}}_{n-1}(i), \ n = 1, \ldots, D-1. \tag{8.37}$$

In the combining phase, the weighting coefficients are designed based on the MMSE criterion, i.e., $\tilde{w}_n$ is chosen so that $\mathbb{E}\left\{|\zeta_{n-1}(i)|^2\right\}$ is minimized. For $n = D, \ldots, 1$, the backward recursion is completed by

$$\tilde{w}_n = \mathbb{E}\left\{d_{n-1}^*(i)\zeta_n(i)\right\} / \mathbb{E}\left\{|\zeta_n(i)|^2\right\} \tag{8.38}$$

$$\zeta_{n-1}(i) = d_{n-1}(i) - \tilde{w}_n^* \zeta_n(i). \tag{8.39}$$

Note that when $n = D$, $\zeta_D(i) = d_D(i)$ and when $n = 1$, $\tilde{w}_1^* \zeta_1(i)$ is the estimate for $d_0(i)$.

Similarly to [HG02], the rank-reduction matrix $\boldsymbol{S}_{a,D}$ defines the D-dimensional subspace spanned by $\tilde{\boldsymbol{f}}_n$ and can be constructed by the Krylov subspace, i.e.,

$$\boldsymbol{S}_{a,D} = \left[\tilde{\boldsymbol{f}}_1, \quad \tilde{\boldsymbol{f}}_2, \quad \ldots, \quad \tilde{\boldsymbol{f}}_D \right] \tag{8.40}$$

$$= \left[\boldsymbol{p}_a, \quad \boldsymbol{R}_a \boldsymbol{p}_a, \quad \ldots, \quad \boldsymbol{R}_a^{D-1} \boldsymbol{p}_a \right]. \tag{8.41}$$

The TWL construction of the rank-reduction matrix fully utilizes the second-order statistics of the observation signal. This scheme is denoted as TWL-MSWF.

Quasi-WL Construction (QWL)

A simpler way to construct the rank-reduction matrix is based on adopting a transformation $\mathbb{T}$ on $\boldsymbol{S}_D$ using the L-MSWF

$$\boldsymbol{S}_{a,D} = \frac{1}{\sqrt{2}} \left[\boldsymbol{S}_D^T, \quad \boldsymbol{S}_D^H \right]^T = \mathbb{T}\{\boldsymbol{S}_D\}, \tag{8.42}$$

where $\boldsymbol{S}_D$ represents the Krylov subspace as shown in (8.27). The reduced-rank vector is thus calculated by $\bar{\boldsymbol{r}}_a(i) = \Re\left\{\boldsymbol{S}_D^H \boldsymbol{r}(i)\right\} = \Re\{\bar{\boldsymbol{r}}(i)\}$, i.e., by taking the real part of the reduced-rank vector from the L-MSWF algorithm. With the QWL design, the general block diagram shown in Figure 8.3 can be simplified to an equivalent model depicted in Figure 8.5, where the block "Widely Linear Reduced-Rank Filter" is still preserved. Compared to the TWL method, the only difference lies in how to construct the the rank-reduction matrix $\boldsymbol{S}_{a,D}$. Both constructions (8.41) and (8.42) can be generalized in the form of $\boldsymbol{S}_{a,D} = \mathbb{T}\left\{\check{\boldsymbol{S}}_D\right\} = \mathbb{T}\{\boldsymbol{S}_D + \Delta\boldsymbol{S}_D\}$, where $\Delta\boldsymbol{S}_D$ contains the difference between the linear and the widely linear designs, i.e., the first M rows of $\boldsymbol{S}_{a,D} - \mathbb{T}\{\boldsymbol{S}_D\}$. If $\Delta\boldsymbol{S}_D = \boldsymbol{0}$, we have a QWL construction, which does not exploit the second-order information contained in the pseudo-covariance matrix $\check{\boldsymbol{R}}$. However, the succeeding filter design still takes advantage of the improper signals, providing a better performance than the L-MSWF. The associated filtering method is named QWL-MSWF. When $D = 1$, i.e., $\boldsymbol{S}_{a,D} = \boldsymbol{p}_a = \mathbb{T}\{\boldsymbol{p}\} = \mathbb{T}\{\boldsymbol{S}_D\}$, the QWL-MSWF and the TWL-MSWF methods have the same performance. We will show in Sections 8.3.2.5 and 8.3.5 that in most cases for improper signals, the TWL-MSWF outperforms the QWL-MSWF.

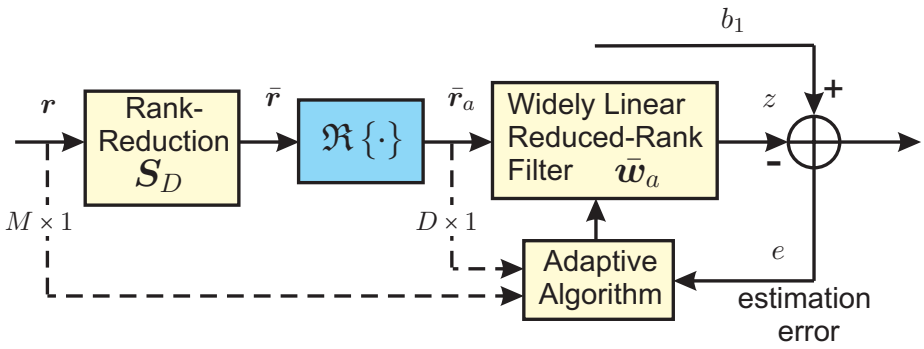

Fig. 8.5: Receiver structure of QWL-MSWF.

8.3.2.4 Comparison with the PCA methods

One of the few WL reduced-rank filters has been proposed in [SS03] using the PCA technique. It is based on the eigen-decomposition of the augmented covariance matrix $\boldsymbol{R}_a = \boldsymbol{V}\boldsymbol{\Sigma}\boldsymbol{V}^H$, where the columns of $\boldsymbol{V} \in \mathbb{C}^{2M\times 2M}$ are the eigenvectors of $\boldsymbol{R}_a$ and $\boldsymbol{\Sigma}$ is a diagonal matrix with the ordered eigenvalues σ_k on its diagonal such that $\sigma_1 \geq \sigma_2 \geq \cdots \geq \sigma_{2M}$. The rank-reduction matrix obtained via PCA is $\boldsymbol{S}_{a,D} = \boldsymbol{V}(:, 1:D)$, which contains the first D columns of $\boldsymbol{V}$, corresponding to the D largest eigenvalues with a descending order. A modified PCA method introduced in [HG02] improves the performance. It chooses the eigenvectors associated with the D largest values of $\left|\boldsymbol{v}_k^H \boldsymbol{p}_a\right|^2 / \sigma_k$, where $\boldsymbol{v}_k$ is the k-th column of $\boldsymbol{V}$. This method selects a set of D eigenvectors to form the rank-reduction matrix that minimizes the MSE.

Compared to the proposed TWL/QWL-MSWF, there are some disadvantages of the above WL-PCA techniques.

1. A larger rank D is required than that for the MSWF.

2. These methods rely on the eigen-decomposition, which is computationally much more expensive.

3. The WL-PCA requires a larger D to achieve a better performance than the linear PCA [SS03].

8.3.2.5 MMSE and SINR Analysis of the WL-MSWF

Let us first consider the L-MSWF described in Section 8.3.1. The eigenvalue decomposition of the reduced-rank covariance matrix can be obtained by $\bar{\boldsymbol{R}} = \boldsymbol{Q}\boldsymbol{\Lambda}\boldsymbol{Q}^H$, where $\boldsymbol{Q}$ contains the eigenvectors $\boldsymbol{q}_k, k = 1, \ldots, D$ and $\boldsymbol{\Lambda}$ is a diagonal matrix consisting of eigenvalues λ_k in a descending order. Applying (8.27) to (8.25), the MMSE of the L-MSWF can thus be expressed as

$$\begin{aligned} \bar{J}_{\min} &= 1 - \boldsymbol{p}^H \boldsymbol{S}_D \boldsymbol{Q}\boldsymbol{\Lambda}^{-1}\boldsymbol{Q}^H \boldsymbol{S}_D^H \boldsymbol{p} \\ &= 1 - \sum_{k=1}^{D} \frac{\left|\boldsymbol{q}_k^H (\boldsymbol{S}_D^H \boldsymbol{p})\right|^2}{\lambda_k}, \end{aligned} \tag{8.43}$$

where it can be easily proven that $\boldsymbol{S}_D^H \boldsymbol{p}$ is real-valued.

Similarly to the linear case, the eigenvalue decomposition of the reduced-rank augmented covariance matrix is computed by

$$\bar{\boldsymbol{R}}_a = \boldsymbol{Q}_a \boldsymbol{\Lambda}_a \boldsymbol{Q}_a^H, \tag{8.44}$$

where the columns of $\boldsymbol{Q}_a$ are the eigenvectors $\boldsymbol{q}_{a,k}, k = 1, \ldots, D$ and $\boldsymbol{\Lambda}_a$ contains the eigenvalues $\lambda_{a,k}$ in a descending order on its diagonal. With $\boldsymbol{p}_a = \mathbb{T}\{\boldsymbol{p}\}$ and $\boldsymbol{S}_{a,D} = \mathbb{T}\left\{\check{\boldsymbol{S}}_D\right\}$, the resulting

MMSE of the WL-MSWF can be written as

$$\begin{aligned}\bar{J}_{a,\min} &= 1 - \boldsymbol{p}_a^H \boldsymbol{S}_{a,D} \boldsymbol{Q}_a \boldsymbol{\Lambda}_a^{-1} \boldsymbol{Q}_a^H \boldsymbol{S}_{a,D}^H \boldsymbol{p}_a \\ &= 1 - \sum_{k=1}^{D} \frac{\left| \boldsymbol{q}_{a,k}^H (\boldsymbol{S}_{\boldsymbol{a},\boldsymbol{D}}^H \boldsymbol{p}_a) \right|^2}{\lambda_{a,k}} \\ &= 1 - \sum_{k=1}^{D} \frac{\left| \boldsymbol{q}_{a,k}^H \left(\check{\boldsymbol{S}}_D^H \boldsymbol{p} + \check{\boldsymbol{S}}_D^T \boldsymbol{p}^* \right) / 2 \right|^2}{\lambda_{a,k}} \\ &= 1 - \sum_{k=1}^{D} \frac{\left| \boldsymbol{q}_{a,k}^H \Re \left\{ \check{\boldsymbol{S}}_D^H \boldsymbol{p} \right\} \right|^2}{\lambda_{a,k}}. \end{aligned} \tag{8.45}$$

The MMSE is mainly determined by the eigenvalues of $\bar{\boldsymbol{R}}_a$. In Appendix D.2, we show that $\lambda_{a,k} < \lambda_k, k = 1, 2, \ldots, D, D \ll K$ with K being the number of eigenvectors of $\boldsymbol{R}$ (or $\boldsymbol{R}_a$) that correspond to the signal subspace. This applies to both the TWL and the QWL constructions, except for the TWL case when there is strong NBI (cf. Section 8.3.5.1). If the QWL is applied, $\check{\boldsymbol{S}}_D = \boldsymbol{S}_D$ holds and thus (8.45) is simplified to

$$\bar{J}_{a,\min} = 1 - \sum_{k=1}^{D} \frac{\left| \boldsymbol{q}_{a,k}^H (\boldsymbol{S}_{\boldsymbol{D}}^H \boldsymbol{p}) \right|^2}{\lambda_{a,k}}. \tag{8.46}$$

When the TWL is used, more information can be explored, yielding a smaller MMSE than the QWL. Therefore, a comparison of (8.43) and (8.45) indicates that even with the same filter length D, the MMSE of the WL-MSWF estimate with both constructions is smaller than that of the L-MSWF, i.e., $\bar{J}_{a,\min} < \bar{J}_{\min}$. Since the SINR has a simple relationship with the MMSE as shown in (8.26), $\overline{\text{SINR}}_a > \overline{\text{SINR}}$ holds. This will be verified in Section 8.3.5.1.

8.3.2.6 Properties of the WL-MSWF

If the real-valued data is estimated, the WL-MSWF has the following key properties.

1. The conjugate symmetric property of the WL receiver processing shows that after the multi-stage decomposition, the reduced-rank vector $\bar{\boldsymbol{r}}_a(i)$, the filter weight vector $\bar{\boldsymbol{w}}_a(i)$, the decision variable $z(i)$, and the estimation error $e(i)$ are all real-valued.

   First, we consider $n = 1$ ($d_0(i)$ is BPSK-modulated and real-valued),

$$\begin{aligned}\tilde{\boldsymbol{f}}_1 &= \mathbb{E}\{d_0^*(i)\tilde{\boldsymbol{r}}_0(i)\} \\ &= \left[\mathbb{E}\left\{d_0^*(i)\boldsymbol{r}^T(i)\right\}, \quad \mathbb{E}\left\{d_0^*(i)\boldsymbol{r}^H(i)\right\} \right]^T / \sqrt{2} \\ &= \left[\boldsymbol{f}_1^T, \quad \boldsymbol{f}_1^H \right]^T / \sqrt{2} = \mathbb{T}\{\boldsymbol{f}_1\}, \end{aligned} \tag{8.47}$$

   where $\boldsymbol{f}_1$ corresponds to the 1-st stage filter for the linear MSWF. Equation (8.47) shows that the forward WL filter of the WL-MSWF $\tilde{\boldsymbol{f}}_1$ can be constructed by $\mathbb{T}\{\boldsymbol{f}_1\}$.

The output of $\tilde{\boldsymbol{f}}_1$ is computed by

$$d_1(i) = \tilde{\boldsymbol{f}}_1^H \tilde{\boldsymbol{r}}_0(i) = \mathbb{T}\{\boldsymbol{f}_1\}^H \mathbb{T}\{\boldsymbol{r}(i)\} = \Re\left\{\boldsymbol{f}_1^H \boldsymbol{r}(i)\right\},$$

which is real as well. The blocking matrix for the WL-MSWF is

$$\begin{aligned}\tilde{\boldsymbol{B}}_1 &= \boldsymbol{I}_{2M} - \tilde{\boldsymbol{f}}_1 \tilde{\boldsymbol{f}}_1^H = \boldsymbol{I}_{2M} - \mathbb{T}\{\boldsymbol{f}_1\}\mathbb{T}\{\boldsymbol{f}_1\}^H \\ &= \boldsymbol{I}_{2M} - \frac{1}{\sqrt{2}}\begin{bmatrix} \boldsymbol{f}_1\boldsymbol{f}_1^H & \boldsymbol{f}_1\boldsymbol{f}_1^T \\ \boldsymbol{f}_1^*\boldsymbol{f}_1^H & \boldsymbol{f}_1^*\boldsymbol{f}_1^T \end{bmatrix} = \begin{bmatrix} \boldsymbol{B}_1 & \check{\boldsymbol{B}}_1 \\ \check{\boldsymbol{B}}_1^* & \boldsymbol{B}_1^* \end{bmatrix},\end{aligned}$$

where $\boldsymbol{B}_1 \triangleq \boldsymbol{I}_M - \boldsymbol{f}_1\boldsymbol{f}_1^H/2$ is the linear counterpart and $\check{\boldsymbol{B}}_1 \triangleq \boldsymbol{I}_M - \boldsymbol{f}_1\boldsymbol{f}_1^T/2$ is called the complementary covariance blocking matrix. We can then compute the "observation" vector as

$$\begin{aligned}\tilde{\boldsymbol{r}}_1(i) &= \tilde{\boldsymbol{B}}_1^H \tilde{\boldsymbol{r}}_0(i) = \begin{bmatrix} \boldsymbol{B}_1 & \check{\boldsymbol{B}}_1 \\ \check{\boldsymbol{B}}_1^* & \boldsymbol{B}_1^* \end{bmatrix}^H \mathbb{T}\{\boldsymbol{r}(i)\} \\ &= \frac{1}{\sqrt{2}}\begin{bmatrix} \boldsymbol{B}_1^H\boldsymbol{r}(i) + \check{\boldsymbol{B}}_1^T\boldsymbol{r}^*(i) \\ \check{\boldsymbol{B}}_1^H\boldsymbol{r}(i) + \boldsymbol{B}_1^T\boldsymbol{r}^*(i) \end{bmatrix} \triangleq \frac{1}{\sqrt{2}}\begin{bmatrix} \check{\boldsymbol{r}}_1(i) \\ \check{\boldsymbol{r}}_1^*(i) \end{bmatrix} \\ &= \mathbb{T}\{\check{\boldsymbol{r}}_1(i)\},\end{aligned} \tag{8.48}$$

which has the same construction as $\tilde{\boldsymbol{r}}_0(i)$. The calculation can be carried out recursively as $n = 2, 3, \ldots, D$. It can be easily shown that the $d_n(i)$, $n = 1, \ldots, D$ in (8.36) are real-valued. Since $\tilde{w}_n$ is computed from $n = D$, where $\epsilon_D(i) = d_D(i)$ is real, the whole combining operation in Figure 8.4 is real-valued.

2. With increasing D, the MMSE and the output SINR of the WL-MSWF converge to the solutions of the WL full-rank Wiener filter.

3. In contrast to the eigen-decomposition methods, the WL-MSWF inherently extracts key characteristics of the processed data and the rank D required to achieve the full-rank performance is much smaller.

4. With the same rank D, the WL-MSWF outperforms the L-MSWF in terms of the MMSE and the maximum SINR.

5. The rank D required to approach the full-rank performance is only slightly affected by the system load such as the number of users N_u, the NBI, as well as the processing gain N and the number of channel taps L, which determine the ISI impact.

6. Compared to the full-rank filters, the complexity is significantly reduced by using the reduced-rank techniques [HG02, dLHSN08]. On the one hand, due to the processing on the augmented received vector, the WL forward decomposition has a higher complexity compared to the linear case. On the other hand, it has been shown that the combining

phase of the WL-MSWF is carried out on real-valued data, which alleviates the computational efforts. It is worth mentioning that the QWL-MSWF design simply deals with the real part of the reduced-rank vector from the L-MSWF algorithm. Consequently, it has an even lower complexity than the L-MSWF. The complete computational complexity analysis will be addressed in Section 8.3.4.

8.3.3 Adaptive Algorithms and Convergence Analysis

In this section we develop two training-based adaptive algorithms, the SG and the RLS, for the proposed WL-MSWF techniques. The convergence performance of the WL adaptive schemes based on the SG has been discussed in [AH10, SGL04]. However, it is of prime interest to evaluate the convergence behavior of the adaptive reduced-rank algorithms. In this section, we focus on the convergence analysis of both the SG and the RLS versions of the WL-MSWF as well as the comparison with their linear counterparts.

8.3.3.1 SG and RLS Adaptive Algorithms for the WL-MSWF

The rank-reduction matrix $\boldsymbol{S}_{a,D}$ for the TWL is constructed based on estimating the augmented covariance matrix $\boldsymbol{R}_a$ and the augmented cross-correlation vector $\boldsymbol{p}_a$ by

$$\boldsymbol{R}_a(i) = \lambda \boldsymbol{R}_a(i-1) + \boldsymbol{r}_a(i)\boldsymbol{r}_a^H(i) \tag{8.49}$$

$$\boldsymbol{p}_a(i) = \lambda \boldsymbol{p}_a(i-1) + b_1^\star(i)\boldsymbol{r}_a(i), \tag{8.50}$$

where $0 < \lambda < 1$ is the forgetting factor and $b_1(i)$ is the i-th training symbol. Using (8.41), the rank-reduction matrix at time instant i can thus be calculated by

$$\boldsymbol{S}_{a,D}(i) = \left[\; \boldsymbol{p}_a(i), \quad \boldsymbol{R}_a(i)\boldsymbol{p}_a(i), \quad \ldots, \quad \boldsymbol{R}_a^{D-1}(i)\boldsymbol{p}_a(i) \; \right]. \tag{8.51}$$

The QWL construction $\boldsymbol{S}_{a,D}$ is obtained by (8.42), where $\boldsymbol{R}(i)$ and $\boldsymbol{p}(i)$ are recursively estimated. Table 8.1 [3] and Table 8.2 show the related SG and RLS algorithms for the WL-MSWF, where δ and $\tilde{\delta}$ are initialization scalars to ensure the numerical stability. In Table 8.2, the reduced-rank augmented covariance matrix is given by $\bar{\boldsymbol{R}}_a(i) = \boldsymbol{S}_{a,D}^H(i)\boldsymbol{R}_a(i)\boldsymbol{S}_{a,D}(i)$ and the RLS scheme estimates its inverse $\bar{\boldsymbol{R}}_a^{-1}(i)$.

8.3.3.2 Convergence Analysis of the WL-MSWF with SG

Weight Error Correlation Matrix and Step Size

The filter weight error is defined by

$$\boldsymbol{\epsilon}_a(i) = \bar{\boldsymbol{w}}_a(i) - \bar{\boldsymbol{w}}_{a,o}, \tag{8.52}$$

[3] We use this "complex conjugate" to have a general expression, since for linear filtering methods, the estimate z might be complex-valued. The real-valued estimate is observed as one special property of the WL algorithms, when the data to be estimated is real (e.g., BPSK).

Tab. 8.1: SG Adaptive Algorithm for WL-MSWF

Initialize the algorithm by setting: $\boldsymbol{p}_a(0) = \mathbf{0}, \boldsymbol{R}_a(0) = \delta \boldsymbol{I}_M, \bar{\boldsymbol{w}}_a(0) = \mathbf{0}$
Choose the rank D and the step size μ For the time index $i = 1, 2, \ldots, N_s$ The rank-reduction matrix is estimated by TWL or QWL The reduced-rank vector $\bar{\boldsymbol{r}}_a(i) = \boldsymbol{S}_{a,D}^H(i)\boldsymbol{r}_a(i)$ The estimate of $b_1(i)$ is $z(i) = \bar{\boldsymbol{w}}_a^H(i)\bar{\boldsymbol{r}}_a(i)$ The estimation error $e(i) = b_1(i) - z(i)$ Update the WL-MSWF $\bar{\boldsymbol{w}}_a(i+1) = \bar{\boldsymbol{w}}_a(i) + \mu e^*(i)\bar{\boldsymbol{r}}_a(i)$ End

Tab. 8.2: RLS Adaptive Algorithm for WL-MSWF

Initialize the algorithm by setting: $\boldsymbol{p}_a(0) = \mathbf{0}, \boldsymbol{R}_a(0) = \delta \boldsymbol{I}_M, \bar{\boldsymbol{p}}_a(0) = \mathbf{0}, \bar{\boldsymbol{R}}_a^{-1}(0) = \tilde{\delta}^{-1}\boldsymbol{I}_D, \bar{\boldsymbol{w}}_a(0) = \mathbf{0}$
Choose the rank D, For the time index $i = 1, 2, \ldots, N_s$ The rank-reduction matrix is estimated by TWL or QWL The reduced-rank vector $\bar{\boldsymbol{r}}_a(i) = \boldsymbol{S}_{a,D}^H(i)\boldsymbol{r}_a(i)$ The estimate of $b_1(i)$ is $z(i) = \bar{\boldsymbol{w}}_a^H(i)\bar{\boldsymbol{r}}_a(i)$ The recursive calculation: $\boldsymbol{k}(i) = \bar{\boldsymbol{R}}_a^{-1}(i-1)\bar{\boldsymbol{r}}_a(i)$ $\boldsymbol{g}(i) = \dfrac{\lambda^{-1}\boldsymbol{k}(i)}{1 + \lambda^{-1}\bar{\boldsymbol{r}}_a^H(i)\boldsymbol{k}(i)}$ $\bar{\boldsymbol{R}}_a^{-1}(i) = \lambda^{-1}\bar{\boldsymbol{R}}_a^{-1}(i-1) - \lambda^{-1}\boldsymbol{g}(i)\bar{\boldsymbol{r}}_a^H(i)\bar{\boldsymbol{R}}_a^{-1}(i-1)$ $\bar{\boldsymbol{p}}_a(i) = \lambda\bar{\boldsymbol{p}}_a(i-1) + b_1^*(i)\bar{\boldsymbol{r}}_a(i)$ Update the WL-MSWF $\bar{\boldsymbol{w}}_a(i) = \bar{\boldsymbol{R}}_a^{-1}(i)\bar{\boldsymbol{p}}_a(i)$ End

where $\bar{\boldsymbol{w}}_{a,o}$ is the optimal WL-MSWF solution (cf. equation (8.32)) with the closed-form reduced-rank matrix $\boldsymbol{S}_{a,D}$ obtained from (8.41) or (8.42). Applying the SG algorithm and the direct-averaging method [Hay02], the adaptation of the weight error can be represented by

$$\boldsymbol{\epsilon}_a(i+1) = \left(\boldsymbol{I}_D - \mu\bar{\boldsymbol{R}}_a(i)\right)\boldsymbol{\epsilon}_a(i) + \bar{\boldsymbol{r}}_a(i)e_o^*(i), \tag{8.53}$$

where $\bar{\boldsymbol{R}}_a(i) = \boldsymbol{S}_{a,D}^H(i)\boldsymbol{R}_a(i)\boldsymbol{S}_{a,D}(i)$ and $e_o(i) = b_1(i) - \bar{\boldsymbol{w}}_{a,o}^H\bar{\boldsymbol{r}}_a(i)$ is the estimation error produced by $\bar{\boldsymbol{w}}_{a,o}$. The correlation matrix of the weight error vector $\boldsymbol{\epsilon}_a(i)$ is defined as

$$\boldsymbol{K}_a(i) = \mathbb{E}\left\{\boldsymbol{\epsilon}_a(i)\boldsymbol{\epsilon}_a^H(i)\right\}. \tag{8.54}$$

Applying the weight error adaptation in (8.53) and the principle of independence, we get

$$\boldsymbol{K}_a(i+1) = \left(\boldsymbol{I}_D - \mu\bar{\boldsymbol{R}}_a\right)\boldsymbol{K}_a(i)\left(\boldsymbol{I}_D - \mu\bar{\boldsymbol{R}}_a\right) + \mu^2\bar{J}_{a,\min}\bar{\boldsymbol{R}}_a, \tag{8.55}$$

with $\bar{J}_{a,\min} = \mathbb{E}\left\{|e_o(i)|^2\right\}$ and $\bar{\boldsymbol{R}}_a$ defined in Section 8.3.2.2. Using the eigen-decomposition of $\bar{\boldsymbol{R}}_a$ shown in equation (8.44) and the matrix transformation $\boldsymbol{X}_a(i+1) = \boldsymbol{Q}_a^H \boldsymbol{K}_a(i+1)\boldsymbol{Q}_a$, we can rewrite (8.55) as

$$\boldsymbol{X}_a(i+1) = (\boldsymbol{I}_D - \mu\boldsymbol{\Lambda}_a)\,\boldsymbol{X}_a(i)\,(\boldsymbol{I}_D - \mu\boldsymbol{\Lambda}_a) + \mu^2 \bar{J}_{a,\min}\boldsymbol{\Lambda}_a, \tag{8.56}$$

For the diagonal element of $\boldsymbol{X}_a(i)$, we get

$$x_{a,k}(i+1) = \left(1 - \mu\lambda_{a,k}\right)^2 x_{a,k}(i) + \mu^2 \bar{J}_{a,\min}\lambda_{a,k}, \quad k = 1, \ldots, D. \tag{8.57}$$

In order to ensure the convergence, $\left(1 - \mu\lambda_{a,k}\right)^2 < 1$ should be satisfied. Thus, the step size should be chosen such that

$$0 < \mu < \frac{2}{\max\{\lambda_{a,k}\}}, \; k = 1, \ldots, D. \tag{8.58}$$

Similarly, the step size of the L-MSWF-SG approach satisfies $0 < \mu < \dfrac{2}{\max\{\lambda_k\}}$, $k = 1, \ldots, D$. Since for $k = 1, \ldots, D, D < K, \lambda_{a,k} < \lambda_k$ is observed, indicating that the step size of the WL-MSWF-SG algorithm can be larger than the L-MSWF-SG.

The Mean Square Error Learning Curve

The MSE of the WL-MSWF-SG algorithm at time i can be expressed as [Hay02]

$$\bar{J}_a(i) = \mathbb{E}\left\{|e(i)|^2\right\} = \bar{J}_{a,\min} + \operatorname{tr}\left\{\bar{\boldsymbol{R}}_a \boldsymbol{K}_a(i)\right\}, \tag{8.59}$$

where $\bar{J}_{a,\min}$ is calculated by (8.33). Applying the eigen-decomposition of $\bar{\boldsymbol{R}}_a$, the excess MSE $\bar{J}_{a,\mathrm{ex}}(i)$ can be represented as

$$\begin{aligned} \bar{J}_{a,\mathrm{ex}}(i) &= \bar{J}_a(i) - \bar{J}_{a,\min} = \operatorname{tr}\left\{\bar{\boldsymbol{R}}_a \boldsymbol{K}_a(i)\right\} \\ &= \operatorname{tr}\left\{\boldsymbol{\Lambda}_a \boldsymbol{X}_a(i)\right\} = \sum_{k=1}^{D} \lambda_{a,k} x_{a,k}(i). \end{aligned} \tag{8.60}$$

When the steady state is achieved, i.e., $i \to \infty$, we get

$$\begin{aligned} \bar{J}_a(\infty) &= \bar{J}_{a,\min} + \mu\bar{J}_{a,\min} \sum_{k=1}^{D} \frac{\lambda_{a,k}}{2 - \mu\lambda_{a,k}} \\ &\approx \bar{J}_{a,\min} + \frac{\mu\bar{J}_{a,\min}}{2} \sum_{k=1}^{D} \lambda_{a,k}, \quad \mu \text{ small}, \end{aligned} \tag{8.61}$$

meaning that $\bar{J}_{a,\mathrm{ex}(\infty)} \approx \dfrac{\mu\bar{J}_{a,\min}}{2} \sum_{k=1}^{D} \lambda_{a,k}$. Considering that $\bar{J}_{a,\min} < \bar{J}_{\min}, \lambda_{a,k} < \lambda_k, k = 1, \ldots, D, D < K$ shown in Section 8.3.2.5, we can conclude that the steady-state MSE and excess MSE of the WL-MSWF-SG method are both smaller than that of the linear case, i.e., $\bar{J}_a(\infty) < \bar{J}(\infty)$ and $\bar{J}_{a,\mathrm{ex}}(\infty) < \bar{J}_{\mathrm{ex}}(\infty)$.

The transient behavior of the MSE is mainly determined by the excess MSE, consisting of the transient excess MSE $\bar{J}_{a,\text{extrans}}(i)$ and the steady-state excess MSE [Hay02] as

$$\bar{J}_{a,\text{ex}}(i) = \boldsymbol{\lambda}_a^H \boldsymbol{x}_a(i) = \bar{J}_{a,\text{extrans}}(i) + \bar{J}_{\text{a,ex}}(\infty), \tag{8.62}$$

where $\boldsymbol{\lambda}_a = [\lambda_{a,1}, \ldots, \lambda_{a,D}]^T$ and $\boldsymbol{x}_a(i) = [x_{a,1}(i), \ldots, x_{a,D}(i)]^T$. The transient quantity can be written as

$$\bar{J}_{a,\text{extrans}}(i) = \sum_{k=1}^{D} c_{a,k}^i \boldsymbol{\lambda}_a^H \boldsymbol{g}_{a,k} \boldsymbol{g}_{a,k}^H \left[\boldsymbol{x}_a(0) - \boldsymbol{x}_a(\infty)\right], \tag{8.63}$$

where $c_{a,k}$ and $\boldsymbol{g}_{a,k}$ are the k-th eigenvalue and eigenvector of a matrix $\boldsymbol{B}_a \in \mathbb{C}^{D\times D}$ with components at the k-th row and j-th column

$$b_{akj} = \begin{cases} \left(1 - \mu\lambda_{a,k}\right)^2, & k = j \\ \mu^2 \lambda_{a,k}\lambda_{aj}, & k \neq j \end{cases}. \tag{8.64}$$

We can further calculate

$$\begin{aligned} \boldsymbol{x}_a(0) &= \text{diag}\left\{\boldsymbol{Q}_a^H \boldsymbol{K}_a(0) \boldsymbol{Q}_a\right\}, \quad \boldsymbol{K}_a(0) = \bar{\boldsymbol{w}}_{a,o} \bar{\boldsymbol{w}}_{a,o}^H \\ x_{a,k}(\infty) &= \frac{\mu}{2 - \mu\lambda_a} \bar{J}_{a,\min}, \quad k = 1, \ldots, D. \end{aligned} \tag{8.65}$$

It will be shown via experiments that the WL-MSWF-SG algorithm has a smaller transient excess MSE than the linear method, showing a superior convergence performance for the WL case even with the same rank D.

8.3.3.3 Convergence Analysis of the WL-MSWF with RLS

Weight Error Correlation Matrix

To analyze the RLS implementation of the WL-MSWF receiver shown in Table 8.2, we assume the forgetting factor $\lambda = 1$ and obtain the weight error as follows [Hay02]

$$\boldsymbol{\epsilon}_a(i) = \bar{\boldsymbol{w}}_a(i) - \bar{\boldsymbol{w}}_{a,o} = \bar{\boldsymbol{R}}_a^{-1}(i) \sum_{n=1}^{i} \bar{\boldsymbol{r}}_a(n) e_o^*(n), \tag{8.66}$$

where

$$e_o(i) = b_1(i) - \bar{\boldsymbol{w}}_{a,o}^H \bar{\boldsymbol{r}}_a(i) \tag{8.67}$$

is the estimation error produced by the optimal solution $\bar{\boldsymbol{w}}_{a,o}$. We assumed $e_o(n)$ to be white with zero-mean and variance σ_e^2, where

$$\mathbb{E}\left\{e_o(m) e_o^*(n)\right\} = \begin{cases} \sigma_e^2 = \bar{J}_{a,\min}, m = n \\ 0, \qquad\qquad m \neq n. \end{cases} \tag{8.68}$$

The weight error correlation matrix can then be expressed as

$$\begin{aligned}\boldsymbol{K}_a(i) &= \mathbb{E}\left\{\boldsymbol{\epsilon}_a(i)\boldsymbol{\epsilon}_a^H(i)\right\} &(8.69)\\ &= \bar{J}_{a,\min}\mathbb{E}\left\{\bar{\boldsymbol{R}}_a^{-1}(i)\sum_{n=1}^{i}\sum_{m=1}^{i}\bar{\boldsymbol{r}}_a(m)\bar{\boldsymbol{r}}_a^H(n)\bar{\boldsymbol{R}}_a^{-1}(i)\right\}\\ &= \bar{J}_{a,\min}\mathbb{E}\left\{\bar{\boldsymbol{R}}_a^{-1}(i)\right\}\\ &= \frac{\bar{J}_{a,\min}}{i-D-1}\bar{\boldsymbol{R}}_a^{-1}, \quad i > D+1 &(8.70)\end{aligned}$$

The Learning Curve of a priori Estimation Error

In RLS algorithms, the a priori estimation error defined by $\xi(i) = b_1(i) - \bar{\boldsymbol{w}}_a^H(i-1)\bar{\boldsymbol{r}}_a(i)$ is chosen to characterize the learning curve [Hay02] (cf. Appendix D.1.1). By eliminating $b_1(i)$ based on the expression of $e_o(i)$, we can represent $\xi(i)$ in terms of the weight error $\boldsymbol{\epsilon}_a(i-1)$ as

$$\xi(i) = e_o(i) - \boldsymbol{\epsilon}_a^H(i-1)\bar{\boldsymbol{r}}_a(i). \tag{8.71}$$

The resulting learning curve is expressed as

$$\begin{aligned}\bar{J}'_a(i) &= \mathbb{E}\left\{|\xi(i)|^2\right\} = \bar{J}_{a,\min} + \mathrm{tr}\left\{\bar{\boldsymbol{R}}_a\boldsymbol{K}_a(i-1)\right\}\\ &= \bar{J}_{a,\min} + \frac{D}{i-D-1}\bar{J}_{a,\min}, \quad i > D+1 &(8.72)\end{aligned}$$

Compared to SG in (8.60) and (8.62), the learning curve of RLS indicates that the excess MSE $\bar{J}'_{a,\mathrm{ex}}(i) = \dfrac{D}{i-D-1}\bar{J}_{a,\min}$ vanishes as $i \to \infty$ and does not depend on the eigenvalue spread of $\bar{\boldsymbol{R}}_a$. In the steady state, a zero excess MSE can be reached by the RLS algorithm, exhibiting a faster convergence and a higher robustness than the SG method. Since $\bar{J}_{a,\min} < \bar{J}_{\min}$, the transient excess MSE of the WL-MSWF-RLS approach is smaller than those of the linear counterparts even with the same rank D, i.e., $\bar{J}'_{a,\mathrm{ex}}(i) < \bar{J}'_{\mathrm{ex}}(i)$.

8.3.4 Complexity Analysis

The computational complexity of the adaptive algorithms is estimated according to the number of real additions and real multiplications per iteration for each received symbol of size M. The estimated computational complexity of the proposed WL-MSWF schemes is summarized in Table 8.3, where we consider the existing algorithms for comparison. Figure 8.6 illustrates the total number of real operations (additions and multiplications) per iteration per symbol for each algorithm as a function of M, where the rank of the MSWF $D = 4$ is chosen. For all the algorithms, the SG always has a lower complexity than RLS. In the full-rank case, the WL-SG is slightly simpler than the L-SG due to the conjugate symmetric property of the WL approaches, while the multiplication of bigger matrices results in a higher complexity of the WL-RLS than that of the L-RLS. In the MSWF, the construction of the rank-reduction

matrix that requires a higher-order matrix multiplication imposes more computational efforts than the full-rank case. A larger D will considerably increase the computational costs. We can observe that the proposed TWL-MSWF SG/RLS methods exhibit the highest complexity. It is worth emphasizing that the proposed QWL-MSWF SG/RLS algorithms are slightly less complex than the L-MSWF counterparts and significantly reduce the complexity compared to the full-rank WL-RLS.

Tab. 8.3: Estimated computational complexity according to the number of real operations

Algorithms	Additions	Multiplications
L-Full-SG	$8M$	$8M+2$
WL-Full-SG	$6M-1$	$6M+1$
L-MSWF-SG	$4(D-1)M^2+2(D+1)M+6D$	$4(D-1)M^2+4D(M+2)+2$
QWL-MSWF-SG	$4(D-1)M^2+2(D+1)M$	$4(D-1)M^2+2D(2M+1)+1$
TWL-MSWF-SG	$8(D-1)M^2+2(D+1)M$	$8(D-1)M^2+2D(2M+1)+1$
L-Full-RLS	$12M^2+2M-1$	$16M^2+10M+2$
WL-Full-RLS	$20M^2+2M-1$	$28M^2+10M+1$
L-MSWF-RLS	$4(D-1)M^2+2M(D+1)+12D^2-1$	$4(D-1)M^2+2D(2M+5)+16D^2+2$
QWL-MSWF-RLS	$4(D-1)M^2+2M(D+1)+(D-1)^2+1$	$4(D-1)M^2+4DM+(2D+1)^2$
TWL-MSWF-RLS	$8(D-1)M^2+2M(D+1)+(D-1)^2+1$	$8(D-1)M^2+4DM+(2D+1)^2$

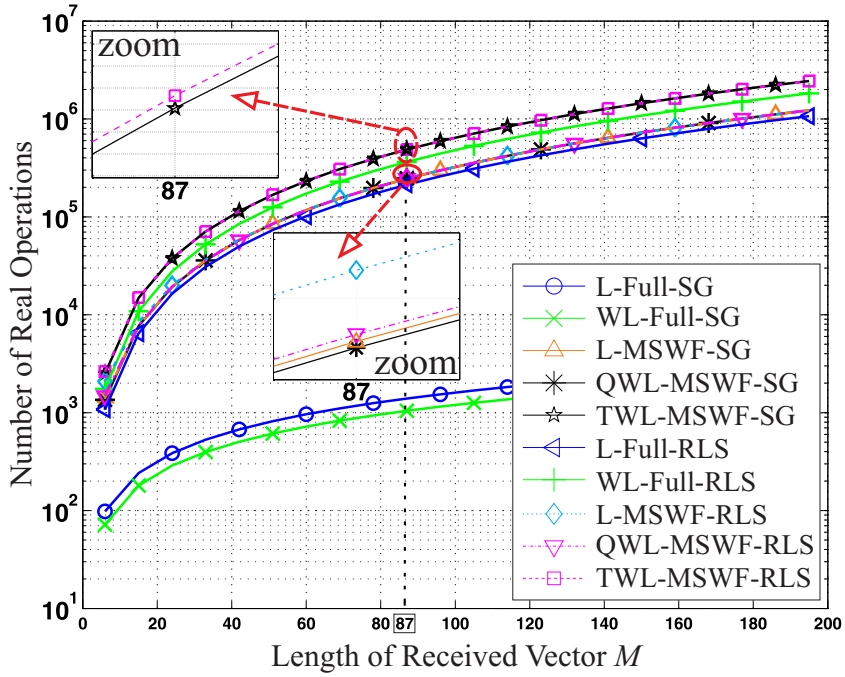

Fig. 8.6: Computational complexity in terms of real additions and multiplications per iteration per symbol as a function of M. For MSWF schemes, $D = 4$ is chosen. The zoomed-in curves are also shown at $M = 87$.

8.3.5 Simulation Results

In this section, we evaluate the steady-state, the transient, and the convergence performance of the proposed TWL/QWL-MSWF schemes and compare them with the linear MSWF, the linear/WL full-rank Wiener filters (cf. Appendix D.1.1), as well as the linear/WL PCA-based reduced-rank methods. The rank-dependent performance along with the adaptive rank selection algorithms are presented. We further analyze the SINR performance of the proposed methods in the case when the desired signal is second-order circular (e.g., QPSK-modulated signal) but the interference (MUI or NBI) is non-circular.

For the multipath propagation channel, we use UWB channels measured in a line-of-sight office of size 5 m × 5 m × 2.6 m (cf. Section 2.3). The RRC pulse is chosen with $B_3 = 500$ MHz and $\beta = 0.3$. At the receiver, the sampling rate of the ADC is 1 GHz and thus the channel resolution is 1 ns. The maximum channel delay is 64 ns. We assume that the UWB channel is time-invariant block fading during the estimation. The DS code of length $N = 24$ is generated pseudo-randomly for the DS-UWB system. The dimension of the received vector $\boldsymbol{r}$ is $M = 87$. The parameters of the OFDM interference used for the simulations are shown in Table 8.4, where the cyclic prefix and the guard interval are not considered for simplicity[4] and the OFDM symbol period T_J is larger than the symbol duration. We consider a scheme in which the proposed adaptive WL-MSWF algorithms are first trained by a pilot sequence of 400 symbols and are then switched to the decision-directed mode.

Tab. 8.4: Parameters for IEEE 802.11a OFDM signal

modulation	f_{OFDM}	N_c	Δf	T_J
BPSK	5.22 GHz	48	312.5 KHz	4 μs

8.3.5.1 Achievable SINR and Transient Analysis

The simulation results are presented to validate the theoretical analysis in Sections 8.3.3.2 and 8.3.3.3. We first compare the eigenvalues of the reduced-rank covariance matrix for both linear and WL cases ($\bar{\boldsymbol{R}}$ and $\bar{\boldsymbol{R}}_a$). Figure 8.7(a) depicts the eigenvalues using linear, QWL, and TWL reduced-rank matrix constructions for $D = 2, 4, 6$, where the number of users $N_u = 16$, $E_b/N_0 = 15$ dB, and NBI is absent. It is observed that the eigenvalues of using both TWL and QWL constructions are smaller than the linear case, i.e., $\lambda_{a,k} < \lambda_k, k = 1, \ldots, D$, meaning that a larger step size for WL-MSWF-SG algorithms can be chosen compared to the L-MSWF-SG (cf. (8.58)). When the NBI is present, the eigenvalues are shown in Figure 8.7(b) with $D = 4$. With very low SIR, the TWL-MSWF method has larger eigenvalues ($k = 3, 4$) than the L-MSWF due to the "contribution" of the strong NBI. However, the dominant eigenvalues (i.e., $k = 1, 2$) of TWL-MSWF are no greater than L-MSWF at various SIR values. Figure

[4] The overall spectrum does not change with the cyclic prefix or the guard interval. This implies that the performance of the algorithms will not be affected by adding the guard interval for the OFDM signal. Therefore, we ignore this for simplicity.

8.7(c) plots the eigenvalues changing with the number of users, which shows the higher values of L-MSWF than those of the TWL/QWL-MSWF algorithms. The SINR values of different schemes as a function of E_b/N_0 (dB), SIR, and the number of users, are also illustrated in Figure 8.9, where the rank $D = 4$ is chosen. It can be clearly seen that both the TWL-MSWF and QWL-MSWF outperform the L-MSWF in terms of the SINR and the TWL construction which utilizes more second-order information produces a higher SINR than the QWL case. The performance gain of the TWL over the QWL increases with the number of users, cf., Figure 8.9(c).

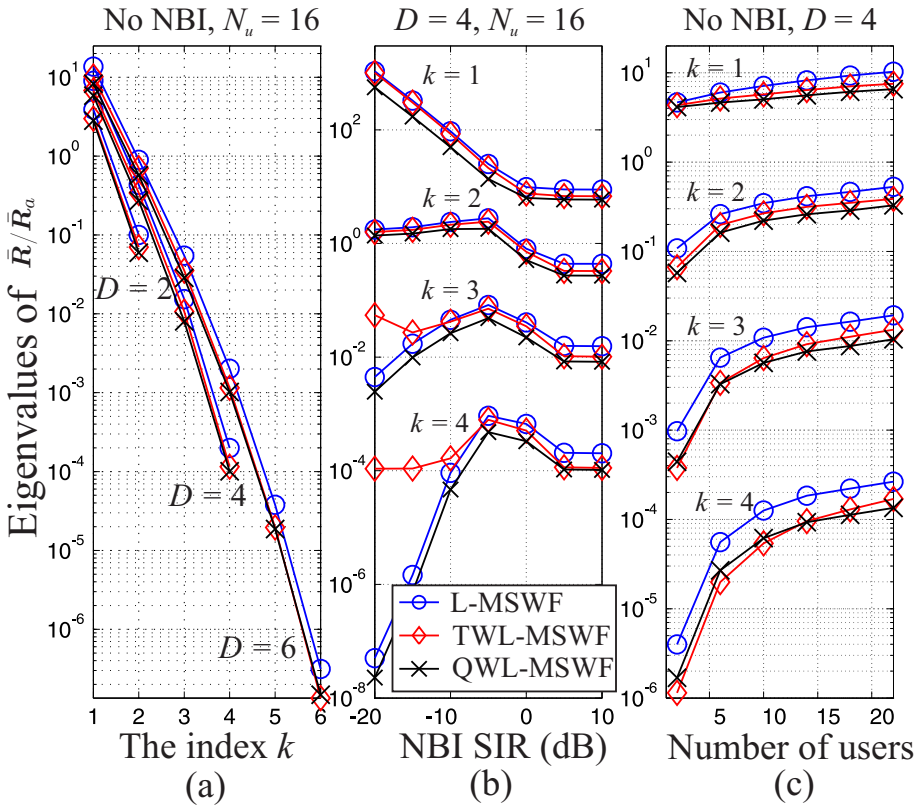

Fig. 8.7: Eigenvalues of the reduced-rank covariance matrix constructed by L/TWL/QWL-MSWF algorithms with $E_b/N_0 = 15$ dB versus (a) the k-th stage projection for different D, (b) various SIR in the presence of OFDM NBI, and (c) different number of users.

The BER with respect to the achievable SINR can be well approximated using a Gaussian approximation by the following equation [Pro01],

$$\text{BER} \approx \text{Q}\left(\sqrt{\text{SINR}}\right), \tag{8.73}$$

where $\text{Q}(\alpha) = \frac{1}{\sqrt{2\pi}} \int_{\alpha}^{\infty} e^{-\frac{x^2}{2}} dx$. Figure 8.8 shows the calculated BERs for L-/TWL-/QWL-MSWF as a function of the number of users in the presence/absence of OFDM NBI for $D = 4$. It can be observed that the number of users that can be supported by TWL-/QWL-MSWF

is much larger than that by L-MSWF [5]. In this specified case, when there is no NBI, TWL-MSWF can accommodate 28 users and 24 users in the presence of NBI. For QWL-MSWF, 19 and 17 users can be served with and without NBI, respectively. The L-MSWF is only able to support 11 and 12 users accordingly. In summary, this shows that given a value of rank D, the proposed TWL-/QWL-MSWF schemes are more robust to interference and can accommodate more users compared to the L-MSWF.

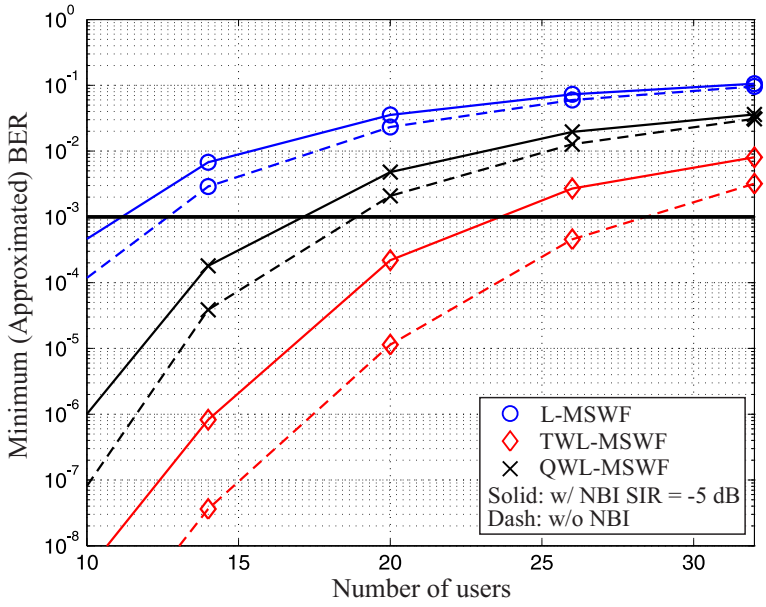

Fig. 8.8: The (approximated) BER of the L/TWL/QWL-MSWF schemes versus N_u. We choose E_b/N_0 = 15 dB and OFDM NBI of SIR = -5 dB.

We assess the SINR of the proposed TWL/QWL-MSWF algorithms as a function of the rank D and compare them to the PCA-based reduced-rank filters shown in Figure 8.10. The performance of the full-rank linear/WL schemes is shown only for the case, where NBI is present and N_u = 16. The conventional PCA method that uses the first D eigenvectors of $\boldsymbol{V}$ corresponding to D largest eigenvalues of $\boldsymbol{R}$ or $\boldsymbol{R}_a$ in a descending order is denoted as "PCA-conv". The modified PCA scheme is called "PCA-modi". As D increases, i.e., more signal information is utilized, the SINR increases until it gets close to the full-rank state. The TWL-MSWF only requires the rank D = 2 to D = 6 to achieve the highest SINR and the selected D is only slightly affected by the number of users and the presence of NBI. For both the PCA-conv and the PCA-modi, the necessary D to approach the full-rank SINR is quite sensitive to the number of users but not to the presence of NBI, e.g., to obtain the best performance, we need D = 10 for the 2-user case and $D > 60$ for N_u = 16. The QWL-MSWF cannot reach the WL full-rank SINR but it still outperforms the PCA-based methods with a much smaller rank. For N_u = 16 with $D < 35$, the advantage of the WL-PCA-conv scheme over the L-PCA-conv is lost, unless a higher rank is chosen. With the same rank D, the WL-

[5] In the uncoded case, 10^{-3} is regarded as the reference BER (or 9.8 dB as the reference SINR) for communications systems.

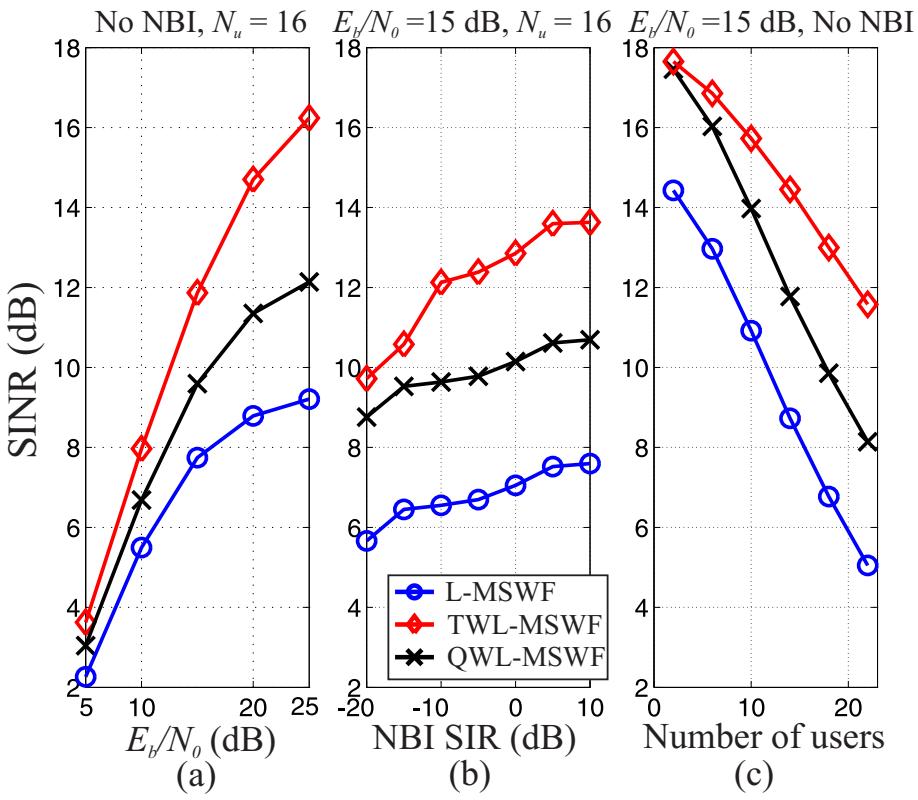

Fig. 8.9: The SINR of L/TWL/QWL-MSWF algorithms versus (a) E_b/N_0 (dB), (b) various SIR in the presence of OFDM NBI, and (c) different number of users.

PCA-modi method exhibits a higher SINR than the L-PCA-modi, since the D eigenvectors are selected to minimize the MSE.

Figure 8.11 shows the transient excess MSE of the training-based SG algorithms $\bar{J}_{a,\text{extrans}}(i)$ for the TWL/QWL-MSWF-SG schemes compared to the linear counterpart. It is assumed that the augmented covariance matrix is known and is computed by (8.29). We consider the step size $\mu = 0.02$ without NBI and $\mu = 0.024$ in the presence of NBI, $N_u = 16, E_b/N_0 = 15$ dB, and $D = 4$. For each time instant, the excess MSE of the WL methods is smaller than that of the linear case and TWL exhibits a better transient performance than QWL.

8.3.5.2 BER Convergence Performance

We show the BER performance of the adaptive TWL/QWL-MSWF algorithms and compare it to the existing methods in Figure 8.12(a) for SG and in (b) for RLS. The rank $D = 4$ is chosen as a representative value to compare the performance of different schemes. It is obvious that all the RLS algorithms outperform the SG in the convergence and tracking performances. Even with the same D, the TWL-MSWF which fully exploits the second-order behavior of the non-circular signal performs the best. Since the QWL-MSWF constitutes the rank-reduction matrix from the linear estimates and utilizes the complementary covariance statistics only for the weight adaptation, it still exhibits a better convergence performance than the L-MSWF

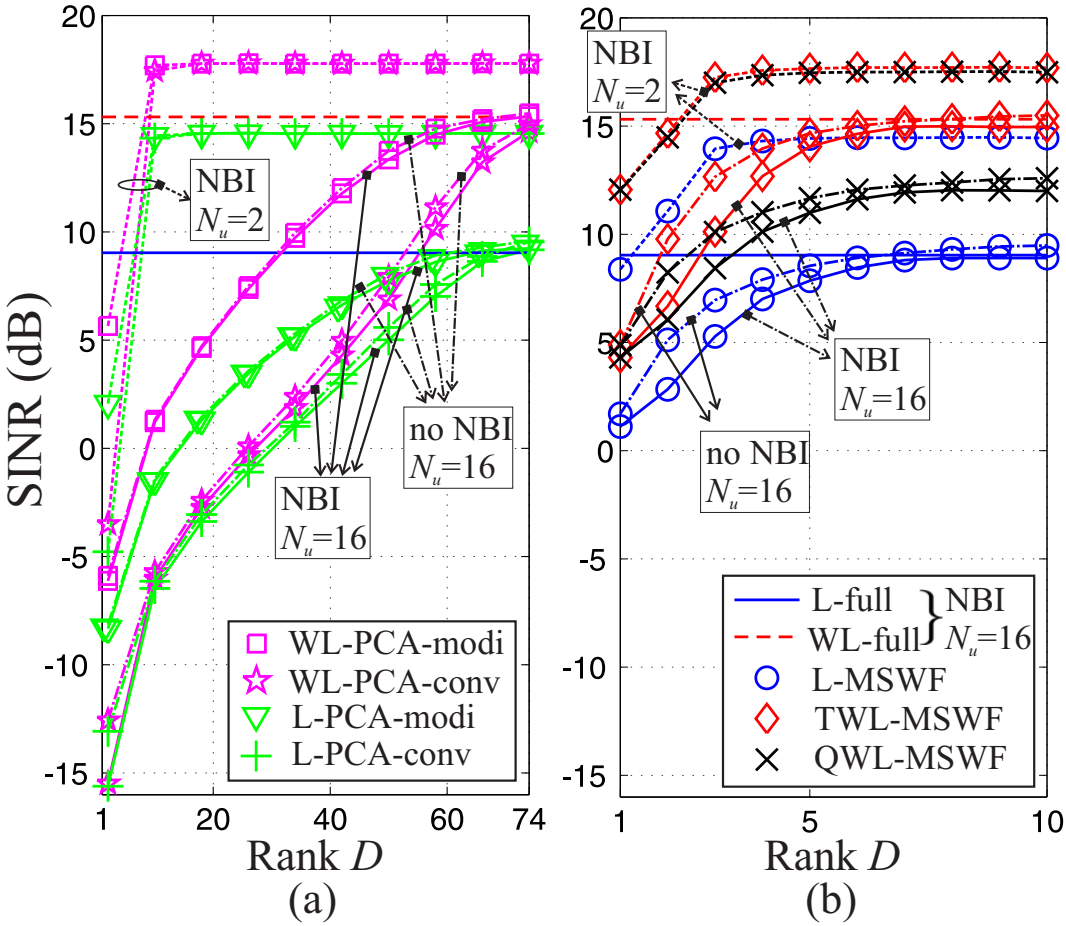

Fig. 8.10: The SINR of the discussed algorithms versus the rank D for (a) the L/WL-PCA algorithms and for (b) the L/TWL/QWL-MSWF algorithms. We consider E_b/N_0 = 15 dB, N_u = 2, 16, OFDM NBI of SIR = -5 dB. The performance of the full-rank linear/WL schemes is shown only for the case, where NBI is present and N_u = 16.

but has a lower complexity. The proposed TWL/QWL-MSWF algorithms show a better BER performance compared to the WL full-rank counterparts. The reason is that after the augmented received signal of a dimension $2M$ is projected onto a Krylov subspace with a much lower dimension D, the estimation of filter weights is only based on a small amount of parameters. This implies a faster convergence to the steady-state performance.

8.3.5.3 Rank-Dependent Performance

The number of parameters for estimating the filter weights, i.e., the rank D, has an influence on the performance of the proposed adaptive algorithms. We first examine the BER performance versus the rank D and then introduce an adaptive rank selection method. Figure 8.13 depicts the BER of the TWL/QWL-MSWF algorithms as a function of the rank D, where the performances of the L-MSWF as well as the full-rank counterparts are included for comparison. It can be observed that for both SG and RLS algorithms, D = 4 provides the best performance. It is worth remarking that D = 3 which performs the same as D = 4 is preferred

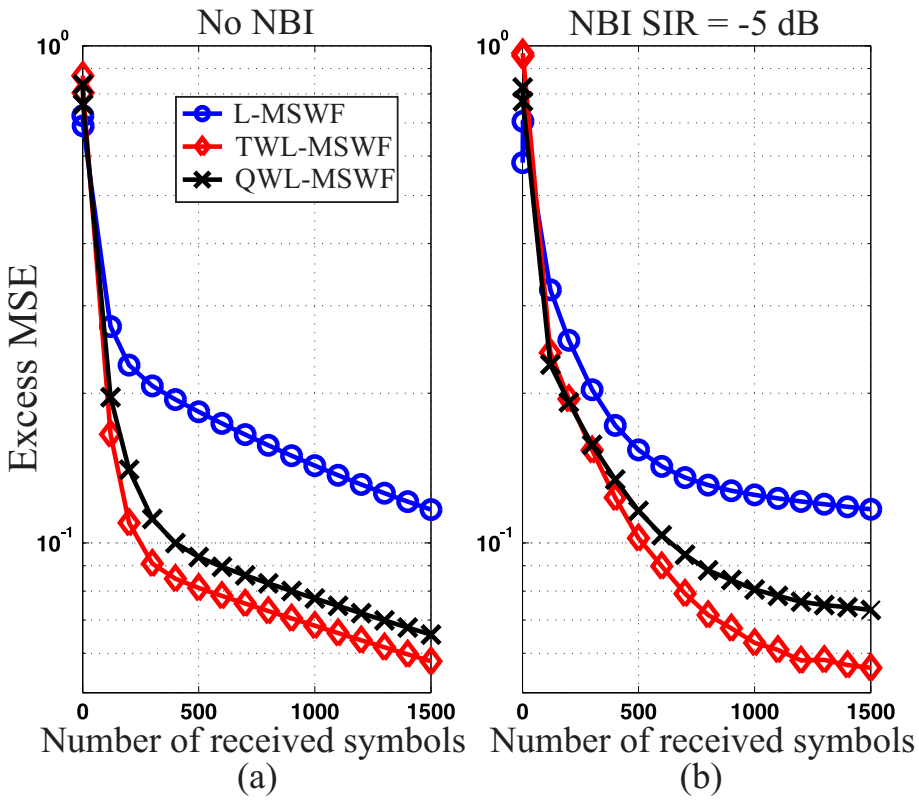

Fig. 8.11: The transient excess MSE of L/TWL/QWL-MSWF-SG algorithms in the cases when OFDM NBI is absent (a) and present (b). It is chosen that $E_b/N_0 = 15$ dB, $D = 4$, and $N_u = 16$.

for the SG methods.

The performance of the proposed algorithms is rank-dependent. A smaller rank D provides a faster convergence at the beginning of the adaptation and a larger D results in a better steady-state performance (cf. Figure 8.14). Thereby, the rank can be adapted to ensure both advantages. We employ an adaptive method proposed in [HG02] to select the rank D, based on the MSE estimate from *a posteriori* least-squares cost function

$$\mathscr{C}_d(i) = \sum_{m=1}^{i} \lambda^{i-m} \left| b_1(m) - \bar{\boldsymbol{w}}_{a,d}^H(m-1)\boldsymbol{S}_{a,d}^H(m-1)\boldsymbol{r}_a(m) \right|^2, \tag{8.74}$$

where d represents the rank to be chosen and λ is the exponential weighting factor. For each received symbol, the optimal rank that minimizes the exponentially weighted cost function (8.74) is selected

$$D_{\text{opt}}(i) = \arg \min_{D_{\min} \le d \le D_{\max}} \mathscr{C}_d(i), \tag{8.75}$$

$D_{\min}$ and $D_{\max}$ are the minimum and maximum ranks considered. We assess the adaptive rank selection technique for the TWL/QWL-MSWF with both SG and the RLS adaptive algorithms as shown in Figure 8.14, where the performance using a fixed rank is also included for comparison. We choose the range of the considered rank is $D_{\min} = 2$ and $D_{\max} = 6$. By adapting the rank at each received symbol, both a fast convergence and a better steady-

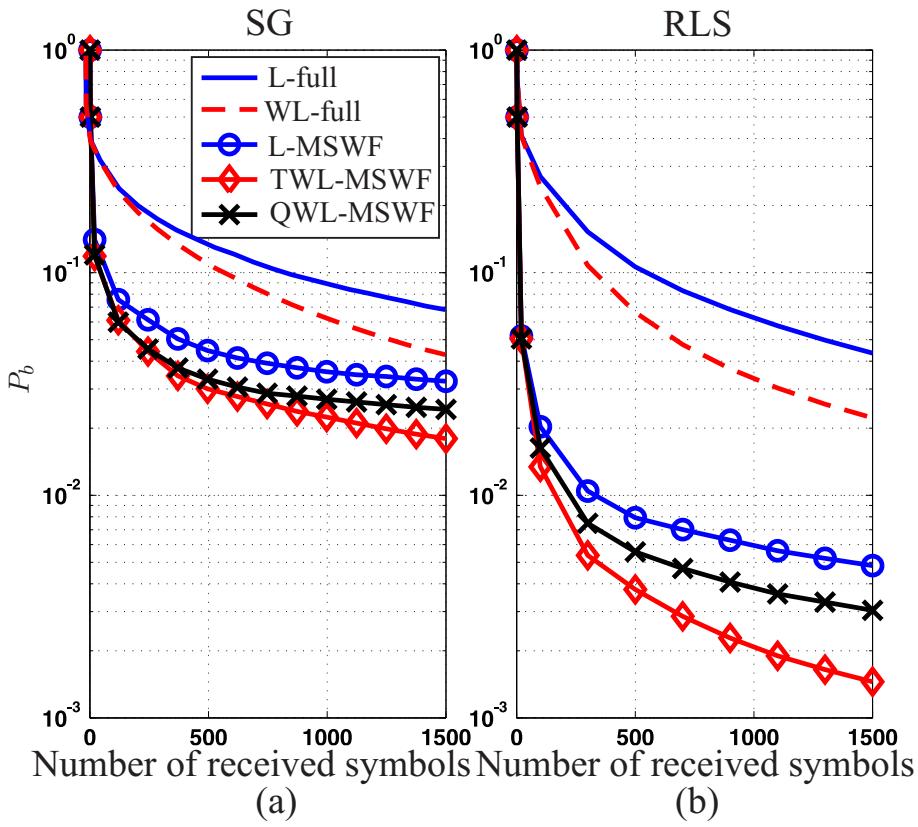

Fig. 8.12: The BER convergence performance of (a) SG and (b) RLS algorithms for E_b/N_0 = 15 dB, N_u = 16, and OFDM-NBI with SIR = -5 dB. We consider D = 4 for the MSWF techniques.

state performance can be attained. The complexity of the adaptive rank selection algorithm lies in the adaptation of the involved quantities for $D_{\min} \leq d \leq D_{\max}$ and the additional calculations of the cost function in (8.74). The complexity can be reduced by switching off the rank-selection after the steady state is reached.

8.3.5.4 Other Applicable Situations

In the above discussions, we consider the case when both the desired signal and the interferences (MUI as well as NBI) are strictly non-circular. In the following, we show the proposed TWL/QWL-MSWF algorithms are still applicable and outperform the L-MSWF in the situation when the desired signal is second-order circular but the interference is non-circular (i.e., the received observation vector $\boldsymbol{r}$ is still non-circular). If $\boldsymbol{r}$ is second-order circular, the performance of the WL algorithms is the same with the linear counterpart. In Figure 8.15(a), QPSK is considered for all the users and the same processing gain N = 24 is chosen for simplicity. It is obvious that since no advantage can be exploited for the circular observation data (QPSK), the WL methods performs the same as the linear one. Figure 8.15(b) and (c) show the case when the desired signal is QPSK modulated (second-order circular) but the interference is non-circular, i.e., MUI is BPSK modulated with N = 24 and NBI is the BPSK-OFDM signal.

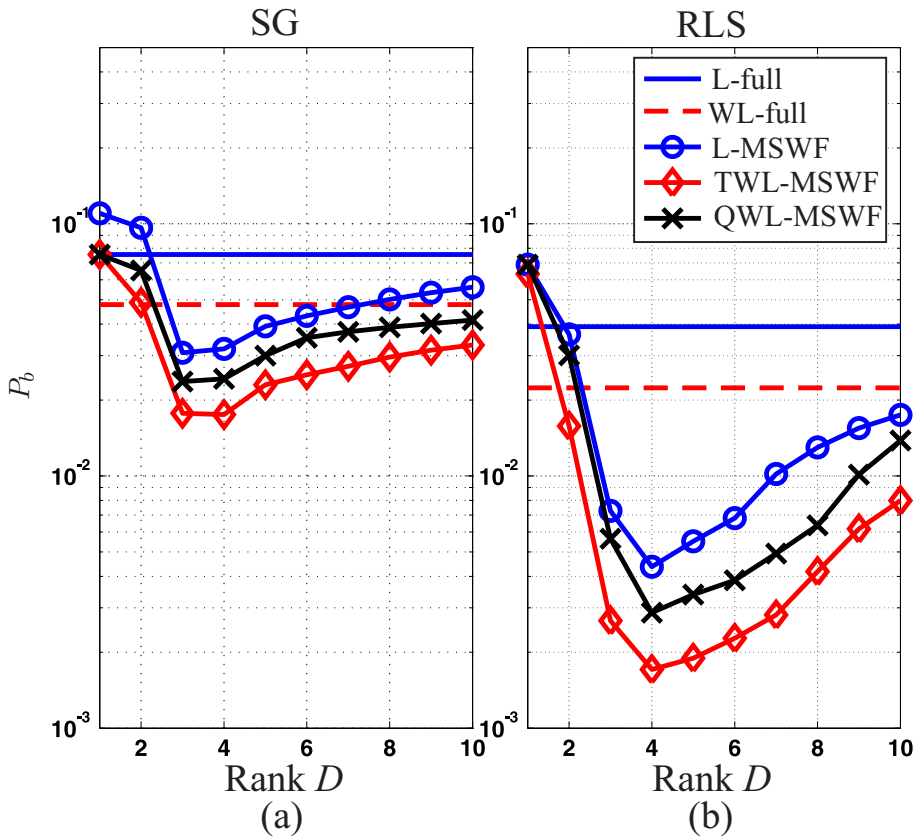

Fig. 8.13: The BER performance of (a) SG and (b) RLS algorithms versus the rank D for E_b/N_0 = 15 dB, N_u = 16, and OFDM-NBI with SIR = -5 dB. The number of the received symbols is chosen as 1500.

The WL schemes fully exploit the second-order information of the interference, showing a superior performance over the linear scheme.

8.3.5.5 Using One-Bit ADC

The proposed method is based on at least the Nyquist sampling rate, which requires a huge technical effort on the UWB transceiver devices such as high-speed Analog-to-Digital Converter (ADC)s. To alleviate the power consumption, we maintain the high sampling rate but restrict the ADC resolution b to be low, e.g., $b = 1$ (cf. Chapter 6). Figure 8.16 illustrates the BER convergence performance for the training-based SG and RLS algorithms using a one-bit ADC and compares it with the full-resolution case. The results indicate the suitability of applying a one-bit ADC to the proposed receiving algorithm, where a small performance degradation due to the quantization is observed.

8.3.6 Conclusions

To suppress the ISI, the MUI, and the NBI in a high data rate DS-UWB system, we propose a WL-MSWF receiver and develop the corresponding adaptive algorithms (i.e., SG and RLS).

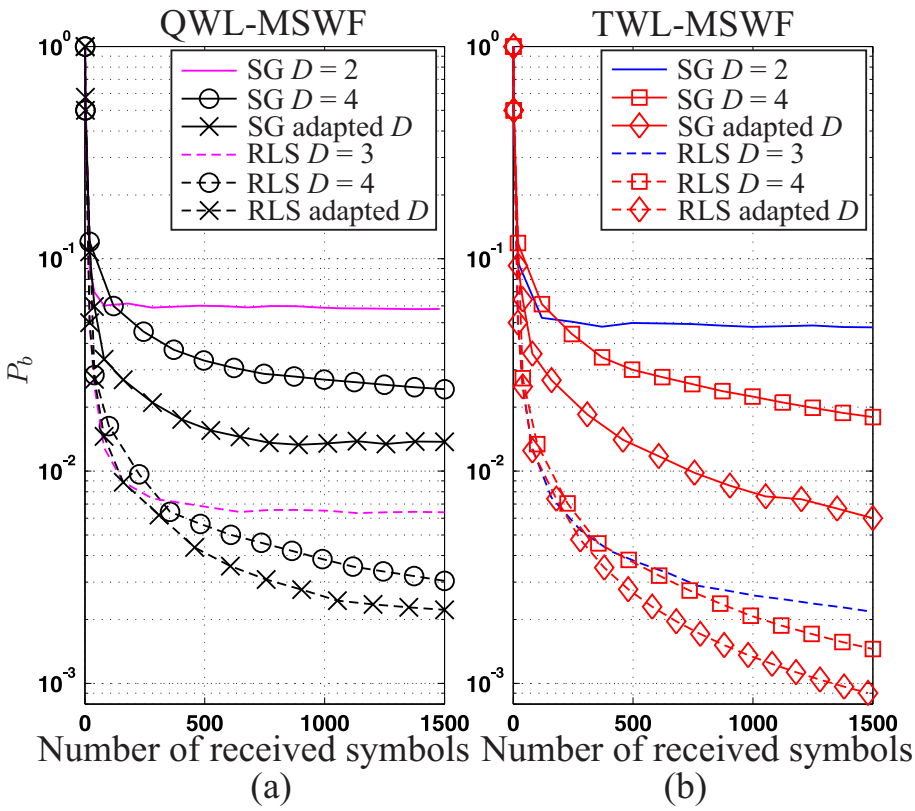

Fig. 8.14: The BER convergence performance of the adaptive rank selection method for (a) the QWL-MSWF and (b) the TWL-MSWF. We choose E_b/N_0 = 15 dB, N_u = 16, and OFDM-NBI with SIR = -5 dB.

Based on the linear MSWF concept, two constructions of the rank-reduction matrix (TWL and QWL) are derived. The TWL/QWL-MSWF schemes fully/partially exploit the second-order information of the non-circular signal, yielding a higher SINR than the L-MSWF. Compared to the WL-PCA methods, the proposed TWL/QWL-MSWF are simpler and can approach the optimal MMSE with a much smaller rank. We show that the QWL-MSWF can be simplified by taking the real part of the reduced-rank vector after the low-rank transformation in the L-MSWF receiver, indicating a lower complexity. The computational complexity in terms of the number of real additions and multiplications is estimated for the associated SG and RLS adaptive algorithms. The convergence analysis shows that the step size of the WL-MSWF-SG can be larger than that of the L-MSWF-SG. From the MSE point of view, the proposed adaptive algorithms (SG and RLS) exhibit a better transient behavior than their linear counterparts.

Extensive simulation results in terms of the SINR and the BER convergence performance are presented to assist the theoretical analyses. It is shown that the TWL/QWL-MSWF perform better than the existing techniques and the TWL-MSWF provides the best performance. The BER of the WL-MSWF is rank-dependent, where the rank $D = 3$ is desired for the SG algorithm and $D = 4$ for the RLS. Furthermore, we assess an adaptive rank selection method for the WL-MSWF to achieve both a faster convergence and a better steady-state

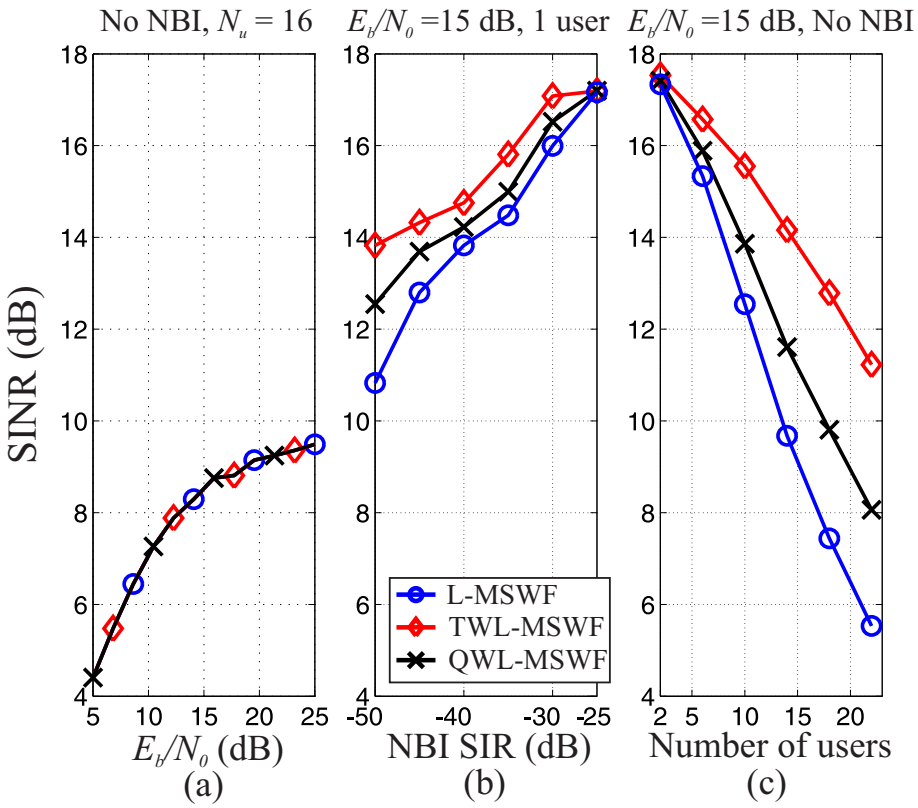

Fig. 8.15: The SINR of L/TWL/QWL-MSWF algorithms for the QPSK system versus (a) E_b/N_0 (dB), (b) various SIR in the presence of BPSK-OFDM NBI, and (c) different number of users (MUI is BPSK modulated with $N = 24$).

performance. Under the situation when the desired signal is second-order circular but the interference (MUI or NBI) is non-circular, the proposed WL-MSWF still outperforms the L-MSWF.

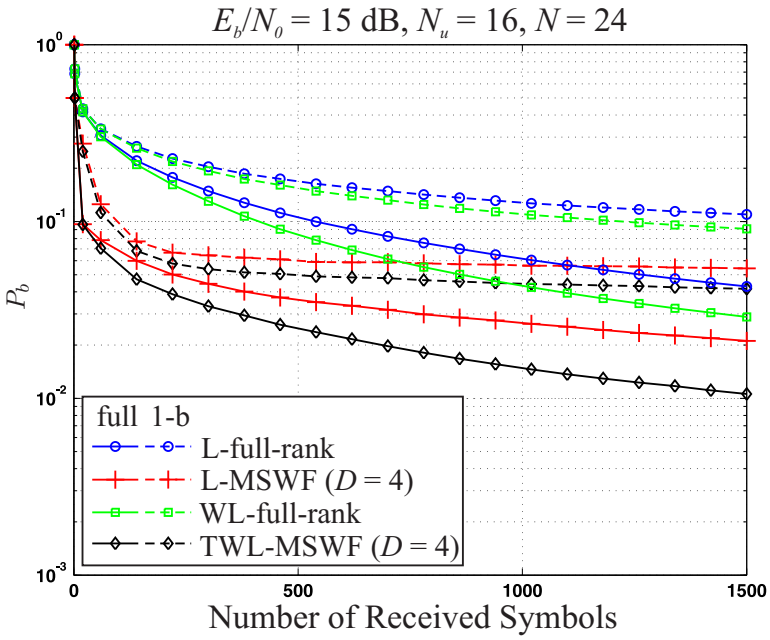

(a) SG

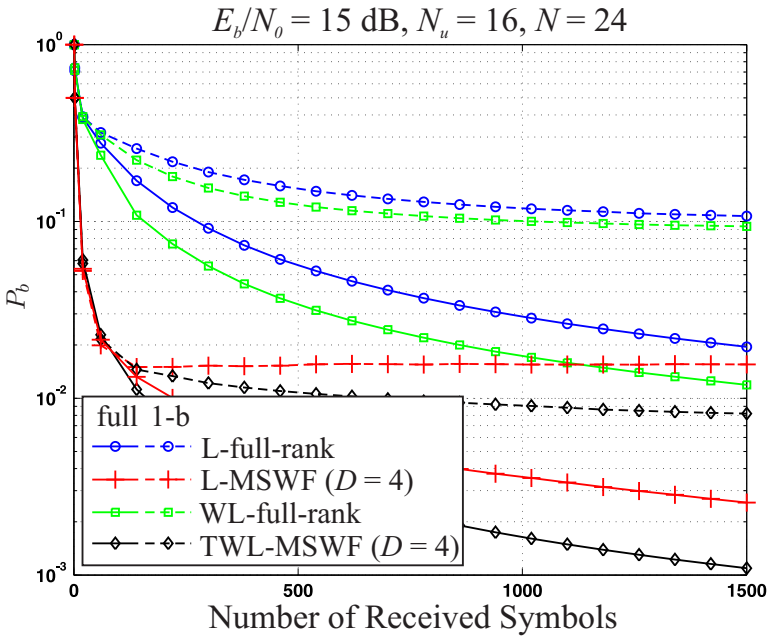

(b) RLS

Fig. 8.16: BER convergence performance of SG and RLS algorithms using full-resolution and one-bit ADCs.

8.4 Iterative Widely Linear Auxiliary Vector Filtering Algorithm

This section proposes another WL reduced-rank framework which combines the WL processing with the AVF, an iterative algorithm to compute the Minimum Variance Distortionless Response (MVDR) filter, for non-circular signals. The data model as described in Section 8.2 is utilized.

8.4.1 WL-MVDR Filter

Similar to the traditional MVDR filter, the WL-MVDR weight vector $\boldsymbol{w}_{a,\mathrm{MVDR}}$ is calculated by solving the following constrained optimization problem

$$\begin{aligned} &\text{minimize } \mathbb{E}\left\{|z|^2\right\} = \mathbb{E}\left\{|\boldsymbol{w}_a^H \boldsymbol{r_a}|^2\right\} = \boldsymbol{w}_a^H \boldsymbol{R}_a \boldsymbol{w}_a \\ &\text{subject to } \boldsymbol{w}_a^H \boldsymbol{p}_a = \gamma, \end{aligned} \tag{8.76}$$

where z is the filter output, γ is a constant corresponding to the constraint, $\boldsymbol{R}_a$ and $\boldsymbol{p}_a$ are the augmented covariance matrix and augmented cross-correlation vector (defined in Appendix D.1), respectively.

The weight vector designed from (8.76) minimizes the output power while preserving the augmented response of the desired vector. The optimum solution is written as

$$\boldsymbol{w}_{a,\mathrm{MVDR}} = \frac{\gamma^* \boldsymbol{R}_a^{-1} \boldsymbol{p}_a}{\boldsymbol{p}_a^H \boldsymbol{R}_a^{-1} \boldsymbol{p}_a}. \tag{8.77}$$

For each received symbol, the instantaneous SINR at the output of an adaptive filter is calculated by

$$\mathrm{SINR} = \frac{\mathbb{E}\{|\boldsymbol{w}_a{}^H \boldsymbol{d}_a|^2\}}{\mathbb{E}\{|\boldsymbol{w}_a^H \boldsymbol{v}_a|^2\}}, \tag{8.78}$$

where $\boldsymbol{d}_a$ and $\boldsymbol{v}_a$ represent the augmented versions of the desired signal and the interference plus noise, respectively.

The corresponding maximum output SINR of the WL-MVDR filter is obtained by

$$\mathrm{SINR}_{\max}^{\mathrm{WL-MVDR}} = \frac{\boldsymbol{p}_a^H \boldsymbol{R}_a^{-1} \boldsymbol{p}_a}{1 - \boldsymbol{p}_a^H \boldsymbol{R}_a^{-1} \boldsymbol{p}_a}. \tag{8.79}$$

As the constraint vector is chosen as $\boldsymbol{p}_a$, there is a close relationship between the WL-MVDR filter (8.77) and the WL-MMSE filter (D.3) [Hay02], i.e., they become scaled versions of each other: $\rho \boldsymbol{R}_a^{-1} \boldsymbol{p}_a,\ \rho \in \mathbb{C}$. Thus $\mathrm{SINR}_{\max}^{\mathrm{WL-MMSE}}$ can also be expressed by equation (8.79).

8.4.2 WL-AVF Design

Figure 8.17 shows the block diagram of the receiver based on the WL-AVF design. The augmented vector $\boldsymbol{r}_a$ is obtained by a bijective transformation as defined in equation (8.28). It is then processed by the WL-AVF filter that is adjusted by the AVF based algorithm to generate the output $z = \boldsymbol{w}_a^H \boldsymbol{r}_a$. The bijective transformation, the WL-AVF filter, and the adaptive algorithm constitute the major part of the proposed WL-AVF receiver.

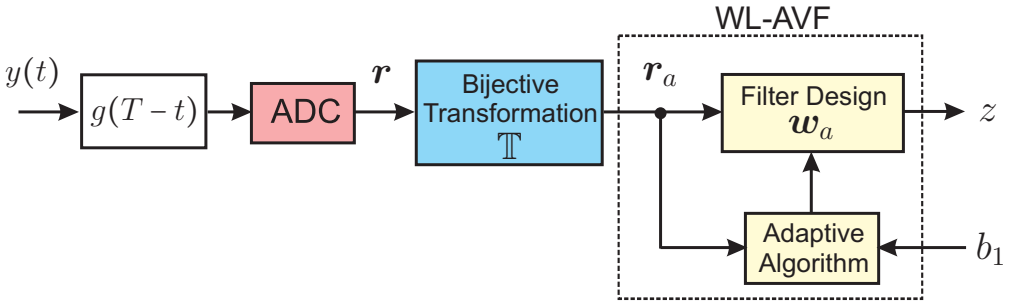

Fig. 8.17: The block diagram of the WL-AVF receiver.

8.4.2.1 Proposed WL-AVF Algorithm

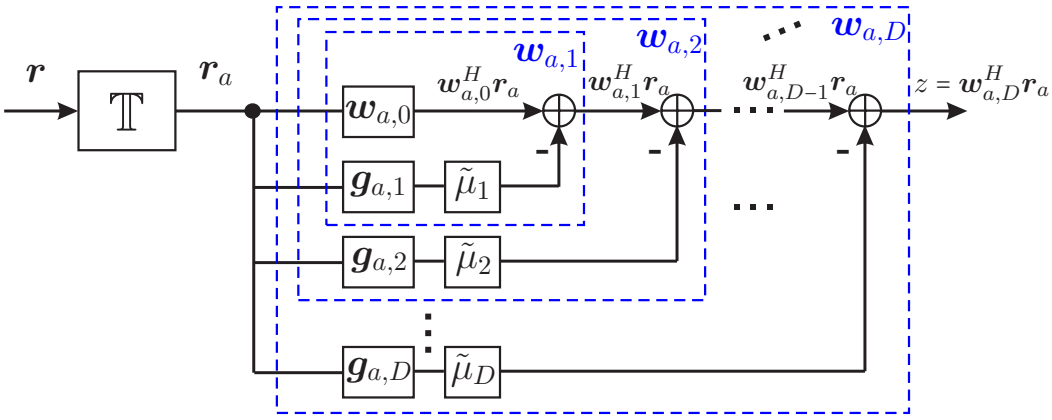

Fig. 8.18: The iterative structure of the WL-AVF algorithm.

The iterative structure of the proposed WL-AVF algorithm is illustrated in Figure 8.18. Specifically, the WL-based weight vector is initialized with $\boldsymbol{w}_{a,0}$, which is the normalized conventional matched filter given by

$$\boldsymbol{w}_{a,0} = \gamma^* \frac{\boldsymbol{p}_a}{\|\boldsymbol{p}_a\|^2}, \tag{8.80}$$

where γ is the desired response and $\boldsymbol{p}_a = \mathbb{E}\{b_1^* \boldsymbol{r}_a\}$ is the augmented cross-correlation vector of the desired signal b_1 and the augmented received vector $\boldsymbol{r}_a$.

After that, the WL weight vector is iteratively computed by subtracting a scaled auxiliary

vector from $\boldsymbol{w}_{a,0}$, that is

$$\boldsymbol{w}_{a,d} = \boldsymbol{w}_{a,0} - \sum_{l=1}^{d} \tilde{\mu}_l \boldsymbol{g}_{a,l} = \boldsymbol{w}_{a,d-1} - \tilde{\mu}_d \boldsymbol{g}_{a,d}, \tag{8.81}$$

where $\boldsymbol{g}_{a,d}$ is a WL auxiliary vector with $\boldsymbol{g}_{a,d}^H \boldsymbol{p}_a = 0$ and $\tilde{\mu}_d$ is a scalar factor to control the weight of $\boldsymbol{g}_{a,d}$. The aim of (8.81) is to suppress interference and noise step by step while maintaining the contribution of the desired user.

From (8.81), it is necessary to determine the WL auxiliary vector $\boldsymbol{g}_{a,d}$ and the scalar factor $\tilde{\mu}_d$ for the calculation of $\boldsymbol{w}_{a,d}$. Given $\boldsymbol{g}_{a,d}$, $\tilde{\mu}_d$ can be obtained by minimizing the variance at the output of $\boldsymbol{w}_{a,d}$

$$\tilde{\mu}_d = \arg\min_{\tilde{\mu}} \ \mathbb{E}\left\{\boldsymbol{w}_{a,d}^H \boldsymbol{r}_a \boldsymbol{r}_a^H \boldsymbol{w}_{a,d}\right\}. \tag{8.82}$$

Substituting the second expression of $\boldsymbol{w}_{a,d}$ in (8.81) into (8.82), computing the gradient with respect to $\tilde{\mu}_d$ and equating it to zero, we have

$$\tilde{\mu}_d = \frac{\boldsymbol{g}_{a,d}^H \boldsymbol{R}_a \boldsymbol{w}_{a,d-1}}{\boldsymbol{g}_{a,d}^H \boldsymbol{R}_a \boldsymbol{g}_{a,d}}, \tag{8.83}$$

where $\boldsymbol{R}_a = \mathbb{E}\left\{\boldsymbol{r}_a \boldsymbol{r}_a^H\right\}$ denotes the augmented covariance matrix and is expressed in equation (8.29).

The calculation of $\boldsymbol{g}_{a,d}$ is determined by maximizing a constrained cost function

$$\begin{aligned} &\boldsymbol{g}_{a,d} = \arg\max_{\boldsymbol{g}_a} \ \mathbb{E}\left\{\boldsymbol{w}_{a,d-1}^H \boldsymbol{r}_a \boldsymbol{r}_a^H \boldsymbol{g}_{a,d}\right\} \\ &\text{subject to } \boldsymbol{g}_{a,d}^H \boldsymbol{p}_a = 0 \text{ and } \boldsymbol{g}_{a,d}^H \boldsymbol{g}_{a,d} = 1, \end{aligned} \tag{8.84}$$

where the maximization of the cross-correlation between $\boldsymbol{w}_{a,d-1}^H \boldsymbol{r}_a$ and $\boldsymbol{g}_{a,d}^H \boldsymbol{r}_a$ strives to determine the auxiliary vector that can capture most of the interference present in $\boldsymbol{w}_{a,d-1}^H \boldsymbol{r}_a$.

According to (8.81), computing the gradient of (8.84) with respect to $\boldsymbol{g}_{a,d}$, we have

$$\boldsymbol{g}_{a,d} = \frac{\left(\boldsymbol{I}_{2M} - \frac{\boldsymbol{p}_a \boldsymbol{p}_a^H}{\|\boldsymbol{p}_a\|^2}\right) \boldsymbol{R}_a \boldsymbol{w}_{a,d-1}}{\left\|\left(\boldsymbol{I}_{2M} - \frac{\boldsymbol{p}_a \boldsymbol{p}_a^H}{\|\boldsymbol{p}_a\|^2}\right) \boldsymbol{R}_a \boldsymbol{w}_{a,d-1}\right\|}, \tag{8.85}$$

where $\boldsymbol{I}_{2M}$ denotes the corresponding identity matrix.

From another perspective, the auxiliary vector $\boldsymbol{g}_{a,d}$ can be considered as the gradient of the WL cost function evaluated at the $(d-1)$-th stage $\boldsymbol{w}_{a,d-1}$ and projected onto a subspace orthogonal to the desired response of the augmented receiving vector determined by $\boldsymbol{p}_a$. The scalar $\tilde{\mu}_d$ can be seen as a variable step size optimized at the d-th stage based on the minimum variance criterion. Thus, the weight adaptation of the WL-AVF algorithm (8.81) iteratively suppresses the interference in the direction of the scaled augmented auxiliary vectors, while maintaining the desired response of the augmented receiving vector.

The expressions $\boldsymbol{w}_{a,0}$, $\boldsymbol{w}_{a,d}$, $\tilde{\mu}_d$, and $\boldsymbol{g}_{a,d}$ with $d = 1, \cdots, D$ compose the iteration of the proposed WL-AVF algorithm, which is summarized in Table 8.5. For simplicity, we drop the normalization of the WL auxiliary vector [PK01]. The estimation of $\boldsymbol{R}_a$ and $\boldsymbol{p}_a$ is calculated by their recursive forms, cf. equations (8.49) and (8.50). It should be noticed that, for the proposed algorithm, the WL weight vector should be adapted at each time instant. Thus, the iteration procedure is performed for each time instant and i is included in the quantities. Generally, there exists a maximum number of iterations D, which is obtained if $\|\boldsymbol{g}_{a,d}(i) - \boldsymbol{g}_{a,d-1}(i)\| < \epsilon$ with ϵ being a small positive value. Alternative termination rules can be found in [MMZ05].

Tab. 8.5: Proposed WL-AVF Algorithm

For the time index $i = 1, 2, \ldots, N_s$.
Initialization:
$\boldsymbol{w}_0(i) = \gamma^* \dfrac{\boldsymbol{p}_a(i)}{\|\boldsymbol{p}_a(i)\|^2}$.
Iterative procedure:
For $d = 1, 2, \ldots, D$
$\boldsymbol{g}_{a,d}(i) = \left(\boldsymbol{I}_{2M} - \dfrac{\boldsymbol{p}_a(i)\boldsymbol{p}_a^H(i)}{\|\boldsymbol{p}_a(i)\|^2}\right)\boldsymbol{R}_a(i)\boldsymbol{w}_{a,d-1}(i)$
if $\left\|\boldsymbol{g}_{a,d}(i) - \boldsymbol{g}_{a,d-1}(i)\right\| < \epsilon$ then EXIT.
$\tilde{\mu}_d(i) = \dfrac{\boldsymbol{g}_{a,d}^H(i)\boldsymbol{R}_a(i)\boldsymbol{w}_{a,d-1}(i)}{\boldsymbol{g}_{a,d}^H(i)\boldsymbol{R}_a(i)\boldsymbol{g}_{a,d}(i)}$
$\boldsymbol{w}_{a,d}(i) = \boldsymbol{w}_{a,d-1}(i) - \tilde{\mu}_d(i)\boldsymbol{g}_{a,d}(i)$
End
Weight expression: $\boldsymbol{w}_a(i) = \boldsymbol{w}_{a,D}(i)$
Output: $z(i) = \boldsymbol{w}_a^H(i)\boldsymbol{r}_a(i)$

8.4.3 Key Properties

We assume that the data from all the users are real. The proposed WL-AVF algorithm has the following key properties.

1. The initial WL weight vector $\boldsymbol{w}_{a,0}$ is a bijective transformation of the original weight vector $\boldsymbol{w}_0$, the one in the linear case, which is

$$\boldsymbol{w}_0 \xrightarrow{\mathbb{T}} \boldsymbol{w}_{a,0}: \qquad \boldsymbol{w}_{a,0} = \left[\begin{array}{cc} \boldsymbol{w}_0^T, & \boldsymbol{w}_0^H \end{array}\right]^T, \tag{8.86}$$

   where $\boldsymbol{w}_0 = \gamma^* \boldsymbol{p}/\|\boldsymbol{p}\|^2$ with $\boldsymbol{p} = \mathbb{E}\{b_1^* \boldsymbol{r}\}$.

2. The d-th WL auxiliary vector $\boldsymbol{g}_{a,d}$ can be constructed by a bijective transformation of

a linear auxiliary vector $\check{\boldsymbol{g}}_d$, i.e.,

$$\boldsymbol{g}_{a,d} = \left\{\boldsymbol{I}_{2M} - \begin{bmatrix} \boldsymbol{P} & \check{\boldsymbol{P}} \\ \check{\boldsymbol{P}}^* & \boldsymbol{P}^* \end{bmatrix}\right\}\begin{bmatrix} \boldsymbol{R} & \check{\boldsymbol{R}} \\ \check{\boldsymbol{R}}^* & \boldsymbol{R}^* \end{bmatrix}\begin{bmatrix} \check{\boldsymbol{w}}_{d-1} \\ \check{\boldsymbol{w}}_{d-1}^* \end{bmatrix} \tag{8.87}$$

$$= \begin{bmatrix} \check{\boldsymbol{g}}_d^T, & \check{\boldsymbol{g}}_d^H \end{bmatrix}^T = \mathbb{T}\{\check{\boldsymbol{g}}_d\}, \tag{8.88}$$

where $\boldsymbol{P} = \boldsymbol{p}\boldsymbol{p}^H/\|\boldsymbol{p}\|^2$ and $\check{\boldsymbol{P}} = \boldsymbol{p}\boldsymbol{p}^T/\|\boldsymbol{p}\|^2$. For BPSK modulated signals, $\check{\boldsymbol{R}} = \mathbb{E}[\boldsymbol{r}\boldsymbol{r}^T]$ is non-zero and thus the improper property of the received vector can be exploited by means of WL processing. Both $\boldsymbol{R}$ and $\check{\boldsymbol{R}}$ can completely describe the second-order information of $\boldsymbol{r}$. The vectors $\check{\boldsymbol{g}}_d$ and $\check{\boldsymbol{w}}_{d-1}$ are not necessary for implementation of the proposed WL-AVF algorithm but are given here to show the improper property of the WL filter.

3. The scalar factor $\tilde{\mu}_d$ can be written as

$$\tilde{\mu}_d = \frac{\mu + \mu^*}{\check{\mu} + \check{\mu}^*}, \tag{8.89}$$

where $\mu = \check{\boldsymbol{g}}_d^H \boldsymbol{R}\check{\boldsymbol{w}}_{d-1} + \check{\boldsymbol{g}}_d^H \check{\boldsymbol{R}}\check{\boldsymbol{w}}_{d-1}^*$ and $\check{\mu} = \check{\boldsymbol{g}}_d^H \boldsymbol{R}\check{\boldsymbol{g}}_d + \check{\boldsymbol{g}}_d^H \check{\boldsymbol{R}}\check{\boldsymbol{g}}_d^*$. It can be easily shown that $\tilde{\mu}_d$ is real-valued.

From the properties 1-3, we conclude that $\boldsymbol{w}_{a,d} = \begin{bmatrix} \check{\boldsymbol{w}}_d^T, & \check{\boldsymbol{w}}_d^H \end{bmatrix}^T$. Thus, after D iterations, the output can be expressed as

$$z = \check{\boldsymbol{w}}^H \boldsymbol{r} + \check{\boldsymbol{w}}^T \boldsymbol{r}^* = \check{z} + \check{z}^* = 2 \cdot \Re\{\check{z}\}, \tag{8.90}$$

which is real-valued. This is the conjugate symmetry property of the WL filter for the real estimated data (cf. Appendix D.1). Thus, $\boldsymbol{w}_a$ minimizes $\mathbb{E}\left\{|\Re\{z\}|^2\right\}$ and equivalently maximizes the output SINR

$$\mathrm{SINR}^{\mathrm{WL-MVDR}} = \frac{\mathbb{E}\left\{\left|\Re\left\{\boldsymbol{w}_a^H \boldsymbol{d}_a\right\}\right|^2\right\}}{\mathbb{E}\left\{\left|\Re\left\{\boldsymbol{w}_a^H \boldsymbol{v}_a\right\}\right|^2\right\}}. \tag{8.91}$$

4. The WL-AVF solution $\boldsymbol{w}_{a,d}, d = 1, \cdots, D$ converges to $\boldsymbol{w}_{a,\mathrm{MVDR}}$ expressed in (8.77), i.e.,

$$\lim_{d\to\infty} \boldsymbol{w}_{a,d} = \frac{\gamma^* \boldsymbol{R}_a^{-1}\boldsymbol{p}_a}{\boldsymbol{p}_a^H \boldsymbol{R}_a^{-1}\boldsymbol{p}_a}. \tag{8.92}$$

This convergence (8.92) can be shown using a similar strategy as in [PK01]. It indicates that the maximum output SINR of the WL-AVF algorithm at the steady state satisfies $\mathrm{SINR}_{\max}^{\text{WL-AVF}} \to \mathrm{SINR}_{\max}^{\text{WL-MVDR}}$.

5. The steady-state performance of the WL-AVF outperforms that of the liner AVF in terms of SINR presented in Theorem 8.4.1.

Theorem 8.4.1. *The maximum output SINRs of the WL-AVF and the linear AVF satisfy* $\mathrm{SINR}_{\max}^{\mathrm{WL-AVF}} \geq 2\ \mathrm{SINR}_{\max}^{\mathrm{L-AVF}}$*, i.e., the WL-AVF provides at least 3 dB gain over the linear AVF.*

Proof: To compare the linear and WL filters, we introduce an intermediate SINR using (8.91). The optimal linear MVDR solution can be considered as a WL-MVDR with the augmented weight vector $\boldsymbol{w}_a = \left[\begin{array}{cc} \boldsymbol{w}_{\mathrm{MVDR}}^T, & \mathbf{0}_M^T \end{array}\right]^T, \boldsymbol{w}_{\mathrm{MVDR}}^H \boldsymbol{p} = \gamma$. From (8.91), the resulting $\widehat{\mathrm{SINR}}^{\mathrm{MVDR}} = \dfrac{\mathbb{E}\{|\Re\{\boldsymbol{w}_{\mathrm{MVDR}}{}^H \boldsymbol{d}\}|^2\}}{\mathbb{E}\{|\Re\{\boldsymbol{w}_{\mathrm{MVDR}}{}^H \boldsymbol{v}\}|^2\}} \leq \mathrm{SINR}_{\max}^{\mathrm{WL\text{-}MVDR}}$ holds. Compared to the maximum SINR of the linear MVDR filter, i.e., $\dfrac{\mathbb{E}\{|\boldsymbol{w}_{\mathrm{MVDR}}{}^H \boldsymbol{d}|^2\}}{\mathbb{E}\{|\boldsymbol{w}_{\mathrm{MVDR}}{}^H \boldsymbol{v}|^2\}} = \dfrac{\boldsymbol{p}^H \boldsymbol{R}^{-1} \boldsymbol{p}}{1 - \boldsymbol{p}^H \boldsymbol{R}^{-1} \boldsymbol{p}}$, since $\Re\{\cdot\}$ leads to half of the interference plus noise power [CGPV09], we can obtain $\widehat{\mathrm{SINR}}^{\mathrm{MVDR}} \approx 2\ \mathrm{SINR}_{\max}^{\mathrm{MVDR}}$.

8.4.4 Simulation Results

The considered iterative WL-AVF algorithm is training-based. We apply the same UWB channel as described in Section 8.3.5 with $L = 64$ channel taps. The DS code of length $N = 24$ is generated pseudo-randomly for the DS-UWB system, where $N_u = 16$ users operate with perfect power control in the system. The NBI is not considered here.

Figure 8.19 shows the output SINR convergence performance of the WL-AVF with the iteration number $D = 8$ at $E_b/N_0 = 15$ dB, where the WL-MMSE based SG and the RLS algorithms as well as their linear counterparts are also included for comparison. The forgetting factor is $\lambda = 0.998$. All the WL methods provide substantial performance improvements over the linear ones. Specifically, the proposed algorithm, which suppresses the interference by iteratively updating the filter weight, outperforms the adaptive WL-MMSE-SG and the WL-MMSE-RLS in terms of both the convergence and the steady state. In agreement with Theorem 8.4.1, the WL-MMSE exhibits a larger maximum output SINR than the linear MMSE due to the advantage of fully exploiting the second-order statistics of the non-circular signal.

In Figure 8.20, we check the impact of the number of iterations D on the proposed algorithm and show the BER performance when the number of snapshots is 1000. The scenario is the same as that in Figure 8.19. We find that the most adequate number of iterations for the proposed WL-AVF algorithm is $D = 8$, whereas $D = 12$ for the linear AVF case. The BER values stay relatively on the same level after such a selected D. This can be explained by the fact that processing of the augmented weight vector provides more information to reach the best solution with fewer iterations. In our simulations the number of iterations is fixed for all the realizations. Note that the appropriate D is different with respect to different E_b/N_0. Besides, a smaller D may provide a faster convergence during the initial stages of the estimation and a slightly larger D tends to yield a better steady-state performance. The performance can be improved by applying an automatic scheme to adaptively adjust D.

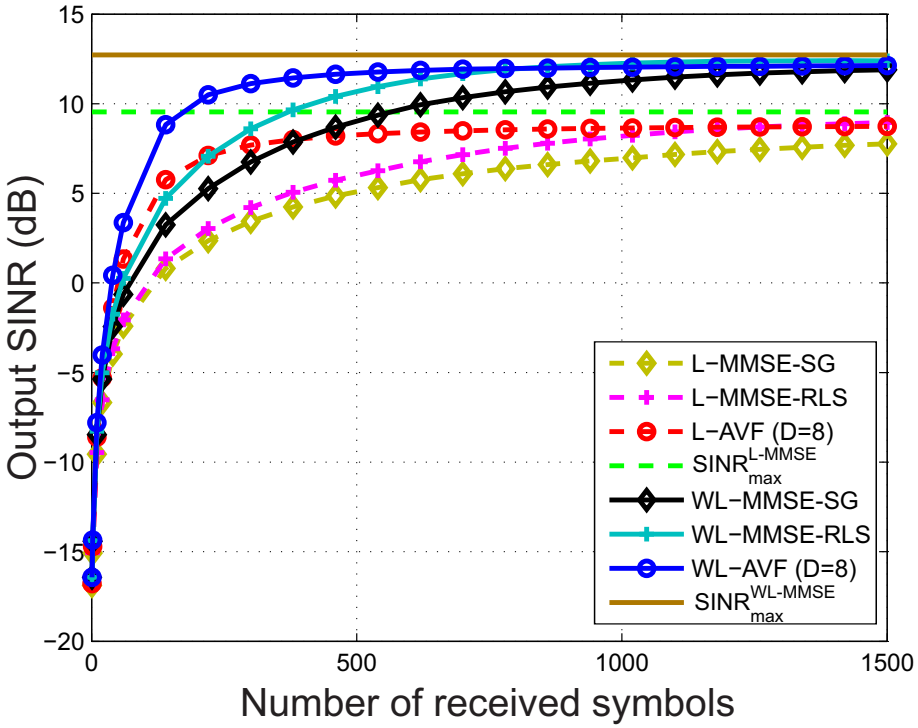

Fig. 8.19: Output SINR versus the number of symbols. E_b/N_0 = 15 dB and perfect power control for N_u = 16 users are considered.

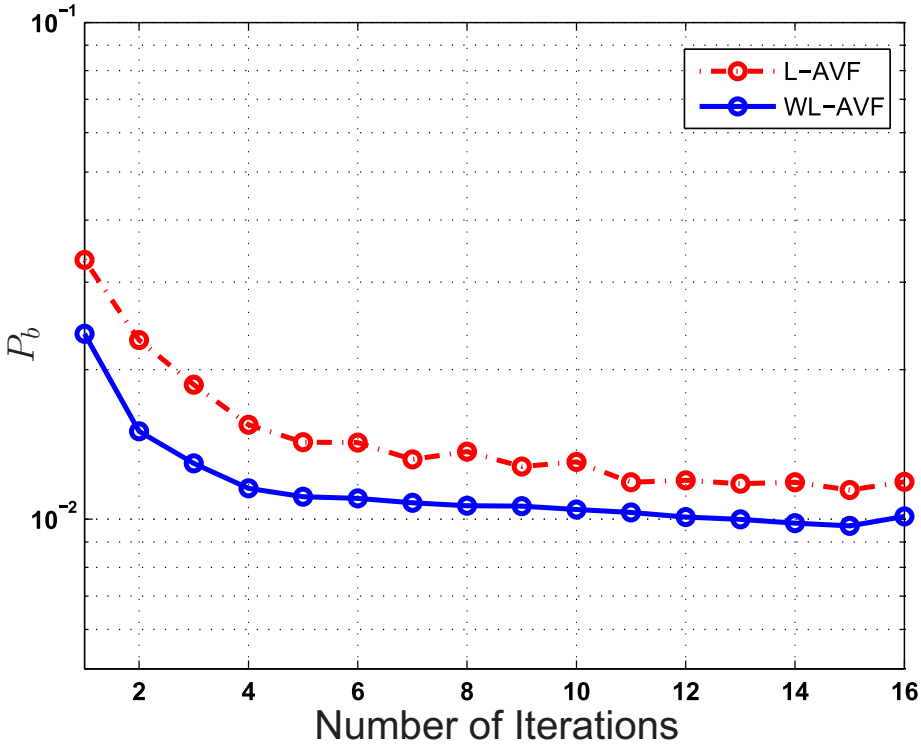

Fig. 8.20: BER versus the number of iterations. E_b/N_0 = 15 dB and perfect power control for N_u = 16 users are considered.

8.4.5 Conclusions

To suppress the MUI and ISI in a high data rate DS-UWB system using the non-circular BPSK modulation, we introduce a new WL receiver based on the AVF technique and develop a training-based adaptive algorithm. This new framework employs the bijective transformation to combine the received vector and its complex conjugate into an augmented vector, which is processed by the WL-AVF filter to estimate the decision variable. The proposed algorithm utilizes an iterative way to update the WL weight vector. The filter weights are adapted in a stochastic gradient fashion by successively subtracting the auxiliary vector $\boldsymbol{g}_{a,d}$ multiplied with an optimized step size (or scalar) $\tilde{\mu}_d$ at each stage. Several key properties of the WL-AVF algorithm are addressed in comparison with the linear AVF. The WL-AVF fully exploits the second-order statistics of the non-circular data, including both the desired signal and the interference. It provides at least a 3 dB SINR gain over the linear AVF scheme when the source signals are real-valued.

The simulation results compare the proposed WL-AVF algorithm with the linear AVF as well as the linear MMSE and the WL-MMSE with both SG and RLS adaptations. The WL-AVF provides a better convergence performance than all the other tested algorithms. The number of iterations D influences the convergence performance of the WL-AVF. An appropriate value for the number of iterations $D = 8$ can be chosen to ensure a good performance and a moderate complexity. Even with a smaller number of iterations D, the WL-AVF exhibits a superior performance than the linear AVF.

8.5 Summary and Discussions

This chapter introduces two WL reduced-rank schemes, i.e., the WL-MSWF and the WL-AVF, for non-circular signals (such as BPSK) in the application of suppressing interference in DS-UWB systems. The WL techniques are able to fully exploit the second-order statistics of non-circular signals and improve the estimation performance. In addition, processing the observation data with a large number of samples (e.g., due to the large bandwidth and accordingly the high sampling rate in UWB communications) will considerably slow down the convergence performance. The reduced-rank techniques can thus be applied in combination with the WL processing.

Extensive analyses show that the proposed schemes take advantage of both the WL and the reduced-rank techniques, outperforming their linear counterparts as well as the full-rank ones in terms of the convergence performance and the steady-state performance. The required number of ranks or iterations is also small, e.g., $D = 3$ or 4 for the WL-MSWF and $D = 8$ for the WL-AVF in the studied scenarios.

Beamforming Applications

The WL adaptive reduced-rank algorithms are proposed to solve beamforming problems [SSW+11, nso]. They are not included in the dissertation but summarized in the following.

1. **WL-AVF**: The WL-AVF beamforming algorithm, which utilizes an iterative procedure to generate a sequence of auxiliary vectors based on the optimized Widely Linear Constrained Minimum Variance (WL-CMV) criterion, is introduced in [SSW+11]. Similar to the descriptions in Section 8.4, the filter weights are adapted in a stochastic gradient fashion by successively subtracting the auxiliary vector $\boldsymbol{g}_{a,d}$ multiplied with an optimized step size (or scalar) $\tilde{\mu}_d$ at each stage. Several key properties of the WL-AVF algorithm are addressed in comparison with the linear AVF, including the bounded range of the variable step size $\tilde{\mu}_d$, the analysis on the maximum/minimum eigenvalues, and the convergence performance. The WL-AVF fully exploits the second-order statistics of the non-circular data, including both the signal-of-interest and the interference. It provides at least a 3 dB SINR gain over the linear AVF scheme when the source signals are real-valued.

   We compare the proposed WL-AVF algorithm with the linear AVF as well as the Linear Constrained Minimum Variance (L-CMV) and the WL-CMV adaptive schemes. The WL-AVF provides a better convergence performance than all the other tested algorithms. The number of iterations D influences the convergence performance of the WL-AVF, where the highest SINR can be achieved with $D = 2$ in our considered scenario. Even with a smaller number of iterations D, the WL-AVF exhibits a superior performance than the linear AVF.

2. **WL Joint Iterative Optimization (WL-JIO)**: One reduced-rank technique, namely JIO, jointly estimates the rank-reduction matrix and the weight vector of the reduced-rank filter by iteratively exchanging the information between each other [dLSN07, dL08, dLWF10]. It provides a much simpler implementation as compared to the previously considered reduced-rank techniques which are based on the Krylov subspace, i.e., MSWF and AVF. In [nso], we propose a WL-JIO beamformer according to the WL-CMV criterion. To fully exploit the second-order statistics of non-circular signals, an augmented vector is often formulated as in (8.28). However, this transformation doubles the dimension of the estimated vector/matrix and accordingly may slow down the convergence. Thanks to the structured property of the augmented covariance matrix $\boldsymbol{R}_a$, the adaptive estimation algorithm can be implemented in a much more efficient way. Unlike the Augmented Recursive Least Squares (ARLS) that directly deals with $\boldsymbol{R}_a^{-1} \in \mathbb{C}^{2M}$, the proposed Structured Recursive Least Squares (SRLS) method separately estimates two block matrices (of size M) inherent in $\boldsymbol{R}_a^{-1}$.

   The results show that WL-JIO-SRLS and WL-JIO-ARLS outperform their linear counterpart as well as the full-rank schemes. Since the WL-JIO-SRLS estimates the parameters related to an order of M in a structured manner, its convergence is faster than that of the WL-JIO-ARLS. Furthermore, we also point out that WL-JIO-SRLS has a lower complexity compared to the ARLS algorithms that are based on both the WL-JIO and the full-rank WL-CMV.

9. CONCLUSIONS

Part I: Non-coherent detection for low data rate UWB

The major idea emphasized in this part is based on applying fully ***digital*** solutions to non-coherent detection. Using time-domain low-resolution Analog-to-Digital Converters (ADCs), ***digital*** solutions show a great potential for simple implementations with a robust performance.

▽ ***From analog to digital***

Let us refer to Figure 1.2 again to summarize our major achievements.

Non-coherent detection, which avoids the channel estimation and considerably alleviates the requirement for synchronization, is an attractive approach for low-complexity UWB communication systems. However, as compared to coherent detection, it is not power efficient and is more susceptible to interference.

△ By analyzing the E_b/N_0 performance of non-coherent detection, it is observed that there exists a Non-Coherent Combining Loss (NC-CL), depending on the product of the integration window T_{i} and the signal bandwidth B. The window size T_{i} includes the *multipath-induced* as well as the *code-induced* non-coherent combining intervals.

To reduce the NC-CL or to improve the power efficiency of non-coherent detection, the following solutions are proposed by decreasing T_{i} and/or B.

△ From the T_{i} perspective to reduce the *multipath-induced* NC-CL, two proposed non-coherent combining techniques, i.e., Single Window Combining (SinW-C) and Weighted Sub-Window Combining (WSubW-C), can effectively capture the multipath energy only with the knowledge of the second-order statistics of the channel profile.

△ The ***analog*** non-coherent receiver is based on digitally implementing the decoding of the user-specific code after the analog multipath combining. The sparse Time Hopping (TH) codes should be carefully selected such that they have good correlation properties for a robust performance in the presence of Multi-User Interference (MUI) and low code weights in order to reduce the *code-induced* T_{i} (or NC-CL).

△ The proposed ***digital*** non-coherent receiver relies on a high-speed but low-resolution ADC followed by a Digital Code Matched Filter (DCMF), which coherently decodes

the user-specific code and restricts the non-coherent combining only to the multipath arrivals. As compared to the ***analog*** counterpart, the *code-induced* NC-CL is completely removed.

→ Thanks to the coherent operation of the DCMF, the proposed receiver offers a superior interference rejection capability.

→ ***Digital*** solutions are quite appropriate for differential receivers, since the delays can be easily realized.

The key component of the ***digital*** receiver is the ADC. To maintain a reasonable power consumption, we can either apply an ADC with a Nyquist sampling rate but a very limited resolution b (e.g., $1 \leq b \leq 4$) or employ a one-bit Sigma-Delta ($\Sigma\Delta$) ADC with oversampling. Most importantly, the quantization loss (with respect to the full-resolution performance) due to the resolution and the sampling rate is characterized in combination with the system design such as modulation schemes and parameters of the TH codes.

→ With a one-bit receiver, only a small loss is observed. Under near-far conditions, it is able to effectively suppress the MUI and shows a higher capability of separating simultaneously operating piconets than the full-resolution case.

→ The full-resolution performance can be almost achieved by increasing the ADC resolution (e.g., $b = 4$) or the sampling rate (e.g., oversampling rate of 4 for the one-bit $\Sigma\Delta$ ADC)

Digital receiver implementations facilitate the design of advanced modulation schemes, such as M-ary Pulse Position Modulation (PPM) and M-ary Walsh combined with TH.

→ The TH M-Walsh scheme is more robust to the quantization loss than TH M-PPM, unless the number of pulse repetitions for TH M-PPM is sufficient.

Moreover,

→ the suitability of applying the soft limiter to suppress the Narrowband Interference (NBI) is shown for the DCMF-based non-coherent receiver.

Besides T_{i}, decreasing the signal bandwidth B can also reduce the NC-CL and consequently the sampling rate.

△ To well trade off the NC-CL and the fading resistance in a single carrier system, an appropriate bandwidth B has to be chosen. Our analyses show that a signal bandwidth of $B \geq 200$ MHz is NOT desirable from the required E_b/N_0 point of view.

△ A Frequency Hopping (FH) concept is proposed according to the selection of the useful bandwidth and the recent UWB regulations, where the baseband bandwidth is brought down to the values that are much lower than 500 MHz. This enables very low-cost ADCs and low-complexity digital signal processing techniques.

▽ ***Future Perspectives***

From both performance and implementation viewpoints, ***digital*** solutions promise a great potential in low-complexity and energy efficient non-coherent UWB receiver designs. We may extend the work which mainly relies on a signal bandwidth of at least 500 MHz to the following perspectives.

△ Synchronization that has not been covered in the current work, is one possible issue to be considered in the future, even though such requirements on non-coherent receivers are relaxed.

△ Forward error correction is also necessary to enhance the overall system robustness. Analyses on channel encoding and decoding can be carried out.

△ Analog delays are avoided by applying digital receivers. It is thus promising to further investigate differential detection combined with symbol-based Differential Phase Shift Keying (DPSK), since it has a 3 dB advantage over the PPM-based energy detection. Possible investigations can be focused on the Inter-/Intra-Symbol Interference (ISI) impact, multiple access techniques, NBI robustness, etc..

In order to develop and analyze the proposed hybrid FH-UWB system, key open research issues are, but not limited to

△ FCC compliance study,

△ evaluation of efficient modulation schemes, e.g., Walsh modulation with non-coherent detection and Binary Phase Shift Keying (BPSK) or Quadrature Phase Shift Keying (QPSK) with coherent detection,

△ comparison of symbol-based FH and packet-based FH,

△ interference robustness analysis, i.e., investigations of fixed FH patterns and/or adaptive FH strategies to deal with the NBI or wideband interference as well as MUI,

△ efficient and robust encoding and decoding techniques, and

△ receiver synchronization for the FH synthesizer and/or the phase recovery for coherent detection.

▽ ***Potential applications***

The performance analysis of non-coherent detection and the proposed transceiver strategies especially with respect to the digital solutions are very suitable and promising for the application of low data rate Wireless Sensor Networks (WSNs). The critical requirement on the transceivers for WSNs lies in the low-cost and low-power consumption, since a considerably large number of sensor nodes is deployed. This application field is multidisciplinary and integrates many concepts, including

- △ *ranging*: low-complexity time-of-arrival estimation schemes based on energy detection are of great interest and promising;
- △ *wireless communications and ad hoc networking*: for example, in Medium Access Control (MAC), due to the centi-meter accuracy of the positioning offered by UWB, the routing and power control schemes can be simplified;
- △ *low-power hardware design*: our proposed schemes will facilitate the hardware modeling and design of the transceiver front-end, such as low-cost antenna developments, integrated circuits technology (low power amplifier, ADC, etc.), and Complementary Metal Oxide Semiconductor (CMOS) technology. Our concept has a high potential in low-power applications that use battery-powered and energy harvesting devices;
- △ *signal processing*: efficient digital signal processing techniques are necessary to mitigate the NBI and/or the MUI; etc..

To be specified, our work is quite promising in a noticeable amount of emerging WSN application scenarios such as

- △ modern healthcare systems (hospital locating, tracking, and communications),
- △ in/around-vehicle wireless sensor network for data communications and location tracking,
- △ Radio Frequency Identification (RFID) tags in logistics (factory monitoring and on-ship container tracking) as well as archival/library science,
- △ life rescue in natural disasters and terrorism attacks (localization),
- △ motion detection security systems, etc..

Part II: Advanced signal processing for high data rate UWB

▽ ***Advantages and suitability of the widely linear reduced-rank techniques***

Widely Linear (WL) processing can fully exploit the second-order statistics of the non-circular signals. The reduced-rank techniques are advantageous in providing a faster convergence by estimating a reduced number of parameters. The combination of both is very promising in numerous applications. Our work considers the following two examples.

→ *Interference suppression for high data rate Direct Sequence (DS) UWB communication systems*:

- BPSK [1] modulated signal is second-order non-circular;
- a large bandwidth results in a high sampling rate and consequently a large number of received samples.

→ *Beamforming*:

- the source signals are second-order non-circular;
- if the antenna array is equipped with many sensors, the resulting received data vector has a lot of samples (cf. [SSW+11, nso]).

The WL adaptive reduced-rank schemes are thus proposed for interference suppression in the above applications.

△ The proposed schemes, namely the WL Multistage Wiener Filter (WL-MSWF), the WL Auxiliary Vector Filtering (WL-AVF), as well as WL Joint Iterative Optimization (WL-JIO) (cf. [nso]), are investigated for strictly non-circular signals (e.g., BPSK) and the corresponding adaptive algorithms are developed.

△ For the real-valued estimated data, one of the key characteristics is the conjugate symmetry due to the structured property of the augmented covariance matrix.

△ The proposed adaptive WL reduced-rank algorithms outperform their linear counterparts as well as the corresponding full-rank case, in terms of the convergence performance and the steady-state performance.

△ By exploiting the structured property of the augmented covariance matrix, an efficient implementation of the Recursive Least Squares (RLS) algorithm for the WL-JIO scheme is proposed. It has a much lower complexity and offers a better performance compared to its augmented counterpart (cf. [nso]).

▽ ***Future perspectives***

The future work regarding the WL reduced rank techniques includes, but is not limited to

△ investigation of efficient adaptive algorithms for WL-MSWF and WL-AVF by exploiting the structured property,

△ development of blind WL reduced-rank techniques based on Constrained Constant Modulus (CCM) and Constrained Minimum Variance (CMV) (e.g., in Direct Sequence Code Division Multiple Access (DS-CDMA) systems), where blind WL channel estimation is required,

[1] The BPSK modulation is mandatory for the DS-UWB system [FKLW05].

- △ design of WL reduced-rank receivers for Multiple Input Multiple Output (MIMO) using space time block codes, etc..

Appendices

Appendix A

RANDOM VARIABLES AND PROBABILITY DISTRIBUTIONS

This appendix is devoted to introducing some definitions of the important statistical averages and listing several frequently encountered probability distributions [Pro01], which are mainly used in Sections 4.1, 5.4.2, and 6.4.2.

A.1 Statistical Average of Random Variables

A.1.1 The Moments

For a single random variable X, characterized by the Probability Density Function (PDF) $f(x)$, the *mean* or *expected value* of X is defined as

$$\mathbb{E}\{X\} = \mu_x = \int_{-\infty}^{+\infty} x f(x) dx, \tag{A.1}$$

where $\mathbb{E}\{\cdot\}$ denotes the statistical averaging. It is also the first moment of X. The k-th moment of X is then defined as

$$\mathbb{E}\left\{X^k\right\} = \int_{-\infty}^{+\infty} x^k f(x) dx. \tag{A.2}$$

The *variance* or the *second central moment* of X (denoted by $\mathbb{V}\{X\}$)is calculated by

$$\mathbb{V}\{X\} = \sigma_x^2 = \int_{-\infty}^{+\infty} (x - \mu_x)^2 f(x) dx. \tag{A.3}$$

It measures the dispersion of the random variable X. The relationship between the first and second moments can be expressed as

$$\mathbb{V}\{X\} = \sigma_x^2 = \mathbb{E}\left\{X^2\right\} - \left(\mathbb{E}\{X\}\right)^2 = \mathbb{E}\left\{X^2\right\} - \mu_x^2. \tag{A.4}$$

Let us consider the random variables $X_i, i = 1, 2, \cdots, K$ with joint PDF $f(x_1, x_2, \cdots, x_K)$. We then elaborate the correlation and covariance between two different random variables X_i

and X_j. The correlation between X_i and X_j is represented by

$$\mathbb{E}\{X_i X_j\} = \int_{-\infty}^{+\infty} \int_{-\infty}^{+\infty} x_i x_j f(x_i, x_j) dx_i dx_j \tag{A.5}$$

and the covariance is given by

$$\rho_{ij} = \mathbb{E}\{(X_i - \mu_i)(X_j - \mu_j)\} = \int_{-\infty}^{+\infty} \int_{-\infty}^{+\infty} (x_i - \mu_i)(x_j - \mu_j) f(x_i, x_j) dx_i dx_j = \mathbb{E}\{X_i X_j\} - \mu_i \mu_j. \tag{A.6}$$

Two random variables are *uncorrelated* if $\rho_{ij} = 0$, i.e., $\mathbb{E}\{X_i X_j\} = \mathbb{E}\{X_i\}\mathbb{E}\{X_j\} = \mu_i \mu_j$. The statistical independence of the random variables holds if and only if

$$f(x_1, x_2, \cdots, x_K) = f(x_1) f(x_2) \cdots f(x_K). \tag{A.7}$$

Therefore, when X_i and X_j are statistically independent, they are also uncorrelated. However, if X_i and X_j are uncorrelated, it is not necessary that they are statistically independent.

If $\mathbb{E}\{X_i X_j\} = 0$, it is said that two random variables X_i and X_j are *orthogonal*. This is also true when X_i and X_j are uncorrelated and at least one of them has zero mean.

A.1.2 Characteristic Functions

The *characteristic function* of a random variable X is defined as

$$\Phi_X(\omega) = \mathbb{E}\left\{e^{j\omega X}\right\} = \int_{-\infty}^{+\infty} e^{j\omega x} f(x) dx, \tag{A.8}$$

where $\omega \in \mathbb{R}$ and $j = \sqrt{-1}$. It can also be interpreted that the characteristic function is the Fourier transformation of the PDF. Thus, we can obtain

$$f(x) = \frac{1}{2\pi} \int_{-\infty}^{+\infty} \Phi_X(\omega) e^{-j\omega x} d\omega. \tag{A.9}$$

The moments of X can be calculated from the k-th derivative of the characteristic function $\Phi_X(\omega)$ at $\omega = 0$, i.e.,

$$\mathbb{E}\left\{X^k\right\} = (-j)^k \left. \frac{d^k \Phi_X(\omega)}{d\omega^k} \right|_{\omega=0}. \tag{A.10}$$

Let us consider $Y = \sum_{i=1}^{K} X_i$, where $X_i, i = 1, 2, \cdots, K$ are statistically uncorrelated random variables. The characteristic function of Y can be calculated by

$$\Phi_Y(\omega) = \prod_{i=1}^{K} \Phi_X(\omega), \tag{A.11}$$

indicating that the characteristic function of K statistically independent random variables is equal to the product of the characteristic functions of the individual random variables. This

offers a much more convenient method in the PDF derivation, since most of the time the K-fold convolution is quite difficult to obtain in the transform domain.

The theorem, which proves that the distribution is uniquely determined by the characteristic function, is called *inversion theorem*.

Theorem A.1.1. *Suppose that the Cumulative Density Function (CDF) of a random variable X is denoted by $F(x)$, the inversion theorem can be shown by the following expression*

$$F(x) = \frac{1}{2} + \frac{1}{2\pi}\int_0^\infty \frac{e^{j\omega x}\Phi_X(-\omega) - e^{-j\omega x}\Phi_X(\omega)}{j\omega} d\omega. \tag{A.12}$$

A.2 Frequently Used Probability Distributions

A.2.1 Binomial Distribution

If X is a discrete random variable with a *Bernoulli distribution*, we can write

$$\begin{cases} \Pr\{X=1\} &= p \\ \Pr\{X=0\} &= 1-p \end{cases}. \tag{A.13}$$

Suppose that $Y = \sum_{i=1}^{K} X_i$, where $X_i, i = 1, 2, \cdots, K$ are statistically independent and identically distributed random variables with Bernoulli distribution. It follows that

$$\Pr\{Y=n\} = \binom{K}{n} p^n (1-p)^{K-n}, \tag{A.14}$$

where $\binom{K}{n}$ is the binomial coefficient. Thus, Y exhibits a *Binomial distribution* and its PDF is expressed as

$$f(y) = \sum_{n=0}^{K} \binom{K}{n} p^n (1-p)^{K-n} \delta(y-n). \tag{A.15}$$

The corresponding first two moments of Y are

$$\mathbb{E}\{Y\} = Kp \tag{A.16}$$

$$\mathbb{E}\{Y^2\} = Kp(1-p) + K^2p^2 \tag{A.17}$$

$$\sigma^2 = Kp(1-p). \tag{A.18}$$

A.2.2 Gaussian Distribution

The PDF of a *Gaussian distributed* random variable X is written as

$$f(x) = \frac{1}{\sqrt{2\pi}\sigma} e^{-\frac{(x-\mu_x)^2}{2\sigma_x^2}}, \tag{A.19}$$

where the corresponding mean and variance are denoted by μ_x and σ_x^2. The CDF of X is given by

$$F(x) = \int_{-\infty}^{x} f(t)dt = \frac{1}{2} + \mathrm{Q}\left(\frac{x-\mu_x}{\sigma_x}\right), \tag{A.20}$$

where $\mathrm{Q}(x) = \frac{1}{\sqrt{2\pi}} \int_x^{\infty} e^{-\frac{t^2}{2}} \mathrm{d}t$. Figure A.1 shows the PDF and the CDF of different Gaussian distributed random variables.

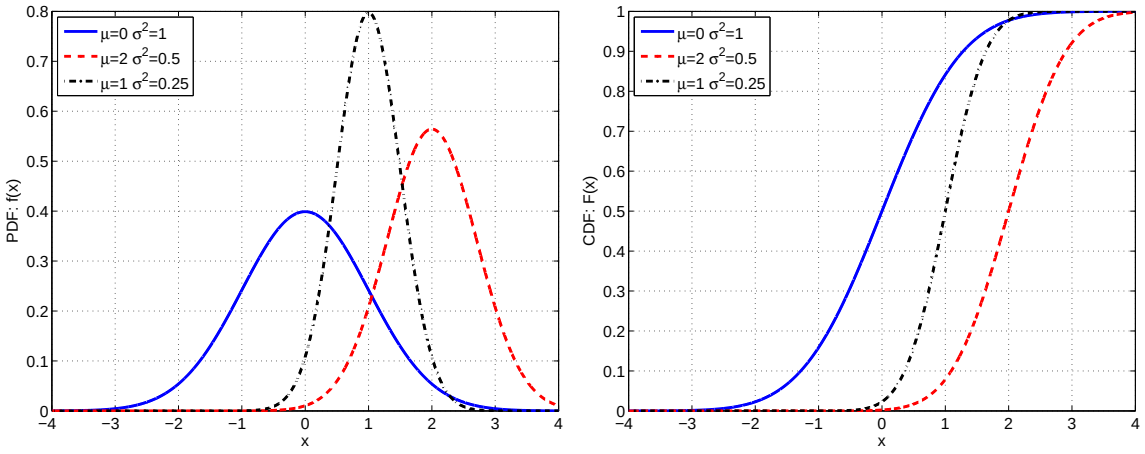

(a) PDF (b) CDF

Fig. A.1: The PDF and CDF of Gaussian random variables

The sum of K statistically independent Gaussian random variables, i.e, $Y = \sum_{i=1}^{K} X_i$ with $X_i, i = 1, 2, \cdots, K$ being statistically independent and identically distributed Gaussian random variables with means μ_i and variances σ_i^2, is also a Gaussian random variable with mean $\mu_y = \sum_{i=1}^{K} \mu_i$ and variance $\sigma_y^2 = \sum_{i=1}^{K} \sigma_i^2$.

A.2.3 Chi-Square Distribution

If $Y = \sum_{i=1}^{K} X_i$, where $X_i, i = 1, 2, \cdots, K$ are statistically independent and identically distributed Gaussian random variables with means μ_i and identical variance σ^2, Y follows a *chi-square (χ^2) distribution with K degrees of freedom*. When X_i has a zero mean, Y has a *central χ^2 distribution*. When X_i has a non-zero mean, Y exhibits a *non-central χ^2 distribution*. The PDF of Y with K degrees of freedom is expressed by

$$f_Y(y) = \frac{1}{2\sigma^2} \left(\frac{y}{\mu^2}\right)^{\frac{K-2}{4}} \exp\left(-\frac{y+\mu^2}{2\sigma^2}\right) I_{\frac{K}{2}-1}\left(\frac{\sqrt{y}\mu}{\sigma^2}\right), \tag{A.21}$$

where $\mu^2 = \sum_{i=1}^{K} \mu_i^2$ is called the *non-centrality parameter* and $I_\alpha(\cdot)$ is the α-th order modified Bessel function of the first kind [GR07]. Figure A.2 displays the PDFs of central and non-

central χ^2 distributed random variables. The characteristic function of Y is given by

$$\Phi_Y(\omega) = \frac{1}{(1-j2\omega\sigma^2)^{\frac{K}{2}}} \exp\left(\frac{j\omega\mu^2}{1-j2\omega\sigma^2}\right). \tag{A.22}$$

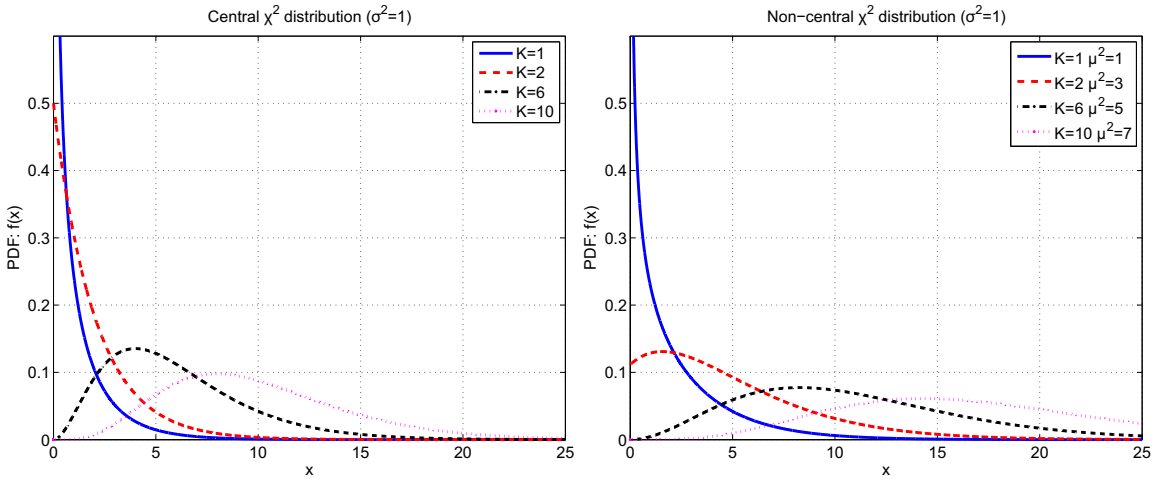

(a) (b)

Fig. A.2: The PDFs of (a) central χ^2 distributed random variables with various degrees of freedom and (b) non-central χ^2 distributed random variables with various non-centrality parameters, where $\sigma^2 = 1$.

The first two moments of a non-central χ^2 distribution random variable are

$$\mathbb{E}\{Y\} = K\sigma^2 + \mu^2 \tag{A.23}$$

$$\mathbb{E}\{Y^2\} = 2K\sigma^4 + 4\sigma^2\mu^2 + \left(K\sigma^2 + \mu^2\right)^2 \tag{A.24}$$

$$\sigma_y^2 = 2K\sigma^4 + 4\sigma^2\mu^2. \tag{A.25}$$

The central χ^2 distribution can be simplified to

$$f_Y(y) = \frac{x^{\frac{K}{2}-1}\exp\left(-\frac{x}{2\sigma^2}\right)}{(2\sigma^2)^{\frac{K}{2}}\,\Gamma\left(\frac{K}{2}\right)}, \tag{A.26}$$

where $\Gamma(\alpha)$ is the Gamma function, defined as

$$\begin{aligned} \Gamma(\alpha) &= \int_0^\infty t^{\alpha-1}e^{-t}dt, \quad \alpha > 0 \\ \Gamma(\alpha) &= (\alpha-1)!, \quad \alpha \text{ is an integer}, \alpha > 0 \\ \Gamma\left(\frac{1}{2}\right) &= \sqrt{\pi}, \quad \Gamma\left(\frac{3}{2}\right) = \frac{1}{2}\sqrt{\pi}. \end{aligned} \tag{A.27}$$

The corresponding characteristic function is

$$\Phi_Y(\omega) = \frac{1}{(1-j2\omega\sigma^2)^{\frac{K}{2}}}. \tag{A.28}$$

A.2.4 Rayleigh Distribution

The Rayleigh distribution is often used to statistically model the propagation effect on the envelope of a signal in a mobile radio channel. Let us consider $Y = \sqrt{X_1^2 + X_2^2}$, where X_1 and X_2 are statistically independent Gaussian distributed random variables with zero mean and variance σ^2. The new random variable Y is the envelop of the sum of two quadrature Gaussian signals, exhibiting a *Rayleigh distribution*. The corresponding PDF can be written as

$$f_Y(y) = \frac{y}{\sigma^2} e^{-\frac{y^2}{2\sigma^2}}, \; y \geq 0. \tag{A.29}$$

The moments of Y are given by

$$\mathbb{E}\left\{Y^k\right\} = \left(2\sigma^2\right)^{\frac{k}{2}} \Gamma\left(1 + \frac{1}{2}k\right). \tag{A.30}$$

An example of the Rayleigh fading with a maximum Doppler shift of 20 Hz is illustrated in Figure A.3. We can observe that the signal envelop fluctuates greatly in time, where deep fades may occur.

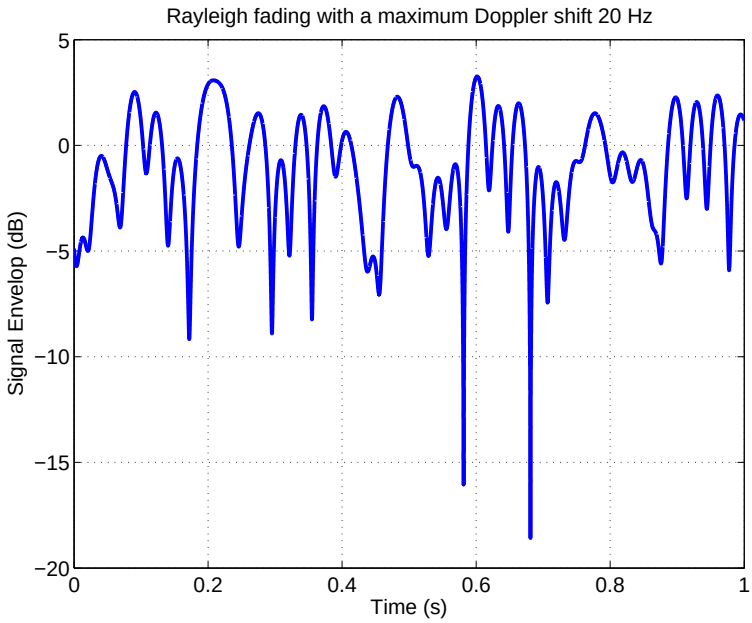

Fig. A.3: The received signal envelop due to Rayleigh fading with a maximum Doppler shift 20 Hz.

Appendix B

DIFFERENTIAL DETECTION

This appendix aims at providing some supplements to Chapter 5 and Chapter 6. We first address some implementation and performance issues for the analog differential receiver. Then, we compare the analog and digital receivers with respect to the interference rejection capability for the DS-DPSK transmission scheme.

B.1 Multiple Access Schemes for Differential Detection

There are various types of multiple access signaling schemes for differential detection. The system we consider here is illustrated in Figure 5.1, where "analog" differential receivers are utilized.

One option is Differential Phase Shift Keying (DPSK) combined with TH [HSFR02], which is represented in Figure B.2(a). Each differentially encoded bit is modulated by a TH code and the corresponding differential receiver requires a delay of the symbol duration. However, it seems infeasible to realize analog delays on the order of 50 ns or more. Taking into account a signal with a 500 MHz bandwidth, an all-pass filter providing a constant group delay of 50 ns requires an order as huge as 25 (the time-bandwidth product [KI90]). It should be emphasized that if the quadrature down-conversion stage is used as shown in Figure 3.6, two of the delay lines have to be implemented. Even if a differential receiver with only one single delay performs the autocorrelation in the bandpass range, such an implementation still does not help, since this delay has to be fine tuned to ensure the phase matching. For example, if the carrier frequency is 5 GHz, the delay accuracy must be less than 200 ps.

An alternative is the TR which enables shorter delays, since the autocorrelation does not take place with the previous modulated symbol but rather with an additional reference pulse. However, considering the office indoor Non-Line-Of-Sight (NLOS) scenario with $\tau_{\max} = 128$ ns and the Transmitted Reference combined with Binary Phase Shift Keying (TR-BPSK) with a delay between two paired pulses of length $\tau = 7$ ns, the resulting Bit Error Rate (BER) performance of the differential detection based on Single Window Combining (SinW-C) varies noticeably from channel realization to realization and an additional loss of 5 dB is introduced (cf. Figure B.1). The reason is that both the unmodulated data pulse and the reference pulse interfere with each other and as a result the Inter-/Intra-Symbol Interference (ISI)

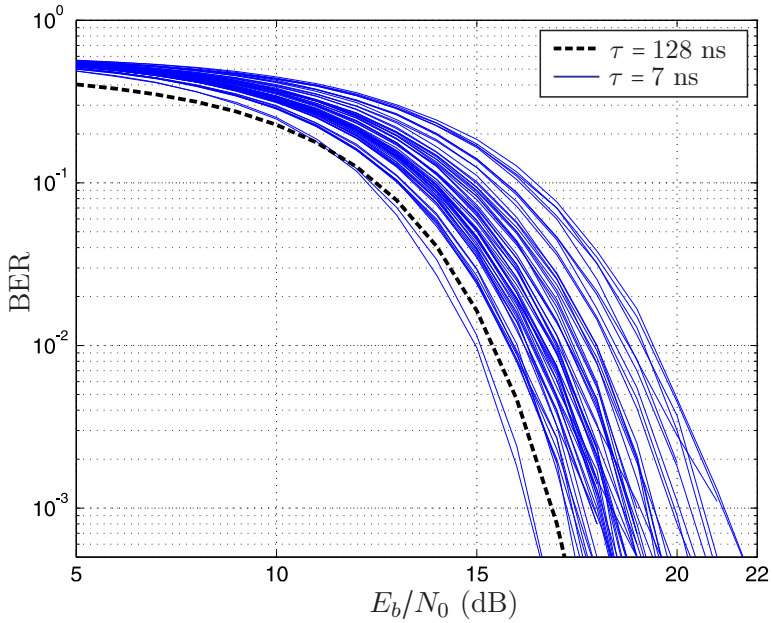

Fig. B.1: BER performance of TR-BPSK differential detection. The various solid curves are the TR performance of different channel realizations with delay between two pulses in doublet of length 7 ns. The black dashed solid curve corresponds to the case where the delay is equal to channel excess delay 128 ns with the reference channel realization (cf. Section 4.3.4).

disturbs the autocorrelation process. Furthermore, the Transmitted Reference (TR) scheme is less efficient (3 dB inferior) than the DPSK, because the transmission of an reference pulse consumes half of the symbol energy. For Multiple Access (MA) purpose, the Delay Hopping (DH) combined with TR modulation is proposed in [HT02]. Figure B.2(b) shows this DH TR signaling approach, where we denote the number of frames or the number of pulse repetitions per symbol interval as N_s. Each frame contains a pair of pulses. Every information bit is represented by a sequence of pulse pairs and the inter-pulse delays $D_n, n = 0, \cdots, N_s - 1$ are distinct, determined by a DH code. The multiple access communications are achieved by assigning multiple users with different DH codes. To demodulate the DH TR signals, N_s parallel delays and correlators are required, resulting in a prohibitive complexity.

Another approach is the frame differential signaling combined with DH [WLPK05], which is able to overcome the 3 dB disadvantage of TR and requires shorter delay lines. The signaling scheme is depicted in Figure B.2(c). Unlike the DH TR scheme, the DH frame differential method contains only one pulse per frame and the data is differentially encoded between two consecutive frames. The delay lags between every two neighboring pulses $D_n, n = 0, \cdots, N_s - 1$ depend on the DH code. The energy is collected by means of N_s fingers, each of which equipped with one analog delay of length D_n and a correlator. However, shorter delay lines are enabled at the expense of severe ISI, which has to be handled by advanced signal processing techniques after the non-coherent operation.

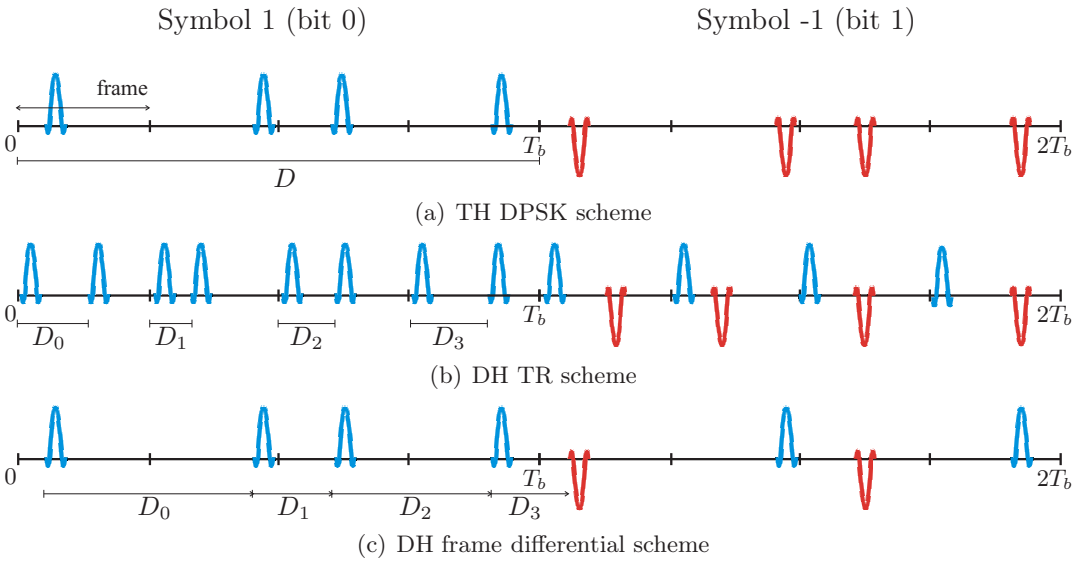

Fig. B.2: Representations of multiple access signaling schemes. The bit interval is T_b and the number of frames per symbol is $N_s = 4$.

B.2 Direct Sequence DPSK using the DCMF-based Symbol Differential Receiver

The main purpose of this part is to evaluate the ISI resilience of both the analog and Digital Code Matched Filter (DCMF)-based receivers. One advantage of the proposed digital solutions is that analog delays can be avoided. This makes the implementation of a differential receiver possible and straightforward. For the DCMF-based differential receiver shown in Figure 6.1(b), we consider the DPSK signaling scheme combined with Direct Sequence (DS), which is illustrated in Figure B.3(a). Its analog counterpart as shown in Figure 5.1(b) can be based on the frame differential method discussed in Section B.1 in combination with DS (cf. in Figure B.3(b)). The DS signal is able to capture the multipath energy and to resolve the ISI if its autocorrelation function is impulse-like. For both schemes, the existence and the level of ISI among subsequent chips depend on the chip delay or interval T_c. We plot the percentage of the received energy that can be recovered by both differential receivers as a function of chip delay T_c in Figure B.4, considering the integration window $T_\mathrm{i} = 128$ ns and the m-sequences of length $L_m = 31, 63$. The measured multipath channels (cf. Section 2.3) are applied and Additive White Gaussian Noise (AWGN) is not included. It can be observed that the DCMF-based receiver can capture over 92% of signal energy even when the chip interval T_c is very small. The analog receiver for frame differential scheme shows an inferior performance and sufficient energy can only be recovered when $T_c \geq 40$ ns. This implies a better ISI rejection capability of the DCMF-based receiver.

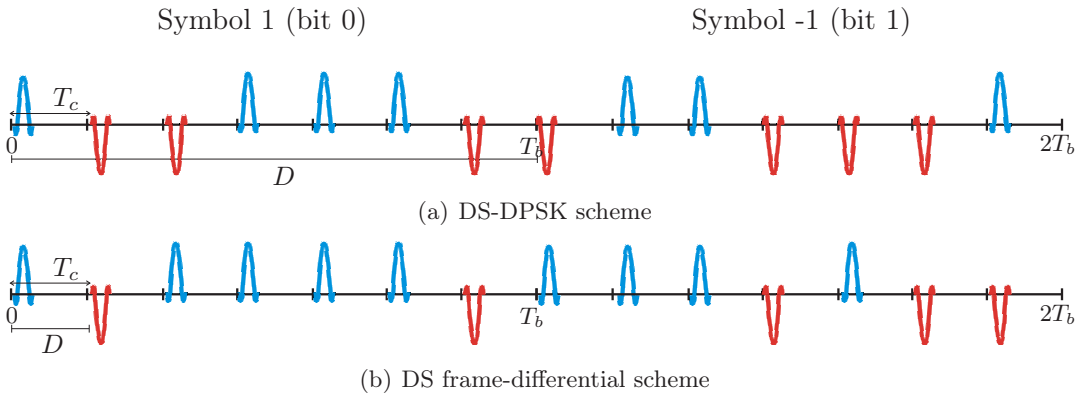

(a) DS-DPSK scheme

(b) DS frame-differential scheme

Fig. B.3: Representations of DS-based binary differential signaling schemes. The bit interval is T_b and the length of the DS code is L_m = 7. The delay used in the receiver is denoted as D.

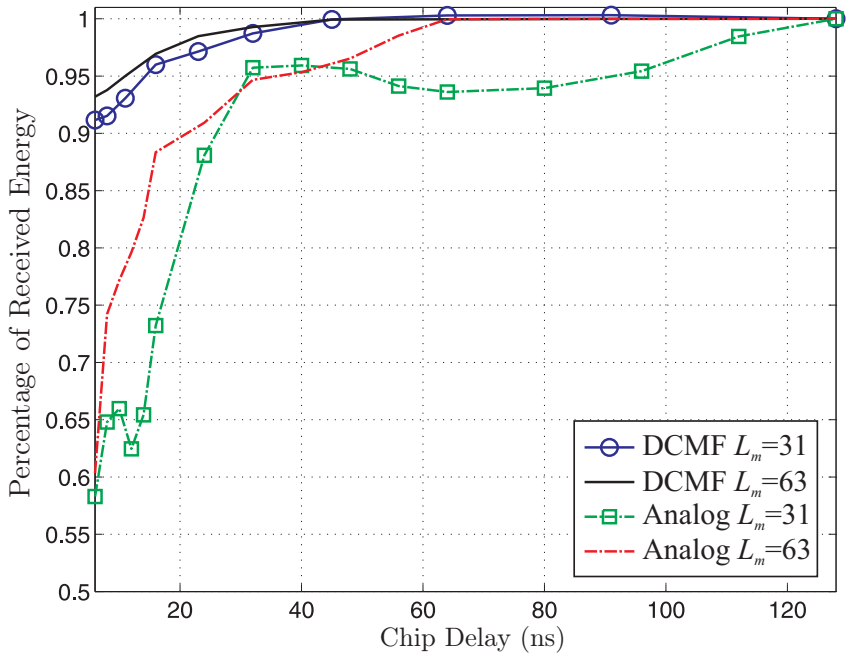

Fig. B.4: Percentage of the received energy versus the chip delay T_c for the symbol-differential DCMF receiver and the frame-differential "analog" receiver. We choose $T_{\rm i}$ = 128 ns.

Appendix C

WALSH HADAMARD TRANSFORMATION

This appendix describes some fundamentals of the Walsh codes and the Walsh Hadamard transformation which are used in Sections 6.7 and 6.8.

C.1 Walsh Codes

Walsh codes belong to the ones that are able to ensure the strictly orthogonality between different codewords. The Walsh code maps the data of length n to the codewords of length $M = 2^n$. An example for $M = 8$ Walsh functions $w_0(t), w_1(t), \cdots, w_7(t)$ is depicted in Figure C.1.

The Walsh Hadamard matrix with ±1 weights is utilized to generate the Walsh codes, which can be written as

$$\boldsymbol{W}_M = \left[\begin{array}{cccc} \boldsymbol{w}_0, & \boldsymbol{w}_1, & \cdots, & \boldsymbol{w}_{M-1} \end{array} \right] \in \mathbb{R}^{M \times M}, \tag{C.1}$$

where $\boldsymbol{w}_n = [w_{n,0}, w_{n,1}, \cdots, w_{n,M-1}]^T$. Some examples of the Walsh Hadamard matrices with $M = 2, 4, 8$ are expressed as

$$\boldsymbol{W}_2 = \begin{bmatrix} 1 & 1 \\ 1 & -1 \end{bmatrix}, \tag{C.2}$$

$$\boldsymbol{W}_4 = \begin{bmatrix} 1 & 1 & 1 & 1 \\ 1 & -1 & 1 & -1 \\ 1 & 1 & -1 & -1 \\ 1 & -1 & -1 & 1 \end{bmatrix}, \tag{C.3}$$

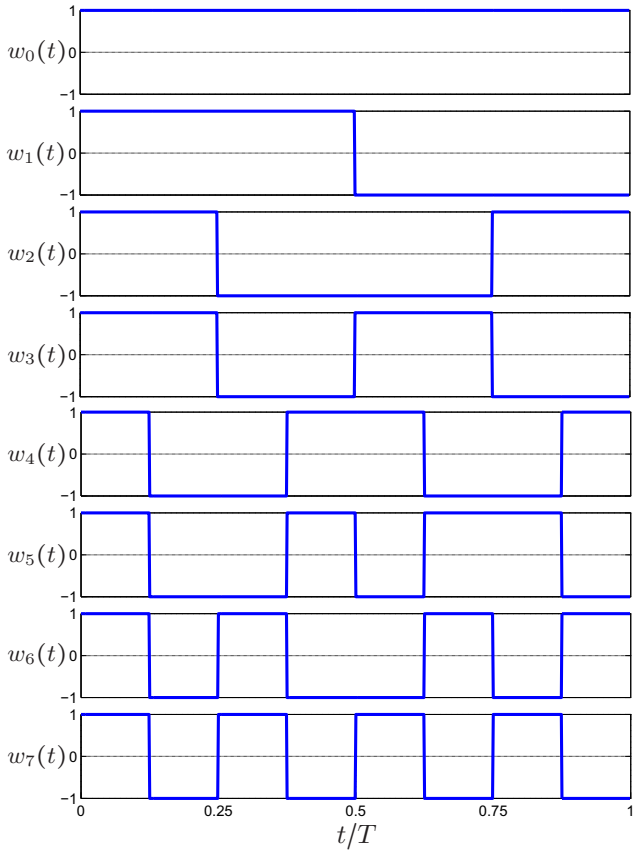

Fig. C.1: The Walsh functions for $M = 8$. The rectangular pulse is adopted and the duration of the waveform is T.

and

$$\boldsymbol{W}_8 = \begin{bmatrix} 1 & 1 & 1 & 1 & 1 & 1 & 1 & 1 \\ 1 & -1 & 1 & -1 & 1 & -1 & 1 & -1 \\ 1 & 1 & -1 & -1 & 1 & 1 & -1 & -1 \\ 1 & -1 & -1 & 1 & 1 & -1 & -1 & 1 \\ 1 & 1 & 1 & 1 & -1 & -1 & -1 & -1 \\ 1 & -1 & 1 & -1 & -1 & 1 & -1 & 1 \\ 1 & 1 & -1 & -1 & -1 & -1 & 1 & 1 \\ 1 & -1 & -1 & 1 & -1 & 1 & 1 & -1 \end{bmatrix}. \tag{C.4}$$

Therefore, the Walsh Hadamard matrix follows the relation

$$\boldsymbol{W}_M = \begin{bmatrix} \boldsymbol{W}_{M/2} & \boldsymbol{W}_{M/2} \\ \boldsymbol{W}_{M/2} & -\boldsymbol{W}_{M/2} \end{bmatrix}, \quad \text{with} \quad \boldsymbol{W}_0 = [1]. \tag{C.5}$$

The following properties can be obtained.

- All the Walsh functions have the same energy, i.e.,

$$E_w = \int_0^T w_n^2(t) = T, \text{ or } \sum_{i=0}^{M-1} w_{n,i}^2 = M, \quad \text{for } n = 0, \cdots, M-1. \tag{C.6}$$

- The orthogonality can be expressed by

$$\sum_{i=0}^{M-1} w_{n,i} w_{m,i} = 0, \quad \text{for } n \neq m. \tag{C.7}$$

  This means that the cross-correlation between Walsh codes is zero when they are perfectly synchronized.

- The Euclidean distance between any two Walsh codes is identical:

$$\sum_{i=0}^{M-1} |w_{m,i} - w_{n,i}|^2 = 2M, \quad \text{for } n \neq m. \tag{C.8}$$

  It indicates that the Euclidean distance increases with the modulation order, yielding a more favorable signal space.

- The Hamming distance between any two Walsh codes is $M/2$, meaning that $\lfloor (M/2-1)/2 \rfloor$ errors can be corrected by using the hard decision.

Due to the orthogonality property of the Walsh codes, they are utilized in Code Division Multiple Access (CDMA) systems to provide orthogonality among the users within a cell. The base station assign each user traffic channel a different Walsh code. The Walsh codes are also employed in modulation schemes.

However, Walsh codes do not have a good auto-correlation property, which makes it difficult for the receiver to detect the arrival of the codeword in the asynchronous transmission scenario. Therefore, Walsh codes are only used on the downlink of the synchronous CDMA system. On the uplink, where completely orthogonal channels are not ensured, the orthogonality of the Walsh codes is lost and thus Walsh is only applied for modulation purpose instead of spreading or multiple access. In this case, each channel or user is assigned a distinct pseudo random sequence for spread spectrum [Kam96].

C.2 Discrete Walsh Hadamard Transformation

If the input signal is denoted by $\boldsymbol{y} \in \mathbb{C}^M$ and the output is $\boldsymbol{v} = [v_0, v_1, \cdots, v_{M-1}]^T$, the *Discrete Walsh Hadamard Transformation* (DWHT) is expressed as

$$\boldsymbol{v} = \boldsymbol{W}_M \cdot \boldsymbol{y}. \tag{C.9}$$

The computational complexity with a matrix of size $M \times M$ has an order of $O(M^2)$.

Similar to the Fast Fourier Transform (FFT), by applying the relation shown in (C.5) to (C.9), we can obtain

$$\boldsymbol{W}_M \cdot \boldsymbol{y} = \begin{bmatrix} \boldsymbol{W}_{M/2} & \boldsymbol{W}_{M/2} \\ \boldsymbol{W}_{M/2} & -\boldsymbol{W}_{M/2} \end{bmatrix} \begin{bmatrix} \boldsymbol{y}_0 \\ \boldsymbol{y}_1 \end{bmatrix} = \begin{bmatrix} \boldsymbol{W}_{M/2}\boldsymbol{y}_0 + \boldsymbol{W}_{M/2}\boldsymbol{y}_1 \\ \boldsymbol{W}_{M/2}\boldsymbol{y}_0 - \boldsymbol{W}_{M/2}\boldsymbol{y}_1 \end{bmatrix}, \tag{C.10}$$

where $\boldsymbol{y}_0$ and $\boldsymbol{y}_1$ are the first and the last $M/2$ elements of the vector $\boldsymbol{y}$, respectively. This algorithm, which recursively breaks down a DWHT of size M into two smaller DWHTs of size $M/2$ until the element-wise calculation, is called the *Fast Walsh Hadamard Transformation* (FWHT). Therefore, the computational complexity of the FWHT is reduced to $O(M \cdot \log_2 M)$. Figure C.2 illustrates the procedure of the FWHT for $M = 4$.

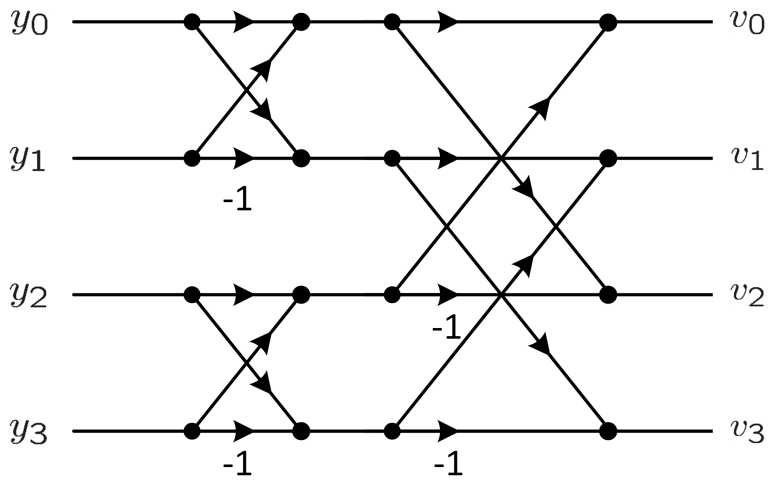

Fig. C.2: The illustration of the FWHT for $M = 4$.

Appendix D

WIDELY LINEAR MINIMUM MEAN SQUARE ERROR FILTER AND SOME RELATED DERIVATIONS

This appendix is intended to assist the development and analysis of adaptive WL algorithms introduced in Chapter 8. We first present the Widely Linear (WL)-Minimum Mean Square Error (MMSE) filter and the corresponding adaptive algorithms. Then, some related derivations and analyses are presented.

D.1 The WL-MMSE Filter

To fully exploit the second-order statistics of the observation vector $\boldsymbol{r} \in \mathbb{C}^M$, we formulate an augmented vector using a bijective transformation [BLT01, SGL04] as

$$\boldsymbol{r}_a = \frac{1}{\sqrt{2}} \begin{bmatrix} \boldsymbol{r}^T, & \boldsymbol{r}^H \end{bmatrix}^T \in \mathbb{C}^{2M}. \tag{D.1}$$

The problem of a WL filter is to design a weight vector $\boldsymbol{w}_a$ such that the filter output $y = \boldsymbol{w}_a^H \boldsymbol{r}_a$ satisfies a certain criterion (e.g., MMSE, Constrained Minimum Variance (CMV), Constrained Constant Modulus (CCM), etc.).

The structure of the WL-MMSE filter is depicted in Figure D.1, where $b_1(i)$ is the desired data and $e(i)$ is the estimation error.

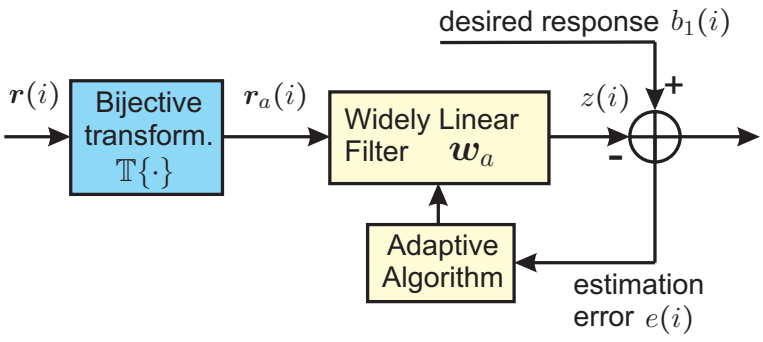

Fig. D.1: Block diagram of the WL-MMSE receiver in the complex baseband.

The optimization problem of WL-MMSE is expressed by calculating the minimization of the cost function J as

$$\min_{\boldsymbol{w}_a} J = \min_{\boldsymbol{w}_a} \mathbb{E}\left\{|e(i)|^2\right\} = \min_{\boldsymbol{w}_a} \mathbb{E}\left\{\left|b_1(i) - \boldsymbol{w}_a^H \boldsymbol{r}_a(i)\right|^2\right\}. \tag{D.2}$$

The optimum solution or Wiener solution in the WL case can be obtained as [PC95]

$$\boldsymbol{w}_{a,o} = \boldsymbol{R}_a^{-1} \boldsymbol{p}_a, \tag{D.3}$$

where $\boldsymbol{R}_a = \mathbb{E}\left\{\boldsymbol{r}_a(i)\boldsymbol{r}_a^H(i)\right\}$ is the *augmented covariance matrix* of the augmented vector $\boldsymbol{r}_a(i)$ and $\boldsymbol{p}_a = \mathbb{E}\left\{b_1^*(i)\boldsymbol{r}_a(i)\right\}$ is the *augmented cross-correlation vector* of the augmented vector $\boldsymbol{r}_a(i)$ and the desired signal $b_1(i)$.

MMSE and SINR

The MMSE of WL-MMSE is calculated by

$$\begin{aligned} J_{a,\min} &= \mathbb{E}\left\{\left|b_1(i) - \boldsymbol{w}_{a,o}^H \boldsymbol{r}_a(i)\right|^2\right\} \\ &= \sigma_b^2 - \mathbb{E}\left\{b_1(i)\boldsymbol{r}_a^H(i)\right\}\boldsymbol{w}_{a,o} - \boldsymbol{w}_{a,o}^H \mathbb{E}\left\{b_1^*(i)\boldsymbol{r}_a(i)\right\} + \boldsymbol{w}_{a,o}^H \mathbb{E}\left\{\boldsymbol{r}_a(i)\boldsymbol{r}_a^H(i)\right\}\boldsymbol{w}_{a,o} \\ &= \sigma_b^2 - \boldsymbol{p}_a^H \boldsymbol{R}_a^{-1} \boldsymbol{p}_a, \end{aligned} \tag{D.4}$$

where $\sigma_b^2 = \mathbb{E}\left\{|b_1(i)|^2\right\}$.

Let us represent the received vector as $\boldsymbol{r}(i) = \boldsymbol{s}(i) + \boldsymbol{v}(i)$, where $\boldsymbol{s}(i)$ is the desired response and $\boldsymbol{v}(i)$ is the received interference plus noise. Accordingly, we can have $\boldsymbol{r}_a(i) = \boldsymbol{s}_a(i) + \boldsymbol{v}_a(i)$ in the augmented form. Assuming that $\boldsymbol{s}(i)$ and $\boldsymbol{v}(i)$ are uncorrelated, the augmented covariance matrix follows $\boldsymbol{R}_a = \boldsymbol{R}_{a,ss} + \boldsymbol{R}_{a,vv}$, where $\boldsymbol{R}_{a,ss} = \mathbb{E}\left\{\boldsymbol{s}_a(i)\boldsymbol{s}_a^H(i)\right\} = \boldsymbol{p}_a\boldsymbol{p}_a^H$ and $\boldsymbol{R}_{a,vv} = \mathbb{E}\left\{\boldsymbol{v}_a(i)\boldsymbol{v}_a^H(i)\right\}$ are the augmented covariance matrix of the desired response and the interference plus noise, respectively.

With the optimum solution $\boldsymbol{w}_{a,o}$, the output Signal-to-Interference plus Noise Ratio (SINR)

can be expressed as

$$\begin{aligned}
\mathrm{SINR}_a &= \frac{\mathbb{E}\left\{\left|\boldsymbol{w}_{a,o}^H \boldsymbol{s}_a(i)\right|^2\right\}}{\mathbb{E}\left\{\left|\boldsymbol{w}_{a,o}^H \boldsymbol{v}_a(i)\right|^2\right\}} \\
&= \frac{\boldsymbol{w}_{a,o}^H \boldsymbol{R}_{a,ss} \boldsymbol{w}_{a,o}}{\boldsymbol{w}_{a,o}^H \boldsymbol{R}_{a,vv} \boldsymbol{w}_{a,o}} \\
&= \frac{\boldsymbol{w}_{a,o}^H \boldsymbol{R}_{a,ss} \boldsymbol{w}_{a,o}}{\boldsymbol{w}_{a,o}^H \left(\boldsymbol{R}_a - \boldsymbol{R}_{a,ss}\right) \boldsymbol{w}_{a,o}} \\
&= \frac{\boldsymbol{p}_a^H \boldsymbol{R}_a^{-1} \boldsymbol{p}_a}{1 - \boldsymbol{p}_a^H \boldsymbol{R}_a^{-1} \boldsymbol{p}_a} \qquad \text{(D.5)} \\
&\overset{(D.4)}{=} \frac{\sigma_b^2 - J_{a,\min}}{1 - \sigma_b^2 + J_{a,\min}} \\
&\overset{\text{with } \sigma_b^2=1}{=} \frac{1}{J_{a,\min}} - 1. \qquad \text{(D.6)}
\end{aligned}$$

The expressions for the MMSE and the maximum achievable SINR shown in (D.4) and (D.5) or (D.6) can be used for the WL reduced-rank schemes based on the MMSE criterion, by replacing the corresponding parameters with reduced-rank counterparts.

Conjugate Symmetry Property

The augmented covariance matrix has a block structure:

$$\boldsymbol{R}_a = \frac{1}{2}\begin{bmatrix} \boldsymbol{R} & \check{\boldsymbol{R}} \\ \check{\boldsymbol{R}}^* & \boldsymbol{R}^* \end{bmatrix}, \qquad \text{(D.7)}$$

where $\boldsymbol{R} = \mathbb{E}\left\{\boldsymbol{r}(i)\boldsymbol{r}^H(i)\right\}$ is the covariance matrix of the observation vector $\boldsymbol{r}$ and $\check{\boldsymbol{R}} = \mathbb{E}\left\{\boldsymbol{r}(i)\boldsymbol{r}^T(i)\right\}$ is the pseudo-covariance matrix (also referred to as complementary covariance matrix). The inverse of the augmented covariance matrix can be written as

$$\boldsymbol{R}_a^{-1} = 2\begin{bmatrix} \boldsymbol{R} & \check{\boldsymbol{R}} \\ \check{\boldsymbol{R}}^* & \boldsymbol{R}^* \end{bmatrix}^{-1} = 2\begin{bmatrix} \boldsymbol{P} & \boldsymbol{Q} \\ \boldsymbol{Q}^* & \boldsymbol{P}^* \end{bmatrix}. \qquad \text{(D.8)}$$

To be specified, it can also be written as

$$\begin{bmatrix} \boldsymbol{R} & \check{\boldsymbol{R}} \\ \check{\boldsymbol{R}}^* & \boldsymbol{R}^* \end{bmatrix}\begin{bmatrix} \boldsymbol{P} & \boldsymbol{Q} \\ \boldsymbol{Q}^* & \boldsymbol{P}^* \end{bmatrix} = \begin{bmatrix} \boldsymbol{I}_M & \boldsymbol{0}_M \\ \boldsymbol{0}_M & \boldsymbol{I}_M \end{bmatrix}. \qquad \text{(D.9)}$$

Then we can obtain the following equations

$$\begin{aligned} \boldsymbol{R}\boldsymbol{P} + \check{\boldsymbol{R}}\boldsymbol{Q}^* &= \boldsymbol{I}_M && \text{(D.10)} \\ \boldsymbol{R}^*\boldsymbol{P}^* + \check{\boldsymbol{R}}^*\boldsymbol{Q} &= \boldsymbol{I}_M && \text{(D.11)} \\ \boldsymbol{R}\boldsymbol{Q} + \check{\boldsymbol{R}}\boldsymbol{P}^* &= \boldsymbol{0}_M && \text{(D.12)} \\ \boldsymbol{R}^*\boldsymbol{Q}^* + \check{\boldsymbol{R}}^*\boldsymbol{P} &= \boldsymbol{0}_M, && \text{(D.13)} \end{aligned}$$

where (D.10) and (D.12) are the conjugates of (D.11) and (D.13), respectively. However, the fact that (D.8) holds does not indicate that $\boldsymbol{R}^{-1} = \boldsymbol{P}$ nor $\check{\boldsymbol{R}}^{-1} = \boldsymbol{Q}$.

If the estimated data is real-valued, i.e., $b_1(i) \in \mathbb{R}$, $\boldsymbol{p}_a$ can also be written as $\boldsymbol{p}_a = \frac{1}{\sqrt{2}}\begin{bmatrix} \boldsymbol{p}^T, & \boldsymbol{p}^H \end{bmatrix}^T$, which has a structured form. By applying the structured expressions of $\boldsymbol{R}_a$ and $\boldsymbol{p}_a$, the optimum solution for the WL-MMSE filter is given by

$$\boldsymbol{w}_{a,o} = \boldsymbol{R}_a^{-1}\boldsymbol{p}_a = 2\begin{bmatrix} \boldsymbol{P} & \boldsymbol{Q} \\ \boldsymbol{Q}^* & \boldsymbol{P}^* \end{bmatrix} \cdot \frac{1}{\sqrt{2}}\begin{bmatrix} \boldsymbol{p} \\ \boldsymbol{p}^* \end{bmatrix} = \sqrt{2}\begin{bmatrix} \boldsymbol{P}\boldsymbol{p} + \boldsymbol{Q}\boldsymbol{p}^* \\ \boldsymbol{P}^*\boldsymbol{p}^* + \boldsymbol{Q}^*\boldsymbol{p} \end{bmatrix} = \sqrt{2}\begin{bmatrix} \check{\boldsymbol{w}} \\ \check{\boldsymbol{w}}^* \end{bmatrix}. \quad \text{(D.14)}$$

The filter output can be reformulated as

$$\begin{aligned} y &= \boldsymbol{w}_{a,o}^H \boldsymbol{r}_a(i) = \sqrt{2}\begin{bmatrix} \check{\boldsymbol{w}}^H & \check{\boldsymbol{w}}^T \end{bmatrix} \cdot \frac{1}{\sqrt{2}}\begin{bmatrix} \boldsymbol{r}(i) \\ \boldsymbol{r}^*(i) \end{bmatrix} \\ &= \check{\boldsymbol{w}}^H \boldsymbol{r}(i) + \check{\boldsymbol{w}}^T \boldsymbol{r}^*(i) = \boldsymbol{r}_a^T(i)\boldsymbol{w}_{a,o}^* = 2\Re\left\{\check{\boldsymbol{w}}^H \boldsymbol{r}(i)\right\}. \end{aligned} \quad \text{(D.15)}$$

This shows the *conjugate symmetry* property of the WL processing when the estimated data is real-valued [CGPV09].

Adaptive algorithms that exploit such conjugate symmetry and structured properties can be designed in order to reduce the computational complexity as well as to enhance the convergence performance [nso].

Compared to L-MMSE

The MMSE of the linear MMSE (L-MMSE) filter is [Hay02]

$$J_{\min} = \mathbb{E}\left\{\left|b_1(i) - \boldsymbol{w}_o^H \boldsymbol{r}(i)\right|^2\right\} \overset{\boldsymbol{w}_o = \boldsymbol{R}^{-1}\boldsymbol{p}}{=} 1 - \boldsymbol{p}^H \boldsymbol{R}^{-1}\boldsymbol{p}. \quad \text{(D.16)}$$

Because of the conjugate symmetry property shown in (D.15), the optimization problem of the WL-MMSE filter is equivalent to [SGL04]

$$\min_{\boldsymbol{w}_a} J = \min_{\boldsymbol{w}_a} \mathbb{E}\left\{\left|b_1(i) - \Re\left\{\boldsymbol{w}_a^H \boldsymbol{r}_a(i)\right\}\right|^2\right\}. \quad \text{(D.17)}$$

Let us introduce an auxiliary WL vector $\tilde{\boldsymbol{w}}_a = \begin{bmatrix} \boldsymbol{w}_o^T, & \boldsymbol{0}^T \end{bmatrix}^T \in \mathbb{C}^{2M}$, where $\boldsymbol{w}_o$ is the optimum solution for the L-MMSE filter. Since the WL weight vector $\tilde{\boldsymbol{w}}_a$ is not the optimum

solution to the WL-MMSE problem, its corresponding Mean Square Error (MSE) $\tilde{J}_a \geq J_{a,\min}$. By inserting $\tilde{\boldsymbol{w}}_a$ into the cost function of the equation (D.17), we can have

$$\begin{aligned} \tilde{J}_a &= \mathbb{E}\left\{\left|b_1(i) - \Re\left\{\tilde{\boldsymbol{w}}_a^H \boldsymbol{r}_a(i)\right\}\right|^2\right\} \\ &= \mathbb{E}\left\{\left|b_1(i) - \Re\left\{\boldsymbol{w}_o^H \boldsymbol{r}(i)\right\}\right|^2\right\} \\ &\leq J_{\min}. \end{aligned} \tag{D.18}$$

The last inequality holds due to the fact that $\Re\{\cdot\}$ takes the real part of $\boldsymbol{w}_o^H \boldsymbol{r}(i)$, leading to a reduced power of the interference and the noise. Therefore, the MMSEs of the WL-MMSE and the L-MMSE filters satisfy $J_{a,\min} \leq J_{\min}$, i.e., the WL-MMSE scheme provides a smaller error than the L-MMSE. A simulation example is shown in Figure D.2, where the same scenario as in Section 8.3.5 is chosen.

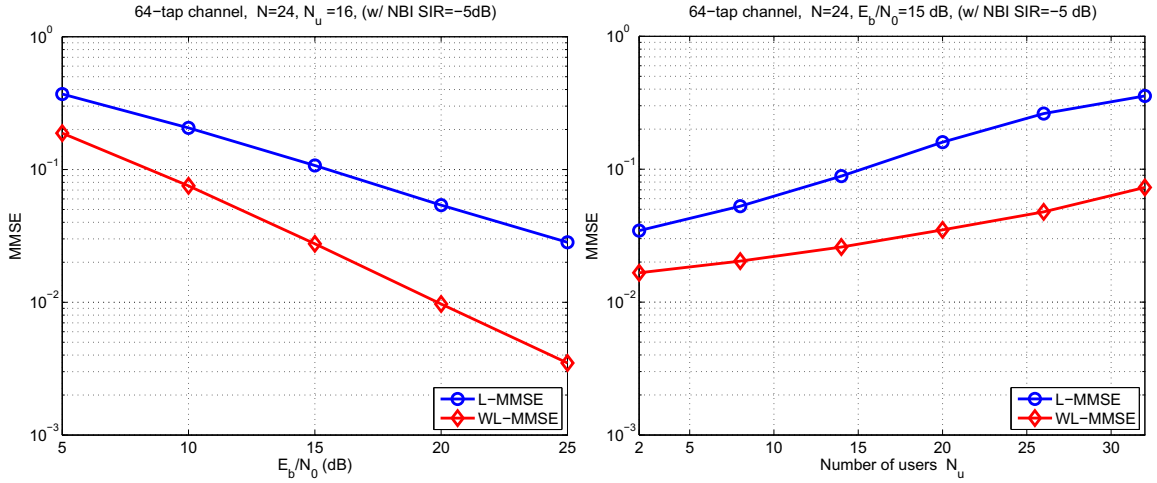

(a) (b)

Fig. D.2: The MMSE of the L-/WL-MMSE algorithms versus (a) E_b/N_0 (dB) and (b) the number of users N_u. We consider E_b/N_0 = 15 dB and OFDM NBI of SIR = -5 dB.

D.1.1 Adaptive Algorithms

Similarly to the linear case shown in [Hay02], two training-based adaptive algorithms for the WL-MMSE filter, namely the Stochastic Gradient (SG) and the Recursive Least Squares (RLS) algorithms, are introduced to adaptively estimate the weight vector shown in equation (D.3) as

$$\boldsymbol{w}_a(i) = \boldsymbol{R}_a^{-1}(i)\boldsymbol{p}_a(i). \tag{D.19}$$

The SG algorithm is derived by

$$\boldsymbol{w}_a(i+1) = \boldsymbol{w}_a(i) - \mu \frac{\partial J(i)}{\partial \boldsymbol{w}_a^*(i)}, \tag{D.20}$$

where μ is the step size and $\frac{\partial J(i)}{\partial \boldsymbol{w}_a^*(i)}$ is the gradient of the instantaneous cost function $J(i)$ for

the WL-MMSE scheme with respect to the weight vector $\boldsymbol{w}_a^*(i)$:

$$\begin{aligned}\frac{\partial J(i)}{\partial \boldsymbol{w}_a^*(i)} &= \frac{\partial\left\{\sigma_b^2 - b_1(i)\boldsymbol{r}_a^H(i)\boldsymbol{w}_a(i) - \boldsymbol{w}_a^H(i)b_1^*(i)\boldsymbol{r}_a(i) + \boldsymbol{w}_a^H(i)\boldsymbol{r}_a(i)\boldsymbol{r}_a^H(i)\boldsymbol{w}_a(i)\right\}}{\partial \boldsymbol{w}_a^*(i)} \\ &= -b_1^*(i)\boldsymbol{r}_a(i) + \boldsymbol{r}_a(i)\boldsymbol{r}_a^H(i)\boldsymbol{w}_a(i). \end{aligned} \tag{D.21}$$

Then we have

$$\begin{aligned}\boldsymbol{w}_a(i+1) &= \boldsymbol{w}_a(i) + \mu\left(b_1^*(i) - \boldsymbol{r}_a^H(i)\boldsymbol{w}_a(i)\right)\boldsymbol{r}_a(i), \\ &\triangleq \boldsymbol{w}_a(i) + \mu e^*(i)\boldsymbol{r}_a(i) \end{aligned} \tag{D.22}$$

as the updated weight vector, where the estimation error is defined as $e(i) = b_1(i) - \boldsymbol{w}_a^H(i)\boldsymbol{r}_a(i)$. The step size μ in the SG algorithm should satisfy

$$0 < \mu < \frac{2}{\lambda_{a,\max}}, \tag{D.23}$$

where $\lambda_{a,\max}$ is the maximum eigenvalue of the augmented covariance matrix $\boldsymbol{R}_a$.

The RLS algorithm directly estimates the inverse of the augmented covariance matrix $\boldsymbol{R}_a^{-1}(i)$ using the matrix inversion lemma:

$$\boldsymbol{k}(i) = \frac{\lambda^{-1}\boldsymbol{R}_a^{-1}(i-1)\boldsymbol{r}_a(i)}{1 + \lambda^{-1}\boldsymbol{r}_a^H(i)\boldsymbol{R}_a^{-1}(i-1)\boldsymbol{r}_a(i)} \tag{D.24}$$

and

$$\boldsymbol{R}_a^{-1}(i) = \lambda^{-1}\boldsymbol{R}_a^{-1}(i-1) - \lambda^{-1}\boldsymbol{k}(i)\boldsymbol{r}_a^H(i)\boldsymbol{R}_a^{-1}(i-1), \tag{D.25}$$

where $\boldsymbol{k}(i)$ is called the gain vector. From equations (D.24) and (D.25), the following relationship can be derived:

$$\boldsymbol{k}(i) = \boldsymbol{R}_a^{-1}(i)\boldsymbol{r}_a(i). \tag{D.26}$$

The recursively updated augmented cross-correlation vector is expressed by

$$\boldsymbol{p}_a(i) = \lambda\boldsymbol{p}_a(i-1) + b_1^*(i)\boldsymbol{r}_a(i), \tag{D.27}$$

where $0 < \lambda < 1$ is the forgetting factor. The equations (D.24), (D.25), (D.27), and (D.19) constitute the RLS algorithm for the WL-MMSE filter.

From another point of view, if we insert (D.27) into (D.19), we can obtain

$$\begin{aligned}\boldsymbol{w}_a(i) &= \lambda\boldsymbol{R}_a^{-1}(i)\boldsymbol{p}_a(i-1) + \boldsymbol{R}_a^{-1}(i)b_1^*(i)\boldsymbol{r}_a(i) \\ &\overset{(D.25)}{=} \boldsymbol{R}_a^{-1}(i-1)\boldsymbol{p}_a(i-1) - \boldsymbol{k}(i)\boldsymbol{r}_a^H(i)\boldsymbol{R}_a^{-1}(i-1)\boldsymbol{p}_a(i-1) + \boldsymbol{R}_a^{-1}(i)b_1^*(i)\boldsymbol{r}_a(i) \\ &= \boldsymbol{w}_a(i-1) - \boldsymbol{k}(i)\boldsymbol{r}_a^H(i)\boldsymbol{w}_a(i-1) + b_1^*(i)\boldsymbol{R}_a^{-1}(i)\boldsymbol{r}_a(i) \\ &\overset{(D.26)}{=} \boldsymbol{w}_a(i-1) + \boldsymbol{k}(i)\left(b_1(i) - \boldsymbol{w}_a^H(i-1)\boldsymbol{r}_a(i)\right)^* \\ &= \boldsymbol{w}_a(i-1) + \boldsymbol{k}(i)\xi^*(i), \end{aligned} \tag{D.28}$$

where $\xi(i) = b_1(i) - \boldsymbol{w}_a^H(i-1)\boldsymbol{r}_a(i)$ is the *a priori* estimation error. The weight vector shown in (D.28) is updated by increasing its old vector by the value that is equal to the product of the gain vector and the complex conjugate of the a priori estimation error.

Tables D.1 and D.2 summarize these two algorithms. The scalar $\delta > 0$ in Table D.2 is the initialization parameter to ensure the numerical stability of the RLS algorithm.

Tab. D.1: SG Adaptive Algorithm for WL-MMSE

Initialize the algorithm by setting: $\boldsymbol{p}_a(0) = \boldsymbol{0}, \boldsymbol{w}_a(0) = \boldsymbol{0}$, choose the step size μ
For the time index $i = 1, 2, \cdots, N_s$ The estimated desired response is $z(i) = \boldsymbol{w}_a^H(i)\boldsymbol{r}_a(i)$ The estimation error $e(i) = b_1(i) - z(i)$ Update the weight vector $\boldsymbol{w}_a(i+1) = \boldsymbol{w}_a(i) + \mu e^*(i)\boldsymbol{r}_a(i)$ end

Tab. D.2: RLS Adaptive Algorithm for WL-MMSE

Initialize the algorithm by setting: $\boldsymbol{p}_a(0) = \boldsymbol{0}, \boldsymbol{R}_a^{-1}(0) = \delta^{-1}\boldsymbol{I}_{2M}, \boldsymbol{w}_a(0) = \boldsymbol{0}$
For the time index $i = 1, 2, \cdots, N_s$ The estimated desired response is $z(i) = \boldsymbol{w}_a^H(i)\boldsymbol{r}_a(i)$ The recursive calculation: $\boldsymbol{k}(i) = \dfrac{\lambda^{-1}\boldsymbol{R}_a^{-1}(i-1)\boldsymbol{r}_a(i)}{1 + \lambda^{-1}\boldsymbol{r}_a^H(i)\boldsymbol{R}_a^{-1}(i-1)\boldsymbol{r}_a(i)}$ $\boldsymbol{R}_a^{-1}(i) = \lambda^{-1}\boldsymbol{R}_a^{-1}(i-1) - \lambda^{-1}\boldsymbol{k}(i)\boldsymbol{r}_a^H(i)\boldsymbol{R}_a^{-1}(i-1)$ $\boldsymbol{p}_a(i) = \lambda\boldsymbol{p}_a(i-1) + b_1^*(i)\boldsymbol{r}_a(i)$ Update weight vector $\boldsymbol{w}_a(i) = \boldsymbol{R}_a^{-1}(i)\boldsymbol{p}_a(i)$ end

D.2 Eigenvalue Analysis of $\bar{\boldsymbol{R}}$ and $\bar{\boldsymbol{R}}_a$

This part is presented to compare the eigenvalues of $\bar{\boldsymbol{R}}$ and $\bar{\boldsymbol{R}}_a$ used in Section 8.3.2.5. We consider the same rank D for both the linear and the WL-Multistage Wiener Filter (MSWF) schemes. Two constructions for the rank-reduction matrix can be represented as $\boldsymbol{S}_{a,D} = \mathbb{T}\left\{\check{\boldsymbol{S}}_D\right\} = \mathbb{T}\{\boldsymbol{S}_D\} + \mathbb{T}\{\Delta\boldsymbol{S}_D\}$, where $\Delta\boldsymbol{S}_D = \boldsymbol{0}$ indicates the Quasi Widely Linear (QWL) construction. We define $\Delta\boldsymbol{S}_{a,D} = \mathbb{T}\{\Delta\boldsymbol{S}_D\}$. The augmented reduced-rank covariance

matrix $\bar{\boldsymbol{R}}_a$ can be written as

$$\begin{aligned}\bar{\boldsymbol{R}}_a &= \frac{1}{2}\left(\mathbb{T}\{\boldsymbol{S}_D\}+\Delta\boldsymbol{S}_{a,D}\right)^H\begin{bmatrix}\boldsymbol{R} & \check{\boldsymbol{R}}\\ \check{\boldsymbol{R}}^* & \boldsymbol{R}^*\end{bmatrix}\left(\mathbb{T}\{\boldsymbol{S}_D\}+\Delta\boldsymbol{S}_{a,D}\right)\\ &= \frac{1}{2}\bar{\boldsymbol{R}}+\frac{1}{2}\underbrace{\Re\left\{\boldsymbol{S}_D^H\check{\boldsymbol{R}}\boldsymbol{S}_D^*\right\}}_{\bar{\check{\boldsymbol{R}}}}\\ &\quad+\frac{1}{4}\underbrace{\left(\Delta\boldsymbol{S}_{a,D}^H\boldsymbol{R}_a\boldsymbol{S}_{a,D}+\boldsymbol{S}_{a,D}^H\boldsymbol{R}_a\Delta\boldsymbol{S}_{a,D}+\Delta\boldsymbol{S}_{a,D}^H\boldsymbol{R}_a\Delta\boldsymbol{S}_{a,D}\right)}_{\Delta\bar{\boldsymbol{R}}_a}\\ &= \frac{1}{2}\bar{\boldsymbol{R}}+\frac{1}{2}\bar{\check{\boldsymbol{R}}}+\frac{1}{4}\Delta\bar{\boldsymbol{R}}_a.\end{aligned} \tag{D.29}$$

Since all the components in (D.29) are Hermitian matrices, by using the theorem (Weyl) 4.3.1 in [HJ90], we can obtain the k-th eigenvalue of the augmented reduced-rank covariance matrix (expressed by $\lambda_k(\cdot), k=1,\cdots,D, D\ll K$ in a descending order) satisfying

$$\begin{aligned}\lambda_k\left(\bar{\boldsymbol{R}}_a\right) &= \lambda_k\left(\frac{1}{2}\bar{\boldsymbol{R}}+\frac{1}{2}\bar{\check{\boldsymbol{R}}}+\frac{1}{4}\Delta\bar{\boldsymbol{R}}_a\right)\\ &\le \frac{1}{2}\lambda_k\left(\bar{\boldsymbol{R}}+\bar{\check{\boldsymbol{R}}}\right)+\frac{1}{4}\lambda_{\max}\left(\Delta\bar{\boldsymbol{R}}_a\right).\end{aligned} \tag{D.30}$$

If the QWL is applied, $\Delta\bar{\boldsymbol{R}}_a=\boldsymbol{0}$ and (D.30) can be simplified by using the corollary 4.3.3 in [HJ90] as

$$\begin{aligned}\lambda_{a,k}^{\mathrm{QWL}} &\le \frac{1}{2}\lambda_k\left(\bar{\boldsymbol{R}}+\bar{\check{\boldsymbol{R}}}\right)<\frac{1}{2}\lambda_k\left(\bar{\boldsymbol{R}}+\bar{\check{\boldsymbol{R}}}+(\bar{\boldsymbol{R}}-\bar{\check{\boldsymbol{R}}})\right)\\ &< \frac{1}{2}\lambda_k\left(\bar{\boldsymbol{R}}+\bar{\boldsymbol{R}}\right)=\lambda_k,\end{aligned} \tag{D.31}$$

where it is given that $\bar{\boldsymbol{R}}-\bar{\check{\boldsymbol{R}}}$ is Hermitian and $\lambda_k\left(\bar{\boldsymbol{R}}-\bar{\check{\boldsymbol{R}}}\right)>0$ [SS03]. For the Total Widely Linear (TWL) construction, the eigenvalue analysis shows that

$$\lambda_{a,k}^{\mathrm{TWL}}<\lambda_k+\frac{1}{4}\lambda_k\left(\Delta\bar{\boldsymbol{R}}_a\right). \tag{D.32}$$

If $\lambda_k\left(\Delta\bar{\boldsymbol{R}}_a\right)$ is not dominant, $\lambda_{a,k}^{\mathrm{TWL}}<\lambda_k$ still holds. However, it is shown in Section 8.3.5.1 that when there is strong NBI, $\lambda_{a,k}^{\mathrm{TWL}}>\lambda_k$ will occur.

D.3 Impact from the Number of Channel Paths on the WL-MSWF Scheme

In our simulations, we have considered realistic UWB channels that have a maximum channel excess delay $\tau_{\max}=64$ ns (cf. Section 8.3.5). The total signal bandwidth is chosen as $B=1$ GHz and thus $L=B\tau_{\max}=64$. Figure D.3 shows the maximum achievable SINR versus D for different signal bandwidths $B=31.25$ MHz, 156.25 MHz, 500 MHz, 1 GHz. Then we have the resulting $L=2,10,32,64$. It can be observed that for all the MSWF algorithms the rank D that is required to achieve the full-rank performance does not scale with the length of the channel. The performance for $L=32$ and $L=64$ is similar. According to the FCC

[Fed02], when $B < 500$ MHz, the UWB emission requirement is not fulfilled. For $L = 10$, the performance is the worst due to the fact that the multipath diversity is not sufficiently exploited and Inter-/Intra-Symbol Interference (ISI) is still considerable. The ISI is alleviated with $L = 2$ but the performance is deteriorated by the multipath fading.

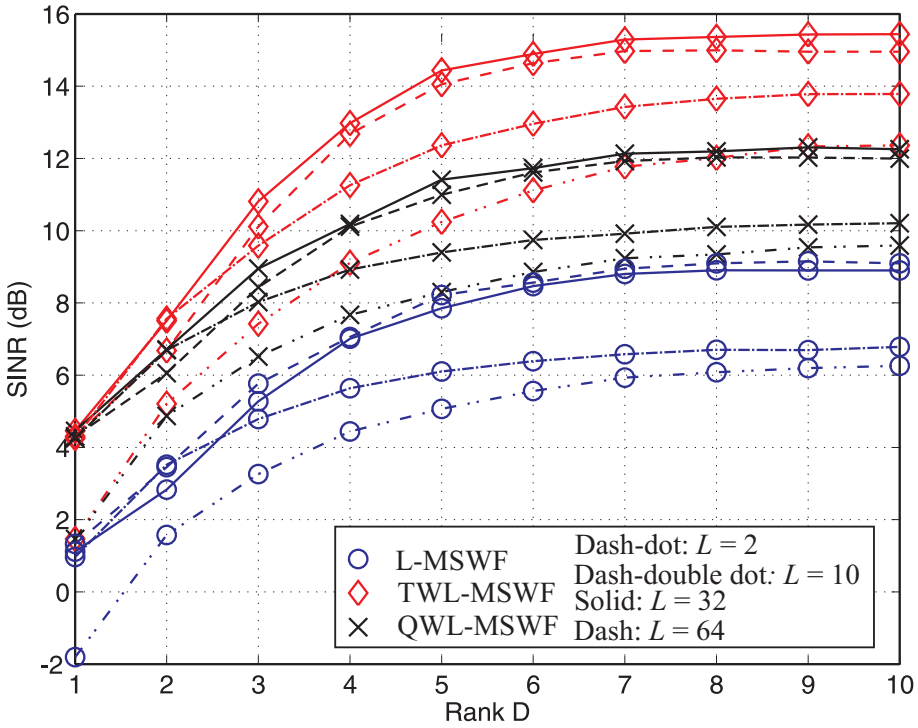

Fig. D.3: The SINR of the L-/TWL-/QWL-MSWF schemes for different number of channel taps L. We choose $E_b/N_0 = 15$ dB, $N_u = 16$, and OFDM NBI of SIR = -5 dB.

GLOSSARY OF ACRONYMS, SYMBOLS AND NOTATION

Acronyms

ADC	Analog-to-Digital Converter
ARLS	Augmented Recursive Least Squares
ASK	Amplitude Shift Keying
AVF	Auxiliary Vector Filter
AWGN	Additive White Gaussian Noise
BER	Bit Error Rate
BPSK	Binary Phase Shift Keying
CCM	Constrained Constant Modulus
CDF	Cumulative Density Function
CDMA	Code Division Multiple Access
CEPT	European Conference of Postal and Telecommunications Administrations
CMOS	Complementary Metal Oxide Semiconductor
CMV	Constrained Minimum Variance
DAC	Digital-to-Analog Converter
DC	Direct Current
DCMF	Digital Code Matched Filter
DH	Delay Hopping
DoD	Department of Defense
DPSK	Differential Phase Shift Keying
DS	Direct Sequence
DS-CDMA	Direct Sequence Code Division Multiple Access
DSSS	Direct Sequence Spread Spectrum
DS-UWB	Direct Sequence Ultra Wideband
DWHT	Discrete Walsh Hadamard Transformation
ECC	European Communications Commission
EIRP	Effective Isotropic Radiated Power
FCC	Federal Communications Commission
FD	Fading Depth
FFT	Fast Fourier Transform
FH	Frequency Hopping
FM	Fading Margin
FWHT	Fast Walsh Hadamard Transformation
GMSK	Gaussian Minimum Shift Keying
GSM	Global System for Mobile Communications
ISI	Inter-/Intra-Symbol Interference
IR	Impulse Radio
JIO	Joint Iterative Optimization
L-CMV	Linear Constrained Minimum Variance
LOS	Line-Of-Sight

MA	Multiple Access
MAC	Medium Access Control
MB-OFDM	Multi-Band Orthogonal Frequency Division Multiplexing
MIMO	Multiple Input Multiple Output
MMSE	Minimum Mean Square Error
MPG	Mean Power Gain
MSE	Mean Square Error
MSK	Minimum Shift Keying
M-Seq	Maximum Length Sequence
MSWF	Multistage Wiener Filter
MUI	Multi-User Interference
MVDR	Minimum Variance Distortionless Response
NBI	Narrowband Interference
NC-CL	Non-Coherent Combining Loss
NLOS	Non-Line-Of-Sight
OFDM	Orthogonal Frequency Division Multiplexing
OOK	On-Off Keying
OQPSK	Offset Quadrature Phase Shift Keying
PAPR	Peak-to-Average Power Ratio
PC	Prime Code
PCA	Principal Components Analysis
PDF	Probability Density Function
PER	Packet Error Rate
PHY-SAP	Physical Layer Service Access Point
PN	Pseudo-Noise
PPM	Pulse Position Modulation
PSD	Power Spectral Density
PSDU	Presentation Service Data Unit
PSM	Pulse Shape Modulation
QCC	Quadratic Congruence Code
QPSK	Quadrature Phase Shift Keying
QWL	Quasi Widely Linear
RBW	Resolution Bandwidth
RC	Random Code
RFID	Radio Frequency Identification
RLS	Recursive Least Squares
RRC	Root Raised Cosine
R-Walsh	Repeated Walsh
ΣΔ	Sigma-Delta
SinW-C	Single Window Combining
SG	Stochastic Gradient
SIR	Signal to Interference Ratio
SINR	Signal-to-Interference plus Noise Ratio
SNR	Signal to Noise Ratio
SOP	Simultaneously Operating Piconets
SRLS	Structured Recursive Least Squares
S-Walsh	Spread Walsh
TCC	Truncated Costas Code
TH	Time Hopping
TH-PPM	Time Hopping combined with Pulse Position Modulation
TR	Transmitted Reference
TR-BPSK	Transmitted Reference combined with Binary Phase Shift Keying
TWL	Total Widely Linear
UWB	Ultra Wideband
WL	Widely Linear

WLAN	Wireless Local Area Network
WL-CMV	Widely Linear Constrained Minimum Variance
WSubW-C	Weighted Sub-Window Combining
WPAN	Wireless Personal Area Network
WSN	Wireless Sensor Network
2-PAM	Binary Phase Amplitude Modulation
2-PPM	Binary Pulse Position Modulation

Symbols and Notation

$x^{\cdot}_{\cdot}$	x appears with a certain superscript and/or subscript
x	scalar
$\boldsymbol{x}$	column vector
$\boldsymbol{X}$	matrix
$\boldsymbol{X}^{-1}$	inversion of a square matrix $\boldsymbol{X}$
$\boldsymbol{I}_M$	Identity matrix of size $M \times M$
$*$	convolution
$*$ as superscript	complex conjugation
$\odot$	Hadamard (element-wise) product
T as superscript	transpose
H as superscript	conjugate transpose
$\lfloor x \rceil / \lceil x \rceil$	rounds the argument x down/up to the closest integer that is less/greater than or equal to x
$\Re\{\cdot\}$	take the real part of a variable
$\mathbb{E}\{\cdot\}$	take the expectation of a variable
$\mathbb{V}\{\cdot\}$	take the variance of a variable
$\Pr\{\cdot\}$	take the probability
$\delta(t)$	Dirac delta function, $\delta(t) = \begin{cases} +\infty & \text{if } t = 0 \\ 0 & \text{if } t \neq 0 \end{cases}$
$\delta[m]$	Kronecker Delta function, $\delta[m] = \begin{cases} 1 & \text{if } m = 0 \\ 0 & \text{if } m \neq 0 \end{cases}$
$\mathrm{Q}\{\cdot\}$	Q-function, $\mathrm{Q}(\alpha) = \frac{1}{\sqrt{2\pi}} \int_{\alpha}^{\infty} e^{-\frac{x^2}{2}} \mathrm{d}x$
$\Gamma(\cdot)$	Gamma function
$I_{\alpha}(\cdot)$	the α-th order modified Bessel function of the first kind
$\mathscr{L}_k^a(\cdot)$	generalized Laguerre polynomial of degree k with $a > -1$
$g(t)$	pulse shape
$g_R(t)$	response of the received pulse matched filter
$\tilde{g}(t)$	pulse shape after the pulse matched filter, i.e., $\tilde{g}(t) = g(t) * g_R(t)$
T_g	pulse duration
β	roll-off factor of the root raised cosine pulse
B_3	3-dB bandwidth of the root raised cosine pulse
B	the total bandwidth of the signal
$s(t), s^{(k)}(t), s_k(t)$	transmitted signal (of user k)
$h(t), h^{(k)}(t), h_k(t)$	channel impulse response (of user k)
$\alpha_l, \alpha_l^{(k)}, \alpha_k(l)$	the l-th channel coefficient (of user k)
L	number of channel taps

$\widehat{n}(t)$	Additive White Gaussian Noise (AWGN)
$n(t)$	AWGN after the pulse matched filter, i.e., $n(t) = \widehat{n}(t) * g_R(t)$
$y(t)$	received signal after the pulse matched filter
$y[i]$	received signal samples after the Analog-to-Digital Converter (ADC)
$\widehat{J}(t)$	Narrowband Interference (NBI)
$J(t)$	NBI after the pulse matched filter, i.e., $J(t) = \widehat{J}(t) * g_R(t)$
P_J	power of the NBI
T_b	bit interval
R_b	bit rate
T_c	chip interval (when multiple access codes are used)
E_b	bit energy of the signal
E_s	symbol energy of the signal
N_0	noise power spectral density

Frequently used symbols and notations specific to Part I

a_i	the i-th transmitted bit
Δ	modulation delay of the Pulse Position Modulation (PPM) scheme
T_{i}	integration interval using the single-window combining
$\mathfrak{L}_{\mathrm{i}}$	the set of taps within the integration window of size T_{i}
L_{i}	number of combined channel taps in the set $\mathfrak{L}_{\mathrm{i}}$
$f(\cdot)$	Probability Density Function (PDF)
$\Phi_{xx}(f)$	Power Spectral Density (PSD) of x
$\Phi_x(\omega)$	characteristic function of x
M	modulation order
$Z_m, Z_m^{(k)}$	the m-th decision variable collected from the m-th branch for Walsh or from the m-th time slot for PPM after the non-coherent multipath combining (for user k), $m = 0, \ldots, M-1$
$Z, Z^{(1)}$	final decision variable in the binary modulation scheme, $Z = Z_0 - Z_1$ (or $Z^{(1)} = Z_0^{(1)} - Z_1^{(1)}$ for the first desired user)
P_b	Bit Error Rate (BER)
N_u	number of users
N_s	number of pulse repetitions or number of frames in Time-Hopping (TH) codes
N_h	number of hopping positions in TH codes [1]
L_m	length of the TH code, $L_m = N_s N_h$
$C_i, C_i^{(k)}$	takes values in $\{0, 1, \ldots, N_h - 1\}$, representing the position of the pulse in each frame for a TH code (of user k), $i = 0, \ldots, N_s - 1$
T_f	frame duration
R_f	pulse repetition rate, $R_f = 1/T_f$
$\Omega.$	the second-order moment of the channel impulse response $\Omega_l = \mathbb{E}\left\{\lvert\alpha_l\rvert^2\right\}$
$\Upsilon.$	the fourth-order moment of the channel impulse response $\Upsilon_l = \mathbb{E}\left\{\lvert\alpha_l\rvert^4\right\}$
δ	threshold factor of the soft or hard limiter

[1] In Section 7.3, N_h represents the number of non-overlapping channels of the frequency Hopping (FH) scheme.

b	resolution of an ADC
G	the input gain or signal level for an ADC
x_p	$p \in \{R, I\}$, representing the real R or the imaginary I of the variable x
$q_\cdot[\cdot]$	quantization noise
$h_\cdot[i]$	takes values in $\{0, 1\}$, denoting whether there is a collision in the i-th frame of the TH code
N	processing factor $N = \frac{T_s}{T_g} = \frac{B}{R_b}$
f_s	sampling frequency
t_s	sampling time
N_{os}	oversampling rate, $N_{os} = f_s/B = \frac{1}{t_s B}$
Γ_m	mean power gain of the m-th channel realization
B_h	bandwidth per hop in the FH scheme

Frequently used symbols and notations specific to Part II

a as subscript	the associated augmented quantities
$\bar{\{\cdot\}}$	"bar" over symbols, reduced-rank quantities
$\mathbb{T}\{\cdot\}$	bijective transformation
$\boldsymbol{R}$	covariance matrix
$\check{\boldsymbol{R}}$	complementary covariance matrix or pseudo-covariance matrix
$\boldsymbol{r}, \boldsymbol{r}[i]$	received signal vector (for the i-th transmitted bit)
M	length of the received signal vector
N	processing gain of the Direct Sequence (DS) code
b_k	transmitted symbol for user k
E_k	transmitted energy per bit for user k
$\boldsymbol{C}_k$	code matrix for the k-th user
$\boldsymbol{h}_k$	channel vector of user k
$\boldsymbol{p}$	cross correlation vector of the received signal vector and the desired signal
$\boldsymbol{w}$	filter weight vector
D	rank or iteration, i.e., dimension of the subspace using the reduced-rank scheme
$\boldsymbol{S}_D$	rank-reduction matrix that transforms the input signal onto a subspace of dimension D
$J.$	Mean Square Error (MSE)
μ	step size of the Stochastic Gradient (SG) adaptive algorithm
$\boldsymbol{g}_{a,d}$	auxiliary vector of stage d in the Widely Linear Auxiliary Vector (WL-AVF) scheme
$\tilde{\mu}_d$	optimized scalar of stage d in the WL-AVF scheme

BIBLIOGRAPHY

Own Publications

[CSR+12] Y. Cheng, N. Song, F. Römer, M. Haardt, H. Henniger, R. Metzig, and E. Diedrich. Satellite ground stations with electronic beam steering. In *Proc. 1st International IEEE-AESS Conference in Europe about Space and Satellite Telecommunications (ESTEL 2012)*, Rome, Italy, Oct. 2012.

[MGS+07] M. Milojević, G. Del Galdo, N. Song, M. Haardt, and A. Heuberger. Spatio-temporal availability in satellite-to-indoor broadcasting. In *2007 European Conference on Wireless Technologies*, pages 162–165, Munich, Germany, 2007.

[MGS+08] M. Milojević, G. Del Galdo, N. Song, M. Haardt, and A. Heuberger. Receive antenna impact on spatio-temporal availability in satellite-to-indoor broadcasting. In *International ITG/IEEE Workshop on Smart Antennas (WSA 2008)*, Darmstadt, Germany, 2008.

[MGS+10] M. Milojević, G. Del Galdo, N. Song, M. Haardt, and A. Heuberger. Impact of the receive antenna arrays on spatio-temporal availability in satellite-to-indoor broadcasting. *IEEE Transactions on Broadcasting*, 56(2):171–183, 2010. received the TU Ilmenau Best Paper Award in the area of "Engineering Sciences".

[SdLHW12] N. Song, R. C. de Lamare, M. Haardt, and M. Wolf. Adaptive Widely Linear Reduced-Rank Interference Suppression based on the Multi-Stage Wiener Filter. *IEEE Transactions on Signal Processing*, 60(8), 2012.

[SdLW+11] J. Steinwandt, R. C. de Lamare, L. Wang, N. Song, and M. Haardt. Widely linear adaptive beamforming algorithm based on the conjugate gradient method. In *Proc. International ITG Workshop on Smart Antennas (WSA 2011)*, Aachen, Germany, 2011.

[SdLWH10] N. Song, R. C. de Lamare, M. Wolf, and M. Haardt. Adaptive Reduced-Rank Interference Suppression for DS-UWB Systems based on the Widely Linear Multistage Wiener Filter. In *Proc. 7-th International Symposium on Wireless Communications Systems (ISWCS 2010)*, York, United Kingdom, Sept. 2010.

[SGM+06] N. Song, G. Del Galdo, M. Milojević, M. Haardt, and A. Heuberger. Spatial availability in satellite-to-indoor broadcasting communications. In *Proc. 7th Workshop Digital Broadcasting*, pages 113–118, Erlangen, Germany, Sept. 2006.

[SSW+11] N. Song, J. Steinwandt, L. Wang, R. C. de Lamare, and M. Haardt. Non-data-aided adaptive beamforming algorithm based on the widely linear auxiliary vector filter. In *Proc. International Conference on Acoustics, Speech, and Signal Processing (ICASSP 2011)*, Prague, Czech Republic, May 2011.

[SWH07a] N. Song, M. Wolf, and M. Haardt. Low-complexity and energy efficient non-coherent receivers for UWB communications. In *Proc. 18-th Annual IEEE International Symposium on Personal Indoor and Mobile Radio Communications (PIMRC 2007)*, Greece, September 2007.

[SWH09a] N. Song, M. Wolf, and M. Haardt. A Digital Code Matched Filter-based Non-Coherent Receiver for Low Data Rate TH-PPM-UWB Systems in the Presence of MUI. In *IEEE International Conference on Ultra Wideband (ICUWB 2009)*, Vancouver, Canada, Sept. 2009.

[SWH09c] N. Song, M. Wolf, and M. Haardt. On the choice of the bandwidth for low-complexity UWB communications with non-coherent detection. In *Proc. of 23rd Wireless World Research Forum (WWRF)*, Beijing, China, October 2009.

[SWH09d] N. Song, M. Wolf, and M. Haardt. Performance of PPM-Based Non-Coherent Impulse Radio UWB Systems using Sparse Codes in the Presence of Multi-User Interference. In *Proc. of IEEE Wireless Communications and Networking Conference (WCNC 2009)*, Budapest, Hungary, April 2009.

[SWH10a] N. Song, M. Wolf, and M. Haardt. A digital non-coherent ultra-wideband receiver using a soft-limiter for narrowband interference suppression. In *Proc. 7-th International Symposium on Wireless Communications Systems (ISWCS 2010)*, York, United Kingdom, Sept. 2010.

[SWH10b] N. Song, M. Wolf, and M. Haardt. A b-bit Non-Coherent Receiver based on a Digital Code Matched Filter for Low Data Rate TH-PPM-UWB Systems in the Presence of MUI. In *Proc. of IEEE International Conference on Communications (ICC 2010)*, Cape Town, South Africa, May 2010.

[SWH10d] N. Song, M. Wolf, and M. Haardt. Time-Hopping M-Walsh UWB transmission scheme for a one-bit non-coherent receiver. In *Proc. 7-th International Symposium on Wireless Communications Systems (ISWCS 2010)*, York, United Kingdom, Sept. 2010.

[SWH12] N. Song, M. Wolf, and M. Haardt. Non-coherent UWB communications. In R. S. Thomä, H.-I. Willms, T. Zwick, R. Knöchel, and J. Sachs, editors, *UKoLoS Ultra-Wideband Radio Technologies for Communications, Localization and Sensor Applications*. InTech, 2012.

[TGS+12] J. Tronc, L. Guillaume, N. Song, M. Haardt, C. Grabowski, J. Arendt, and C. Schlund. Overview and Comparison of on Ground and on-Board Beamforming Techniques in MSS Applications. In *2nd ESA Workshop on Advanced Flexible Telecom Payloads*, Noordwijk, The Netherlands, April 2012.

[WS09] M. Wolf and N. Song. Chapter 5: Non-Coherent Detection. In R. Kraemer and M. D. Katz, editors, *Short-Range Wireless Communications: Emerging Technologies and Applications*. Wiley, 2009.

[WSdLH10] L. Wang, N. Song, R. C. de Lamare, and M. Haardt. An iterative widely linear Interference Suppression Algorithm based on Auxiliary Vector Filtering. In *Proc. of the 44th Asilomar Conference on Signals, Systems and Computers*, Pacific Grove, CA, Nov. 2010.

[WSH09] M. Wolf, N. Song, and M. Haardt. Non-Coherent UWB Communications. *FREQUENZ Journal of RF-Engineering and Telecommunications*, 63:187–191, Oct. 2009. special issue on Ultra-Wideband Radio Technologies for Communications, Localisation and Sensor applications.

Invited Talks

[SWH07b] N. Song, M. Wolf, and M. Haardt. Non-coherent and autocorrelation receivers for energy efficient UWB-transmission. In *Kickoff Meeting Project UKoLoS*, Berlin, Germany, Feb. 2007.

[SWH08] N. Song, M. Wolf, and M. Haardt. Non-coherent receivers for energy efficient UWB-transmission. In *UKoLoS Annual Colloquium*, Ilmenau, Germany, May 2008.

[SWH09b] N. Song, M. Wolf, and M. Haardt. Non-coherent receivers for energy efficient UWB transmission. In *UKoLoS Annual Colloquium*, Erlangen, Germany, Feb. 2009.

[SWH10c] N. Song, M. Wolf, and M. Haardt. Digital non-coherent UWB receiver based on TH-Walsh transmission schemes. In *UKoLoS Annual Colloquium*, Günzburg, Germany, Mar. 2010.

[SWH10e] N. Song, M. Wolf, and M. Haardt. Ultra wideband communications: from analog to digital. In *Institution seminar in Department of Electronics, University of York*, York, UK, Sept. 2010.

References by Other Authors

[AH10] T. Adali and S. Haykin. *Adaptive Signal Processing: Next Generation Solutions*. John Wiley and Sons Ltd, 2010.

[AS96] P. M. Aziz and H. V. Sorensen. An overview of sigma-delta converters. *IEEE Signal Processing Magazine*, 13(1):61–84, 1996.

[AW07] Y. D. Alemseged and K. Witrisal. Modeling and mitigation of narrowband interference for transmitted-reference UWB systems. *IEEE Journal of Selected Topics in Signal Processing*, 1(3):456–469, 2007.

[AY10] Q. Z. Ahmed and L.-L. Yang. Reduced-rank adaptive multiuser detection in hybrid direct-sequence time-hopping ultra wide bandwidth systems. *IEEE Transactions on Wireless Communications*, 9(1):156–167, Jan 2010.

[Bat01] A. Batra. Multi-Band OFDM Physical Layer Proposal. In *IEEE P802.15-03/268r0-TG3a*, July 2001.

[BBM08] M. Bolatkale, L. Breems, and K. Makinwa. High-Speed Sigma-Delta Converters. In *Proc. of Program for Research on Integrated Systems and Circuits (ProRISC)*, Nov. 2008.

[BH08] N. C. Beaulieu and B. Hu. Soft-Limiting Receiver Structures for Time-Hopping UWB in Multiple Access Interference. *IEEE Transactions on Vehicular Technology*, 57, 2008.

[BLT01] S. Buzzi, M. Lops, and A. M. Tulino. A new family of MMSE multiuser receivers for interference suppression in DS/CDMA systems employing BPSK modulation. *IEEE Transactions on Communications*, 49(1):154–167, Jan 2001.

[BR78] C. L. Bennett and G. F. Ross. Time-domain electromagnetics and its applications. *Proceedings of the IEEE*, 66(3):299–318, March 1978.

[BV01] T. W. Barrett and VA Vienna. Technical Features - History of Ultra Wideband Communications and Radar: Part I, UWB Communications. *Microwave Journal*, 2001.

[CA06] J. F. Cardoso and T. Adali. The maximum likelihood approach to complex ICA. In *IEEE International Conference on Acoustics, Speech and Signal Processing (ICASSP 2006)*, volume 5, pages V–V, 2006.

[CB07] Y. Chen and N. C. Beaulieu. SNR Estimation Methods for UWB Systems. *IEEE Transactions on Wireless Communications*, 6(10):3836–3845, 2007.

[CGPV09] A. S. Cacciapuoti, G. Gelli, L. Paura, and F. Verde. Widely linear versus linear blind multiuser detection with subspace-based channel estimation: finite sample-size effects. *IEEE Transactions on Signal Processing*, 57(4):1426–1443, 2009.

[CM06] C. Carbonelli and U. Mengali. Synchronization algorithms for UWB signals. *IEEE Transactions on Communications*, 54(2):329–338, 2006.

[Com08] Electronic Communications Committee. Final report on UWB in response to a request from the European Commission. In *Doc. ECC(08)023 ANNEX 12*, March 2008.

[CP06] P. Chevalier and F. Pipon. New insights into optimal widely linear array receivers for the demodulation of BPSK, MSK, and GMSK signals corrupted by noncircular interferences-application to SAIC. *IEEE Transactions on Signal Processing*, 54(3):870–883, 2006.

[CPD07] P. Chevalier, F. Pipon, and F. Delaveau. Second-order optimal array receivers for synchronization of BPSK, MSK, and GMSK signals corrupted by noncircular interferences. *EURASIP Journal on Advances in Signal Processing*, 2007(3):1–16, 2007.

[CS02] J. D. Choi and W. E. Stark. Performance of ultra-wideband communications with suboptimal receivers in multipath channels. *IEEE Journal on Selected Areas in Communications*, 20(9):1754–1766, 2002.

[CS04] Y. L. Chao and R. A. Scholtz. Multiple access performance of ultra-wideband transmitted reference systems in multipath environments. In *IEEE Wireless Communications and Networking Conference (WCNC 2004)*, volume 3, pages 1788–1793, 2004.

[CTBR03] C. M. Canadeo, M. A. Temple, R. O. Baldwin, and R. A. Raines. Code Selection for Enhancing UWB Multiple Access Communication Performance using TH-PPM and DS-BPSK Modulations. In *IEEE Wireless Communications and Networking Conference (WCNC 2003)*, volume 1, 2003.

[CWL+04] Z. N. Chen, X. H. Wu, H. F. Li, N. Yang, and M. Y. W. Chia. Considerations for source pulses and antennas in UWB radio systems. *IEEE Transactions on Antennas and Propagation*, 52(7):1739–1748, 2004.

[CWVM07] D. Cassioli, M. Z. Win, F. Vatalaro, and A. F. Molisch. Low complexity rake receivers in ultra-wideband channels. *IEEE Transactions on Wireless Communications*, 6(4):1265–1275, 2007.

[DB03] G. Durisi and S. Benedetto. Performance evaluation of TH-PPM UWB systems in the presence of multiuser interference. *IEEE Communications Letters*, 7(5):224–226, 2003.

[DDdRO05] S. Dubouloz, B. Denis, S. de Rivaz, and L. Ouvry. Performance analysis of LDR UWB non-coherent receivers in multipath environments. In *IEEE International Conference on Ultra-Wideband*, 2005.

[DK06] Y. Dhibi and T. Kaiser. On the Impulsiveness of Multiuser Interferences in TH-PPM-UWB Systems. *IEEE Transactions on Signal Processing*, 54(7):2853–2857, 2006.

[dL08] R. C. de Lamare. Adaptive reduced-rank LCMV beamforming algorithms based on joint iterative optimisation of filters. *Electronics Letters*, 44(9):565–566, 2008.

[dLHSN08] R. C. de Lamare, M. Haardt, and R. Sampaio-Neto. Blind adaptive constrained reduced-rank parameter estimation based on constant modulus design for CDMA interference suppression. *IEEE Transactions on Signal Processing*, 56(6):2470–2482, 2008.

[dLSN07] R. C. de Lamare and R. Sampaio-Neto. Reduced-rank adaptive filtering based on joint iterative optimization of adaptive filters. *IEEE Signal Processing Letters*, 14(12):980–983, 2007.

[dLSN09] R. C. de Lamare and R. Sampaio-Neto. Adaptive Reduced-Rank Processing Based on Joint and Iterative Interpolation, Decimation and Filtering. *IEEE Transactions on Signal Processing*, 57(7):2503 – 2514, July 2009.

[dLSN10] R. C. de Lamare and R. Sampaio-Neto. Reduced-Rank Space-Time Adaptive Interference Suppression With Joint Iterative Least Squares Algorithms for Spread-Spectrum Systems. *IEEE transactions on vehicular technology*, 59(3):1217–1228, 2010.

[dLWF10] R. C. de Lamare, L. Wang, and R. Fa. Adaptive reduced-rank LCMV beamforming algorithms based on joint iterative optimization of filters: Design and analysis. *Signal Processing*, 90(2):640–652, 2010.

[DM03] O. Dabeer and U. Madhow. Detection and Interference Suppression for Ultra-Wideband Signaling with Analog Processing and One Bit A/D. In *Conference Record of the Thirty-Seventh Asilomar Conference on Signals, Systems and Computers*, volume 2, pages 1766 – 1770, Nov. 2003.

[DM05] A. A. D'Amico and U. Mengali. GLRT receivers for UWB systems. *IEEE Communications Letters*, 9(6):487–489, 2005.

[Dou09] S. C. Douglas. Widely-linear recursive least-squares algorithm for adaptive beamforming. In *IEEE International Conference on Acoustics, Speech and Signal Processing (ICASSP 2009)*, pages 2041–2044, Taipei, Taiwan, 2009.

[DvdV06] Q. H. Dang and A. J. van der Veen. Narrowband interference mitigation for a transmitted reference ultra-widenband receiver. In *Proc. European Signal Processing Conference (EUSIPCO)*, Florence, Italy, Sept. 2006.

[DvdV07] Q. H. Dang and A. J. van der Veen. A decorrelating multiuser receiver for transmit-reference UWB systems. *IEEE Journal of Selected Topics in Signal Processing*, 1(3):431–442, 2007.

[ECC07] ECC. ECC Decision of 24 March 2006 amended 6 July 2007 at Constanta on the harmonised conditions for devices using Ultra-Wideband (UWB) technology in bands below 10.6 GHz. amended ECC/DEC/(06)04, July 2007.

[EHO+02] K. Eshima, Y. Hase, S. Oomori, F. Takahashi, and R. Kohno. M-ary UWB system using Walsh codes. In *2002 IEEE Conference on Ultra Wideband Systems and Technologies. Digest of Papers*, pages 37–40, 2002.

[Eur06] Public Safety Communication Europe. D.4.1.1. Public Report EUROPCOM (Emergency Ultrawideband RadiO for Positioning and COMmunications), summary of the system architecture, Issue 1. In *project no. 004154*, June 2006.

[FCC05] FCC 05-58. Petition for Waiver of the Part 15 UWB Regulations Filed by the Multi-band OFDM Alliance Special Interest Group. In *ET Docket 04-352*, March 2005.

[Fed02] Federal Communications Commission. First Report and Order: Revision of Part 15 of the Commission's Rules Regarding Ultra-Wideband Transmission Systems. ET Docker 98-153, April 2002.

[FKLW05] R. Fisher, R. Kohno, M. Mc Laughlin, and M. Welbourn. DS-UWB Physical Layer Submission to 802.15 Task Group 3a. *IEEE standard proposal IEEE P802.15-04/0137r4*, Jan 2005.

[FM07] S. Franz and U. Mitra. Quantized UWB transmitted reference systems. *IEEE Transactions on Wireless Communications*, 6(7):2540–2550, 2007.

[FNKS02] A. R. Forouzan, M. Nasiri-Kenari, and J. A. Salehi. Performance Analysis of Time-Hopping Spread-Spectrum Multiple-Access Systems: Uncoded and Coded Schemes. *IEEE Transactions on Wireless Communications*, 1(4):671–681, 2002.

[Foe02] J. Foerster. Channel modeling subcommittee report (Final). *IEEE P802. 15-02/490r1-SG3a*, 2002.

[GA04] I. Güvenc and H. Arslan. Design and Performance Analysis of TH Sequences for UWB-IR Systems. In *Wireless Communications and Networking Conference (WCNC 2004)*, volume 2, 2004.

[GMK04] M. Ghavami, L. S. Michael, and R. Kohno. *Ultra wideband signals and systems in communication engineering.* John Wiley & Sons, Ltd, 2004.

[Goo63] N. R. Goodman. Statistical analysis based on a certain multivariate complex Gaussian distribution (an introduction). *Annals of Mathematical Statistics*, pages 152–177, 1963.

[GQ06] N. Guo and R. C. Qiu. Improved autocorrelation demodulation receivers based on multiple-symbol detection for UWB communications. *IEEE Transactions on Wireless Communications*, 5(8):2026–2031, 2006.

[GQS05] N. Guo, R. C. Qiu, and B. M. Sadler. An Ultra-Wideband Autocorrelation Demodulation Scheme with Low-Complexity Time Reversal Enhancement. *IEEE Military Communications Conference (MILCOM 2005)*, pages 1–7, 2005.

[GR97] J. S. Goldstein and I. S. Reed. Reduced-rank adaptive filtering. *IEEE Transactions on Signal Processing*, 45(2):492–496, 1997.

[GR07] I. S. Gradshteyn and I. M. Ryzhik. *Table of integrals, series, and products*. Academic Press, seven edition, 2007.

[Gra87] R. Gray. Oversampled sigma-delta modulation. *IEEE Transactions on Communications*, 35(5):481–489, 1987.

[GRS98] J. S. Goldstein, I. S. Reed, and L. L. Scharf. A Multistage Representation of the Wiener Filter Based on Orthogonal Projections. *IEEE Transactions on Information Theory*, 44(7):2943, 1998.

[Hay01] S. Haykin. *Communication Systems 4th Edition*. John Wiley & Sons, Inc., 2001.

[Hay02] S. Haykin. *Adaptive Filter Theory, 4th edition*. Englewood Cliffs, New Jersey, USA: Prentice Hall Inc, 2002.

[HB04] B. Hu and N. C. Beaulieu. Accurate evaluation of multiple-access performance in TH-PPM and TH-BPSK UWB systems. *IEEE Transactions on Communications*, 52(10):1758–1766, 2004.

[HG02] M. L. Honig and J. S. Goldstein. Adaptive reduced-rank interference suppression based on the multistage Wiener filter. *IEEE Transactions on Communications*, 50(6):986–994, 2002.

[HJ90] R. A. Horn and C. R. Johnson. *Matrix analysis*. Cambridge University Press, 1990.

[HR04] M. Haardt and F. Römer. Enhancements of unitary ESPRIT for non-circular sources. In *IEEE International Conference Acoustics, Speech and Signal Processing (ICASSP)*, volume 2, pages 101–104, Montreal, Canada, 2004.

[HS05] S. Hoyos and B. M. Sadler. Ultra-wideband analog-to-digital conversion via signal expansion. *IEEE Transactions on Vehicular Technology*, 54(5):1609–1622, 2005.

[HSA05] S. Hoyos, B. M. Sadler, and G. R. Arce. Monobit Digital Receivers for Ultra-wideband Communications. *IEEE Transactions on Wireless Communications*, 4(4):1337–1344, 2005.

[HSFR02] M. Ho, V. S. Somayazulu, J. Foerster, and S. Roy. A differential detector for an ultra-wideband communications system. In *IEEE 55th Vehicular Technology Conference (VTC Spring 2002)*, volume 4, pages 1896–1900, 2002.

[HT02] R. Hoctor and H. Tomlinson. Delay-hopped transmitted-reference RF communications. pages 265–269, May 2002.

[HW95] M. J. Hao and S. B. Wicker. Performance Evaluation of FSK and CPFSK Optical Communication Systems: a Stable and Accurate Method. *Journal of Lightwave Technology*, 13(8):1613–1623, 1995.

[HX01] M. L. Honig and W. Xiao. Performance of reduced-rank linear interference suppression. *IEEE Transactions on Information Theory*, 47(5):1928–1946, 2001.

[IEE07] IEEE 802.15 TG4a. Part 15.4: Wireless Medium Access Control (MAC) and Physical Layer (PHY) Specifications for Low-Rate Wireless Personal Area Networks (WPANs). *IEEE Standard for Information Technology*, 2007.

[IHQ04] S. J. Ingram, D. Harmer, and M. Quinlan. UltraWideBand Indoor Positioning Systems and their use in Emergencies. In *Position Location and Navigation Symposium*, pages 706–715, 2004.

[Kam96] K. D. Kammeyer. *Nachrichtenübertragung*. BG Teubner Stuttgart, 1996.

[KI90] D. Kreß and D. Irmer. *Angewandte Systemtheorie*. Oldenbourg Verlag, München und Wien, 1990.

[KP02] J. Kunisch and J. Pamp. Measurement results and modeling aspects for the UWB radio channel. *IEEE Conference on Ultra Wide-Band Systems and Technologies*, May 2002.

[KP03] J. Kunisch and J. Pamp. An Ultra-Wideband Space-Variant Multipath Indoor Radio Channel Model. In *IEEE Conference on Ultra Wideband Systems and Technologies*, pages 290–294, 2003.

[LH03] N. H. Lehmann and A. M. Haimovich. The power spectral density of a time hopping UWB signal: a survey. In *IEEE Conference on Ultra Wideband Systems and Technologies*, pages 234–239, 2003.

[LRRB05] B. Le, T. W. Rondeau, J. H. Reed, and C. W. Bostian. Analog-to-digital converters. *IEEE Signal Processing Magazine*, 22(6):69–77, Nov. 2005.

[MBC+05] A. F. Molisch, K. Balakrishnan, C. Chong, S. Emami, A. Fort, J. Karedal, J. Kunisch, H. Schantz, U. Schuster, and K. Siwiak. IEEE 802.15.4a channel model - final report. In *Tech. Rep. Document IEEE 802.15-04-0662-02-004a*, 2005.

[MG09] D. Mandic and V. S. L. Goh. *Complex valued nonlinear adaptive filters: Noncircularity, widely linear and neural models*. John Wiley and Sons Ltd, 2009.

[MGK02] L. B. Michael, M. Ghavami, and R. Kohno. Multiple pulse generator for ultra-wideband communication using Hermite polynomial based orthogonal pulses. *IEEE Conference on Ultra Wideband Systems and Technologies. Digest of Papers.*, pages 47–51, 2002.

[MGSH06] R. Meyer, W. H. Gerstacker, R. Schober, and J. B. Huber. A single antenna interference cancellation algorithm for increased GSM capacity. *IEEE Transactions on Wireless Communications*, 5(7):1616–1621, 2006.

[MHT95] S. V. Maric, M. D. Hahm, and E. L. Titlebaum. Construction and Performance Analysis of a New Family of Optical Orthogonal Codes for CDMA Fiber-Optic Networks. *IEEE Transactions on Communications*, 43(234):485–489, 1995.

[MKT93] S. V. Maric, Z. I. Kostic, and E. L. Titlebaum. A New Family of Optical Code Sequences for Use in Spread-Spectrum Fiber-Optic Local Area Networks. *IEEE Transactions on Communications*, 41(8):1217–1221, 1993.

[MMPR08] S. Majhi, A. S. Madhukumar, A. B. Premkumar, and P. Richardson. Combining OOK with PSM Modulation for Simple Transceiver of Orthogonal Pulse-Based TH-UWB Systems. *EURASIP Journal on Wireless Communications and Networking*, 2008.

[MMZ05] B. L. Mathews, L. Mili, and A.I. Zaghloul. Auxiliary vector selection algorithms for adaptive beamforming. In *IEEE Antennas and Propagation Society International Symposium*, volume 3, pages 271–274, 2005.

[MN08] A. Mezghani and J. A. Nossek. Analysis of Rayleigh-fading channels with 1-bit quantized output. In *IEEE International Symposium on Information Theory (ISIT 2008)*, pages 260–264, July 2008.

[Mol09] A. F. Molisch. Ultra-wide-band propagation channels. *Proceedings of the IEEE*, 97(2):353–371, 2009.

[MPP06] A. Mirbagheri, K. N. Plataniotis, and S. Pasupathy. An enhanced widely linear CDMA receiver with OQPSK modulation. *IEEE Transactions on Communications*, 54(2):261, 2006.

[MWS03] B. Mielczarek, M. O. Wessman, and A. Svensson. Performance of coherent UWB Rake receivers with channel estimators. In *IEEE 58th Vehicular Technology Conference (VTC Fall 2003)*, volume 3, pages 1880–1884, 2003.

[Nam01] W. Namgoong. ADC and AGC requirements of a direct-sequence spread spectrum signal. In *Proceedings of the 44th IEEE 2001 Midwest Symposium on Circuits and Systems (MWSCAS 2001)*, volume 2, 2001.

[Nam03] W. Namgoong. A channelized digital ultrawideband receiver. *IEEE Transactions on Wireless Communications*, 2(3):502–510, 2003.

[NK96] D. Nikolai and K. D. Kammeyer. Noncoherent RAKE-Receiver with Optimum Weighted Combining and Improved Closed-Loop Power Control. In *Proc. IEEE Fourth International Symposium on Spread Spectrum Techniques and Applications*, pages 239–243, Germany, September 1996.

[NM03] Y. P. Nakache and A. F. Molisch. Spectral shape of UWB signals-influence of modulation format, multiple access scheme and pulse shape. In *The 57th IEEE Semiannual Vehicular Technology Conference (VTC Spring 2003)*, volume 4, pages 2510–2514, 2003.

[NS07] Y. Na and M. Saquib. Analysis of the channel energy capture in ultra-wideband transmitted reference systems. *IEEE Transactions on Communications*, 55(2):262–265, 2007.

[OCWB02] I. D. O'Donnell, M. Chen, S. Wang, and R. W. Brodersen. An integrated, low power, ultra-wideband transceiver architecture for low-rate, indoor wireless systems. In *IEEE CAS Workshop on Wireless Communications and Networking*, pages 1–23, 2002.

[OK08] M. K. Oh and J. Y. Kim. Ranging implementation for IEEE 802.15. 4a IR-UWB systems. In *IEEE Vehicular Technology Conference (VTC Spring 2008)*, pages 1077–1081, 2008.

[OSR+04] I. Oppermann, L. Stoica, A. Rabbachin, Z. Shelby, and J. Haapola. UWB wireless sensor networks: UWEN-a practical example. *IEEE Communications Magazine*, 42(12):S27–S32, 2004.

[PC95] B. Picinbono and P. Chevalier. Widely linear estimation with complex data. *IEEE Transactions on Signal Processing*, 43(8):2030–2033, 1995.

[PCWD03] B. Parr, B. L. Cho, K. Wallace, and Z. Ding. A novel ultra-wideband pulse design algorithm. *IEEE Communications Letters*, 7(5):219–221, 2003.

[PF86] P. S. Prucnal and M. T. Fan. Spread Spectrum Fiber-Optic Local Area Network using Optical Processing. *Journal of Lightwave Technology*, 4(5):547–554, 1986.

[PK01] D. A. Pados and G. N. Karystinos. An iterative algorithm for the computation of the MVDR filter. *IEEE Transactions on Signal Processing*, 49(2), 2001.

[PLSL07] A. Parihar, L. Lampe, R. Schober, and C. Leung. Equalization for DS-UWB Systems - Part I: BPSK Modulation. *IEEE Transactions on Communications*, 55(6):1164–1173, 2007.

[Pro01] J. G. Proakis. *Digital Communications*. McGraw-Hill, 4th edition, 2001.

[PYP06] P. Popovski, H. Yomo, and R. Prasad. Strategies for adaptive frequency hopping in the unlicensed bands. *IEEE Wireless Communications*, 13(6):60–67, 2006.

[QB03] H. Qian and S. N. Batalama. Data record-based criteria for the selection of an auxiliary vector estimator of the MMSE/MVDR filter. *IEEE transactions on communications*, 51(10):1700–1708, 2003.

[QW05] T. Q. S. Quek and M. Z. Win. Analysis of UWB Transmitted-Reference Communication Systems in Dense Multipath Channels. *IEEE Journal on Selected Areas in Communications*, 23(9):1863–1874, 2005.

[QWD07] T. Q. S. Quek, M. Z. Win, and D. Dardari. Unified analysis of UWB transmitted-reference schemes in the presence of narrowband interference. *IEEE Transactions on Wireless Communications*, 6(6):2126–2139, 2007.

[RE04] P. Rouzet and J. Ellis. P802.15.4a Alt PHY Selection Criteria. In *IEEE 802.15-04-0232-16-004a*, San Antonio, TX, Nov. 2004.

[RH07] F. Römer and M. Haardt. Deterministic Cramér-Rao Bounds for strict sense non-circular sources. In *Proc. International ITG/IEEE Workshop on Smart Antennas (WSA 2007)*, Vienna, Austria, Feb 2007.

[RK03] J. Romme and B. Kull. On the relation between bandwidth and robustness of indoor UWB communication. In *2003 IEEE Conference on Ultra Wideband Systems and Technologies*, pages 255–259, 2003.

[Ros73] G. F. Ross. Transmission and reception system for generating and receiving base-band duration pulse signals without distortion for short base-band pulse communication system, April 1973.

[SC07] R. Singh and A. Chaturvedi. Suitability of FH Codes as TH Codes for Multiuser UWB Systems. In *2nd International Conference on Communication Systems Software and Middleware (COMSWARE 2007)*, pages 1–7, 2007.

[Sch82] R. Scholtz. The origins of spread-spectrum communications. *IEEE Transactions on Communications*, 30(5):822–854, 1982.

[Sch93] R. A. Scholtz. Multiple Access with Time-Hopping Impulse Modulation. In *Military Communications Conference*, volume 2, 1993.

[SD84] A. A. Shaar and P. A. Davies. A survey of one-coincidence sequences for frequency-hopped spread-spectrum systems. *IEE Proceedings for Communications, Radar and Signal Processing*, 131(7):719–724, 1984.

[SGL04] R. Schober, W. H. Gerstacker, and L. H. J. Lampe. Data-aided and blind stochastic gradient algorithms for widely linear MMSE MAI suppression for DS-CDMA. *IEEE Transactions on Signal Processing*, 52(3):746–756, March 2004.

[SR99] Y. Song and S. Roy. Blind adaptive reduced-rank detection for DS-CDMA signals in multipath channels. *IEEE Journal on Selected Areas in Communications*, 17(11), 1999.

[SS03] P. J. Schreier and L. L. Scharf. Second-order analysis of improper complex random vectors and processes. *IEEE Transactions on Signal Processing*, 51(3):714–725, March 2003.

[SS10] P. J. Schreier and L. L. Scharf. *Statistical Signal Processing of Complex-Valued Data: The Theory of Improper and Noncircular Signals*. Cambridge University Press, 2010.

[Sta08] Standard ECMA-368. High Rate Ultra Wideband PHY and MAC Standard. 3rd edition, December 2008.

[SUCH10] Y. S. Shen, F. B. Ueng, J. D. Chen, and S. T. Huang. A High-Capacity TH Multiple Access UWB System with Performance Analysis. *IEEE Transactions on Vehicular Technology*, 59(2):742 – 753, Feb 2010.

[SV87] A. Saleh and R. Valenzuela. A statistical model for indoor multipath propagation. *IEEE Journal on Selected Areas in Communications*, 5(2):128–137, 1987.

[SW07] C. Steiner and A. Wittneben. On the interference robustness of ultra-wideband energy detection receivers. In *IEEE International Conference on Ultra-Wideband.*, pages 721–726, Singapore, 2007.

[SZ08] S. H. Song and Q. T. Zhang. TH-CDMA-PPM with noncoherent detection for low rate WPAN. *IEEE Transactions on Wireless Communications*, 7(2):446–451, 2008.

[TGM06] F. Tufvesson, S. Gezici, and A. F. Molisch. Ultra-Wideband Communications using Hybrid Matched Filter Correlation Receivers. *IEEE Transactions on Wireless Communications*, 5(11):3119–3129, 2006.

[TM04] F. Tufvesson and A. F. Molisch. Ultra-Wideband Communication using Hybrid Matched Filter Correlation Receivers. *IEEE 59th Vehicular Technology Conference (VTC Spring 2004)*, 3, 2004.

[TS00] H. Trigui and D. Slock. Performance bounds for cochannel interference cancellation within the current GSM standard. *Signal processing*, 80(7):1335–1346, 2000.

[TXS07] J. Tang, Z. Xu, and B. M. Sadler. Performance Analysis of b-bit Digital Receivers for TR-UWB Systems with Inter-Pulse Interference. *IEEE Transactions on Wireless Communications*, 6(2):494–505, 2007.

[vdB94] A. van den Bos. Complex gradient and Hessian. In *IEE Proceedings Vision, Image and Signal Processing*, volume 141, pages 380–383, 1994.

[VLD06] Y. Vanderperren, G. Leus, and W. Dehaene. An Approach for Specifying the ADC and AGC Requirements for UWB Digital Receivers. In *The Institution of Engineering and Technology Seminar on Ultra Wideband Systems, Technologies and Applications*, pages 196–200, 2006.

[Wah09] T. Waho. Chapter 15. Analog-to-Digital Converters for UWB. In R. Kraemer and M. D. Katz, editors, *Short-Range Wireless Communications: Emerging Technologies and Applications*. Wiley, 2009.

[Wal99] R. H. Walden. Analog-to-digital converter survey and analysis. *IEEE Journal on Selected Areas in Communications*, 17(4):539–550, 1999.

[WdL10] L. Wang and R. C. de Lamare. Robust auxiliary vector filtering algorithm based on constrained constant modulus design for adaptive beamforming. In *IEEE International Conference on Acoustics Speech and Signal Processing (ICASSP)*, pages 2530–2533, Dallas, TX, 2010.

[WGH05] M. Wolf, G. Del Galdo, and M. Haardt. Performance Evaluation of Ultra-Wide Band Compared to Wireless Infrared Communications. In *European Conference on Wireless Technology (ECWT 2005)*, Paris, France, October 2005. invited paper.

[WH04a] M. Weisenhorn and W. Hirt. Impact of the FCC average- and peak power constraints on the power of UWB radio signals. *IBM Research Report RZ3544, IBM Zurich Research Laboratory*, Sept. 2004.

[WH04b] M. Weisenhorn and W. Hirt. Robust Noncoherent Receiver Exploiting UWB Channel Properties. *2004 International Workshop on Joint UWBST & IWUWBS.*, pages 156–160, 2004.

[wla99] Part 11: Wireless LAN Medium Access Control (MAC) and Physical Layer (PHY) specifications High-speed Physical Layer in the 5 GHz Band, 1999.

[WLJ+09] K. Witrisal, G. Leus, G. J. M. Janssen, M. Pausini, F. Trösch, T. Zasowski, and J. Romme. Noncoherent Ultra-Wideband Systems: An Overview of Recent Research Activities. *IEEE Signal Processing Magazine*, July 2009.

[WLPK05] K. Witrisal, G. Leus, M. Pausini, and C. Krall. Equivalent System Model and Equalization of Differential Impulse Radio UWB Systems. *IEEE Journal on Selected Areas in Communications*, 23(9):1851–1862, 2005.

[WP98] X. Wang and H. V. Poor. Blind multiuser detection: a subspace approach. *IEEE Transactions on Information Theory*, 44(2):677–690, 1998.

[WS98] M. Z. Win and R. A. Scholtz. Impulse radio: How it works. *IEEE Communications Letters*, 2(2):36–38, 1998.

[WS02] M. Z. Win and R. A. Scholtz. Ultra-wide bandwidth time-hopping spread-spectrum impulse radio for wireless multiple-access communications. *IEEE Transactions on Communications*, 48(4):679–689, 2002.

[WTDG06] X. Wu, Z. Tian, T. N. Davidson, and G. B. Giannakis. Optimal waveform design for UWB radios. *IEEE Transactions on Signal Processing*, 54(6):2009–2021, 2006.

[ZL08] Q. F. Zhou and F. C. M. Lau. Analytical performance of M-ary time-hopping orthogonal PPM UWB systems under multiple access interference. *IEEE Transactions on Communications*, 56(11):1780–1784, 2008.

[ZOM+07] S. Zhao, P. Orlik, A. F. Molisch, H. Liu, and J. Zhang. Hybrid ultrawideband modulations compatible for both coherent and transmit-reference receivers. *IEEE Transactions on Wireless Communications*, 6(7):2551–2559, 2007.

[ZZG03] Z. Zhang, F. Zeng, and L. Ge. Correlation Properties of Time-Hopping Sequences for Impulse Radio. *IEEE International Conference on Acoustics, Speech, and Signal Processing (ICASSP 2003)*, 4, 2003.

Miscellaneous

[nso]